Solvothermal Synthesis of Oxides for Catalysis

by

Daniel Sean Cook

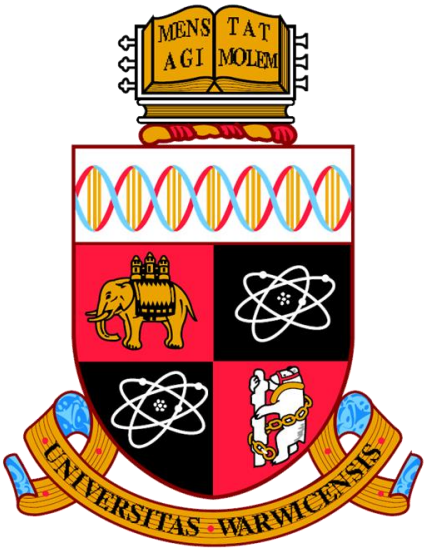

Thesis

Submitted to the University of Warwick

for the degree of

Doctor of Philosophy

September 2017

Contents

Acknowledgements

Richard, it is not possible for me to convey my gratitude to you in just one paragraph of a thesis acknowledgements section. Thank you for all the marvellous opportunities you've given me during my time at Warwick. It has been a real pleasure and privilege to have been a part of your group for these last 4 years. Thank you for your unwavering support, encouragement, enthusiasm, your eternal optimism, and for believing in me! Thanks for the project: I hope it's been as interesting to you as it has been to me. Thank you for taking me on, and with that in mind I also thank Ann Chippindale for suggesting I go to Warwick for an interview in the first place.

Thank you to Janet Fisher and David Thompsett for your supervision, useful discussions and enthusiasm in my project. The trips to Johnson Matthey Technology Centre were fun and provided a fascinating insight to industrial chemistry. I am thankful to others at Johnson Matthey who helped conduct catalysis experiments: Kerry Simmance, Mark Feaviour, and Pilar Gomez-Jimenez - thank you for all your help and support.

I thank all members of the Walton group past and present for all the good and fun memories. Thanks for all the help, advice and useful discussions along the way. Luke, Dave and Lucy – I've cherished our friendship and hope it continues long after I've left. Thanks to Luke for teaching me everything, and Dave for teaching me everything else. Thank you, Lucy, for listening to me practice my talks over and over.

I am immensely grateful to all technical staff at Warwick for their assistance and expertise throughout the duration of this project. In particular, I thank David Walker and Dave Hammond. I am also enormously thankful to the beamline scientists at central facilities who have helped enormously with data collection, setting up experiments and in some cases helping to understand the results. In particular, I thank Oxana Magdysyuk, Helen Playford, Giannantonio Cibin, and Diego Gianolio. I am thankful to Karla Lienau and Greta Patzke in Zürich for running photocatalysis measurements and I am thankful to Daniel Dawson and Joseph Hooper at St. Andrews for measuring the solid-state MAS NMR on many of my samples.

Thanks to James Crosland for all the TGA collection, Alex Dunn for SEM imaging, and thanks to Reza Jalilikashtiban for teaching me about TEM and colleting many of the images shown in this thesis. Thanks to Jason Noone for your support in particular during my second year. A big thank you to Lucy and Andrew for letting me stay at yours during the thesis write-up period!

A big thank you to Felicity and Roger for your guidance and wisdom, and for taking an interest in my education. Thanks for the lovely dinners and music we've enjoyed this summer! Most importantly thanks for your friendship and constant support.

Thanks to Matthew Ball-Jones for your wit, friendship, and for the regular (chemistry) chats over beer(s) in Birmingham pubs during these last four years! Thanks to my friends Thomas Thrower, Louis Malyon and Matthew Kibble for all the fun times, and for getting me out the house this summer! Thanks to Thomas Hood, the Chaplin group past and present, and Scott Dwyer for all the memories we've shared at Warwick.

Thanks to my brother for finding me a new hobby this summer and getting me away from writing at the computer from time to time – I wish you all the best in Canada.

Thanks to Nan Ena and Nan Sheila for all the love and support over the last four years, (and thanks to Nan Ena for all the tea making, and ice creams I've enjoyed over this summer…)

A huge thanks to my parents for the endless love and encouragement and support. I would not have made it to the end without you. Thank you so much for everything.

Finally, thank you again to everyone, for everything over the last four years and for giving me the best four years of my life so far.

Declarations

This thesis is submitted to the University of Warwick in support of my application for the degree of Doctor of Philosophy. The thesis has been composed by myself and has not been submitted at any other academic institution or submitted in any previous application for any degree.

The work presented in this thesis has been carried out by the author except when duly stated otherwise in the text.

A part of this thesis has been published, and it is expected that further work from this thesis will be published in due course.

1. "Time-Resolved Powder X-ray Diffraction of the Solvothermal Crystallisation of Cobalt Gallate Spinel Photocatalyst Reveals Transient Layered Double Hydroxides" D.S. Cook, Y. Wu, K. Lienau, R. Moré, R.J. Kashtiban, O.V. Magdysyuk, G.R. Patzke and R.I. Walton**,** *Chem. Mater.* **29** (2017) 5053−5057.

In addition, the following publications arose through collaboration where the author performed data collection and analysis during the course of the work presented in this thesis.

1. "$Ag_2Cu_3Cr_2O_8(OH)_4$: A New Bidimensional Silver-Copper Mixed-Oxyhydroxide with In-plane Ferromagnetic Coupling" N. Casañ-Pastor, J. Rius, O. Vallcorba, I. Peral, J. Oró-Solé, A. García, D.S. Cook, R.I. Walton and D. Muñoz-Rojas, *Dalton Trans.* **46** (2017) 1093-1104.
2. "A NMR Crystallography Study of the Hemihydrate of 2', 3'-O-Isopropylidineguanosine" G.N.M. Reddy, D.S. Cook**,** R.I. Walton, A. Marsh, S. P. Brown, *Solid State Nucl. Magn. Reson.* **65** (2015) 41–48.

Abstract

Hydro(solvo)thermal synthesis was used to synthesise a range of oxide, oxyhydroxide and hydroxide materials. Their structures were characterised by a wide variety of diffraction, spectroscopic, and other analytical techniques. Many of the oxides were screened for potential applications in catalysis.

High energy X-ray diffraction was used to follow *in situ* the crystallisation of a cobalt gallium oxide prepared from metallic gallium in ethanolamine. Two transient metastable layered double hydroxide phases were observed prior to the formation of the spinel product when a solvent of 1:1 water:ethanolamine mixture was used. Photocatalytic studies showed that the spinel had activity as a water oxidation catalyst.

A different cobalt gallium oxide spinel was prepared by solvothermal reaction using pre-formed γ-Ga_2O_3 and a solution of Co^{2+}. Its metastable structure was characterised by a variety of techniques including analysis of Bragg and diffuse neutron scattering data. The material was investigated for three-way catalysis.

The polymorphism of $Ga_{2-x}Al_xO_3$ was investigated and the structures of materials characterised. The solvothermal synthesis of the defect spinel γ-$Ga_{2-x}Al_xO_3$ in 2-propanol was optimised for 240 °C with up to 90% of the Ga replaced by Al. A novel oxyhydroxide $Ga_{5-x}Al_xO_7(OH)$ was prepared by solvothermal reaction in 1,4-butanediol. Solid-state MAS NMR was used to determine the coordination of the metals in these materials. All the materials are found to be metastable, transforming into thermodynamically stable polymorphs above 1400 °C. Ga_2O_3 and $Ga_{2-x}Al_xO_3$ polymorphs were tested as palladium supports in the diesel oxidation reaction and the semi-hydrogenation of acetylene.

A novel oxyhydroxide, $Ga_{2.52}V_{2.48}O_{7.31}(OH)_{0.69}$, was prepared by reaction of Ga metal and Na_3VO_4 in a 1:1 ethanolamine:water mixture. The structure of this material was investigated by neutron diffraction and found to isostructural with the minerals tohdite and nolanite. The material is metastable, dehydrating around 300 °C to form $Ga_{2.52}V_{2.48}O_8$, and then decomposing above 500 °C. The material was found to show good activity as a catalyst for oxidative propane dehydrogenation.

A new chromium substituted γ-Ga_2O_3 has been prepared and characterised. This material was prepared by solvothermal reaction in 1,4-butanediol and found to be very poorly crystalline. The spinel is stable to 900 °C before phase separating into its respective binary oxides.

The hydrothermal reaction of $RhCl_3 \cdot 3H_2O$ with AO_2 or $A(OH)_2$ (A = Ca, Sr, Ba) in either NaOH or KOH at 200 °C yielded a range of hydroxides. $Ca_3Rh_2(OH)_{12}$ and $Sr_3Rh_2(OH)_{12}$ are hydrogarnets which can be dehydrated to oxides on heating. A new hydroxide in the system Ca-Na-Rh-OH was synthesised. Reaction with barium salts in NaOH yielded $BaNaRh(OH)_6$ a new hydroxide. The structure of this material was solved by single crystal diffraction and found to contain isolated Rh-OH octahedra, two crystallographically different 8 coordinate Na sites and a 10 coordinate Ba site.

Chapter 1: Introduction

1. Introduction

1.1 Metal oxides as supports for precious metals

The study of catalysis remains at the forefront of scientific research in the chemical, physical and material sciences. The importance of heterogenous catalysis to industry cannot be stressed enough. Some examples include ammonia synthesis (Haber process), hydrogenation of fatty acids (for margarine production), hydroformylation of propene, sulfuric acid synthesis (Contact process), nitric acid synthesis, (Ostwald process), steam reforming (for hydrogen production) and the Ziegler-Natta polymerisation of olefins. Of particular importance is the use of heterogeneous catalysis for the mitigation of vehicle exhaust fumes. With ever increasing stringent emissions legislation on petrol and diesel vehicles, research into the discovery and design of new catalysts with improved function remains strongly active. For example, the current legislation in Europe, the so-called Euro6b, requires a 56% reduction in NO_x compared to the previous stage of legislation.[1] The use of precious metals, which includes the platinum group metals: Ru, Rh, Pd, Ir, and Pt in catalysis such as in vehicle exhaust catalytic convertor systems for example, (Figure 1.1), is well documented.[2–12] In the 2017 status report by Johnson-Matthey PLC the gross demand for precious metals for the autocatalysis industry remained highest representing just over 40% the total supply compared to the jewellery, industrial and investment demand.

Although there is a move to electric powered cars which will remove some of the necessity of these catalytic systems (by 2040 the sale of all new diesel and petrol vehicles in the UK will be banned), there will still be a drive to produce catalysts which will produce cleaner emissions when fuel is burnt for a long time to come.

The study of bulk oxide catalysts, such as $LaRhO_3$ and $SrRuO_3$,[13,14] initiated in the 1970s, revealed that platinum-group metal ions may have a catalytic advantage over the metallic state metals. Whilst bulk oxides of the precious metals have been studied as catalysts the routine employment of such oxides is not economically viable. The more familiar use of the platinum-group metals in catalysis is when highly dispersed over a relevant metal oxide support. The types of support vary but γ-Al_2O_3 is very

widely used for such purpose,[5] but other oxides[15] including TiO_2,[16] SiO_2,[17,18] ZrO_2[19] among others such as Fe_3O_4,[20] and zeolites[21,22] are commonly employed as supports.

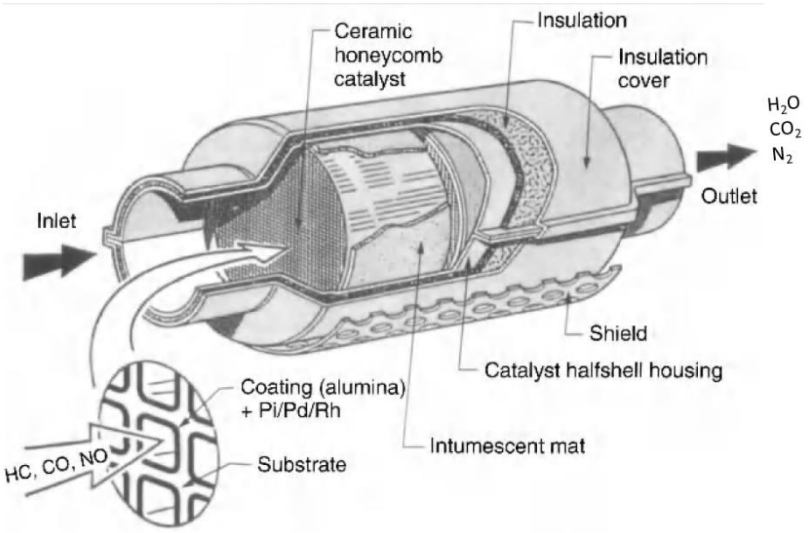

Figure 1.1 Schematic of a typical catalytic convertor system in a vehicle. Reproduced and modified from Heck *et al*.[23] HC refers to hydrocarbons.

The most common metals used in heterogeneous catalysts are the platinum-group metals Pd, Pt and Rh, and these are typically supported on a γ-Al_2O_3 coated monolith.[9,12] For example, alumina supported Pd and Pt are excellent catalysts for CO and hydrocarbon oxidation in the diesel oxidation system and, whilst Rh is occasionally used too for this catalyst since it can provide stability to Pt-based diesel oxidation catalysts,[23] it is more frequently found in the three-way catalyst system in petrol engines for reduction of NO_x.[9]

As well as supporting platinum-group metals, alumina supported metallic Co or Co_3O_4 are of importance in heterogeneous catalysis, for example in the Fisher-Tropsch reaction,[5,24–26] (a collection of reactions by where liquid hydrocarbons are prepared from CO and H_2 over a catalyst). Much focus remains on the study of Co deposition on the oxide surface, whilst other studies regard the formation and elucidation of the active Co species. As an example, the temperature at which the wet impregnation method is carried out influences whether $Co(OH)_2$ or $CoAl_2O_4$ predominates on the surface.[27]

The catalytic activity of a metal is crucially determined by its oxidation state, an example is found in hydrocarbon oxidation where the platinum-group metals show very different activities depending on their oxidation state.[28] The operation

temperature also has a profound effect on the catalytic performance of the precious metal.[29] Palladium catalysts are affected by high temperatures as PdO is reduced to the metallic state, decreasing its activity.[30] Furthermore, palladium catalysts are more strongly affected by sulfur oxides, a common catalyst poison in diesel oxidation systems, as PdO interacts with both SO_2 and SO_3.[31] Where high levels of sulfur oxides are present often Pt-catalysts are required. There is ongoing research suggesting the sulfur also strongly interacts with the alumina support material also leading to catalyst deactivation.[32]

The activity of the active component usually depends on how it is introduced on to the support with the major route being wet-impregnation, though homogeneous deposition-precipitation, and ion-exchange are other techniques used.[5]

The choice of alumina as a support for catalysis is based on a variety of reasons aside from the obvious reasons of its being cheap and readily available. It is selected for its textural properties: γ-Al_2O_3 can be prepared with very high surface areas, and its pore volume and pore size distribution tuned for its application. The surface chemical composition and local microstructure affect the acid-base characteristics of the oxide, a property which again can be modified by the method of fabrication.[4,5] The support itself is not only a carrier for the active compounds and the interaction between the metal and the support is also very important affecting the dispersion of the metal, which may help to supress sintering at high temperatures, in turn enhancing catalytic performance and durability.[4] The interaction between the precious metal and the support must be neither too strong nor weak for good catalytic activity. For example, it has been found that too strong an interaction inhibits the catalytic activity of the catalyst Pt(1%)/$Ce_{0.6}Zr_{0.4}O_2$ when reduced at 1050 °C, as inward diffusion of Pt occurs reducing the amount of surface active Pt.[33]

In another example, sintering of Ag nano-particles supported on cerium oxide, CeO_2, was suppressed enhancing catalytic activity, compared to larger Ag particles, owing to a stronger metal-support interaction; the support acting as an anchor for Ag.[34] The interaction between metal and support can also influence properties of the support itself. For example, Pd, Pt and Rh supported on CeO_2 is well-known to promote the reduction of surface oxygen of CeO_2.[35]

Exposure of Rh/Al_2O_3 catalysts under oxidising conditions not only causes loss of the active area by particle growth but also by inward diffusion into the bulk of the support and furthermore, Rh is cited to react with Al_2O_3 forming rhodium aluminate.[36]

1.2 Overview of hydro(solvo)thermal synthesis and its application to catalyst preparation

In this thesis, the majority of materials that are presented were prepared under hydro or solvothermal conditions. In some instances, materials that were precursors to other functional oxides were prepared hydro(solvo)thermally. This method of preparation features heavily throughout this thesis and so a brief overview of the technique is presented.

Hydrothermal synthesis may be described simply as a reaction between reagents in water in a sealed vessel above the boiling point.[37] Alternatively, if a solvent other than water is used then the synthesis is described as solvothermal and the temperature adjusted to be above the boiling point of the solvent used. Upon heating above the boiling point an autogenous pressure develops within the reaction vessel, and this pressure will be dependent on the temperature used and the fill in the autoclave.

Usually no external pressure is applied. It takes its name from geothermal conditions by where many minerals in the Earth's crust may form under these sort of conditions.[38] Early important examples of this technique were used to synthesize microcrystalline quartz and in the mid-20th century to synthesize $Cr^{IV}O_2$ (reaction scheme 1) the latter which was hugely important in the recording industry as CrO_2 is ferromagnetic and was used as a magnetic recording medium.[39]

$$Cr_2O_3 + CrO_3 \xrightarrow[H_2O]{350\ ^\circ C;\ 440\ bar} 3Cr^{IV}O_2$$

Reaction scheme 1.1

As well as mineral analogues and dense metal oxides, hydro(solvo)thermal synthesis is widely employed in the synthesis of porous materials such as zeolites, and metal-organic frameworks (MOFs).[40–43]

Reagents which are often insoluble in the solvent at room temperature and pressure are solubilised under the solvothermal conditions and then upon reaction form insoluble materials which crystallise out of solution.[44] Often a mineraliser is

introduced into the reaction to aid solubilisation. Hydrothermal synthesis has many advantages over the traditional high temperature procedures, the so called "ceramic" method. In the ceramic method, solid reagents are usually ground mechanically so that, ideally, they are well mixed and often the ground precursor powder is pressed into a pellet. The powder, or pellet, is then placed inside a furnace and heated to temperatures usually in excess of 1000 °C in order to aid diffusion between the grains of the reagents at the interface. Often repeated cycles of this are required in order to synthesise a homogenous material and reaction times of days or weeks are common.[45] Owing to the high temperatures used it is difficult to control particle size and shape as sintering and agglomeration occurs at these high temperatures. Inert or reactive gases are frequently needed to prepare materials other than oxides.

The lower temperatures and milder conditions of hydrothermal reactions in particular the use of a solvent as a reaction medium offer scope for control over particle size and morphology[46,47] which can sometimes be tuned by addition of additives[48] or by adjusting the pH of the reaction medium.[49] This is of huge importance in the catalysis industry where nano-crystalline materials with high surface areas are highly desirable. It is in part for this reason why hydrothermal synthesis was used in this work since many of the materials synthesised were made with interest in their application in catalysis.

The lower temperatures of hydrothermal synthesis also offer scope for the formation of new metastable materials which would not normally be accessible from the ceramic method since the high temperatures used often results in isolation of only the thermodynamically stable material.[50,51] The low temperature used has been cited by some to hail hydrothermal synthesis as a "green" chemistry route, which is attractive in industry.

Other advantages of hydro(solvo)thermal reactions are that quite often the materials are prepared directly, that is, no post-synthetic annealing is required, which is often a necessary step in other *chimie-douce* methods such as sol-gel.[52–54]

The role of precursor and solvent are often very important in the formation of crystalline materials from hydro(solvo)thermal synthesis. Often the choice of precursor dictates the oxidation state of the final product formed, occasionally allowing access to metals in unusual oxidation states.[55] This is especially true for the

hydrothermal synthesis of some manganese and some ruthenium containing materials (Table 1.1). The choice of reagent can also have an effect on the crystallinity of the material formed. The choice of solvent also can play an active as well as passive role in the synthesis. For example, in the solvothermal synthesis of a glycol derivative of boehmite using glycols and aluminium isopropoxide the number of carbons in the glycol chain was found to be important: a chain of 4 carbons allowed formation of a 5-membered ring transition state allowing heterolytic cleavage of C-O in the C-O-Al bond, yielding $^{-}$O-Al. Longer and shorter chains proved ineffective in the synthesis.[53]

Table 1.1 Some examples of transition metal containing materials in different oxidation states, formed from careful choice of precursor.

Product	Metal oxidation state	Precursor	Solvent	Reference
MnO	+2	$Mn(ac)_2$	Benzyl alcohol	[56]
Mn_3O_4	+2.67	$Mn(acac)_2$	Benzyl alcohol	[56]
$SrMn(OH)_6$	+2	$MnCl_2 \cdot 4H_2O$	H_2O	[57]
$Na_2Mn_3O_7$	+4	MnO_2	H_2O	[57]
$Sr_5(MnO_4)OH$	+5	$KMnO_4$	H_2O	[57]
$La_{0.5}Ba_{0.5}MnO_3$	+3.5	$MnSO_4 \cdot H_2O + KMnO_4$	H_2O	[58]
$Ca_{1.5}Ru_2O_7$	+5.5	$KRuO_4$	H_2O	[55]
$SrRu_2O_6$	+5	$KRuO_4$	H_2O	[55]
$Ba_2Ru_3O_9(OH)$	+5	$KRuO_4$	H_2O	[55]

It is not too unusual to find examples where hydrothermal reactions are performed at high temperatures (~400-900 °C)[39,59] though typically the standard temperature used in many hydrothermal reactions is 240 °C. This is because the cup in which reactions are performed is usually made from Teflon, (PTFE), which begins to melt and deform above 250 °C.

1.3 Synthesis of γ-Al_2O_3

Polymorphs of Al_2O_3 are traditionally prepared by thermal dehydration of aluminium hydroxides and oxyhydroxides.[60,61] Since there are at least 11 known Al_2O_3 polymorphs the choice of precursor and temperature becomes very important when preparing a certain polymorph. γ-Al_2O_3 can be prepared from the oxyhydroxide boehmite, AlOOH, and is reported to appear as a crystalline phase between 350 – 1200 °C.[5] γ-Al_2O_3 has a cubic defect spinel (Section 1.6.2), with a cubic close packed oxide lattice. Whilst hydrothermal synthesis typically favours the formation of

aluminium oxyhydroxides,[62,63] the works of Inoue *et al.* have shown that γ-Al_2O_3 can be prepared from solvothermal synthesis from $Al(O\text{-}iPr)_3$ in some organic solvents at a temperature of 300 °C.[64]

1.4 Non-platinum metal group oxides as heterogeneous catalysts.

Metal oxide spinels are not restricted to just being a support for the active catalyst component and have found use as catalysts themselves. Examples include the use of γ-Al_2O_3-Ga_2O_3 which has found remarkable activity when employed as a catalyst in selective NO reduction in the presence of hydrocarbons.[64–67] Further details on this catalyst is found in Chapter 4.

Rare-earth perovskite single crystals containing manganese and cobalt were found to rival platinum in CO oxidation in vehicle exhaust emissions.[68] It has been noted by other authors that these single crystal perovskites were prepared in platinum crucibles which may have led to contamination by the catalytically-active platinum metal.[7]

Nano-crystalline CeO_2 has been prepared by a hydrothermal method for use in the catalytic oxidation of volatile aromatic compounds (VOCs),[69] whilst copper oxide, CuO, supported on ceria zirconia, $Ce_xZr_{1-x}O_2$ (x = 0.8) has also been prepared by a hydrothermal method for this application.[70] A copper containing catalyst was prepared by a high temperature hydrothermal reaction (500 °C) and found to have a high activity in converting NO_x to N_2 (>90%).[71]

1.5 Platinum group metal substituted oxides for catalysis

In order to counter sintering, ablation and catalyst deactivation often it is found that high loadings of the precious metal must be used to provide a catalyst which is durable and has adequate activity over its lifetime.[7] Substitution of precious metals into oxide hosts offers an effective strategy in an attempt to overcome these issues.

Isovalent, or aliovalent substitution of a precious metal for a cation in an oxide presents an alternative method to supporting precious metals on an oxide surface for use in heterogeneous catalysis. The redox properties of CeO_2 have led to wide-spread industrial application of it in diesel oxidation, three-way catalysis, and other heterogeneous catalysis systems.[3,72] Whilst platinum-group metals dispersed on the surface of cerium oxide have been found to improve the low temperature reducibility

of ceria, incorporation of these platinum-group metals into the oxide lattice also offers improvement on the mobility of the oxide by direct causation of formation of oxide vacancies or other lattice distortions.[73]

Among the preparative techniques of substituted cerias, including sol-gel and solution combustion, hydrothermal synthesis features quite regularly.[74] A wide range of metals from all parts of the Periodic Table have been substituted into CeO_2[51] of which many can be incorporated using mild hydrothermal synthesis. In terms of precious metals ruthenium has been incorporated into CeO_2 by mild hydrothermal synthesis, whilst a recent publication shows that up to ~15% Pd^{2+} in a square planar geometry can be incorporated into CeO_2.[75] The incorporation of palladium into ceria leads to low temperature, <200 °C, reduction of the oxide.

1.6 Introduction to spinels and their applications

1.6.1 The spinel structure

Spinels feature widely throughout this thesis and so it is worthwhile providing an introduction to the structure and synthesis of spinels.

Spinel is the name given to the mineral $MgAl_2O_4$. The spinel oxides are a large family of materials usually found in the cubic space group $Fd\bar{3}m$. The spinel structure consists of a close packed array of anions with cations occupying the tetrahedral and octahedral interstitials, (Figure 1.2 and Table 1.2).[76] Most frequently the composition of the spinel contains divalent and trivalent cations, the latter of which is usually twice the amount of the former, but binary metal oxides and metals in higher or lower oxidation states than +2 and +3 can also adopt the spinel structure.[77,78] For the oxides, AB_2O_4, there is great flexibility in the arrangement of cations which can range from a normal spinel, to a fully inverse spinel, or an arrangement in between the two extremes. A normal spinel contains divalent cations on the tetrahedral 8a site and trivalent cations on the octahedral 16d site. An inverse spinel has the tetrahedral 8a site fully occupied by half the total amount of trivalent cations, whilst the remaining trivalent and all the divalent cations occupy the octahedral 16d site. Spinels in between normal and inverse have a random distribution of metal cations. The degree to which a spinel is inverted can be quantified by the inversion parameter, *x*, such that

$^{IV}(A_{1-x}B_x)^{VI}[A_xB_{2-x}]O_4$ (*i.e.* the inversion parameter is the total amount of trivalent cation on the tetrahedral site), therefore $x = 0$ represents a normal spinel and $x = 1$ a fully inverse spinel. Cation distribution in spinels has been studied intensively and can often be rationalised by taking into account the Madelung potential,[79–83] anion polaraization,[84] ionic radii, the covalent contribution to chemical bonds[82] and crystal field theory.[79] Crystal field theory is routinely used to predict the cation site preference if transition metal ions are involved. The cation arrangement in the spinel is also influenced by the synthesis procedure and so the cation distribution can also be sensitive to temperature and pressure.[85] The cationic distribution is also sensitive to and influenced by crystallite sizes and a cationic rearrangement can be very different at the nano-scale compared to larger crystallites.

Table 1.2 Ideal crystal parameters for a spinel in space group $Fd\bar{3}m$

		Coordinates		
Site	**Wyckoff position**	**x**	**y**	**z**
A	8a	0.125	0.125	0.125
B	16d	0.5	0.5	0.5
O	32e	0.375*	0.375*	0.375*

*0.375 represents a perfect cubic close packing of oxygen atoms, the atomic coordinates of the oxide may deviate from these positions in reality.

.

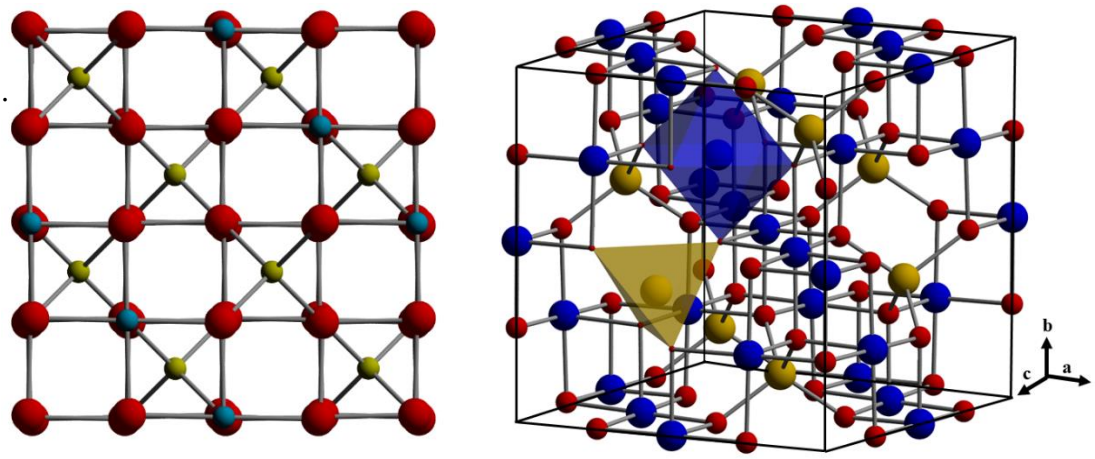

Figure 1.2 *(left)* The normal cubic spinel structure and *(right)* unit cell of a spinel displaying a tetrahedral and octahedral unit. Yellow spheres are the divalent metal occupying tetrahedral sites and blue spheres the trivalent cations on octahedral sites, red spheres are oxygen.

Spinel oxides containing at least one transition metal have attracted a great deal of attention in both fundamental and practical areas of material science research[86] and are routinely employed for catalytic applications.[87–89] This is largely due to their interesting electronic and magnetic properties, which is a consequence of the type of

metals present and their arrangement within the structure. Owing to the flexibility of the spinel structure the cation distribution can often be tuned to tailor the properties of the oxide, for example, by adapting the synthetic approach. In particular, magnetic properties are very sensitive to the cation distribution and knowledge of, and how to control, the inherent crystal structure can forecast the magnetic property.[90]

1.6.2 Defect spinels

If only trivalent cations are present, then the defect spinel is adopted that is deficient in metal cations, (*e.g.* some binary metals sesquioxides of the general form M_2O_3, such as γ-Al_2O_3 or γ-Ga_2O_3, which can be written as γ-$\square_{0.33}M_{2.67}O_4$, where □ represents vacant sites in the structure). The trivalent cation may still be distributed over tetrahedral and octahedral sites.

γ-Al_2O_3 is an important oxide for it is routinely employed as a support for dispersed precious metals in many areas of catalysis. This is elaborated upon in Chapter 4 so no further discussion will provided here. γ-Ga_2O_3 has only found limited use as a support for precious metals though there has been a recent surge in interest owing to the formation of intermetallic Ga-Pd compounds that can form when Ga_2O_3 supports with Pd are reduced *in situ*.[91] Again, further discussion on this is found in Chapter 4 and so it is not the purpose to discuss catalysis with these defect spinels here. Important to the current discussion is that both γ-Al_2O_3 and γ-Ga_2O_3 adopt the defect spinel structure. The defect spinel structure is also found for some first-row transition metals: γ-Fe_2O_3, maghemite, and γ-Mn_2O_3 both adopt the defect spinel structure.

Is it interesting to note that all known defect spinels, that is of Al, Ga, Fe and Mn are metastable polymorphs transforming to different polymorphs at higher temperature and therefore low temperature techniques are required to form them. γ-Al_2O_3 transforms into the well-known and well-studied α-Al_2O_3 (corundum), whilst γ-Ga_2O_3 transforms into β-Ga_2O_3 a material well studied for power devices [92,93] since it has a large band gap of ~4.7 eV. γ-Fe_2O_3 becomes α-Fe_2O_3 (corundum) when calcined vigorously in air, and γ-Mn_2O_3 can be converted into the black Mn_3O_4 (hausmannite) above 1000 °C. Mn_3O_4 is also a spinel though there is, however, a tetragonal distortion due to the Jahn-Teller d^4 Mn^{3+} cation. Among the first-row transition metals the cubic bixbyite M_2O_3 polymorph is more prevalent (Figure 1.3 and Table 1.3). This structure type is adopted by both β-Fe_2O_3 and α-Mn_2O_3 (in fact the mineral bixbyite is an oxide

of manganese usually stabilised by the presence of iron: $(Mn, Fe)_2O_3$) and contains only 6-coordinate metals. For Mn_2O_3 the bixbyite structure is more thermally stable than the defect spinel polymorph though both eventually convert to Mn_3O_4 above 1000 °C. The most common structure found for the sesquioxide formulation, M_2O_3, is certainly the corundum structure which is adopted by many first-row transition metals (Figure 1.3 and Table 1.3). Unlike its Group 13 congeners indium does not crystallise in a binary defect spinel probably due to its larger size but does adopt both the bixbyite and corundum type polymorphs. Indium can, however, be incorporated into the defect spinel structure for example as found in the defect spinel systems γ-Al_2O_3-Ga_2O_3-In_2O_3[94] and γ-Ga_2O_3-In_2O_3, where it resides in octahedral sites.[95]

Table 1.3 Common sesquioxide phases adopted by first row transition metal oxides and oxides of Group 13 metals.

M_2O_3 polymorph	**Ti_2O_3**	**V_2O_3**	**Cr_2O_3**	**Mn_2O_3**	**Fe_2O_3**	**Al_2O_3**	**Ga_2O_3**	**In_2O_3**
Corundum	×	×	×	×	×	×	×	×
Bixbyite		×		×	×	×		×
Spinel				×	×	×	×	

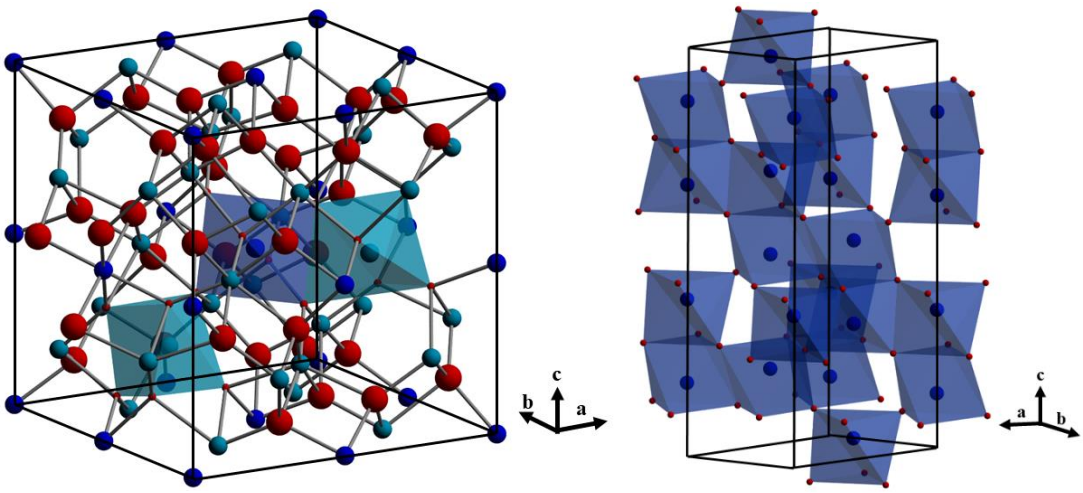

Figure 1.3 *(left)* α-Mn_2O_3 bixbyite-type structure showing two crystallographically different Mn^{3+} cations, *(right)* α-Al_2O_3 corundum-type structure, with and blue spheres trivalent cations in octahedral coordination. Both structures show there is edge-sharing and face-sharing octahedra.

Whilst vanadium was only known until recently to crystallise in the corundum structure type a metastable bixbyite polymorph has been prepared via a high-pressure synthesis.[96] V_2O_3 is not known to crystallise with the defect spinel structure but the defect spinel $AlVO_3$ has been synthesised. 2/3 of available Al^{3+} cations on the tetrahedral sites with the rest of the Al^{3+} together with all the V^{3+} cations randomised on the octahedral sites.[97] Other mixed-metal defect spinels are known such as the partially defective $Mg_{0.3388}Al_{2.408}O_4$ prepared at a temperature of 2050 °C.[98]

Defect spinel oxides of lithium and manganese, for example $\{\square_{0.15}Li_{0.85}\}[Mn_{1.74}Li_{0.26}O_4]$, have been investigated as insertion electrodes for rechargeable lithium batteries.[99]

No known defect spinels are known for the binary oxides of the 2nd and 3rd row transition elements, the reasons are probably two-fold: a larger cation size, and an increased crystal field stabilisation energy would not favour the tetrahedral coordination required in the spinel. Furthermore, the binary oxide chemistry of the platinum group metals is much less structurally diverse than the first-row metals in general owing to their oxophobic nature. Au for example is not known to form any binary oxides at ambient pressure. Bixbyite and corundum type structures for 2nd and 3rd row transition metals are known which includes the platinum group metals (one polymorph of Rh_2O_3 has the corundum structure type).[100,101]

Sesquioxides with purely tetrahedral coordination do not exist: Au_2O_3 crystallising in an orthorhombic cell with space group $Fdd2$ has 4-coordination but contains square planar Au^{3+}.[102]

1.7 Solvothermal synthesis and catalysis of Fe_2O_3 and Mn_2O_3 defect spinels

Fe_3O_4 can be oxidised to γ-Fe_2O_3 under carefully controlled oxidation environments. For example, acicular γ-Fe_2O_3 nanoparticles, required for magnetic data storage, are typically prepared by hydrolysis of Fe^{2+} salts, followed by dehydration to α-Fe_2O_3 haematite, followed by reduction to magnetite and then by re-oxidation to γ-Fe_2O_3 maghemite.[103] Thus, there is a desire for a one step synthesis to maghemite. This can be achieved by solvothermal synthesis as Seshadri and co-workers have shown: by solvothermal reaction of iron cupferron complex ($Fe(cupf)_3$) in a solution of toluene and n-octylamine at 220 °C for 1 hour.[104]

Solvothermal synthesis of pure γ-Fe_2O_3 can be problematic due to the possible formation of Fe_3O_4 or the thermodynamically stable α-Fe_2O_3. Synthesis of γ-Fe_2O_3 can be achieved via solvothermal reaction of $Fe(NO_3)_3{\cdot}9H_2O$ dissolved in a solution of ethanol and polyvinylpyrrolidone at 240 °C yielding nano-platelets. These nano-platelets were then shown to be reduced to Fe_3O_4 using hydrazine solution whilst maintaining their nano-plate morphology.[105]

γ-Fe_2O_3 is studied primarily for its use in magnetic applications but finds some use in catalysis. Nanoconfined γ-Fe_2O_3 in a nitrogen doped graphene framework was recently shown to be a highly efficient oxygen reduction catalyst,[106] a critical reaction for electrochemical energy storage in fuel cells.

Whilst solvothermal synthesis of a variety of manganese oxides exists in abundance in the literature (in particular MnO, MnO_2 and Mn_3O_4) there is limited information on solvothermal syntheses of γ-Mn_2O_3. It is usually prepared by firing MnO_2 in air at 800 °C[107] but the material suffers from sintering and agglomeration which is undesirable for catalytic applications. A low temperature solvothermal route takes β-MnO_2 and reacts it with ethanol under solvothermal conditions at 130 °C.[108]

Polymorphs of Mn_2O_3 have found application as catalysts for removing CO and NO_x from waste gases,[109] as an oxygen storage component for a three-way catalyst,[110] but

it is most widely researched for its use in battery materials as precursor to lithium intercalated manganese oxide compounds.[107,111]

1.8 Solvothermal synthesis of AB_2O_4 and ternary spinels and their catalytic and energy applications

Mixed metal spinels find application in a variety of catalysis[5,67,86] and the following provides a mini-review into the solvothermal synthesis of ternary spinel oxides and their application in heterogeneous catalysis. The solvothermal synthesis of binary and ternary metal oxides is developing as a useful route to obtain oxides, often metastable phases, from low temperature synthesis. The synthesis of nano-scale binary and ternary metal oxides by non-aqueous synthesis (sol-gel, surfactant-assisted, solvothermal *etc.*) was reviewed extensively by Pinna and Niederberger.[112] The same authors have also published work regarding the solvothermal synthesis of CoO, ZnO, Fe_3O_4, MnO, Mn_3O_4 and $BaTiO_3$ from reaction in benzyl alcohol in a "one-minute synthesis."[56]

1.8.1 Ferrites and cobaltites

Fe_3O_4 and mixed-metal spinels with iron are well-studied for their magnetic properties and it is not the purpose to review that here. Instead the focus of these spinels is their application to catalysis and energy applications.

Niederberger reported that Fe_3O_4 can be synthesised under microwave-solvothermal conditions using $Fe(acac)_2$, $Fe(acac)_3$ or $Fe(ac)_2$ using benzyl alcohol as the solvent.[56] However, another solvothermal preparation is to take $FeCl_3 \cdot 6H_2O$ and dissolve it in diglycol prior to addition of sodium acetate.[113] Whilst stirred vigorously at room temperature the orange solution turns black, presumably amorphous Fe_3O_4, which becomes crystalline Fe_3O_4 after solvothermal treatment at 200 °C forming hexagonal nano-plates of about 100 nm in diameter. More recently, a very similar method but using polyvinylpyrrolidone instead of diglycol was found to produce porous magnetite, which served as effective recyclable catalysts for the degradation of xylenol orange.[114] Fe_3O_4 encapsulated in a shell of amorphous carbon has been produced from simple solvothermal reaction with a tuneable size of the Fe_3O_4 core made possible by changing the amount of glucose used in the reaction. The iron core is protected from degradation and agglomeration by the carbon shell. The material is useful for

removing toxic Cr^{6+} from waste solvents by adsorption of the ion onto the surface of the carbon shell.[115]

As for Fe_3O_4, nano-particles of mixed-metal ferrites AFe_2O_4 (*A* = Mn, Co and Ni) can be prepared by a simple modification of the benzyl alcohol method using acetylacetonate salts of the transition metals and reacting them between 180 – 190 °C for 24 – 48 h.[116]

$CoFe_2O_4$-TiO_2 nanocomposites have successfully been prepared from a hydrothermal route. This nano-composite showed excellent photocatalytic activity in the photo-degradation of organic dyes.[117]

Hydrothermally prepared $MnFe_2O_4$ has been assessed for its application as a hydrogen storage material, in particular how well MgH_2 is adsorbed on the spinel.[118]

Hydrothermal synthesis of $ZnFe_2O_4$, a normal spinel, has intensified as researchers looks for ways to control particle shape and size for a variety of applications. $ZnFe_2O_4$ has found use as a high capacity anode material for lithium ion batteries,[119] as a heterogeneous catalyst for multi-substituted imidazoles (for anti-inflammatory purposes),[120] as a heterogeneous photo-Fenton catalyst,[121] and as part of a Fe_2O_3-$ZnFe_2O_4$-ZnO composite for the photocatalytic degradation of malachite green in aqueous media.[122] The activity of ferrites prepared by a variety of methods focusing on how the structure/property relationships between method of synthesis and photocatalytic activity was scrutinised in a review in a 2012.[123]

$ZnFe_2O_4$ prepared by hydrothermal synthesis was reported as non-stoichiometric as well as containing a large portion of tetrahedral Fe (*i.e.* more inverse than the usually reported normal spinel structure found for $ZnFe_2O_4$). This sample was applied for the catalytic oxidative dehydrogenation of 1-butene to butadiene and it was found that the activity of the spinel was different dependent on the method of preparation as the choice of synthetic method produced zinc ferrites with differently arranged cations in the structure.[124]

Ni, and Mn substituted Fe_3O_4 have been prepared by hydrothermal synthesis and were tested as catalysts for total oxidation of toluene.[125]

Co_3O_4 is a normal spinel due to the large crystal field stabilisation energy gained from the low-spin Co^{3+} d^6 configuration. This oxide has also been studied for its catalytic applications, in particular it finds use as a water oxidation catalyst in the photocatalytic splitting of water to form O_2 and H_2.[88,126] Nanoscale Co_3O_4 used for this purpose was prepared by hydrothermal treatment of cobalt acetate tetrahydrate in ethanol-water media. The BET surface area and water oxidation activity were found to be very different depending on the duration of the hydrothermal treatment with the surface area generally decreasing with increased reaction time. The O_2 turn-over-frequency (TOF) as might be expected was not determined by surface area alone and a complex interplay of other factors including the morphology, crystallinity, and cobalt valence states ultimately determined the TOF of these cobalt oxide catalysts. Solvothermal synthesis of Co_3O_4 has been studied by other researchers for similar applications[127] with nanoflakes displaying excellent photocatalytic activity,[128] whilst niche applications have been found for flower shaped Co_3O_4 prepared by a two-step solvothermal synthesis from cobalt acetate. These are cited to show remarkable catalytic activity for thermal decomposition of ammonium perchlorate.[129] Incidentally the morphology of nano-cubed Co_3O_4 has been found to show good catalytic activity for oxidation of 1,2-dichloroethane.[130]

Mesoporous $NiCo_2O_4$ was prepared via a facile hydrothermal strategy by dissolving the respective metal nitrates in water, followed by addition of dilute sodium hydroxide and then heated under autogenous pressure at 140 °C for 12 h. The catalytic behaviour for methanol electro-oxidation and hydrogen peroxide electro-reduction was tested and the high activity for both reactions suggested that the spinel should be considered for further development as a non-Pt catalyst for alkaline fuel cell applications.[131]

Hydrothermal synthesis has been employed in the development of $FeCo_2O_4$ and $MnCo_2O_4$ spinels with the former applied for electrode materials in lithium ion batteries[132] and the latter for supercapacitor applications,[133] but also as a catalyst for the oxygen evolution reaction (OER) and oxygen reduction reaction (ORR).[134] As has been highlighted, the need for hydro(solvo)thermal synthesis for these materials is often a requirement to synthesise mesoporous materials, or for tuning the morphology of the spinel which often has a direct influence on its catalytic properties.

1.8.2 Vanadates and manganates

Vanadium containing spinels have received very little attention for catalysis and are instead researched for their interesting magnetic and electronic properties.[136–138] Solvothermal synthesis using the reagents $VO(acac)_2$ and $ZnCl_2$ in *N*,*N*-dimethyl formamide at 220 °C for 4 h yields ZnV_2O_4. Electron microscopy revealed the formation of spherical hollow particles in the range 0.8-1 μm.[139]

The synthesis of hierarchical ZnV_2O_4 nanospheres was achieved through an involved hydrothermal route: first ammonium metavanadate was dissolved in methanol, followed by sonication, which was then followed by addition of zinc nitrate. Oxalic acid was then added to the reaction mixture as the chelating agent. After equal volumes of hydrogen peroxide and nitric acid were added to the solution the mixture was sealed in a PTFE lined autoclave and reacted at 200 °C for 24 h. Hydrogen storage measurements of these novel hierarchical nanospheres of ZnV_2O_4 suggested this material should be considered for applications in energy storage. [140]

A range of vanadium spinels AV_2O_4 (*A* = Mg, Mn, Fe and Co) have been prepared by a microwave-assisted solvothermal synthesis using vanadium triisopropoxide, and the acetate tetrahydrate of the divalent metal, with tetraethylene glycol as the solvent.[141] A temperature of 300 °C was used and it was found that the reaction dwell significantly affected the crystallinity of the material formed. The CoV_2O_4 prepared by this method was found to be metastable, because it decomposed at high temperatures. It was further claimed that by systematically tuning the V-V distance in the spinels by changing the spinel composition in $Co_{1-x}A_xV_2O_4$ (*A* = Mg, Mn, or Fe) it would be possible to understand the role of V-V distance on localized to itinerant electron transition.

LiV_2O_4 displays heavy fermion behaviour, which is rare to see among *d*-electron metals, whereas most heavy fermions are *f*-electron compounds. In order to study this phenomenon single crystals are required. The first report of single crystal LiV_2O_4 was from a hydrothermal synthesis in 1967.[142] Research remains ongoing into growing crystals of this spinel though researchers have typically moved away from hydrothermal synthesis towards flux reactions.[143]

Manganese oxide spinel, Mn_3O_4, has been studied for a few catalytic applications. For example, Pd supported on Mn_3O_4 has shown tremendous activity for the low

temperature oxidation of CO.[144] Mn_3O_4 outperformed α-Mn_2O_3 and MnO_2 as a catalyst for the decomposition of volatile aromatic compounds (VOCs), in particular benzene and toluene.[145] Mn_3O_4 has been more frequently studied as an electrode material for lithium ion batteries and in high performance supercapacitor applications.[146–148] Nanocrystalline Mn_3O_4 can be prepared by solvothermal reaction of $KMnO_4$ in ethanol,[149,150] or by reduction of $KMnO_4$ in benzyl alcohol also under solvothermal conditions.[151] Mn_3O_4 single crystals can be prepared from a low temperature hydrothermal synthesis in a solution containing hydrated manganese acetate and potassium thiosulfate. The level of oxygen saturation in the solution was identified as a key determinant on whether single crystals of Mn_3O_4 or MnOOH formed.[152]

Mn_3O_4 nanorods on graphene sheets were synthesised from a facile hydrothermal reaction and showed long cycle stability for supercapacitor electrode applications. To synthesise these nanorods, $KMnO_4$ was first added to a solution of suspended graphene particles followed by addition of ethylene glycol. The mixture was then transferred to an autoclave and heated under autogenous pressure at 120 °C for 4 h.[153]

In a very recent study, solvothermally prepared Mn_3O_4 with a sphere-like morphology exhibited the highest activity for methyl-ethyl-ketone oxidation at low temperature when compared against other manganese and iron based catalysts.[155]

γ-MnOOH nanorods have been prepared by a simple hydrothermal route using $KMnO_4$ in a mixed water:ethanol solvent, which upon heat treatment, the nanorods can be transformed into Mn_3O_4. Experiments showed that the spinel had good catalytic activity for oxidation and decomposition of methylene blue dye with H_2O_2.[156]

The spinel $LiMn_2O_4$ has received a great deal of attention as a cathode material in lithium ion applications.[157–159] Nanosized $LiMn_2O_4$ offers improved capacity and rate capability owing to shorter Li diffusion pathways within the particle and hence controlling the particle shape and size becomes important both can often be tuned by hydrothermal synthesis. It is then no surprise that there have been many studies into hydro(solvo)thermal synthesis of $LiMn_2O_4$.[107,160–162] An *in situ* powder X-ray diffraction (PXRD) study of the hydrothermal synthesis of $LiMn_2O_4$ has been reported by Iverson and co-workers.[163] The synthesis of $LiMn_2O_4$ takes place from reduction of $KMnO_4$ in ethanol. At room temperature an exothermic reaction takes place when

ethanol is added to $KMnO_4$ forming disordered δ-MnO_2 (birsennite). The reaction to $LiMn_2O_4$ proceeds first by an ordering of the MnO_2 prior to spinel formation. However, $LiMn_2O_4$ was found to be unstable and prolonged reaction times led to formation of Mn_3O_4 as an impurity phase. These *in situ* experiments can therefore be used to probe reaction kinetics, phase purity control and particle size by analysis of the time resolved X-ray diffraction data, which may often reveal favourable conditions to synthesise materials with desirable textural properties.

1.8.3 Ternary spinels of Group 13

Ternary spinels with metals in Group 13 (Al, Ga and In) can be prepared with the transition metals (Mn, Fe, Co, Ni, Cu and Zn) and also with Mg. The following summarises some recent literature regarding solvothermal synthesis to such spinels and their application to catalysis.

Of particular importance is the aluminium spinel $CoAl_2O_4$ which is a well-studied oxide.[164–170] It has an intense blue colour, Thénard's blue, and early applications of this oxide were largely in ceramics and as a pigment by artists. In terms of catalytic applications $CoAl_2O_4$ has been studied for the selective catalytic reduction, (SCR), of NO_x to N_2 with hydrocarbons,[171] and as a Fisher-Tropsch catalyst.[24] Co supported on Al_2O_3 has also been studied for catalysis applications.[172] $CoAl_2O_4$ has been described as a largely normal spinel with divalent cobalt cations occupying the tetrahedral interstitials and trivalent aluminium cations on the octahedral sites. $CoAl_2O_4$ has been prepared by a variety of solvothermal preparations in the recent literature. One method takes cobalt acetate and aluminium isopropoxide and reacts them in a benzyl alcohol solvent between temperatures of 150 – 300 °C for 2 days. The nanoparticles formed by this method were of an average size between 2.5 – 6.2 nm with reaction temperature controlling the average size.[173]

Rojanapipatkul and co-workers have prepared a Co on $CoAl_2O_4$ catalyst by a similar one-pot solvothermal process using aluminium isopropoxide, cobalt(II) acetylacetonate and reacting them in toluene at 300 °C. The spinel showed higher activities for CO hydrogenation than the conventional solvothermal-derived alumina-supported cobalt catalyst.[174]

Cobalt aluminate nanocrystals have also been reported from hydrothermal synthesis in which the use of an organic additive could provide control over the size and shape of the crystals.[175]

In addition to the ternary oxide $CoAl_2O_4$, a solvothermal approach has been used to synthesise Co_3O_4/Al_2O_3 hollow core-shell microspheres. These hollow core-shell microparticles are prepared by first dissolving aluminium nitrate in water, followed by addition of acetone and trisodium citrate dihydrate. The mixture is stirred vigorously for 30 minutes and then urea is added to the mixture and finally an appropriate amount of cobalt nitrate. The reaction takes place at 200 °C for 24 h. These microstructures were found to show high performance for the catalytic oxidation of CO attributed to their large surface area, high porosity and mesoporous structure.[176]

A microwave-assisted solvothermal synthesis was implemented to synthesise colloidal Pd and a nanocrystalline $ZnAl_2O_4$. After preparation of each material the two were combined to yield a catalyst which showed good activity for light hydrocarbon oxidation.[177] More recently a solvothermal synthesis using 1,4-butanediol was used to react aluminium isopropoxide with zinc acetate at 200 °C to yield nanocrystalline $ZnAl_2O_4$, which when supporting 1% Pt was found to exhibit good activity in *iso*-butane combustion.[178]

Unlike $CoAl_2O_4$, $CoGa_2O_4$ has not been studied as much for catalytic applications, but has been studied for potential magnetic properties and recently as a water oxidation catalyst.[170,179,180] $ZnGa_2O_4$ has been investigated as a photocatalyst for the degradation of benzene,[181] $CuGa_2O_4$ for the photocatalytic evolution of solar hydrogen,[182] and $NiGa_2O_4$ has been applied as a catalyst for the reduction of NO with propene.[183]

Gallium spinels containing a transition metal (Fe, Co, Ni, Zn) can be prepared by solvothermal oxidation of gallium metal in an aminoalcohol based solvent.[184,185]

Hollow rods of nano-crystalline $NiGa_2O_4$ can be prepared hydrothermally directly from commercial Ga_2O_3 and an appropriate Ni reagent. Ga_2O_3 is used as a template as the morphology of the original material is retained after reaction, thus rod-like $NiGa_2O_4$ can be prepared from rod-like Ga_2O_3 (the precursor polymorph is unidentified). The material shows promising photocatalytic activity as a water splitting catalyst when loaded with 1 wt% RuO_2.[186]

A microwave-assisted hydrothermal synthesis was used to prepare spinels with a composition in the system (Co, Mn)Ga_2O_4. These spinels are promising candidates as water oxidation catalysts.[187] The spinels produced from this synthesis contained a high portion of both Co^{3+} and Mn^{3+} and the spinels showing high thermal stability up to 1400 °C.

Microwave-assisted hydrothermal synthesis is becoming an increasingly more popular route to synthesise oxides with energy and time saving attributes considered to be attractive. In recent years this microwave synthesis has lent itself to the preparation of other mixed-metal gallates including $ZnGa_2O_4$,[188,189] and in synthesising a Cu^{2+} doped γ-Ga_2O_3 spinel with the latter considered a preparative challenge by many other synthetic approaches.[190]

1.9 Aims of the work described in this thesis

The primary aim of this work was to investigate the performance of gallium oxides as supports for palladium in catalysis with particular emphasis on γ-Ga_2O_3. A recent detailed study into the structure by analysis of the Bragg and total neutron diffraction data by Rietveld and Monte Carlo simulations have confirmed the structure of γ-Ga_2O_3 to be structurally analogous to γ-Al_2O_3, but with a different distribution of metals occupying octahedral and tetrahedral sites[191,192] and therefore γ-Ga_2O_3 may display interesting and potentially useful catalytic properties when used as a support. Three areas of catalysis were identified for screening samples: diesel oxidation, three-way catalysis and acetylene semi-hydrogenation.

For diesel oxidation the use of three gallium oxide polymorphs was to be examined: α-Ga_2O_3, β-Ga_2O_3 and γ-Ga_2O_3. For three-way catalysis the spinel γ-Ga_2O_3 and a cobalt gallium oxide spinel were to be studied. For semi-hydrogenation of acetylene mixed metal γ-$Ga_{2-x}Al_xO_3$ oxides were to be studied. The latter required an investigation into the synthesis and polymorphism of this system prior to any catalysis as although the polymorphism in Ga_2O_3, and Al_2O_3 is now well-understood an in-depth understanding of the polymorphism in $Ga_{2-x}Al_xO_3$ is currently lacking.

For an in-depth understanding of the catalytic activity of functional oxides it is crucial to understand how these dense oxides crystallise under different reaction conditions. Materials prepared by different reaction techniques often have different catalytic

activities often owing to many different reasons including differences in surface chemistry, and the arrangement of cations in a material. An understanding of this would be highly desirable in that it might provide information on how to alter the synthesis conditions to tailor materials with useful catalytic properties. For this purpose, an investigation into the crystallisation and reaction pathway of a cobalt gallium oxide under solvothermal conditions, the synthesis of which has only recently been reported,[184] was to be investigated using high energy X-rays.

In addition, this solvothermal reaction of mixed metal gallium oxide spinels was to be developed in order to try and synthesise new materials from early first row transition metals.

A series of new Group II ruthenates prepared by hydrothermal reaction of AO_2 (A = Ca, Sr, Ba) with $KRuO_4$ has been investigated recently.[55] Similar reactions were to be investigated with $RhCl_3$ in an attempt to synthesise new oxide materials with interesting magnetic and electronic properties, and potentially catalytic properties.

1.10 References

1 *UK plan for tackling roadside nitrogen dioxide concentrations*, Department for Environment, Food & Rural Affairs, London, 2017.

2 H. C. Yao, H. K. Stepien and H. S. Gandhi, *J. Catal.*, 1980, **61**, 547–550.

3 A. Trovarelli, *Catal. Rev.*, 2017, **38**, 439–520.

4 Z. Tingting, H. E. Junjun, Z. Yunkun, X. I. A. Wenzheng and H. E. J. Б, *J. Rare Earths*, 2014, **32**, 97–107.

5 M. Trueba and S. P. Trasatti, *Eur. J. Inorg. Chem.*, 2005, **2005**, 3393–3403.

6 J. Wang, H. Chen, Z. Hu, M. Yao and Y. Li, *Catal. Rev.*, 2015, **57**, 79–144.

7 J. A. Kurzman, L. M. Misch and R. Seshadri, *Dalton Trans.*, 2013, **42**, 14653–67.

8 H. J. Stein, *Appl. Catal. B Environ.*, 1996, **10**, 69–82.

9 A. Russell and W. S. Epling, *Catal. Rev.*, 2011, **53**, 337–423.

10 D. Dou, *Platin. Met. Rev*, 2012, **56**, 144–154.

11 L. Lizarraga, S. Souentie, A. Boreave, C. George, B. D. Anna, P. Vernoux, B. Lyon and A. A. Einstein, *Environ. Sci. Technol.*, 2011, **45**, 10591–10597.

12 H. S. Gandhi, G. W. Graham and R. W. McCabe, *J. Catal.*, 2003, **216**, 433–442.

13 G. L. Bauerle, J. D. Pinkerton and K. Nobe, *Atmos. Environ.*, 1974, **8**, 217–219.

14 H. S. Gandhi, H. K. Stepien and M. Shelef, *Mat. Res. Bull*, 1975, **10**, 837–846.

15 P. Munnik, P. E. De Jongh and K. P. De Jong, *Chem. Rev.*, 2015, **115**, 6687–6718.

16 P. Weerachawanasak, G. J. Hutchings, J. K. Edwards, S. A. Kondrat, P. J. Miedziak, P. Prasertham and J. Panpranot, *Catal. Today*, 2015, **250**, 218–225.

17 U. Bremen and T. U. Wien, *Appl. Catal. A, Gen.*, 1997, **155**, 75–85.

18 E. V Ramos-Fernandez, J. Ruiz-Martinez, J. C. Serrano-Ruiz, J. Silvestre-Albero, A. Sepulveda-Escribano and F. Rodriguez-Reinoso, *Appl. Catal. A Gen.*, 2011, **402**, 50–58.

19 T. Yamaguchi, *Catal. Today*, 1994, **20**, 199–218.

20 Y. Huang, S. Wang, A. Tsai and S. Kameoka, *J. Power Sources*, 2015, **281**, 138–145.

21 X. Li, C. Liu, J. Sun, H. Xian, Y. Tan, Z. Jiang, A. Taguchi, M. Inoue, Y. Yoneyama, T. Abe and N. Tsubaki, *Sci. Rep.*, 2013, **3**, 1–5.

22 U. Akhmetzyanova, M. Opanasenko, J. Horacek, E. Montanari, J. Cejka and O. Kikhtyanin, *Microporous Mesoporous Mater.*, 2017, **252**, 116–124.

23 R. M. Heck, R. J. Farrauto and S. T. Gulati, *Catalytic Air Pollution Control: Commercial Technology*, Van Nosrand Reinhold, NY, 1995.

24 J. Han, L. Jia, B. Hou, D. Li, Y. Liu and Y. Liu, *J. Fuel Chem. Technol.*, 2015, **43**, 846–851.

25 B. Jager and R. Espinoza, *Catal. Today*, 1995, **23**, 17–28.

26 A. K. Dalai and B. H. Davis, *Appl. Catal. A Gen.*, 2008, **348**, 1–15.

27 J. Vakros, K. Bourikas, S. Perlepes, C. Kordulis and A. Lycourghiotis, *Langmuir*, 2004, **20**, 10542–10550.

28 Y. Y. Yung-Fang, *Ind. Eng. Chem. Prod. Res. Dev*, 1980, **19**, 293–298.

29 T. Watanabe, K. Kawashima, Y. Tagawa, K. Tashiro, H. Anoda, K. Ichioka, S. Sumiya and G. Zhang, *SAE Tech. Pap. Ser.*, 2007, **19**, 1–6.

30 R. J. Farrauto, M. C. Hobson, T. Kennelly and E. M. Waterman, *Appl. Catal. A Gen.*, 1992, **81**, 227–237.

31 A. K. Neyestanaki, F. Klingstedt, T. Salmi and D. Y. Murzin, *Fuel*, 2004, **83**, 395–408.

32 F. C. Galisteo, R. Mariscal, L. Granados, M, M. D. Poves, J. L. G. Fierro, V. Kroege and R. L. Keiski, *Appl. Catal. B Environ.*, 2007, **72**, 272–281.

33 P. Fornasiero, J. Kaspar, V. Sergo and M. Graziani, *J. Catal.*, 1999, **182**, 56–69.

34 J. A. Farmer and C. T. Campbell, *Science.*, 2010, **329**, 933–937.

35 B. B. Harrison, A. F. Diwell and C. Hallett, *Platin. Met. Rev*, 1988, **32**, 73–83.

36 C. Hwang, C. Yeh and Q. Zhu, *Catal. Today*, 1999, **51**, 93–101.

37 A. Rabenau, *Angew. Chem.*, 1985, **24**, 1026–1040.

38 R. A. Laudise, *Chem. Eng. News*, 1987, **65**, 30–43.

39 H. Y. Chen, D. M. Hiller, J. E. Hundson, C. J. A. Westenbroek and E. I. du Pont de Nemours, *IEEE Trans. Magn.*, 1984, **20**, 24–26.

40 C. S. Cundy and P. A. Cox, *Chem. Rev*, 2003, **103**, 663–701.

41 N. Stock and S. Biswas, *Chem. Rev*, 2012, **112**, 933–969.

42 O. M. Yaghi and H. Li, *J. Am. Chem. Soc.*, 1995, **117**, 10401–10402.

43 Y. Lee, J. Kim and W. Ahn, *Korean J. Chem. Eng*, 2013, **30**, 1667–1680.

44 M. Shandilya, R. Rai and J. Singh, *Adv. Appl. Ceram.*, 2016, **115**, 354–376.

45 C. N. R. Rao, *Mater. Sci. Eng.*, 1993, **8**, 1–21.

46 L. Shi, J. Zhang, S. Wu, Y. Li, L. Jiang and Q. Cui, *J. Am. Ceram. Soc.*, 2014, **97**, 2607–2614.

47 Y. Quan, S. Q. Liu, K. L. Huang, D. Fang, X. Y. Zhang and H. W. Hou, *Trans. Nonferrous Met. Soc. China*, 2010, **20**, 1458–1462.

48 K. Sardar, M. R. Lees, R. J. Kashtiban, J. Sloan and R. I. Walton, *Chem. Mater.*, 2011, **23**, 48–56.

49 A. Zhang, J. Zhang, N. Cui, X. Tie, Y. An and L. Li, *J. Mol. Catal. A*, 2009, **304**, 28–32.

50 J. Gopalakrishnan, *Chem. Mater.*, 1995, **7**, 1265–1275.

51 C. I. Hiley and R. I. Walton, *CrystEngComm*, 2016, **18**, 7656–7670.

52 M. Haneda, Y. Kintaichi, H. Shimada and H. Hamada, *Chem. Lett.*, 1998, 27, 181–182.

53 M. Takahashi, N. Inoue, T. Takeguchi, S. Iwamoto, M. Inoue and T. Watanabe, *J.*

Am. Ceram. Soc., 2006, **89**, 2158–2166.

54 S. Ohkoshi, A. Namai, M. Yoshikiyo, K. Imoto, K. Tamazaki, K. Matsuno, O. Inoue, T. Ide, K. Masada, M. Goto, T. Goto, T. Yoshida and T. Miyazaki, *Angew. Chem.*, 2016, **55**, 11403–11406.

55 C. I. Hiley, M. R. Lees, J. M. Fisher, D. Thompsett, S. Agrestini, R. I. Smith and R. I. Walton, *Angew. Chem.*, 2014, **126**, 4512–4516.

56 I. Bilecka, I. Djerdj and M. Niederberger, *Chem. Commun.*, 2008, 886–888.

57 M. W. Chance, PhD Thesis, University of South Carolina, 2014.

58 J. Spooren, R. I. Walton and F. Millange, *J. Mater. Chem.*, 2005, **15**, 1542–1551.

59 V. G. Hill, R. Roy and E. F. Osborn, *J. Am. Ceram. Soc.*, 1952, **35**, 135–142.

60 I. Levin and D. Brandon, *J. Am. Ceram. Soc.*, 1998, **81**, 1995–2012.

61 K. Wefers and C. Misra, *Alcoa Tech. Pap.*, 1987, **19**, 1–100.

62 T. S. Kannan, P. K. Panda and V. A. Jaleel, *J. Mater. Sci. Lett.*, 1997, **16**, 830–834.

63 P. K. Panda, V. A. Jaleel and S. Usha Devi, *J. Mater. Sci.*, 2006, **41**, 8386–8389.

64 M. Takahashi, T. Nakatani, S. Iwamoto, T. Watanabe and M. Inoue, *Appl. Catal. B Environ.*, 2007, **70**, 73–79.

65 T. Masuda, T. Watanabe, Y. Miyahara, S. Iwamoto, H. Kanai and M. Inoue, *J. Mol. Catal. A Chem.*, 2009, **307**, 71–76.

66 T. Nakatani, T. Watanabe, M. Takahashi, Y. Miyahara, H. Deguchi, S. Iwamoto, H. Kanai and M. Inoue, *J. Phys. Chem. A*, 2009, **113**, 7021–7029.

67 T. Masuda, T. Watanabe, Y. Miyahara, H. Kanai and M. Inoue, *Top. Catal.*, 2009, **52**, 699–706.

68 R. J. H. Voorhoeve, J. P. Remeika, P. E. Freeland and B. T. Matthias, *Science.*, 1972, **177**, 353–354.

69 G. Zhou, B. Gui, H. Xie, F. Yang, Y. Chen, S. Chen and X. Zheng, *J. Ind. Eng. Chem.*, 2014, **20**, 160–165.

70 Q. Deng, T. Ren, B. Agula, Y. Liu and Z. Yuan, *J. Ind. Eng. Chem.*, 2014, **20**, 3303–3312.

71 L. Song, Z. Zhan, X. Liu, H. He, W. Qiu and X. Zi, *Chinese J. Catal.*, 2014, **35**, 1030–1035.

72 P. Fornasiero, M. Graziani and J. Kas, *Catal. Today*, 1999, **50**, 285–298.

73 G. B. Balazs and R. S. Glass, *Solid State Ionics*, 1995, **76**, 155–162.

74 K. Yamashita, K. V Ramanujachary and M. Greenblatt, *Solid State Ionics*, 1995, **81**, 53–60.

75 C. I. Hiley, J. M. Fisher, D. Thompsett, R. J. Kashtiban and R. I. Walton, *J. Mater. Chem. A*, 2015, **3**, 13072–13079.

76 K. E. Sickafus, J. M. Wills and N. W. Grimes, *J. Am. Ceram. Soc.*, 2004, **82**, 3279–3292.

77 R. B. Von Dreele and A. Navrotsky, *Acta Crystallogr. Sect. B Struct. Crystallogr.*

Cryst. Chem., 1967, **52**, 2287–2288.

78 A. D. Fortes, *Acta Crystallogr. Sect. E Crystallogr. Commun.*, 2015, **71**, 592–596.

79 A. Miller, *J. Appl. Phys.*, 1959, **30**, S24–S25.

80 H. S. C. O'Neill and A. Navrotsky, *Am. Mineral.*, 1983, **68**, 181–194.

81 P. Piero and A. Anichini, *J.C.S. Faradat I*, 1980, **76**, 2448–2456.

82 J. B. Goodenough and A. L. Loeb, *Phys. Rev.*, 1955, **98**, 391–408.

83 C. Otero Arean and E. Garcia Diaz, *Mater. Chem.*, 1982, **7**, 675–683.

84 J. Smit, *Solid State Commun.*, 1968, **6**, 745–746.

85 K. Datta, R and R. Rustum, *J. Am. Ceram. Soc.*, 1967, **50**, 578–583.

86 N. W. Grimes, *Phys. Technol.*, 1975, **6**, 22–27.

87 I. E. Wachs and K. Routray, *ACS Catal.*, 2012, **2**, 1235–1246.

88 F. Conrad, M. Bauer, D. Sheptyakov, S. Weyeneth, D. Jaeger, K. Hametner, P.-E. Car, J. Patscheider, D. Günther and G. R. Patzke, *RSC Adv.*, 2012, **2**, 3076–3082.

89 F. Conrad, Y. Zhou, M. Yulikov, K. Hametner, S. Weyeneth, G. Jeschke, D. Günther, J. D. Grunwaldt and G. R. Patzke, *Eur. J. Inorg. Chem.*, 2010, **13**, 2036–2043.

90 A. Nakatsuka, Y. Ikeda, Y. Yamasaki, N. Nakayama and T. Mizota, *Solid State Commun.*, 2003, **128**, 85–90.

91 K. Föttinger, *Catal. Today*, 2013, **208**, 106–112.

92 A. E. Romanov, S. I. Stepanov, V. I. Nikolaev and V. E. Bougrov, *Rev. Adv. Mater. Sci*, 2016, **44**, 63–86.

93 M. Higashiwaki, K. Sasaki, H. Murakami, Y. Kumagai, A. Koukitu, A. Kuramata, T. Masui and S. Yamakoshi, *Semicond. Sci. Technol.*, 2016, **31**, 34001.

94 S. Tan, S. Kim, J. S. Moore, Y. Liu, R. S. Dixit, J. G. Pendergast, D. S. Sholl, S. Nair and C. W. Jones, *ChemCatChem*, 2016, **8**, 214–221.

95 S. Tan, L. Briones, N. Subramanian, D. S. Sholl, S. Nair, C. W. Jones, J. S. Moore, Y. Liu, R. S. Dixit and J. G. Pendergast, *Appl. Catal. A, Gen.*, 2015, **498**, 167–175.

96 D. Weber, A. Stork, S. Nakhal, C. Wessel, C. Reimann, W. Hermes, T. Ressler, T. Bredow, R. Dronskowski and M. Lerch, *Inorg. Chem*, 2011, **50**, 6762–6766.

97 A. F. Reid and T. M. Sabine, *J. Solid State Chem.*, 1970, **208**, 203–208.

98 R. Basso, S. Carbonin and A. D. Guista, *Z. Krist.*, 1991, **194**, 111–119.

99 M. M. Thackeray, A. de Kock and W. I. F. David, *Mat. Res. Bull*, 1993, **28**, 1041–1049.

100 J. W. M. Biesterbos and J. Hornstra, *J. Less-Common Met.*, 1973, **30**, 121–125.

101 S. Musić, A. Šarić, S. Popović and M. Ivanda, *J. Mol. Struct.*, 2009, **924**–**926**, 221–224.

102 B. Y. P. G. Jones, H. Rumpel, E. Schwarzmann and G. M. Sheldrick, *Acta Cryst*, 1979, **B35**, 1435–1437.

103 A. Tasaki, S. Harada and T. Kusunose, *IEEE Trans. Magn.*, 1981, **17**, 3026–3028.

104 S. Thimmaiah, M. Rajamathi, N. Singh, P. Bera, F. Meldrum, N. Chandrasekhar and R. Seshadri, *J. Mater. Chem.*, 2001, **11**, 3215–3221.

105 J. Lu, X. Jiao, D. Chen and W. Li, *J. Phys. Chem. C*, 2009, **113**, 4012–4017.

106 K. Qiu, G. Chai, C. Jiang, M. Ling, J. Tang and Z. Guo, *ACS Catal.*, 2016, **6**, 3558–3568.

107 M. Tabuchi, K. Ado, H. Kobayashi, H. Kageyama, C. Masquelier, A. Kondo and R. Kanno, *J. Electrochem. Soc*, 1998, **145**, 49–52.

108 W. He, Y. Zhang, X. Zhang, H. Wang and H. Yan, *J. Cryst. Growth*, 2003, **252**, 285–288.

109 Â. M. Gallardo, M. Baldi, V. Sanchez, F. Milella and G. Busca, *Appl. Catal. B Environ.*, 1998, **17**, 175–182.

110 Y. Chang and J. G. Mccarty, *Catal. Today*, 1996, **30**, 163–170.

111 T. Nakamura and A. Kajiyama, *Solid State Ionics*, 1999, **124**, 45–52.

112 M. Niederberger and N. Pinna, *Metal Oxide Nanoparticles in Organic Solvents: Synthesis, Formation, Assemby and Application*, Springer Science & Business Media, London, 2009.

113 W. Zhang, H. Xiao, L. Zhu and S. Fu, *J. Alloys Compd.*, 2009, **477**, 736–738.

114 M. Zhu and G. Diao, *J. Phys. Chem. C*, 2011, **115**, 18923–18934.

115 A. Lapresta-fernández, T. Doussineau and S. Dutz, *Nanotechnology*, 2012, **23**, 165601.

116 S. Yanez-Vilar, M. Sanchez-Andujar, C. Gomez-Aguirre, J. Mira, M. A. Senaris-Rodriguez and S. Castro-Garcia, *J. Solid State Chem.*, 2009, **182**, 2685–2690.

117 S. Masoud and M. Payam, *J. Mater. Sci. Mater. Electron.*, 2016, **27**, 4879–4886.

118 N. H. Idris, N. S. Mustafa and M. Ismail, *Int. J. Hydrogen Energy*, 2017, **42**, 21114–21120.

119 Z. Xing, Z. Ju, J. Yang, H. Xu and Y. Qian, *Nano. Res*, 2012, **5**, 477–485.

120 A. A. Marzouk and A. M. Abu, *Appl. Organomet. Chem.*, 2017, 1–15.

121 C. G. Anchieta, A. Cancelier, M. A. Mazutti, S. L. Jahn, R. C. Kuhn, A. Guendel, O. Chiavone-Filho and E. L. Foletto, *Materials.*, 2014, **7**, 6281–6290.

122 J. P. Dhal, B. G. Mishra and G. Hota, *RSC Adv.*, 2015, **5**, 58072–58083.

123 E. Casbeer, V. K. Sharma and X. Li, *Sep. Purif. Technol.*, 2012, **87**, 1–14.

124 J. A. Toledo-antonio, N. Nava, M. Mart and X. Bokhimi, *Appl. Catal. A Gen.*, 2002, **234**, 137–144.

125 M. Florea, M. Alifanti, V. I. Parvulescu, D. Mihaila-tarabasanu and L. Diamandescu, *Catal. Today*, 2009, **141**, 361–366.

126 H. Liu and G. R. Patzke, *Chem. Asian J*, 2014, **9**, 2249–2259.

127 L. Zhang, H. Li, K. Li, L. Li, J. Wei, L. Feng and Q. Fu, *J. Alloys Compd.*, 2016, **680**, 146–154.

128 S. Yan, L. Zhou, Y. Shi, Z. Cao, D. Hu and X. Xu, *J. Green Sci. Technol.*, 2013, 1, 131–135.

129 S. Jamil, M. Ramzan, S. Ashraf and T. Ahmad, *Solid State Sci.*, 2014, **36**, 73–79.

130 J. Gonzalez-Prior, R. Lopez-Fonseca, J. I. Gutierrez and B. de Rivas, *Appl. Catal. B, Environ.*, 2016, **199**, 384–393.

131 R. Ding, L. Qi, M. Jia and H. Wang, *Catal. Sci. Technol.*, 2013, **3**, 3207–3215.

132 S. G. Mohamed, C. Chen, C. K. Chen, S. Hu and R. Liu, *Appl. Mater. Interfaces*, 2014, **6**, 22701–22708.

133 N. Padmanathan and S. Selladurai, *Ionics.*, 2014, **20**, 479–487.

134 L. Sun, L. Cong, X. Gao, C. Yao, X. Guo, L. Tai, P. Mei, Y. Zeng, H. Xie and R. Wang, *J. Phys. Chem. C*, 2013, **117**, 25890.

135 J. Zhu and Q. Gao, *Microporous Mesoporous Mater.*, 2009, **124**, 144–152.

136 H. Marniya and M. Onoda, *Solid State Commun.*, 1995, **95**, 217–221.

137 O. Tchernyshyov, *Phys. Rev. Lett.*, 2004, **93**, 157206.

138 D. B. Rogers, R. J. Arnott, A. Wold and J. B. Goodenough, *J. Phys. Chem. Solids*, 1963, **24**, 347–360.

139 F. Duan, Q. Zhang, C. Wei, D. Shi and M. Chen, *Mater. Lett.*, 2013, **92**, 231–234.

140 F. K. Butt, M. Tahir, C. Cao, F. Idrees, R. Ahmed, W. S. Khan, N. Mahmood, M. Tanveer, A. Mahmood and I. Aslam, *ACS Appl. Mater. Interfaces*, 2014, **6**, 13635–13641.

141 A. Gutierrez and A. Manthiram, *Inorg. Chem.*, 2014, **4**, 2–8.

142 D. B. Rogers, J. L. Gillson and T. E. Gier, *Solid State Commun.*, 1967, **5**, 263–265.

143 O. Liv, Y. Matsushita, H. Ueda and Y. Ueda, *Nat. Mater.*, 2005, **4**, 845–850.

144 G. Li, L. Li, Y. Yuan, Y. Yuan, Y. Li, W. Zhao and J. Shi, *RSC Adv.*, 2014, **4**, 35762–35768.

145 S. C. Kim and W. G. Shim, *Appl. Catal. B Environ.*, 2010, **98**, 180–185.

146 S. Nagamuthu, S. Vijayakumar and G. Muralidharan, *Energy Fuels*, 2013, **27**, 3508–3515.

147 J. Gao, M. A. Lowe and D. Abru, *Chem. Mater.*, 2011, **23**, 3223–3227.

148 L. Yang, S. Cheng, X. Ji, Y. Jiang and M. Liu, *J. Mater. Chem. A*, 2015, **3**, 7338–7344.

149 Z. Weixin, W. Cheng, Z. Xiaoming, X. Yi and Q. Yitai, *Solid State Ionics*, 1999, **117**, 331–335.

150 W. Zhang, Z. Yang, Y. Liu, S. Tang, X. Han and M. Chen, *J. Cryst. Growth*, 2004, **263**, 394–399.

151 I. Djerdj, D. Arcon, Z. Jaglicic and M. Niederberger, *J. Phys. Chem. C*, 2007, **111**, 3614–3623.

152 C. Hu, Y. Wu and K. Chang, *Chem. Mater*, 2008, **20**, 2890–2894.

153 J. W. Lee, A. S. Hall, J. Kim and T. E. Mallouk, *Chem. Mater*, 2012, **24**, 1158–

1164.

154 Z. Wan and J. Wang, *J Chem Technol Biotechnol*, 2017, **92**, 874–833.

155 H. Pan, Y. Jian, C. Chen, C. He, Z. Hao, Z. Shen and H. Liu, *Environ. Sci. Technol.*, 2017, **51**, 6288–6297.

156 Z. Yang, Y. Zhang, W. Zhang, X. Wang, Y. Qian, X. Wen and S. Yang, *J. Solid State Chem.*, 2006, **179**, 679–684.

157 T. Yi, Y. Zhu, X. Zhu, J. Shu, C.-B. Yue and A.-N. Zhou, *Ionics.*, 2009, **15**, 779–784.

158 M. M. Thackeray, P. J. Johnson, L. A. de Picciotto, P. G. Bruce and J. B. Goodenough, *Mat. Res. Bull*, 1984, **19**, 179–187.

159 M. Lanz, C. Kormann, H. Steininger, G. Heil, O. Haas and P. Novák, *J. Electrochem. Soc.*, 2000, **147**, 3997–4000.

160 E. Hosono, T. Kudo, I. Honma, H. Matsuda and H. Zhou, *Nano Lett.*, 2009, **9**, 1045–1051.

161 H. Yue, X. Huang, D. Lv and Y. Yang, *Electrochim. Acta*, 2009, **54**, 5363–5367.

162 X. Lv, S. Chen, C. Chen, L. Liu, F. Liu and G. Qiu, *Solid State Sci.*, 2014, **31**, 16–23.

163 S. Birgisson, K. Marie, Ø. Jensen, T. L. Christiansen, J. F. Von Bülow and B. B. Iversen, *Dalt. Trans.*, 2014, **43**, 15075–15084.

164 W. Li, J. Li and J. Guo, *J. Eur. Ceram. Soc.*, 2003, **23**, 2289–2295.

165 C. O. Areán, M. P. Mentruit, E. E. Platero, F. X. L. I. X. Xamena and J. B. Parra, *Mater. Lett.*, 1999, **39**, 22–27.

166 L. Xu, J. Zhang, F. Wang, K. Yuan, L. Wang, K. Wu, G. Xu and W. Chen, *RSC Adv.*, 2015, **5**, 48256–48268.

167 T. Suzuki, H. Nagai, M. Nohara and H. Takagi, *J. Phys. Condens. Matter*, 2007, **19**, 145265.

168 Z. Chen, E. Shi, W. Li, Y. Zheng and W. Zhong, *Mater. Lett.*, 2002, **55**, 281–284.

169 D. M. A. Melo, J. D. Cunha, J. D. G. Fernandes, M. I. Bernardi, M. A. F. Melo and A. E. Martinelli, *Mater. Res. Bull.*, 2003, **38**, 1559–1564.

170 Z. Xu, S. C. Yan, Z. Shi, Y. F. Yao, P. Zhou, H. Y. Wang and Z. G. Zou, *ACS Appl. Mater. Interfaces*, 2016, **8**, 12887–12893.

171 M. M. Azis and D. Creaser, *Catal. Sci. Technol.*, 2015, **5**, 296–309.

172 L. Ji, J. Lin and H. C. Zeng, *J. Phys. Chem. B*, 2000, **104**, 1783–1790.

173 M. Karmaoui, O. Silva, N, J, V. S. Amaral, A. Ibarra, A. Millan and F. Palacio, *Nanoscale*, 2013, **5**, 4277–4283.

174 S. Rojanapipatkul and B. Jongsomjit, *Catal. Commun.*, 2008, **10**, 232–236.

175 D. Rangappa, S. Ohara, T. Naka and A. Kondo, *J. Mater. Chem.*, 2007, **17**, 4426–4429.

176 L. Zhang, T. Liu, X. Zhao, N. Qian, P. Xiong and W. Ma, *CrystEngComm*, 2014, **16**, 6126–6134.

177 M. Zawadzki, *J. Alloys Compd.*, 2007, **439**, 312–320.

178 W. Staszak, M. Zawadzki and J. Okal, *J. Alloys Compd.*, 2010, **492**, 500–507.

179 D. Fiorani and S. Viticoli, *Solid State Commun.*, 1978, **25**, 155–157.

180 J. L. Soubeyroux, D. Fiorani and E. Agostinelli, *J. Magn. Magn. Mater.*, 1986, **54**–**57**, 83–84.

181 X. Chen, H. Xue, Z. Li, L. Wu, X. Wang and X. Fu, *J. Phys. Chem. C*, 2008, **112**, 20393–20397.

182 K. Gurunathan, J. O. Baeg, S. M. Lee, E. Subramanian, S. J. Moon and K. jeong Kong, *Int. J. Hydrogen Energy*, 2008, **33**, 2646–2652.

183 L. Chen, T. Horiuchi and T. Mori, *Appl. Catal. A Gen.*, 2001, **209**, 97–105.

184 H. Y. Playford, A. C. Hannon, M. G. Tucker, M. R. Lees and R. I. Walton, *J. Phys. Condens. Matter*, 2013, **25**, 454212.

185 D. L. Burnett, M. H. Harunsani, R. J. Kashtiban, H. Y. Playford, J. Sloan, A. C. Hannon and R. I. Walton, *J. Solid State Chem.*, 2014, **214**, 30–37.

186 H. Xue, Z. Li, Z. Ding, L. Wu, X. Wang and X. Fu, *Cryst. Growth Des.*, 2008, **8**, 4511–4516.

187 F. Conrad, M. Bauer, D. Sheptyakov, S. Weyeneth, D. Jaeger and P. Car, *RSC Adv.*, 2012, **2**, 3076–3082.

188 M. Sun, D. Li, W. Zhang, Z. Chen, H. Huang, W. Li, Y. He and X. Fu, *J. Solid State Chem.*, 2012, **190**, 135–142.

189 F. Conrad, C. Massue, K. Stefanie, E. Kunkes, F. Girgsdies, I. Kasatkin, B. Zhang, M. Friedrich, Y. Luo, M. Armbr, R. Patzke and M. Behrens, *Nanoscale*, 2012, **4**, 2018–2028.

190 F. Conrad, M. Bauer, S. Weyeneth, Y. Zhou, K. Hametner, D. Günther and G. R. Patzke, *Solid State Sci.*, 2013, **24**, 125–132.

191 H. Y. Playford, A. C. Hannon, M. G. Tucker, D. M. Dawson, S. E. Ashbrook, R. J. Kastiban, J. Sloan and R. I. Walton, *J. Phys. Chem. C*, 2014, **118**, 16188−16198.

192 H. Y. Playford, A. C. Hannon, E. R. Barney and R. I. Walton, *Chem. Eur. J*, 2013, **19**, 2803–2813.

Chapter 2: Experimental

2. Experimental

2.1 General overview

In this chapter a brief description of the experimental techniques that were used in this work are outlined.

2.2 Hydro(solvo)thermal synthesis

In this thesis most hydro(solvo)thermal reactions presented took place inside 23 ml PTFE lined cups, with fill volumes typically 10-12 ml. These were then placed into a stainless-steel autoclave and sealed first with a PTFE lid. On top of this is placed a steel cap, a thin corrosion disc and then a thicker bursting disc. Since the thermal coefficient of PTFE is much greater than steel a spring loaded top lid is placed on top of everything else to maintain constant pressure on the PTFE cup. A schematic of the autoclave reaction vessel is given in Figure 2.1 This fully sealed autoclave was then placed inside a pre-heated oven at the desired temperature and heated for however long was required. The autoclaves were removed and left to cool naturally to room temperature and the solid materials formed were collected by either vacuum filtration or by centrifugation (depending on particle size). Since the conditions required to synthesise the materials in this work are highly specific to each reaction no further detail will be provided here: instead a synthesis procedure is given for every material in the relevant section of this thesis.

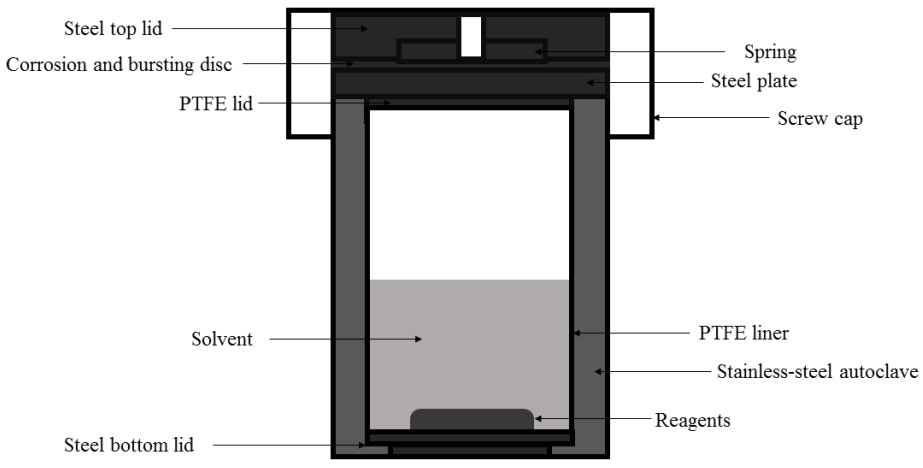

Figure 2.1 Schematic of an autoclave

Typical amounts of material obtained from hydro(solvo)thermal reactions using 23 ml PTFE cups ranged anywhere between 0.01 – 0.8 g, whilst typical amounts of material obtained from reactions in the 100 ml PTFE cups were found to yield anywhere between 0.5 – 5 g. Many hydro(solvo)thermal reactions described in this thesis were found to be reproducible (non-reproducibility of reactions is described where necessary in the experimental section of each chapter). Whilst every effort was provided to ensure or maximise reproducibility (such as using the same autoclave(s) and liner for reactions, using the same oven, the same precursor, the same length of time and temperature, and whether the mixture was stirred on not), other factors may influence the course of and ultimately affect the outcome of the reaction. Such factors include positioning of the autoclave in the oven, and whether the oven door was opened during the reaction causing a small fluctuation in temperature gradient, as well as the duration of cooling down after reaction, and the duration of stirring and stirring vigour and whether the stirrer bar was left in the autoclave during the reaction. Whether and how the reagents were ground and mixed together using a pestle and mortar may also affect the outcome of the reaction.

2.3 Ceramic method

High temperature reactions, whether to bring about reaction between two solid reagents or to cause a change in phase of the starting material, were carried out in box furnaces within a temperature range typically between 700 °C - 1400 °C. Details on individual experiments are provided in the relevant synthesis sections of materials presented in chapters 3, 4, 5 and 6.

2.4 A Brief Overview of Crystallography and X-ray Diffraction

Powder X-ray crystallography was the primary method of characterisation of the materials presented in this thesis and therefore a brief overview of crystallography and diffraction is presented below.

If a solid has a regular periodic repetition of atoms in space, then it is said to possess long range order and is crystalline. The periodicity can be described by a unit cell which is the simplest representation of the ordered arrangement and can be constructed by translational parameters. Six lattice parameters define the unit cell: $a, b, c, \alpha, \beta, \gamma$.

There are seven different crystals systems ranging from cubic with the highest symmetry to triclinic with the lowest, (Table 2.1).

Table 2.1 The seven crystal systems

Crystal system	Unit Cell Parameters	Bravais Lattices
Triclinic	$a \neq b \neq c$, $\alpha \neq \beta \neq \gamma$	*P*
Monoclinic	$a \neq b \neq c$, $\alpha = \gamma = 90°$, $\gamma \neq 90°$	*P, C*
Orthorhombic	$a \neq b \neq c$, $\alpha = \beta = \gamma = 90°$	*P, C, I, F*
Hexagonal/Trigonal	$a = b \neq c$, $\alpha \neq \beta = 90°$, $\gamma = 120°$	*P, R**
Tetragonal	$a = b \neq c$, $\alpha = \beta = \gamma = 90°$	*P, I*
Cubic	$a = b = c$, $\alpha = \beta = \gamma = 90°$	*P, I, F*

* R = Rhombohedral; translational symmetry $(x + {}^{2}/_{3}, y + {}^{1}/_{3}, z + {}^{1}/_{3})$ and $(x + {}^{1}/_{3}, y + {}^{2}/_{3}, z + {}^{2}/_{3})$.

A lattice is a three-dimensional array of points describing the translational symmetry of the crystal. The centring of a lattice can be primitive *(P),* body-centred *(I),* base-centred *(C),* or face-centred *(F)* (Figure 2.2). When combined with the possible centring of points within the unit cell there are then 14 Bravais lattices.

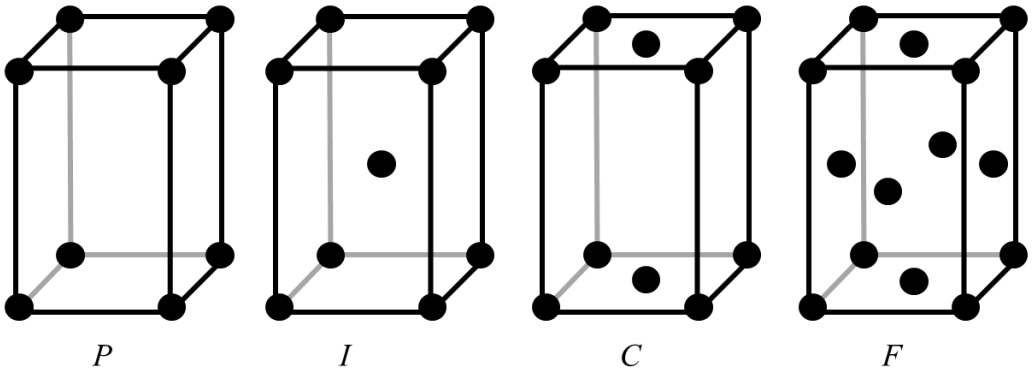

Figure 2.2 The four types of lattice centring

Since not all lattices can be combined with every type of lattice centring to give a unique Bravais lattice as some combinations will lead to duplicates there are only 14 and not 28 as might initially be expected (7 crystal systems and 4 lattice centrings). Other elements of symmetry (rotation, mirror plane, glide plane and screw axis *etc.*) give rise to a space group of which there are 230. The space group $P3_221$ describes a primitive Bravais lattice with a 3_2 screw axis and a 2-fold rotational axis.

This ordered array of atoms can act as a diffraction grating for radiation with a wavelength of an appropriate size such as X-rays. When X-rays are scattered

coherently from interaction with the electron cloud around the nucleus of an atom interference occurs and a diffraction pattern can be measured.

The father and son team, William and Lawrence Bragg first put forward a model for X-ray diffraction from crystals. The Bragg theory requires a crystal to consist of parallel planes of atoms and it is from these planes that X-rays are said to be reflected, (Figure 2.3).[1]

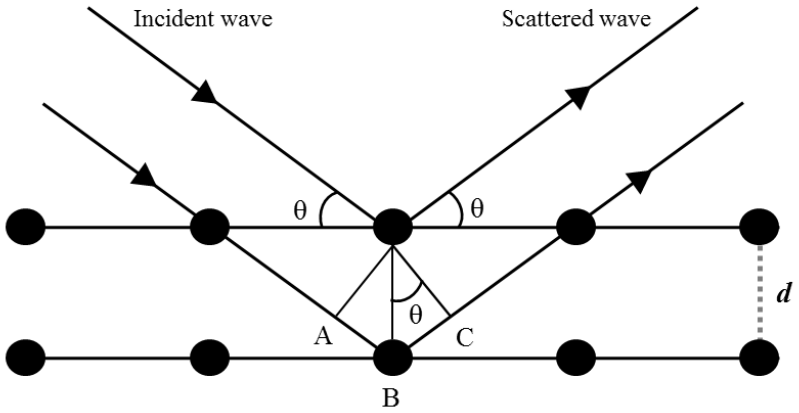

Figure 2.3 Bragg reflection of X-rays from lattice planes within a crystal

In accordance with the Bragg theory, constructive interference of X-rays occurs when X-rays are diffracted from these parallel planes of atoms in a crystal at certain angles of incidence so that they are in phase. The angle at which this constructive interference occurs is dependent on the wavelength of the radiation and the interplanar separation. The incident waves are considered parallel and reflect from a plane. A parallel wave may penetrate further and reflect from the plane below and must travel the extra distance *AB* + *BC*. From trigonometry the *d*-spacing can be determined from this extra path difference (Equation 2.1):

$$AB = dsin(\theta)$$
$$BC = dsin(\theta)$$
$$AB + BC = 2dsin(\theta)$$

Equation 2.1

The scattered waves will be in phase, and hence constructive interference will occur, when the extra path difference travelled is an integer value of λ which gives the Bragg equation, (Equation 2.2):

$$AB + BC = 2dsin(\theta) = n\lambda$$

Equation 2.2

Hence, different interplanar separations, d_{hkl}, can be calculated provided the wavelength is constant and the angle of incidence measured. Different planes will therefore meet the Bragg condition at different angles.

2.4.1 Powder X-ray diffraction

The ideal powder should have a large number of randomly oriented crystallites such that each orientation is represented equally. The X-ray powder diffraction experiment typically records the intensity of the diffracted radiation as a function of 2θ by varying the angle of incidence and the detector angle (the Bragg-Brentano configuration is commonly used). Each lattice spacing produces a cone of diffraction, with 2θ being the angle between the incident and diffracted beam, (Figure 2.4).

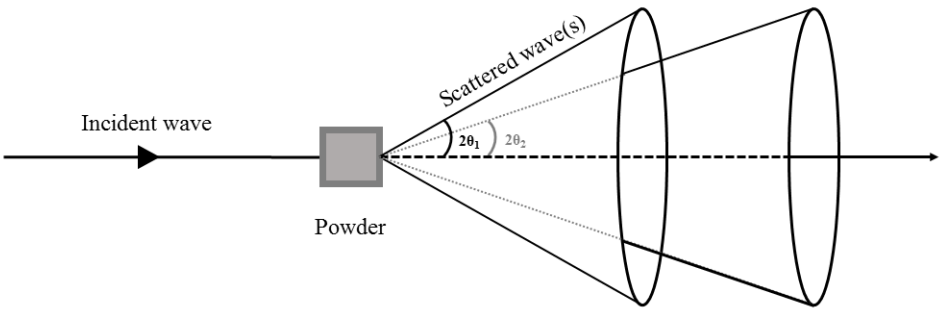

Figure 2.4 Illustration of diffraction from randomly orientated crystallites producing cones of diffraction at different angles.

This is typically represented as a 1-dimensional diffraction pattern with each peak representing a plane of atoms within the unit cell of the crystal. Miller indices can be assigned to these planes, (Figure 2.5).

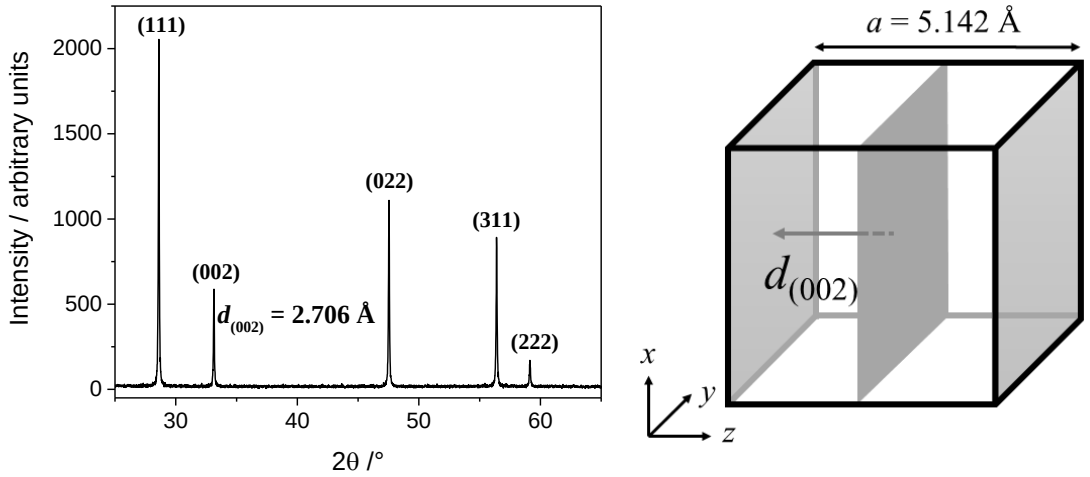

Figure 2.5 Powder pattern of ceria (λ = 1.54056 Å) *(left)*, and unit cell displaying the (002) Miller plane *(right)*.

Miller indices, *h*, *k* and *l*, are integer numbers and are the reciprocal of the fractional coordinates of the unit cell where the lattice plane intercepts the *x*, *y* and *z* axes. The relationship between the unit cell parameter, the interplanar separation and the Miller indices of that plane for a cubic system is presented below in Equation 2.3.

$$d_{hkl} = \frac{a}{\sqrt{h^2 + k^2 + l^2}}$$

Equation 2.3

The relationship between *d*-spacing, unit cell parameter(s), and the Miller indices become increasingly more complicated as the symmetry is lowered with different crystal systems.

The intensity, position and shape of the Bragg reflections observed in a 1-D powder XRD pattern are mainly a consequence of the inherent crystal structure. For example, position of the Bragg reflections provides information on the translational symmetry: the size and shape of the unit cell. The intensity of the Bragg reflections is a consequence of the electron density inside the unit cell. The intensity of diffraction peaks is determined by the arrangement of atoms in the crystal and is proportional to the square of the sum of the structure factor. The structure factor F_{hkl} sums the result of scattering from all the atoms in the unit cell to form a diffraction peak from the (*hkl*) planes of atoms. The amplitude of the scattered X-ray is therefore determined by where the atoms are on the atomic planes and what type of atom it is. The shape of the peak is largely dependent on the crystallite size and the instrument. Large crystallites

often produce sharp diffraction peaks whilst broader reflections are measured for small particle sizes. Microstrain within the crystallite can also cause peaks to broaden.

The scattering power of an atom is related to the number of electrons it has. The strength of the scattering scales with the number of electrons and so light atoms such as hydrogen can be almost invisible in the presence of heavier scatterers such as barium. Each atom has its own scattering factor, f_j, (Equation 2.4).

$$f_j = \frac{amplitude\ of\ the\ wave\ scattered\ by\ the\ atom\ j}{amplitude\ of\ the\ wave\ scattered\ by\ a\ single\ electron}$$

Equation 2.4

The size of the electron cloud is similar to the wavelength of the X-ray so there is also an angular dependence in that the intensity of the scattered wave rapidly becomes smaller with increasing 2θ.

In a unit cell containing multiple scatterers the scattering factor of each scatterer contributes to the amplitude of the diffracted wave. The structure factor, F_{hkl}, is the sum of these atomic scattering factors, (Equation 2.5):

$$F_{hkl} = \sum_j f_j \, e^{2\pi i(hx_j + ky_j + lz_j)}$$

Equation 2.5

Where x_j, y_j and z_j are the atomic coordinates of the j^{th} atom and h, k, and l refer to the Miller indices of the reflection. F_{hkl} is complex which is a result of the diffracted waves exhibiting a phase difference relative to the incident wave. In the diffraction experiment the intensities are measured and are proportional to the square of F_{hkl}, but information on this phase relationship is lost: this is the phase problem, and whilst it will not be considered here it is the focus of single crystal structure solution to determine these phases, often by direct methods.

The observed intensity of a diffracted peak is not only related to the structure factor but also on other terms shown in Equation 2.6.

$$I_{hkl} = \left(\frac{N^2 e^4 \lambda^3}{2m^2 c^4}\right) |F_{hkl}|^2 \left(\frac{TLp}{A}\right)$$

Equation 2.6

Where, N = number of unit cells, e = charge on an electron, m = mass of an electron, c = speed of light, T = temperature factor, Lp = Lorentz polarisation, and A = absorption factor.

The intensity of a reflection is proportional to the square of the structure factor, and the electron density can be calculated as a Fourier transform of the structure factors and the phases, (Equation 2.7).

$$\rho_{hkl} = \left({}^{1}/_{V}\right) \sum_{h} \sum_{k} \sum_{l} |F_{hkl}| e^{[-2\pi i(h_x + k_y + l_z) + i\alpha_{hkl}]}$$

Equation 2.7

Powder X-ray diffraction (XRD) was routinely used throughout the work presented in this thesis. Three laboratory diffractometers were used. A Siemens D5000 diffractometer with Cu $K\alpha_{1/2}$ radiation (λ_1 = 1.54056 Å, λ_2 = 1.54443 Å) was used for phase identification of materials and other general measurements. Samples were either loaded into an aluminium holder which resulted in the presence of aluminium Bragg reflections in the diffraction patterns or samples were loaded on to a zero-background sample holder made from silicon cut in such a way that no plane fulfils the Bragg condition and thus no Bragg scattering is observed. The step size for a typical scan was 0.02 °2θ and the time step was 1.1 seconds per step. For poorly crystalline samples the step size was increased to 0.05 °2θ and the time at each step was increased 2.75 seconds per step thus improving the overall signal:noise.

A Bruker D8 Advance powder diffractometer with $K\alpha_{1/2}$ and equipped with a VÅNTEC-1 solid state detector with an Anton Parr XRK900 chemical reaction chamber was used to collect powder XRD with *in situ* heating. A typical data collection would involve heating from 30 °C to 810 °C or 900 °C at 10 °C min^{-1} with 30 °C intervals holding for 300 seconds at each interval prior to data collection.

High resolution data were acquired from a Panalytical X-Pert Pro MPD with monochromated $K\alpha_1$ radiation and was equipped with a PiXcel solid-state detector. A typical scan ranged from 10 – 80 °2θ with a step size of 0.0131 ° and a time per step of 2300 seconds.

2.5 Time-of-flight neutron diffraction theory

The neutron, discovered by Chadwick in 1932,[2] is described as having wave-particle duality by the de Broglie equation, (Equation 2.8),[3] and so the neutron may be described as a wave which could be diffracted. The energy of a neutron is proportional to the temperature and the speed of a neutron can be estimated using classical mechanics, (Equation 2.8). Consequently, the wavelength of a neutron may be calculated using de Broglie equation. At 293 K this equates to ~1.81 Å. Therefore, the wavelength of neutrons is of a size that can be scattered by an atomic lattice.

$$\lambda = \frac{h}{mv}$$

$$E = K_b T = \frac{1}{2} m v^2$$

Equation 2.8

Where λ is the wavelength, h is the Plank constant, m is the mass of the neutron, v is the velocity of the neutron, K_b is the the Boltzmann constant, T is the temperature, and E is the energy associated with the neutron.

Unlike X-rays, neutrons are scattered by the nuclei of atoms rather than the electron cloud. This offers advantages over X-rays since unlike X-rays the neutron scattering length is independent of atomic number. Light atoms, such as hydrogen, can have large scattering lengths, and usually elements next to each other in the Periodic Table have widely differing scattering lengths. This is useful for studying metal oxides since it allows for the oxygen parameters to be sensibly refined in the presence of heavier metals. In general scattering lengths do not vary as widely as form factors, but they do so in a random way with Z. Secondly the angle dependence which sees X-ray intensity fall with increasing angle is much less intense for neutrons as the nucleus can be considered a point charge meaning that small *d*-spacings can be measured more accurately. Thirdly, neutrons possess spin which means that they can have an interaction with spins on unpaired electrons (*i.e.* the magnetic moment) and so in the powder neutron diffraction data magnetic Bragg peaks may also be present, for example, if long range antiferromagnetic order is present.

Two types of neutron source may provide neutrons: steady state reactors, such as the ILL in Grenoble which can generate neutrons at a constant wavelength, and pulsed

spallation sources such as at ISIS in the UK. Neutrons from pulsed sources are suited to time-of-flight diffraction and stationary fixed angle detectors surround the sample and neutrons are counted related to their time-of-flight as opposed to their angle.

The time-of-flight is related to the Bragg equation from which the *d*-spacing may be calculated by the derivation shown below in Equation 2.9.

$$\lambda = 2dsin(\theta)$$

$$\lambda = \frac{h}{mv} \qquad \left(= \frac{ht}{mL}\right)$$

$$t = \left(\frac{2m}{h}\right) Lsin(\theta)d$$

Equation 2.9

Where λ is the wavelength, d is the interplanar separation, h is the Plank constant, θ is the angle of diffraction, m is the mass of the neutron, v is the velocity of the neutron, t is the time taken, L is the distance the neutron travels from the sample to the detector.

This is the theoretical time of flight and is referred to as DIFC and is a property which can be refined if multiple banks of data are being used in the refinement provided it remains fixed for the highest resolution bank.

The neutron absorption cross-section is wavelength dependent. Low time-of-flight neutrons (short wavelengths) are absorbed less than longer time-of-flight. This means that the average penetration into the sample, and therefore the apparent total flight path will vary with neutron wavelength and the observed times-of-flight reflections may be noticeably different from that expected from the theoretical time-of-flight. Longer *d*-spacings, where the absorption is greater, are affected more. A correction for this is introduced, DIFA, and it is a parameter which can be refined.

Small differences between various timing signals in the accelerator and the instrument data acquisition time can be accounted for by the “zero” parameter and this is a parameter dependent on the instrument and may not be refined.

The real time-of-flight is really a function of these three diffractometer constants related to the equation shown below (Equation 2.10):

$$t = DIFC\ d + DIFA\ d^2 + ZERO$$

Equation 2.10

All powder neutron data were collected on the Polaris instrument at ISIS. Diffraction data from the vanadium gallium oxyhydroxide material presented in Chapter 5 were collected by Dr. Ronald I. Smith. Samples were dried in a vacuum oven overnight prior to data collection to remove any surface contaminants (in particular surface bound water or organic molecules) to keep the incoherent scattering from the protons associated with these contaminants to a minimum. Since vanadium has a scattering cross section of 0.0184 barns it is essentially invisible to neutrons and so was used as the holder into which samples were loaded. These loaded vanadium cans of 6 mm diameter were then placed inside a chamber which was subsequently evacuated.

2.6 Analysis of diffraction data

Structure solution of an unknown material using powder diffraction data can be a monumental challenge. Faced with diffraction data of a new or unknown material the first step is to index the powder pattern and obtain lattice parameters. Examination of systematic absences provides a set of potential space groups. It is often the case that the unknown material may have a similar structure type to known materials. Then, using the structure of the known material it is possible to calculate the powder pattern of the unknown material and compare it against the observed data and the fit may be improved through a cycle of least squares refinement of structural parameters. Ultimately, the quality of the refinement, which is not a structure solution, depends on how good the initial model was and on how good the collected data was. The Rietveld method, developed in the 1960s,[4,5] is used to perform this least squares refinement. It was a big step forward in powder diffraction which at the time was regarded as inferior to single crystal structure refinement.

The Rietveld method does not focus on individual peaks but rather on every data point in the powder pattern, described in Equation 2.11.

$$S_y = \sum_i w_i\,(y_{oi} - y_{ci})^2$$

Equation 2.11

Where y_{oi} is the observed data, y_{ci} the calculated intensity, and w_i the weighted profile.

Algorithms were developed to compare the full measured pattern with the calculated and then reduce the difference through adjusting the instrument, structure and profile parameters. The initial calculated pattern must be reasonably close to the measured pattern otherwise the refinement may immediately become unstable and diverge.

Structural parameters that may be refined include the lattice parameters, fractional coordinates of the atoms, the site occupancies and the thermal parameters. Other structural information such as microstrain, particle shape may also be determined by refining, for example, the peak shape.

Instrumental and other non-structure parameters that should be considered include the background, Lorentz-polarisation and the instrumental contribution to the peak shape.

Profile terms for peak shapes may be described by a variety of different functions but typically for X-ray data peak shapes are accurately described by a pseudo-Voigt function which is a convolution of Gaussian and Lorentzian components which generally provides a better fit to the observed Bragg peaks, (Figure 2.6).

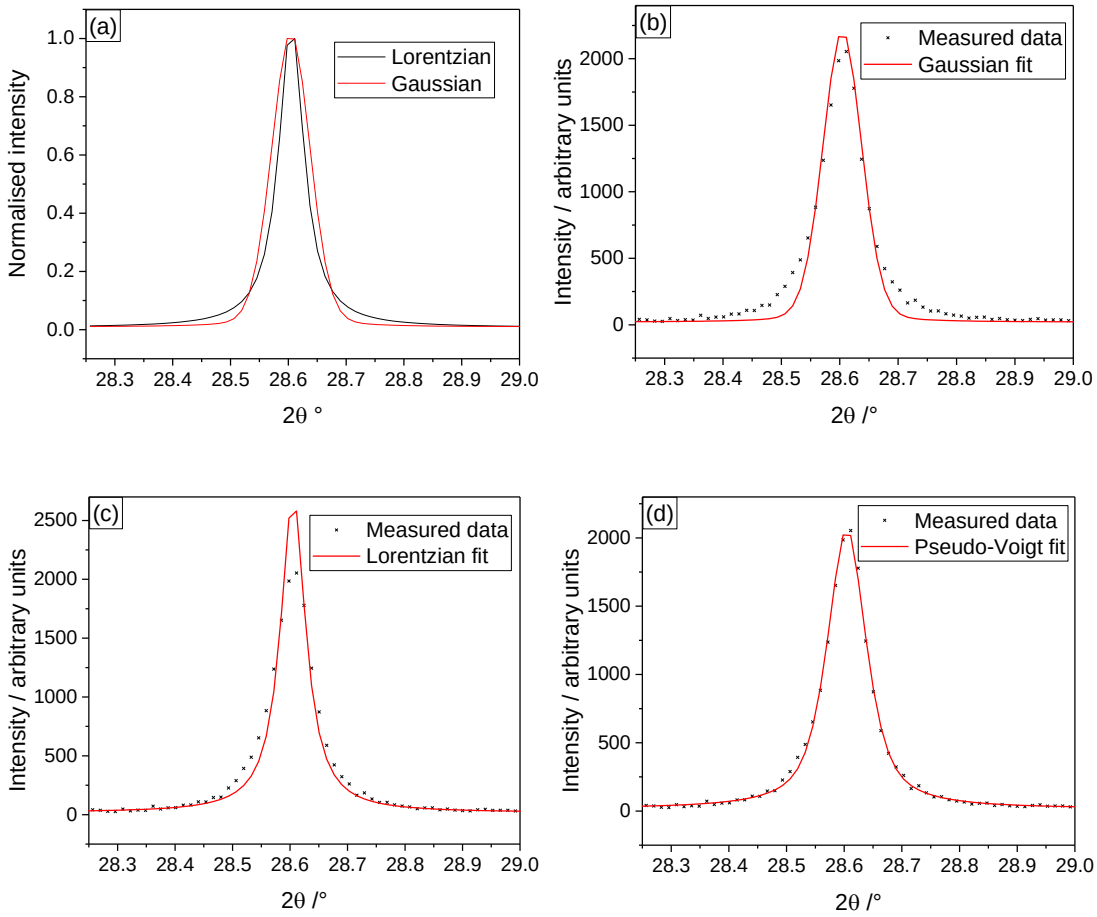

Figure 2.6 (a) Gaussian and Lorenztian peak shapes overlaid: note the longer tail for the Lorentzian shape, (b) Gaussian fit to the (111) reflection of ceria, (c) Lorentzian fit to the same reflection, and (d) pseudo-Voigt peak shape fitted to the same reflection.

Time-of-flight neutron peaks often have a complex shape (Figure 2.7) caused by the moderated neutron pulse but can be modelled by convolution of a pseudo-Voigt function with an Ikeda-Carpenter function.

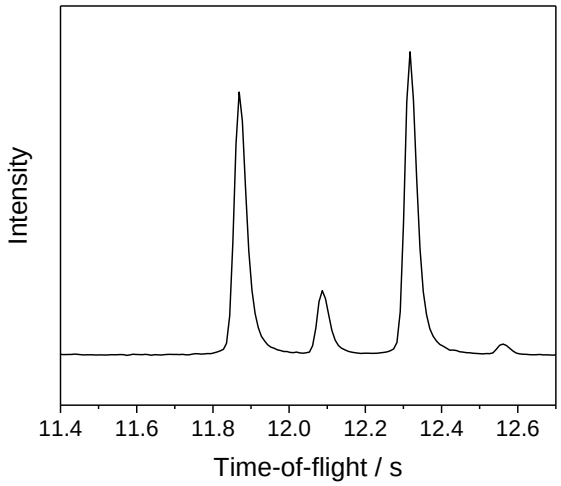

Figure 2.7 Neutron time-of flight peak shape displaying a sharp leading edge and then a slowly decaying tail. Data is of yttrium aluminium garnet measured on bank 5 of the Polaris instrument at ISIS.

There are other parameters which should be refined such as a zero point and sample displacement offset. The former has a linear dependence and the latter a cosinusoidal effect on the observed peak position. The sample displacement offset has a greater effect on the lower angle peaks and more accurate lattice parameters are determined using higher angle reflections.

As much known information should be provided before proceeding with the refinement of the structural parameters. However, given the large number of parameters it is not unusual to fall into a local minimum where the residual between the observed and calculated gives a false impression of a good fit. Similarly, refining too many parameters can also make the calculated pattern appear well fitted but might really be unphysical which would be represented in the refined parameters. Knowledge of chemistry and X-ray diffraction are also of significant importance when refining crystal structure data: the refined composition must make chemical sense, and it would be unfavourable to refine the lighter atoms in a structure before refining the heavier atoms, for example.

Often the parameters must be refined one at a time at the start of the refinement in order to obtain a stable refinement. Once a few parameters have converged more and more parameters can be refined, and at the same time, until a stable refinement is achieved and the difference between the observed and calculated patterns is minimal. Towards the end of a refinement it is usually possible to refine all parameters at the same time. This description is of course an over-simplification of a very complex and powerful technique but was intended to explain why the least squares method is useful and routinely used for analysis of the Bragg scatter from X-ray and neutron diffraction.

If a good starting model cannot be obtained or a Rietveld refinement does not converge a Pawley refinement may be undertaken instead.[6] The intensities calculated in a Pawley refinement are arbitrary *i.e.* the calculated intensities do not reflect the structure contents of the unit cell, however it is possible to refine the lattice parameters, profile parameters and the background, which often serves as a very good starting point for a Rietveld refinement.

The progress of a refinement can be monitored through a series of refinement statistics, *R*-factors.[7] Commonly R_{wp} is quoted. R_{wp} is a measure of how well the calculated pattern agrees with the observed data as is given in equation 2.12:

$$R_{wp} = \sqrt{\frac{\sum_i w_i (y_{oi} - y_{ci})^2}{\sum_i w_i (y_{oi})^2}}$$

Equation 2.12

Where y_{oi} is the observed data, y_{ci} the calculated intensity, and w_i the weighted profile.

In this work indexing, Pawley and Rietveld refinements of both X-ray and neutron diffraction data were performed using TOPAS implemented with jEdit.[8] GSAS,[9] implemented with EXPGUI[10] was often used for calculating the FWHM for all observable reflections in Scherrer analysis. Scherrer analysis estimates domain size from the peak broadening given that information of instrumental broadening is taken into account.

2.7 Total neutron scattering

Total scattering is a combination of both the Bragg and diffuse scattering. It is particularly useful for glasses and other amorphous materials where the Bragg scattering is weak or absent. It is a very powerful technique providing information on the local structure which may deviate substantially from the average crystal structure observed in the Bragg diffraction only. In the Bragg diffraction described above the diffuse scattering is treated by a background function as the intensity is very weak. In order to obtain the diffuse scattering the non-sample scattering components include scattering from the instrument, from the air, and from the sample container and these must be subtracted. A simple treatment of the data is provided in Equation 2.13. Computer programs are used to treat the data to perform the corrections and normalisations.

$$Corrected\ data = \frac{Sample - Empty\ container}{Vanadium\ rod - empty\ instrument}$$

Equation 2.13

A Fourier transform then transforms the corrected and normalised data to a differential correlation function *D(r)* which is also known as the pair distribution function, (Equation 2.14). The pair distribution function provides information on the distribution of differences and the probability of finding a pair of atoms at a certain

distance, *r*, and therefore reveals structural information on the interatomic distances in a material.

$$D(r) = \frac{2}{\pi}\int_{Q_{min}}^{Q_{max}} Qi(Q)sin\, r(Q)d(Q)$$

Equation 2.14

Where *Q* is the wavelength independent scale of plotting diffraction data, and $i(Q)$ is the distinct scattering which needs to be obtained as accurately as possible.

In this work total neutron scattering was performed on Polaris at ISIS, UK. Data was processed using Gudrun.[11]

A pair distribution function of a known material can then be calculated from its crystal structure and compared against the pair distribution of the measured data and, providing the calculated starting model is sufficiently close to the measured PDF, the calculated PDF can be refined against the measured data in a similar way as the Rietveld method described above. For a material whose average structure is known then comparison of the calculated average structure PDF against the measured PDF of the material can often reveal the presence of any local structural disorder in the material.

In this work analysis of the pair distribution function was carried out using PDFGUI.[12]

2.8 Other techniques

2.8.1 Electron microscopy

2.8.1.1 Scanning electron microscopy

Scanning electron microscopy (SEM) was used to collect images of the materials in order to visually ascertain the particle shape and size. Images were recorded using a Zeiss Supra 55-VP field emission gun scanning electron microscope (FEGSEM) or ZEISS GEMINI. A FEGSEM was used owing to high electron brightness and small spot sizes achieved from low accelerating potentials. A small amount of sample was

placed on to a carbon tape prior to analysis. Energy dispersive X-ray analysis (EDX) is element specific and was therefore used to provide an estimate of the compositional ratio of metals within the material. Some images presented in this thesis were collected by Dr David Burnett or Alexander Dunn. The software Genesis, and AZtec were used to collect spectra and quantify the metal ratio.

2.8.1.2 Transmission electron microscopy

Transmission electron microscopy (TEM) was used for similar purposes as SEM but also to show atomic scale resolution of materials. Energy dispersive X-ray spectroscopy, (EDX) and electron energy loss spectroscopy, (EELS) were also used to quantify the metal ratio within samples. Images were collected on a JEOL 2000FX instrument or by Dr Reza Kashtiban on a JEOL 2100 or JEOL ARM200F instrument.

2.8.2 Infrared spectroscopy

Fourier transform infrared spectroscopy was performed using a Perkin Elmer Paragon 1000 FT-IR spectrometer. This technique was often used to look for strong structurally bound O-H stretching modes typically found in hydroxides at around 3300 cm^{-1}.

2.8.3 BET surface area measurement

Surface area measurements of samples were performed using either a Micromeritics ASAP2020 Gas Adsorption Apparatus, or a Quadrasorb-*evo*. Samples were degassed at 200 °C for 6 hours prior to analysis to remove surface contaminants. Then known amounts of N_2 were introduced into the evacuated sample tubes and adsorbed onto the particle surface at cryogenic temperature whilst measuring the change in relative pressure from which the surface area is determined based on the theory by Brunauer, Emmett and Teller.[13]

2.8.4 Thermogravimetric Analysis

Thermogravimetric analysis (TGA) was used to determine mass loss in samples upon heating from room temperature to usually 1000 °C. This was carried out by Alexander Dunn, James Crosland or David Hammond using a Mettler Toledo TGA/DSC 1-600 instrument. TGA coupled with mass spectrometry used a Mettler Toledo TGA/DSC

1-600 thermogravimetric instrument with a Hiden HPR-20 WUIC R&D specialist gas analysis mass spectrometry system.

2.8.5 Nuclear magnetic resonance

Solid-state ^{71}Ga MAS NMR spectra were recorded using a Bruker Avance III spectrometer equipped with a 20.0 T superconducting magnet (Larmor frequency of 259.3 MHz). Samples were packed into standard ZrO_2 rotors with outer diameters of 1.0 or 1.3 mm and rotated at the magic angle at 50-75 kHz. The spectra were recorded with signal averaging for 16384-23768 transients with a recycle interval of 0.5-1 s. Spectra were recorded with a rotor-synchronised spin-echo sequence with an echo delay of 1 rotor period. Chemical shifts are reported in ppm relative to $Ga(NO_3)_3$ (1 M in H_2O) using $GaPO_4$ berlinite (δ_{iso} = 111.2 ppm, C_Q = 8.8 MHz, η_Q = 0.45) as a secondary solid reference.

Solid-state ^{27}Al NMR spectra were recorded using a Bruker Avance III spectrometer equipped with a 14.1 T superconducting magnet (Larmor frequency of 156.3 MHz). Samples were packed into standard ZrO_2 rotors with outer diameters of 3.2 mm and rotated at the magic angle at 20 kHz. The spectra were recorded with signal averaging for 2048 transients with a recycle interval of 1-3 s. To ensure the spectra were as quantitative as possible, a short flip angle pulse (0.1 μs, ~π/90). Chemical shifts are reported in ppm relative to $Al(NO_3)_3$ (1 M in H_2O) using $Al(acac)_3$ (δ_{iso} = 0.0 ppm, C_Q = 3.0 MHz, η_Q = 0.2) as a secondary solid reference.

All solid-state NMR presented in this thesis was collected by Dr Daniel Dawson and Joe Hooper, both affiliated with the University of St. Andrews.

2.8.6 SQUID magnetometry

A superconducting quantum interference device (SQUID) was used to measure the magnetic susceptibly of samples presented in this thesis. Interpretation of the data was carried out with the assistance of Dr Martin Lees. Two instruments were used: a Quantum Design MPMS XL7 SQUID and a Quantum Design MPMS-5S SQUID. Samples (5 – 25 mg) were placed inside a small gel capsule, in turn placed inside a plastic straw. Experimental conditions varied for each sample but a general

measurement was carried out between 5 – 300 K with an applied magnetic field of 1000 Oe.

2.8.7 XANES

X-ray absorption near-edge spectroscopy was performed on Beamline B18[14] at the Diamond Light Source, UK in order to probe the oxidation state and local coordination environment of materials. The samples were diluted with polyethylene powder and then pressed into a thin pellet of 12 mm diameter and approx. 1 mm thick. Absorption data were collected in transmission mode, and spectra were normalised using ATHENA.[15]

X-ray absorption spectroscopy is element specific due to the specific absorption required to eject a core electron. The measured X-ray absorption spectroscopy (XAS) is split into two regions: X-ray absorption spectroscopy (XANES) and Extended X-ray Absorption Fine Structure. The work in this thesis concerns only the XANES data, as this offers a suitable amount of information to infer the oxidation state of a metal and its local environment, (Figure 2.8).

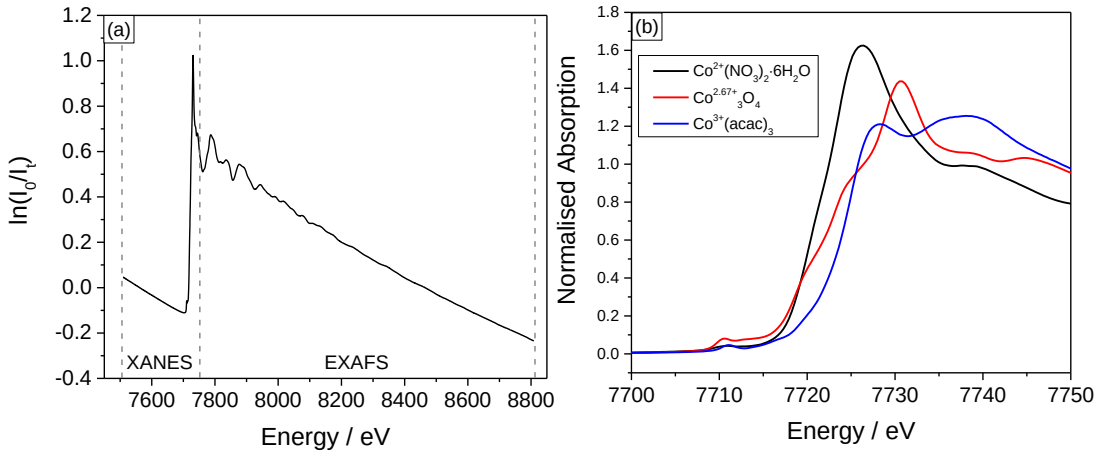

Figure 2.8 (a) Raw spectrum of Co_3O_4 showing both the XANES and EXAFS region and (b) normalised spectra of three Co references showing increase in energy with increasing oxidation state.

The oxidation state can be determined from the position of the edge jump relative to appropriate standards whilst the intensity of the pre-edge feature is a consequence of the symmetry of the local environment. The position of the edge is affected by the oxidation state since generally more energy is required to eject a core electron as the

oxidation state of the metal increases. The pre-edge feature (in transition metals) arises from an electronic transition (1s→3d) that is forbidden in an environment possessing a centre of inversion. Hence, a strong pre-edge feature is typically observed with a tetrahedral environment and a much weaker transition in an octahedral environment, (often other effects such as 3d→4p orbital mixing causes the absorption to deviate from a perfectly centrosymmetric environment resulting in a small pre-edge intensity).

2.9 Catalysis

2.9.1 Diesel Oxidation and Three-way Catalysis

Diesel oxidation catalysts (DOCs) were introduced to limit the amount of harmful emissions released into the environment from diesel engines and new DOCs are still needed to meet the stringent legislation being introduced.[16–20] The primary objective of a diesel oxidation catalyst is to oxidise CO, unburnt hydrocarbons, and NO.[19] The oxygen rich environment (lean fuel) of a diesel engine usually means that reduction of NO_x to N_2 is difficult, whilst oxidation of NO to other nitrogen oxides helps improve NO_x abatement systems further downstream in the exhaust. Pd or Pt supported on a high surface area alumina is a typical catalyst used in diesel oxidation offering good oxidation capability and thermal durability. Owing to the lean environment of diesel engines three-way catalysts (TWCs) do not effectively operate and are better suited to petrol engines where the air/fuel ratio is stoichiometric. The DOC is typically the first component after the engine and has been used since their inception in 1967. The positioning of the DOC component close to the engine means that a higher temperature is achieved improving the oxidation function of the catalysts and reaching light-off earlier (the temperature at which oxidation begins to occur).

Whilst Pd and Pt are good catalysts for oxidation it is found that a supported Rh catalyst is better for the reduction of NO to N_2 which is added to some systems. Usually NO_x abatement systems are used in conjunction with diesel oxidation catalysts and are usually the component immediately after the diesel oxidation catalysts. In diesel oxidation NO is oxidised to NO_2 which is the preferred nitrogen oxide species in some NO_x abatement systems such as the lean NO_x trap (LNT) and NO_x storage and reduction (NST). Selective catalytic reduction (SCR) using NH_3 as the reducing agent is also used for the reduction of NO_x to N_2. For fast SCR of NO_x an equimolar ratio of

NO and NO_2 is required, and since the level of NO_2 is well below 50% in diesel engines the DOC plays a crucial role in NO oxidation to reach the 50% for the fast SCR of NO_x to N_2 (Equation 2.15).[19]

$$2NO + 2NO_2 + 4NH_3 \rightarrow 4N_2 + 6H_2O \text{ (fast SCR)}$$

$$4NO + 4NH_3 + O_2 \rightarrow 4N_2 + 6H_2O \text{ (standard SCR).}$$

Equation 2.15

Since the 1980s three-way catalysts have been installed and used in petrol engines. The primary objective of these catalysts is to reduce NO_x to N_2 and O_2, whilst oxidising the unburnt hydrocarbons and CO. The air-rich environment, necessary for diesel engines is not a requirement for petrol engines. As such the three-way catalysts can operate in a nearly stoichiometric environment. When the engine is running lean (higher oxygen to fuel ratio), then the oxidation of CO and unburnt hydrocarbons is maximised but the catalyst becomes inefficient in reducing NO_x, and the opposite is true when the engine is running rich (higher fuel to oxygen ratio). An oxygen sensor and feedback loop alternate the environment around the stoichiometric point of the air/fuel ratio, *i.e.* between the rich and lean conditions in an effort to maximise the overall efficiency of the catalyst.

Diesel oxidation experiments were performed on the SCAT 3 rig and the three-way catalysis experiments on the Transient 2 rig at the Johnson Matthey Technology Centre site in Sonning Common. The diesel oxidation catalyst testing was performed under the supervision of Dr Mark Feaviour who also helped interpret the data after collection. The three-way catalyst testing experiments were performed by Dr Kerry Simmance who also collected and helped to provide an interpretation of the data. Both rigs are fixed-bed flow reactors. The polycrystalline powders were coated with a precious metal by the wet impregnation method and then dried in an oven. (Full details of experimental conditions are reported in Chapters 3 and 4 for three-way catalysis and diesel oxidation respectively).

The catalysts are then pelletised to within a narrow range (250- 355 μm) so that the fine powder catalysts do not pack and restrict the gas flow, and not too large that the diffusion of the gases becomes the rate limiting step. The catalysts are loaded into a sample holder packed between quartz wool. The rig is then heated to 500 °C whilst

passing a controlled flow of a gas mixture over the sample. The effluent gas mixture is monitored by FTIR outputting an *intensity vs time* plot. These measured data are then converted to a function of temperature. Photographs of a typical rig used in three-way catalysis is shown in the following figures (Figures 2.9 to 2.11) and have been reproduced from the Transient 2 rig log book with permission from Dr Kerry Simmance.

Figure 2.9 Photograph of the Transient 2 rig showing (1) FTIR and Bypass flow meters, (2) Furnace, (3) Sample oven, (4) IN/OUT pressure transducers, (5) Heated rotameter enclosure (6) MFC control panel, (7) Oxygen analyser, (8) Micro GC monitor.

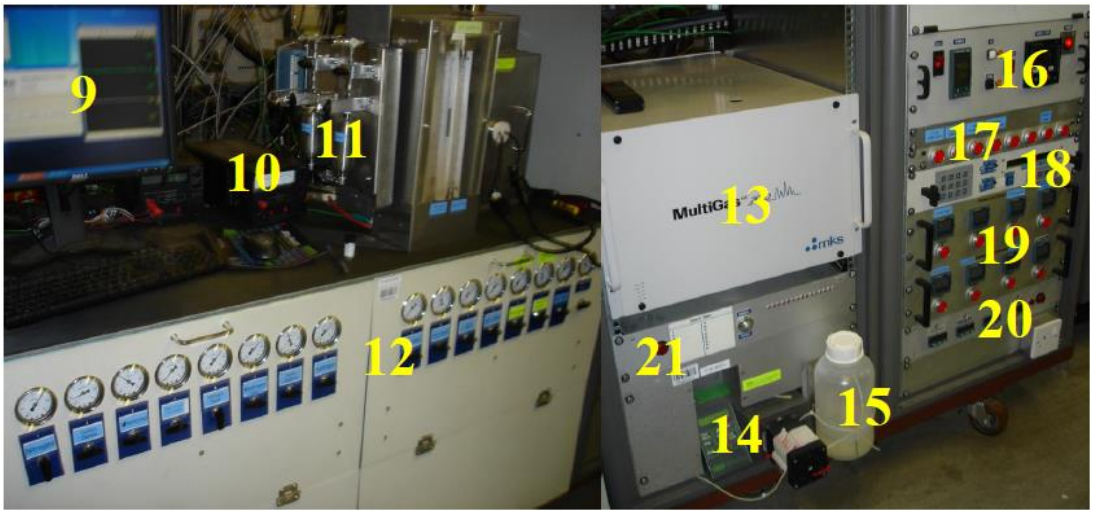

Figure 2.10 Photograph of the Transient 2 rig showing (9) FTIR control computer, (10) Lambda sensors, (11) bubblers, (12) Front gas isolation valves, (13) FTIR, (14) Water pump controls, (15) DI water tank, (16) Furnace controls, (17) General pump controls, (18) Perturbation unit/controls, (19) Controls for heated lines and tapes, (20) mA controller, (21) Remote panel.

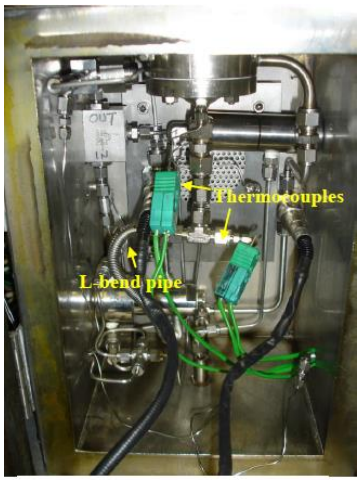

Figure 2.11 Photograph showing inside the sample oven displaying thermocouples

2.9.2 Oxidative propane dehydrogenation (ODH)

As the demand for olefins increases, in particular for ethylene and propylene for the production of polymers, so does the need to devise better synthetic methods of obtaining them. Currently steam-cracking, fluid-catalytic-cracking, and catalytic dehydrogenation are among the widely employed techniques.[21] However, all these techniques suffer from certain restraints: steam cracking and fluid-catalytic-cracking do not meet the required production of propylene favouring ethylene, and thermodynamics restraints limit alkane conversion in catalytic dehydrogenation. Therefore, there is increasing interest in oxidative dehydrogenation, which is less energy intensive, being an exothermic process and can therefore operate at lower temperatures as opposed to the endothermal dehydrogenation and cracking methods, and it is thermodynamically unrestrained. Currently ODH is not as widely used as the older technologies partly owing to the yields obtained from the reactions and formation of unwanted side productions from consecutive and parallel combustion reactions (propene is more reactive than propane). Thus, a catalyst for ODH to increase conversion and selectivity of propylene from propane remains highly desirable. Several excellent reviews have critically analysed the current literature in the search, and design of suitable catalysts for this area of catalysis.[22–25] Supported vanadium oxides (in particular V_2O_5) and molybdenum oxides are the most widely studied catalysts for ODH.[26–28] The presence of a relatively inert secondary surface metal species (such as MoO_x or WO_x) can weakly adsorb propane in a precursor state that supplies the catalytically active VO_x site for propane activation to propylene.[29] The best current conditions for propylene conversion also produce unwanted side products

such as other propylene derivatives as well as coproducing ethylene so there is a major objective in finding a catalyst capable of producing a high conversion of propane under conditions which also maintain a high selectivity to propylene, whilst also minimising the formation of unwanted side products such as CO, CO_2 and coke (Figure 2.12).

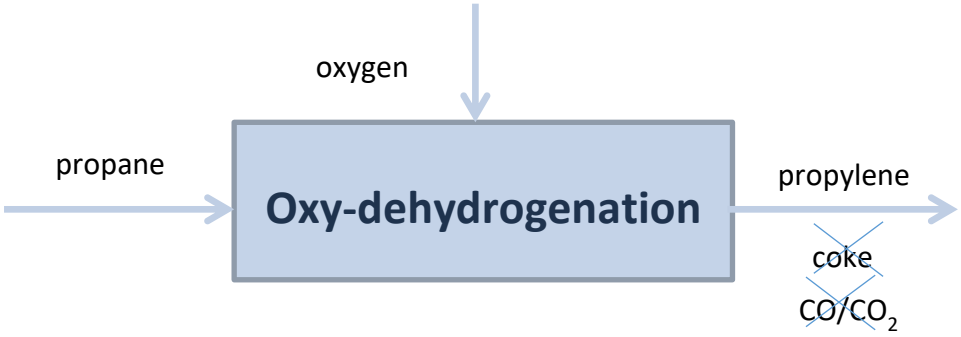

Figure 2.12 Schematic showing desired reaction scheme for ODH.

All catalysts were tested at the Johnson-Matthey Technology Centre in Sonning Common by Dr Pilar Gomez Jimenez who also collected and normalised the data. The catalysts were tested on a high-throughput screening rig with 8 fixed bed reactors in parallel located inside an oven in order to reach the desired temperature. The catalyst was held inside the reactor between two layers of glass wool. The outlet gases were analysed by gas chromatography. An example of a typical rig used in this catalyst is shown in Figure 2.13.

The catalysts were tested for propane oxy-dehydrogenation under a gas flow consisted of 20% propane and 20% oxygen in nitrogen. The temperature was varied between 350 and 500 °C, with the purpose of obtaining data at different conversion levels.

Figure 2.13 Oxidative dehydrogenation testing rig, *(left)* photograph of rig, *(right)* photograph of sample container.

2.9.3 Semi-hydrogenation of acetylene

The catalytic semi-hydrogenation of acetylene is an important reaction for removing acetylene in the feed for the production of polyethylene.[30] The presence of acetylene can lead to deactivation of the ethylene polymerisation catalysts and so a catalyst which selectively hydrogenates acetylene to ethylene and does not hydrogenate the ethylene in the feed is highly desired. Supported palladium catalysts are active catalysts for this but usually suffer from poor selectivity and stability.[31,32] Part of the reason for the poor selectivity is due to the large number of active sites enabling side reactions such as full hydrogenation to ethane. This active-site isolation to increase selectivity in this reaction was first achieved with palladium-silver alloys[33] but too few active palladium sites were found to be present. Currently well-ordered palladium-gallium intermetallic compounds are being studied and have shown excellent stability and selectivity in the semi-hydrogenation of acetylene.[34–38] These catalysts generally show high selectivity owing to the ordered crystal structure where palladium is isolated by gallium, unlike in the binary palladium-silver alloys which show a disordered distribution of metals. These catalysts also have a higher stability owing to the partly covalent bonding between palladium and gallium which preserves the structural motive of isolated palladium sites under the reaction conditions.[35] Recently an aluminium-iron catalyst has been investigated as a low-cost alternative for acetylene semi-hydrogenation.[39]

All catalytic testing for the semi-hydrogenation of acetylene in this thesis were conducted at the Jonson-Matthey Technology Centre in Sonning Common. Experiments were performed by Dr Pilar Gomez Jimenez who also collected and helped interpret the data.

Approximately 0.1 g of each solid in the form of a powder was used for each reaction. The catalysts were tested on a fixed-bed reactor located inside an oven in order to reach the desired temperature. The catalyst was held inside the reactor between two layers of glass wool. The outlet gases were analysed by gas chromatography.

The catalysts were subjected to an *in situ* pre-reduction step at 140 °C with hydrogen. The samples were flushed with nitrogen while cooling to room temperature. Then the catalysts were tested for acetylene hydrogenation under ethylene rich conditions. Full details on the experimental conditions can be found in Chapter 4.

CO chemisorption on palladium was conducted at the Johnson-Matthey Technology Centre by Dr Loredana Mantarosie to probe the palladium species present on each support. All samples were diluted with KBr (75% catalyst / 25% KBr) in order to allow preparation of self-supporting wafers. Samples were measured on a Perkin Elmer Frontier instrument using a Harrick transmission cell with calcium fluoride windows. Measurements were performed in transmission mode; 4200-700 cm^{-1}; 2 cm^{-1} resolution; 64 accumulations; 122.2 sec/spectra; spectra reported to the spectrum of the material measured under the same conditions before the CO adsorption. Samples were pre-treated in 10% H_2/He at room temperature and heated to 150°C at 10 °C min^{-1} and held for 30 min.

For CO adsorption the samples were cooled to 30 °C; purged with He; then exposed to 500 ppm CO/He for 30 min.

Due to the very low Pd loading and respectively the low intensity of the CO associated bands spectra from minute 2.5 to min 30 were averaged, normalised by sample weight and then CO gas phase subtracted.

2.10 References

1 W. H. Bragg and W. L. Bragg, *Proc. R. Soc. A*, 1913, **88**, 428–438.

2 J. Chadwick, *Nature*, 1932, **129**, 312.

3 L. de Broglie, *Phil. Mag. S*, 1924, **47**, 446–457.

4 H. M. Rietveld, *J .Appl. Crystallogr.*, 1969, **2**, 65–71.

5 H. M. Rietveld, *Acta Cryst*, 1966, **20**, 508–513.

6 G. S. Pawley, *J. Appl. Crystallogr.*, 1981, **14**, 357–361.

7 B. H. Toby, *Powder Diffr.*, 2006, **21**, 67–70.

8 A. A. Coelho, *J .Appl. Crystallogr.*, 2000, **33**, 899–908.

9 A. C. Larson and R. B. Von Dreele, *Los Alamos Natl. Lab. Rep. LAUR*, 2004, 86–748.

10 B. H. Toby, B. H. Toby and B. H. Toby, *J. Appl. Cryst*, 2001, **34**, 210–213.

11 A. K. Soper, *Rutherford Appleton Laboratory Technical Report RAL-TR-2011-013*, 2011.

12 C. L. Farrow, P. Juhas, J. W. Liu, D. Bryndin, E. S. Bozin, J. Bloch, T. Proffen and S. J. L. Billinge, *J. Phys. Condens. Matter*, 2007, **19**, 335219.

13 S. Brunauer, P. H. Emmett and E. Teller, *J. Am. Chem. Soc.*, 1938, **60**, 309–319.

14 A. J. Dent, G. Cibin, S. Ramos, A. D. Smith, S. M. Scott, L. Varandas, M. R. Pearson, N. A. Krumpa, C. P. Jones and P. E. Robbins, *J. Phys. Conf. Ser.*, 2009, **190**, 12039.

15 B. Ravel and M. Newville, *J. Synchrotron Radiat.*, 2005, **12**, 537–541.

16 H. J. Stein, *Appl. Catal. B Environ.*, 1996, **10**, 69–82.

17 L. Lizarraga, S. Souentie, A. Boreave, C. George, B. D. Anna, P. Vernoux, B. Lyon and A. A. Einstein, *Environ. Sci. Technol.*, 2011, **45**, 10591–10597.

18 D. Dou, *Platin. Met. Rev*, 2012, **56**, 144–154.

19 A. Russell and W. S. Epling, *Catal. Rev.*, 2011, **53**, 337–423.

20 J. A. Kurzman, L. M. Misch and R. Seshadri, *Dalton Trans.*, 2013, **42**, 14653–67.

21 H. M. T. Galvis and K. P. De Jong, *ACS Catal.*, 2013, **3**, 2130–2149.

22 X. Rozanska, R. Fortrie and J. Sauer, *J. Am. Chem. Soc.*, 2014, **136**, 7751–7761.

23 F. Cavani, N. Ballarini and A. Cericola, *Catal. Today*, 2007, **127**, 113–131.

24 R. Grabowski, *Catal. Rev.*, 2006, **48**, 199–268.

25 C. A. Carrero, R. Schloegl, I. E. Wachs and R. Schomaecker, *ACS Catal.*, 2014, **4**, 3357–3380.

26 W. Chu, J. Luo, S. Paul, Y. Liu, A. Khodakov and E. Bordes, *Catal. Today*, 2017, 0–1.

27 A. A. Lemonidou, L. Nalbandian and I. A. Vasalos, *Catal. Today*, 2000, **61**, 333–341.

28 X. Rozanska, R. Fortrie and J. Sauer, *J. Am. Chem. Soc.*, 2014, **136**, 7751–7761.

29 B. Mitra, I. E. Wachs and G. Deo, *J. Catal.*, 2006, **240**, 151–159.

30 A. Borodinski and G. C. Bond, *Catal. Rev.*, 2006, **48**, 91–144.

31 P. Albers, J. Pietsch and S. F. Parker, *J. Mol. Catal. A*, 2001, **173**, 275–286.

32 A. Molnar, A. Sarkany and M. Varga, *J. Mol. Catal. A*, 2001, **173**, 185–221.

33 N. A. Khan, S. Shaikhutdinov and H. Freund, *Catal. Letters*, 2006, **108**, 159–164.

34 J. Osswald, K. Kovnir, M. Armbrüster, R. Giedigkeit, R. E. Jentoft, U. Wild, Y. Grin and R. Schlögl, *J. Catal.*, 2008, **258**, 219–227.

35 J. Osswald, R. Giedigkeit, R. E. Jentoft, M. Armbrüster, F. Girgsdies, K. Kovnir, T. Ressler, Y. Grin and R. Schlögl, *J. Catal.*, 2008, **258**, 210–218.

36 M. Armbrüster, R. Schlögl and Y. Grin, *Sci. Technol. Adv. Mater*, 2014, **15**, 34803.

37 T. N. Afonasenko, N. S. Smirnova, V. L. Temerev, N. N. Leont, T. I. Gulyaeva and P. G. Tsyrul, *Kinet. Catal.*, 2016, **57**, 490–496.

38 A. Ota, M. Armbru, M. Behrens, D. Rosenthal, M. Friedrich, I. Kasatkin, F. Girgsdies, W. Zhang, R. Wagner and R. Schlo, *J. Phys. Chem. C*, 2011, **115**, 1368–1374.

39 M. Armbrüster, K. Kovnir, M. Friedrich, D. Teschner, G. Wowsnick, M. Hahne, P. Gille, L. Szentmiklósi, M. Feuerbacher, M. Heggen, F. Girgsdies, D. Rosenthal, R. Schlögl and Y. Grin, *Nat. Mater.*, 2012, **11**, 690–693.

Chapter 3: Solvothermal Synthesis and Characterisation of Cobalt Gallium Oxide Catalysts

3.1 Introduction and scope of this chapter

This chapter presents the findings from two different studies.

The first study made use of synchrotron X-rays to follow *in situ* the crystallisation of a cobalt gallium oxide from gallium metal under solvothermal conditions, showing that crystalline intermediate phases are present depending on the choice of solvent.

The second study presents the synthesis and characterisation of a cobalt gallium oxide prepared by adding cobalt directly to γ-Ga_2O_3 under solvothermal conditions. A particular emphasis will be on the characterisation showing how the oxide made at low temperature solvothermally is metastable and changes upon application of heat after synthesis highlighting the flexibility and stability of the spinel structure.

Tests of photocatalysis and three-way catalysis with these cobalt gallium spinels is presented at the end of the chapter.

3.2 Time-resolved in situ X-ray diffraction of the crystallisation of cobalt gallium oxide under solvothermal conditions

3.2.1 Introduction

The high temperatures required for solid state reactions usually prohibit the study of the mechanistic and kinetic pathways of the formation of the materials formed. It has recently been demonstrated that using high energy X-ray sources, such as at synchrotrons, time resolved *in situ* powder X-ray diffraction can be carried out to identify unambiguously and follow reaction pathway of dense metal oxides, such was the case for the Aurivillius phase $Bi_5Ti_3Fe_{0.5}Cr_{0.5}O_{15}$.[1] The use of high energy X-rays allowed for structural refinements to be undertaken on a host of metastable intermediate phases observed during the reaction. Powder X-ray diffraction is, of course, only one of many different methods for studying the early stages of crystallisation and there are examples in the literature where other techniques such as spectroscopic analysis have been carried out on the formation of materials.[2] There is a growing body of data regarding the crystallisation of porous materials such as metal organic frameworks (MOFs) in the literature which, since they typically require low temperatures (~100° C), reactions can be carried out in sealed glass vessels.[3–5] There are fewer reports of the *in situ* study of crystallisation of dense oxide materials and fewer still on their formation under hydro(solvo)thermal conditions.[6–9]

The solvothermal synthesis of gallium oxide can be effected directly from oxidation of gallium metal in an aminoalcohol.[10,11] Mixed metal spinels can also be synthesised by a similar preparation if a transition metal salt (*e.g.* of Fe, Co, Ni, Zn) is included in the reaction.[12] It was found that for some mixed metal spinels their formation was facilitated by the presence of an aqueous solution of the aminoalcohol.

The time resolved *in situ* experiment described here was performed at the Diamond Light Source, UK on beamline I12[13] to probe the reaction pathway of the formation of cobalt gallium oxide from cobalt nitrate and gallium metal with different reaction media. High energy X-rays are used on this beam line (65.62 keV, λ = 0.18893 Å). These high energy X-rays combined with a fast acquisition time allow the crystallisation to be followed directly and in real time also offering the advantage that

real hydro(solvo)thermal conditions that would be used in conventional laboratory synthesis can be mimicked in the synchrotron environment. However, the quality of the data may be affected since diffraction of the vessel will dominate the pattern. Although some groups have used reaction vessels such as glass capillaries and miniature reactors are used to obtain data from which the pair distribution function can be calculated, the reactions will not necessarily be representative of real hydrothermal conditions. Developments in *in situ* diffraction techniques show that lattice parameter, phase evolution, full Rietveld analysis and in some favourable cases atomic scale analysis and total scattering can be studied.[14–17]

Gallium metal was selected as the precursor owing to its being a liquid above 29 °C and so would be amorphous to X-rays under solvothermal conditions at 210 °C. The oxide formed from a similar solvothermal reaction was previously shown to be a largely inverse spinel with composition $Co_{0.973(8)}Ga_{1.767(8)}O_{3.752(8)}$,[12] a composition and inversion parameter different to cobalt gallium oxides prepared from high temperature.[18,19] The results from two studies are presented. The first study is the solvothermal reaction of gallium metal and cobalt nitrate in 1:1 monoethanolamine(MEA):H_2O. The second study has the same reagents but the reaction is conducted in MEA only.

3.2.2 Synthetic Procedure

To follow the synthesis reactions were carried out within the Oxford-Diamond In Situ Cell (ODISC)[20] on beamline I12 at the Diamond Light Source, UK[13] which makes use of a large 43 × 43 cm^2 Thales Pixium RF4343 image plate detector allowing powder diffraction patterns to be recorded on the order of seconds with excellent *d*-spacing resolution. The acquisition time for each frame was 12.447 s. The energy of the monochromated X-ray beam was 65.62 keV (λ = 0.18893 Å) which was sufficient for penetration of the steel autoclave and the PTFE liner. The sample-detector distance was 2038.58 mm and the slit size was 1 mm x 1 mm. Energy and distance were calibrated using the multi-distance calibration implemented in DAWN.[21]

0.3 g (4.30 mmol) of Ga metal (Alfa-Aesar, 99.9%) and 0.626 g (2.15 mmol) of $Co(NO_3)_2 \cdot 6H_2O$ (Aldrich, ≥98%) were placed inside a 23 ml PTFE liner. To this either 10 ml of a mixed solution of water and ethanolamine (Acros, 99%) (1:1 by volume) was added **(Reaction 1)** or 10 ml ethanolamine only **(Reaction 2)**. This liner was

sealed inside a steel autoclave and placed inside ODISC (Figure 3.1). The material was magnetically stirred to ensure the reagents and products were well dispersed in the path of the X-ray beam. A glassy carbon sheath was placed around the autoclave to ensure transfer of heat. Infrared lamps in ODISC rapidly heated the material inside the autoclave to 210 °C and this was controlled and maintained by use of a proportional-integral-derivative controller (PID controller) with temperature being relayed to the PID by use of two thermocouples. At the end of the reaction the autoclave was allowed to cool naturally to room temperature and the products were isolated by vacuum filtration, washed with copious amounts of methanol and dried by washing with acetone.

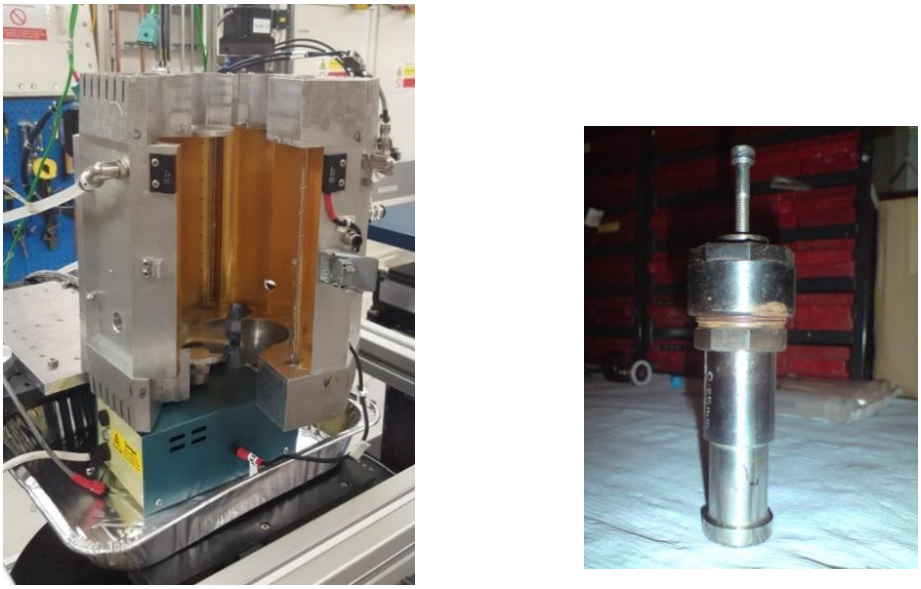

Figure 3.1 Photograph showing the Oxford-Diamond *In Situ* Cell (ODISC), *(left)* and autoclave used for in situ reactions, *(right)*.

3.3 Reaction 1: Reaction in 1:1 water:ethanolamine

3.3.1 General Overview

An overview of the first study is presented below and shows that the formation of two crystalline transient phases precede the formation of cobalt gallium oxide spinel (Figure 3.2). The 3D colour map focuses on the higher angle reflections of the experiment since this is where the diffraction from steel and PTFE were least

pronounced and diffraction peaks for all 3 phases are present at some point during this region.

The *in situ* experiment shows that after fifteen minutes intense reflections found at ~6.85 and ~7.03 2-theta present themselves signalling the start of a first period of growth and decay, and can be described as the first transient phase. This phase rapidly grows in intensity before falling in intensity without reaching a plateau. This fall in intensity coincides with a shift to higher angle (*i.e.* a decreased *d*-spacing) and a change in relative peak intensities and does not completely fall to zero. Instead a second period of growth occurs, and can be described as the second transient phase. It is quite clear that this second phase is related to the first phase since the peak intensities clearly grow into one another. This secondary phase begins to grow after 45 minutes then, upon reaching a maximum intensity at 120 minutes, the intensity starts to decrease almost simultaneously with the emergence of the spinel phase. That the onset of spinel growth occurs simultaneously with the decrease in the second transient phase peak intensity suggests that the two are closely related. After 450 minutes the spinel phase begins to plateau whilst the transient phase intensity has almost disappeared, which together indicate that the reaction is coming to a completion. The spinel phase was isolated at the end of the reaction and PXRD confirmed phase pure highly crystalline cobalt gallium oxide, (nominally $CoGa_2O_4$).

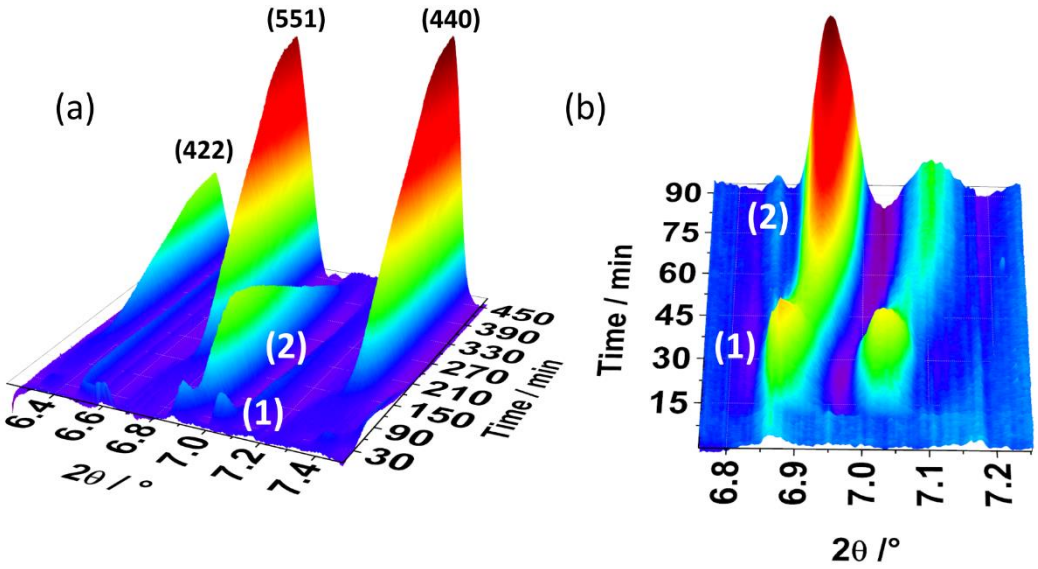

Figure 3.2 (a) Colour map of the higher angle peaks of the *in situ* experiment (λ = 0.18893 Å) with MEA:H_2O as solvent with Miller indices of spinel product labelled, (b) close-up of the contour map showing the emergence of the transient phase (1) after 15 minutes with rapid decay before a slower secondary period of growth occurs (2).

The data before any background subtraction are shown below in Figure 3.3, (every 10th powder XRD pattern (approx. 2 min interval)). Intense peaks around 2.25, 5.25 and 6 °2θ are of the steel autoclave which dominate the PXRD patterns. The feature around 0.5 °2θ is the beamstop. The inset shows a close up of the region 1.0 – 3.5 °2θ where clear differences are observed in the background. Although difficult to assign with certainty this could be due to small sub-diffraction nuclei and amorphous reagents (gallium metal, cobalt nitrate).

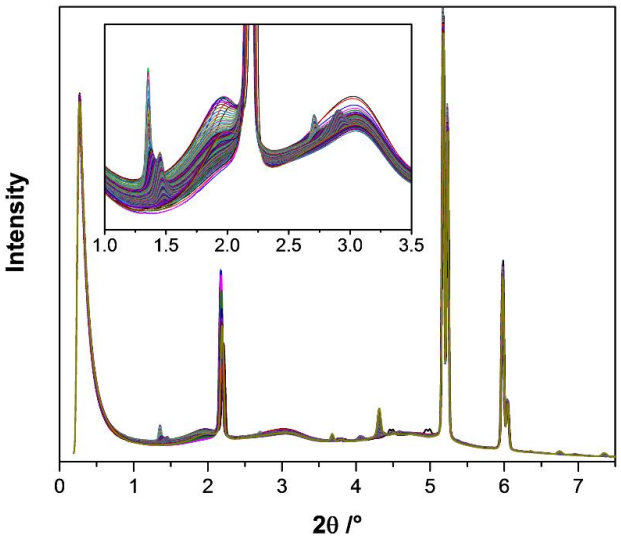

Figure 3.3 Overlay plot of every tenth powder XRD pattern before any background subtraction with, inset, showing the changes in the background.

The first transient phase showed very intense Bragg reflections and analysis of the *in situ* data identified reflections which all showed a simultaneous growth followed by simultaneous decay period. The diffraction from the steel autoclave and to a lesser degree the PTFE liner dominate the powder pattern (Figure 3.4) but enough peaks were identified from which a unit cell could be indexed: a rhombohedral unit cell with space group $R\bar{3}m$ and lattice parameters a = 3.146 Å, c = 23.9847 Å. This suggested that the transient materials could be layered double hydroxides, (LDHs).[22]

It was not possible to conduct full pattern fitting or even a structure-less fit of all the observed reflections of the LDH owing to the presence of steel and PTFE, the former dominating the pattern and diffraction from both steel and PTFE causing overlap of some peaks which masked the presence of the transient phases.

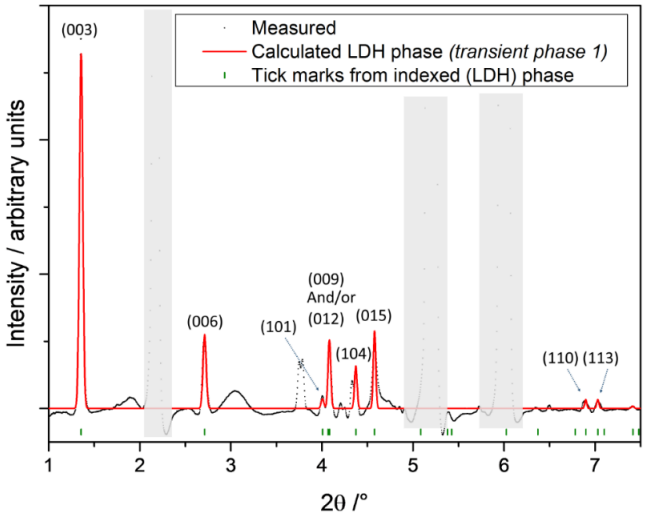

Figure 3.4 Fitted XRD pattern (after a background subtraction using the rolling-ball method) of the observed *in situ* transient phase 1 using an LDH model with Miller indices labelling each LDH Bragg peak. Faded peaks are steel autoclave.

The second transient phase was much less crystalline than the first (Figure 3.5) showing broader reflections, many hidden by the diffraction from the autoclave and could not be indexed readily from the *in situ* data.

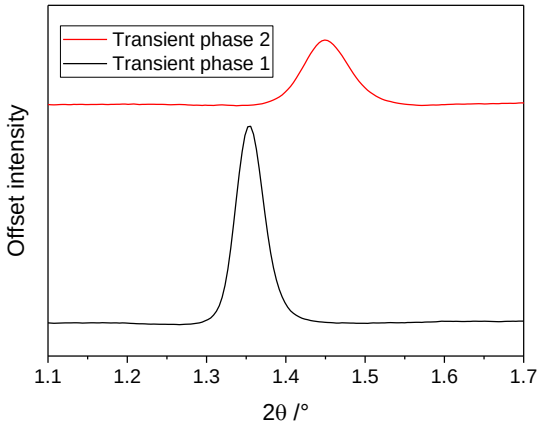

Figure 3.5 PXRD plot of both transient phases at their maximum peak intensity showing the change in the (003) reflection position and broadening from transient phase 1 to transient phase 2.

3.3.2 Isolation of the second transient phase

Off line experiments (*i.e.* without use of *in situ* X-ray diffraction) with ODISC at the Diamond Light Source successfully isolated the secondary transient phase. The observed peaks in the powder diffraction pattern of the isolated phase after approximately 80 minutes are in good agreement with the observed data in the *in situ*

data after the same length of time (Figure 3.6). Indexing and subsequent Pawley refinement of this isolated phase yield refined parameters of $a = 3.111(2)$ Å, $c = 22.65(3)$ Å, again indicative of a layered double hydroxide and indeed the refined parameters are similar to those reported for Co-Ga layered double hydroxides in the literature.[23,24] Turbostratic perturbation, the irregularity in the interlayer separations causing slight differences in the basal spacings of the LDH lattice, is the likely cause of the anisotropic peak broadening of the *(00l)* reflections seen in the powder XRD pattern of the isolated LDH.[25–27]

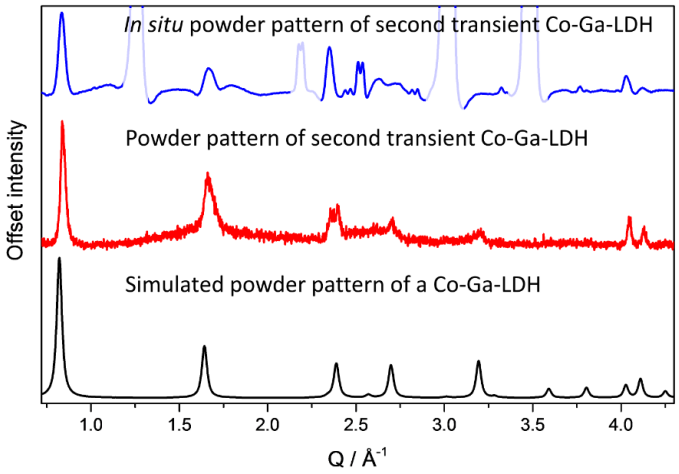

Figure 3.6 Powder XRD patterns of a simulated Co-Ga-LDH (black), isolated Co-Ga-LDH after 80 minutes (red) and from the Co-Ga-LDH formed *in situ* (blue). Faded peaks are steel autoclave and PTFE. *In situ* Co-Ga-LDH is from data obtained after applying a rolling-ball background subtraction.

A second shorter offline experiment (30 minutes) shows the LDH phase (present amongst other unidentified material(s)), (Figure 3.7), with a larger *d*-spacing of the (003) peak of 7.78 Å, compared to the LDH quenched from the 80 minute reactions with a *d*-spacing of the (003) peak corresponding to 7.56 Å. This is in agreement with the shift in *d*-spacing of the diffraction data observed *in situ*. The difficulty in isolating the LDH as a phase pure material from quenching experiments is in contrast to the observation of its being the only observable intermediate phase *in situ* during the time that it exists. This suggests that upon quenching other materials not present during the reaction are forced out of solution upon cooling.

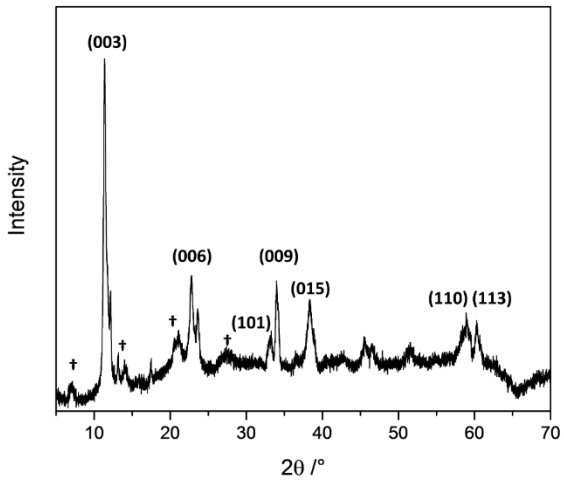

Figure 3.7 Powder XRD of material isolated after 30 minutes. † denotes some unidentifiable reflections from phases also present from the quenching reaction.

Typical crystal structure of an LDH

The crystal structure of an LDH is shown in Figure 3.8. The layered structure of LDHs is based on brucie ($Mg(OH)_2$) but where a portion of the divalent cation is either oxidised, or substituted with a trivalent cation. These cations are surrounded by hydroxyl groups in approximately octahedral geometry which are edge-shared to form infinite layers which stack on top of each other. The presence of the trivalent cation results in an excess of positive charge which is charged balanced by intercalation of an anion species usually associated with water. The general formula of a layered double hydroxide may be written as: $[M^{2+}_{1-x}M^{3+}_{x}(OH)_2]^{x+}[A^{n-}]_{x/n}\cdot yH_2O$. Typically, only a small amount of trivalent cation may be substituted with x usually found between $0.20 \leq x \leq 0.33$.[25]

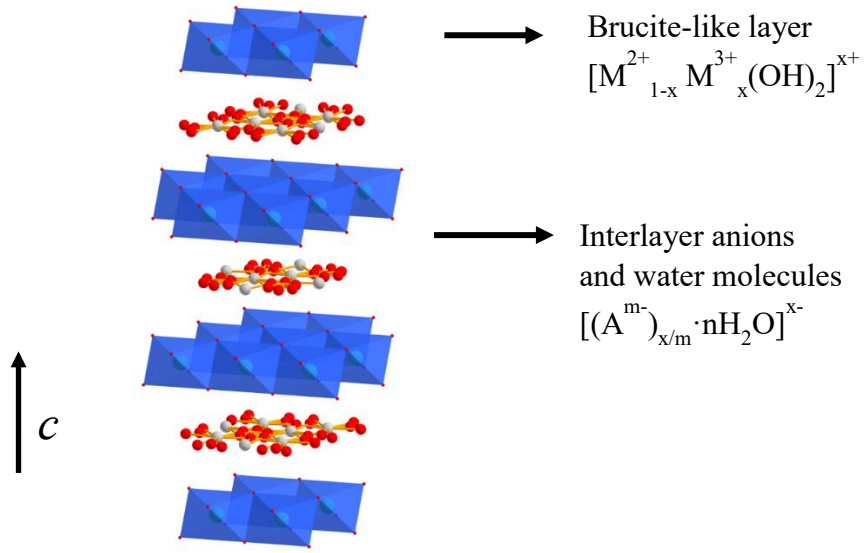

Figure 3.8 The crystal structure of an LDH. Changes in the interlayer gallery strongly affect the basal spacing of the LDH.

3.3.3 Characterisation of isolated Co-Ga-LDH

Electron microscopy has been used to show that the morphology of the isolated second transient phase consists of large but thin hexagonal plates (Figure 3.9). EELS (TEM) and EDX (SEM) were used to confirm the presence of both Co and Ga in a ratio close to 1:1, (Table 3.1). LDHs reported with values of $x > 0.33$ are seldom reported in the literature but are claimed to exist.[25,28–32] Most LDHs are found with a maximum value of $x = 0.33$ which was long thought to be the maximum due to charge repulsion (the 'cation avoidance' rule) of placing trivalent cations close together.[33,34] Many studies find that above $x = 0.33$ the lattice parameter *a*, which is largely dependent on the amount of trivalent cation, does not decrease with further incorporation suggesting that amorphous impurity phases are present instead. Yet, according to Pausch, who once claimed the maximum value of $x = 0.44$, the constancy in *a* above $x = 0.33$ is related to the repulsion of M^{3+} causing an increase in *a* versus the decrease in *a* due to increased trivalent metal effectively cancelling out any observed change.[35] It may be the case that the presence of an amorphous gallium phase (such as gallium metal or amorphous gallium oxide) accounts for the high level of trivalent cation observed although none is obvious by electron microscopy as a secondary phase.

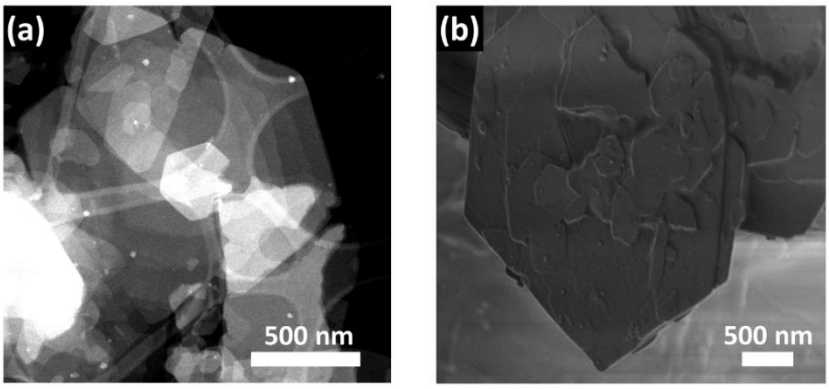

Figure 3.9 (a) ADF-STEM image of isolated Co-Ga-LDH showing large hexagonal plate morphology, (b) SEM image showing similar hexagonal plate morphology.

Table 3.1 EDX analysis showing an approximate 1:1 ratio of Co:Ga in the isolated LDH.

EDX	Average Atomic %
Co	48.5
Ga	51.5

TGA revealed that the isolated LDH phase is stable up to 270 °C before decomposing, shown by a sudden mass loss observed around this temperature (Figure 3.10a). Smaller steps are observed at 100-150 °C which could be loss of surface bound water molecules followed by loss of interlayer water and interlayer anions. Simultaneous mass spectrometry confirmed the presence of the occluded water showing loss of water at each mass loss step in the TGA but also confirmed the presence of the nitrate anion by observation of the NO fragment (Figure 3.10a).

X-ray thermodiffractometry supports the TGA showing that the LDH decomposes around 250 °C and that it decomposes into a spinel (Figure 3.10b). Closer inspection of this contour map shows that the unit cell contracts as temperature is applied before the structure collapses into the spinel likely due to the removal of the water and interlayer anions which is observed in the TGA-MS. The spinel becomes increasingly more crystalline as observed by the sharpening of the Bragg reflection intensities up to 810 °C. Upon cooling to room temperature the spinel was found to be green in colour whereas cobalt gallium oxides are usually blue. EDX analysis shows that the 1:1 ratio is maintained in the spinel obtained from the decomposed layered double hydroxide.

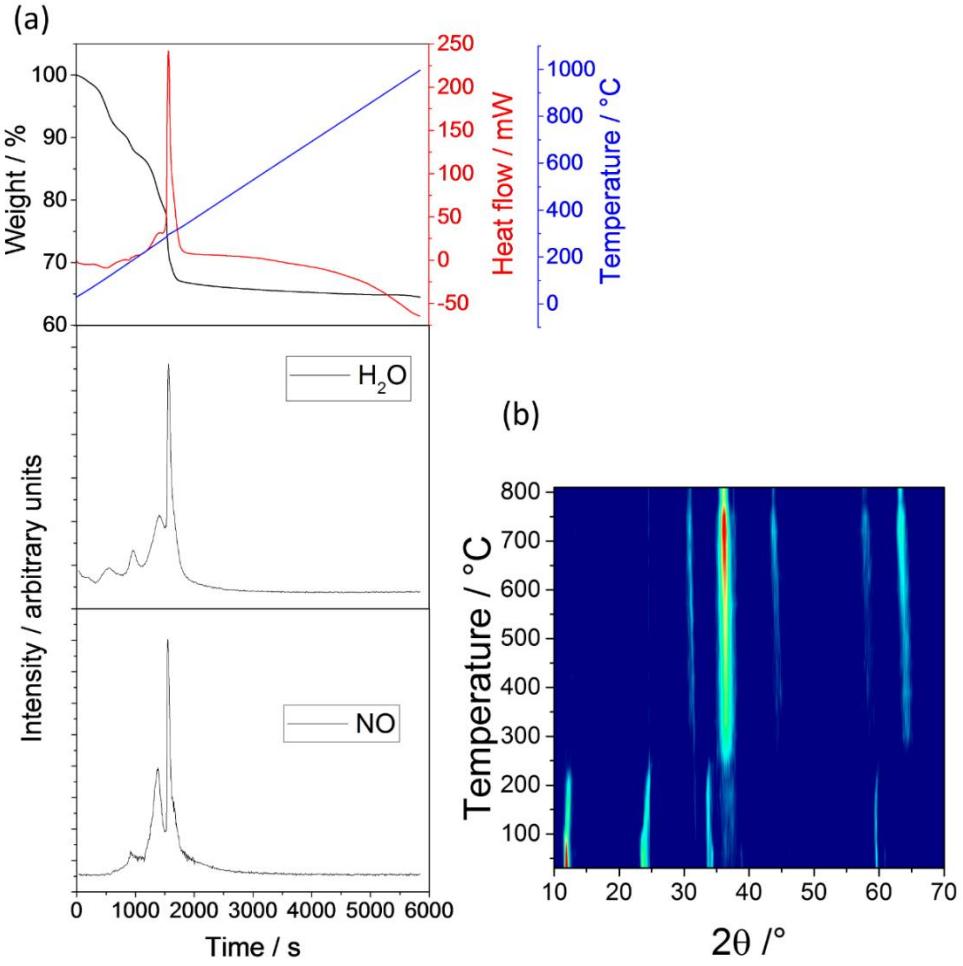

Figure 3.10 (a) TGA-MS of the isolated 2nd phase LDH clearly indicating the presence of occluded water and nitrate interlayer anion, (b) X-ray thermodiffractometry showing the collapse of the LDH at ~270 °C in to a single phase spinel.

Refinement of the lattice parameter of this green spinel (Figure 3.11) gives a lattice parameter of $a = 8.3026(13)$ Å, smaller than for cobalt gallium oxides with a composition of $CoGa_2O_4$ (e.g. $a = 8.3291(3)$ Å[18]). This is at first surprising since the composition of this spinel is close to 1:1 and so a larger cell may be expected with the increase cobalt content.[18,19]

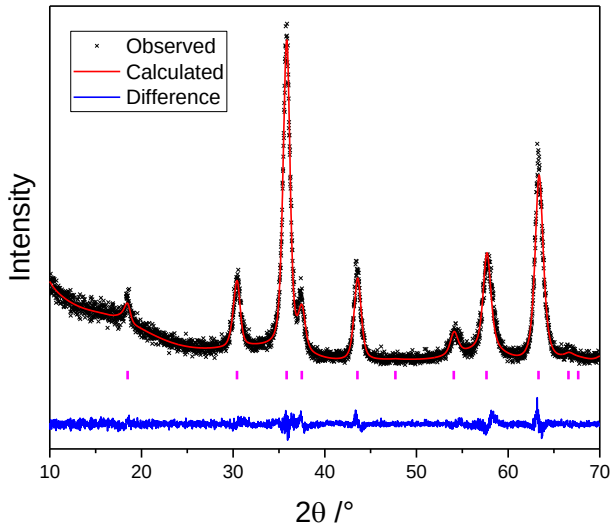

Figure 3.11 Pawley refinement of the green cobalt gallium oxide.

XANES carried out on beamline B18[36] at the Diamond Light Source indicated the presence of Co^{3+} in the LDH and a significant portion of Co^{3+} in the spinel obtained from thermal decomposition of the LDH, a plausible explanation for the different colour observed, (Figure 3.12). Furthermore, a significant portion of Co^{3+} may account for the unusually small unit cell parameter as the Co^{3+} ion will be more contracted than the Co^{2+} cation.

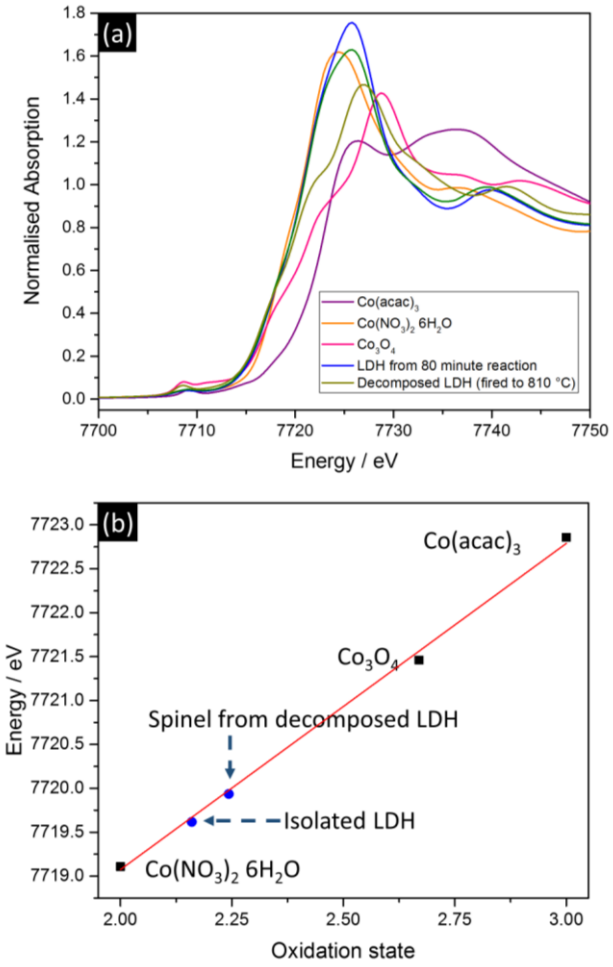

Figure 3.12 (a) Co-K edge XANES spectra normalised to the edge step, and (b) plot of edge position (defined as the energy at which normalised absorption = 0.5) as a function of oxidation state with a linear fit to reference materials providing the calculated oxidation states of Co-Ga-LDH and spinel from thermally decomposed LDH (both in blue).

3.3.4 Analysis of in situ powder X-ray diffraction data

Owing to the steel peaks dominating the powder pattern and the overlap of these peaks plus of peaks from the diffraction from the PTFE liner, it was not possible to do a full phase refinement of the transient phases over the whole 2-theta range. Instead Pawley refinements over one peak were performed. Evolution of all three phases could be followed by plotting the change in the integrated phase intensity as a function of time (Figure 3.13a). These integrated intensities were obtained from sequential refinements *(vide infra)*. Evolution of the *c* lattice parameter for both LDHs was obtained from sequential refinements (Figure 3.13c). There is a contraction in the unit cell *c* parameter during the decay of the first LDH, (LDH 1). The unit cell continues to contract throughout both the growth and decay of the second LDH, (LDH 2), albeit at a much slower rate. The temperature of the reaction vessel can be seen to stabilise at

210 °C after only a few minutes, (Figure 3.13b). This shows the evolution of lattice parameters is not a thermal effect.

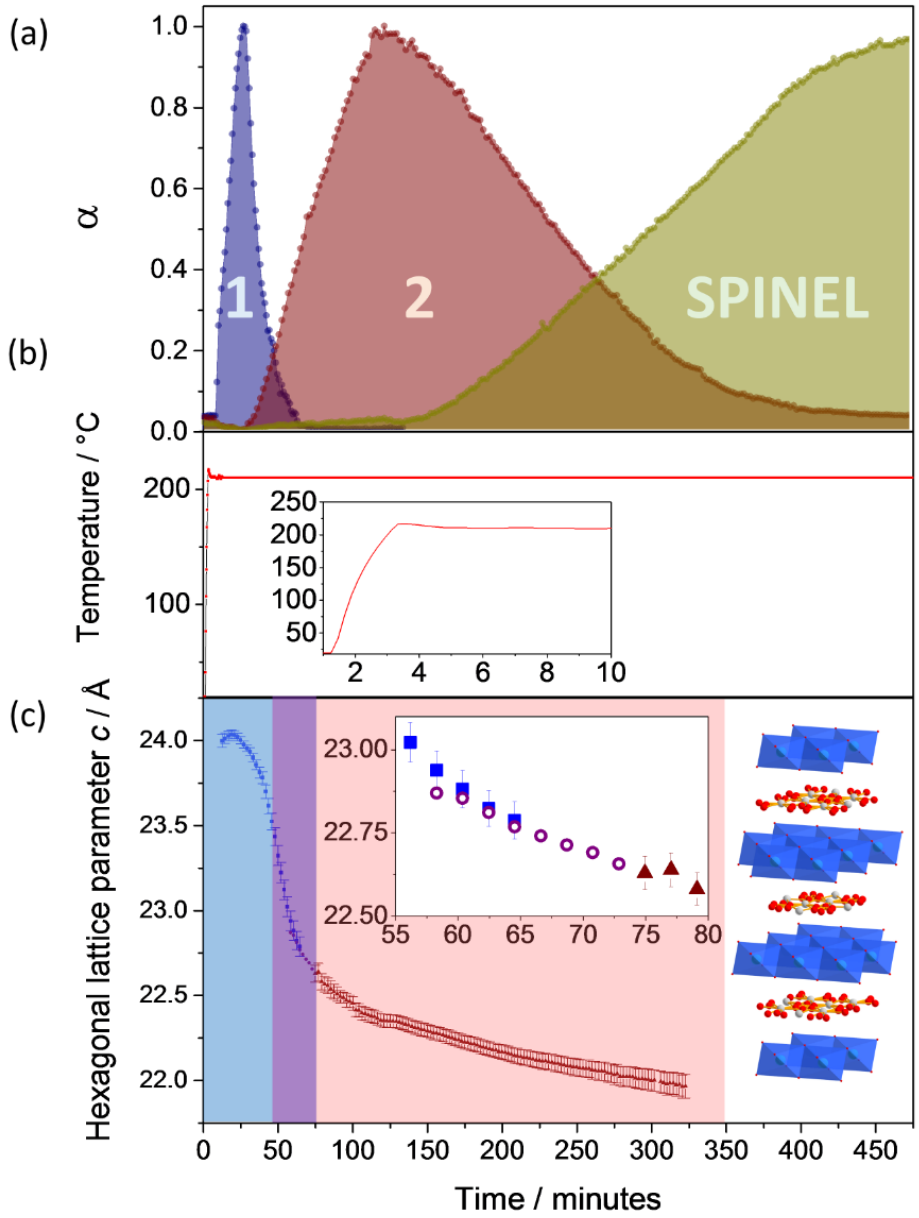

Figure 3.13 (a) Reaction overview from integrated intensities of LDH and spinel Bragg peaks, (b) Plot of temperature of reactor, (c) evolution of LDH *c* lattice parameter as a function of time with inset, blue squares the 1st LDH, mauve circles the 2nd LDH coexisting with the 1st LDH, and maroon triangles the 2nd LDH after disappearance of the 1st LDH and a schematic representation of the LDH.

3.3.5 Phase evolution

All refinements were performed against data after a rolling-ball background subtraction had been applied within the DAWN software. Since the acquisition time

for each frame was 12.447 s only every 10th powder XRD pattern was used for the refinements in both phase and lattice parameter evolution providing approximately a 2-minute interval between each data set.

TOPAS[37] was used to perform sequential refinements through the command line to integrate the relative intensities of each phase to provide the reaction overview seen above in Figure 3.13a. The change in the area under the LDH (006) reflection (Figure 3.14) was calculated independently for both LDHs. An arbitrary cell was used for this and all data outside the range of the (006) peak were excluded. This reflection was selected as there was minimal overlap of the (006) from the second phase present and as such it could be modelled as arising from a single phase from start to finish. An initial fit was obtained at the point where the maximum peak intensity was recorded (29 minutes and 124 minutes for transient phase 1 and 2 respectively) and then sequential refinements either side of this to when the peak first appeared to the last pattern where the peak is observed were conducted.

Similar methods were employed in obtaining the intensity of the spinel phase and the area under the most intense reflection (311) was used.

The decay of the second LDH and growth of the spinel do not cross at $\alpha = 0.5$, (α was calculated by normalising each phase to its maximum peak intensity value), this suggests that it is likely that re-dissolution of the LDH back into solution occurs to provide the correct ratio of metals from which the spinel crystallises. This is more likely than a direct solid-solid transformation given the difference in structure between the LDH (edge-shared octahedral metal sites) and spinel (close-packed oxide with octahedral and tetrahedral metal sites). The stoichiometry of the LDH from EDX suggests too that the LDH is not directly decomposing into the spinel since the Co:Ga ratio is different. The thermal transformation of LDHs into spinels usually occurs via phase separation into binary oxides or amorphous materials.[38]

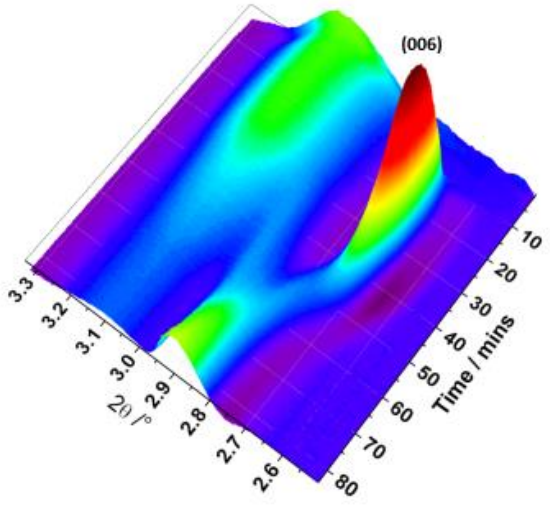

Figure 3.14 Growth and decay of the (006) reflection of the first LDH.

3.3.6 LDH unit cell contraction

During the sequential refinements of the LDH lattice parameters the *a* parameter was kept fixed (at 3.146 Å, typical of an LDH) and only the *c* parameter was refined using the position of the (003) and (006) reflections, (Figure 3.15). As for the peak intensity described above, initial lattice parameters were inputted into the refinement from when the peak intensity of both phases were at maximum and then refined either side to when each phase was either beginning to form (LDH 1) or present only as a single phase (such as in the case of LDH 2).

During the time 30 - 75 minutes when both transient phases were present only the lattice parameter of LDH 1 could be refined sensibly. Peak fitting to give a meaningful pseudo-Voigt fit using the Origin software allowed for the *c* parameter of LDH 2 to be estimated at this time. Independently refining the *c* parameter of LDH 2 using TOPAS resulted in unphysical results as was found to be the case in a biphasic fit of both LDHs.

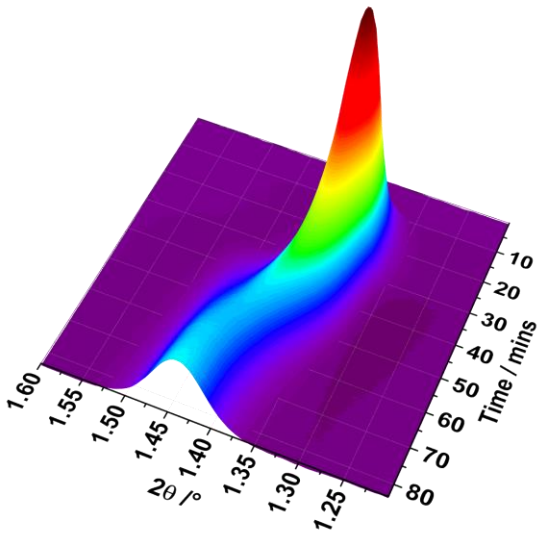

Figure 3.15 Colour map showing the progression of the (003) peak of the intermediate during the *in situ* experiment reaction with MEA:H_2O.

It should be noted that the data obtained during this experiment allowed for a detailed investigation into the pathway of the reaction but a thorough structural analysis by refinement was prohibited by i) the weak intensity of materials formed *in situ* compared to the steel autoclave and PTFE liner, ii) overlap of some reflections were with steel and PTFE, iii) cobalt and gallium (present in spinel and LDH) are virtually indistinguishable by X-rays. Therefore, no further detailed structural refinement was undertaken on the *in situ* data.

The final powder pattern collected showing the spinel *in situ*, *i.e.* after reaction had gone to completion, is shown below in Figure 3.16 to highlight the difference in intensity between the reaction vessel and the materials formed inside.

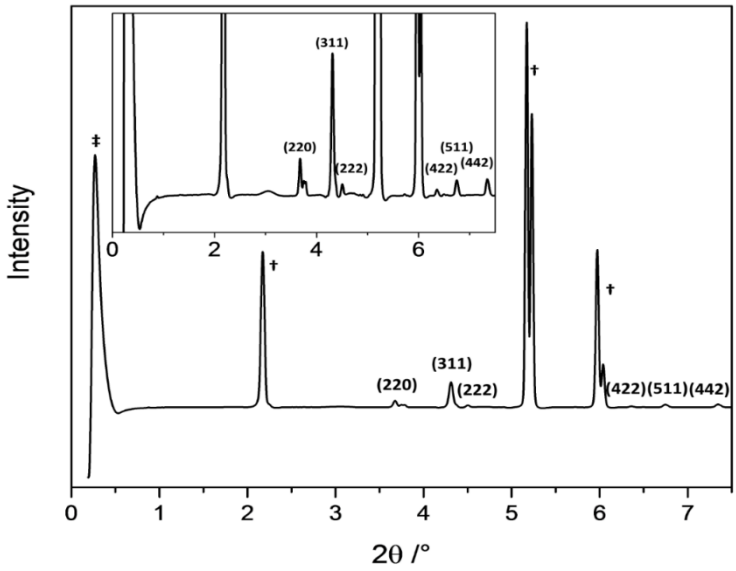

Figure 3.16 Plot of typical *in situ* pattern showing relative peak intensities of spinel product and features from the reactor. ‡ denotes beamstop and † denotes steel autoclave peaks.

3.3.7 Discussion regarding the two intermediate phases

Both LDHs are clearly related. This is deduced since many of the peaks observed in the first phase reach a minimum intensity (with a corresponding shift to higher angle) and then begin to increase in intensity again, *i.e.* the two LDHs share Bragg reflections.

Transient phase 2 has been identified as a layered double hydroxide and so transient phase 1 is therefore also very likely to be a layered (double) hydroxide.

One explanation for the observed changes in both peak intensity and position of some Bragg reflections is dehydration. It is quite clear that the most intense peak of the layered double hydroxide, (003), moves to higher angle and clearly shows the decrease in intensity followed by a secondary growth phase. Since this is the (003) reflection this corresponds to changes in the *c* parameter of the unit cell, which means that removal of water molecules from the interlayer gallery is certainly plausible, as is reorganisation of the interlayer anion and water molecules which has also been observed in LDHs.[39]

A possible reaction pathway could therefore be as follows: after 15 minutes of reaction time an initial LDH forms. This LDH consists of an unstable composition and immediately decomposes ejecting water molecules which reduces the basal spacing until a more stable layered double hydroxide forms. This secondary more stable

layered double hydroxide will continue to grow in intensity until the onset of spinel growth. This would explain why a plateau is never observed in either layered double hydroxide. It also explains the overlap of LDH 1 and LDH 2 in the reaction overview and the asymmetry in the observed reflections: a concentration of LDH 2 is beginning to accumulate (hence an increase in peak intensity) whilst LDH 1 is still decaying (Figure 3.17).

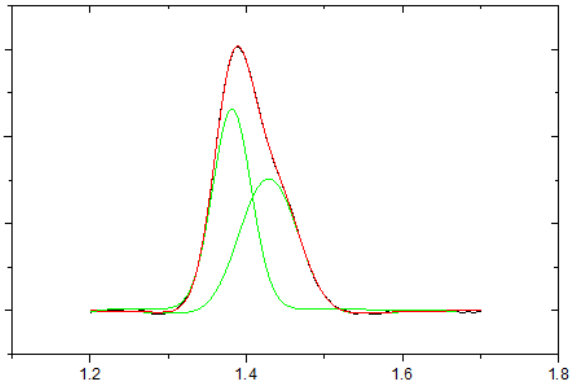

Figure 3.17 The (003) reflection at 54 minutes showing asymmetry. This is attributed to the decay of LDH1 and the growth of LDH2 and modelled by 2 pseudo-Voigt profile functions.

Sasika *et al* reported the synthesis of a layered cobalt hydroxide.[40,41] In this material the cobalt is solely in the +2 oxidation state and the charge between the brucite layers and the interanion layers is balanced due to the presence of protonated OH groups. This material is described as being metastable and that soon after its formation is converts to the well-known β-$Co(OH)_2$ phase. It is possible that LDH 1 is similar to this layered cobalt hydroxide. The lattice parameters are in good agreement with those indexed from the *in situ* data, in particular the *a* parameter a = 3.146 Å (this work) *cf.* a = 3.1439(5)[40], which is typical of Co-Co bond distances within the brucite layers.[41] LDH 1 is transient and though kinetically stable and begins to form within 15 minutes of reaction time, although it soon decays via a structural transformation in to the second LDH similar to the decomposition of the layered cobalt hydroxide into the more stable β-$Co(OH)_2$. Furthermore, in test reactions of just Ga with MEA:H_2O that were carried out using ODISC the onset of oxidation of gallium metal into spinel phase γ-Ga_2O_3 did not occur until after 2 hours of reaction time suggesting that 15 minutes of reaction time is not sufficient to oxidise the gallium metal.

If LDH 1 is a layered hydroxide containing only cobalt and LDH 2 a layered double hydroxide with both cobalt and gallium, then a decrease in the lattice parameters for LDH 2 would be expected relative to LDH 1. Both the *a* and *c* lattice parameters are smaller for LDH 1 compared to LDH 2. Typically, *c* decreases with increasing M^{3+} owing to the increase in the electrostatic attraction between the positive brucite-like sheets and the negatively charged interlayer,[42,43] though, conversely, the opposite has also been observed when the anion is nitrate.[44] A decrease in '*a*' occurs because M^{3+} is usually smaller than M^{2+}. It is proposed that LDH 1 does not directly transform into LDH 2 by reaction with gallium metal but rather LDH 1 decays significantly before LDH 2 is formed since α does not cross at 0.5, (Figure 3.13c).

3.3.8 Decay of LDH 2

A contraction in both *a* and *c* lattice parameters occurs during the transformation of LDH 1 to LDH 2. Since the (003) peak position is determined by the *c* lattice parameter and the (110) determined by the *a* lattice parameter a comparison of how both parameters change, by way of change in their *d*-spacing, can be obtained (Figure 3.18a). It is observed that there is a much larger change in the (003) *d*-spacing also with a broadening of the peak (Figure 3.18b) whilst the (110) *d*-spacing hardly changes during the same time. It must be noted here the *d*-spacings shown below were obtained from estimating the centre point of each peak (through peak fitting in Origin) and were not obtained from a least squares refinement. A change in the basal spacing corresponding to ~0.3 Å occurs over the time period from when the transient phase reaches a maximum peak intensity (125 minutes) to when almost fully re-dissolved (395 minutes). This is likely due to the removal of occluded water or rearrangement of the interlayer nitrate anion.

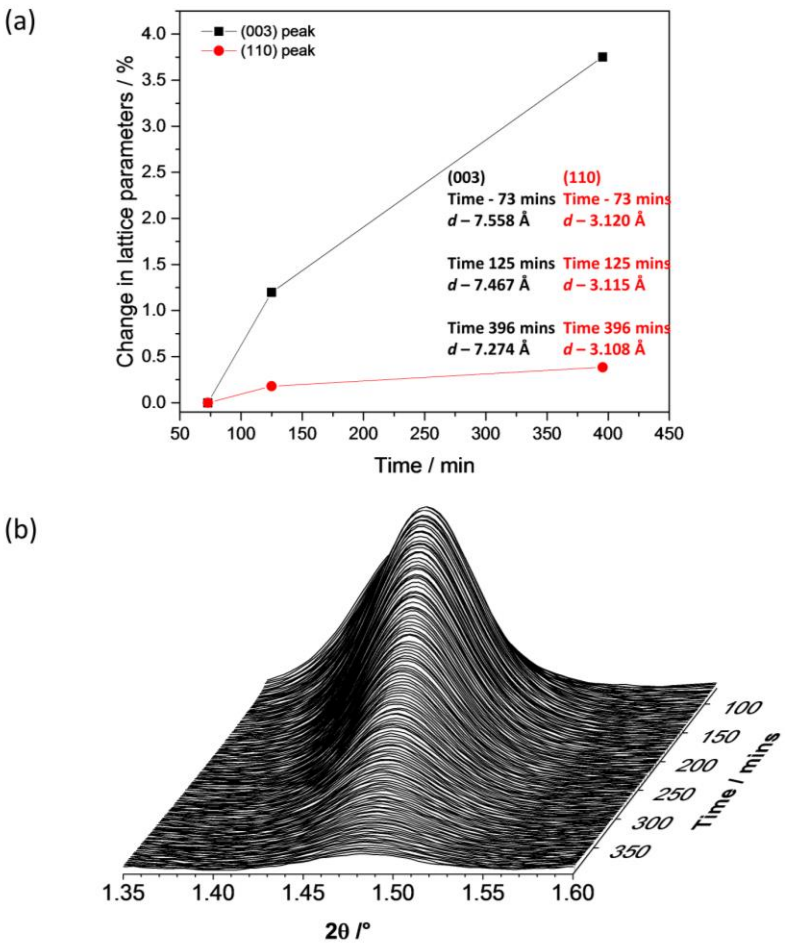

Figure 3.18. (a) Change in both the (003) and (110) *d*-spacings during the re-dissolution of the 2nd transient phase, (b) change in the (003) reflection of the second transient phase during re-dissolution.

A complicated interplay of nitrate anion intercalation and its hydration sphere may explain this behaviour.[45] Similar behaviour has been studied in LDHs when subjected to anion exchange,[42,44,46] dehydration (dehumidification),[47] or reorientation of the nitrate anion (or other interlayer species)[39] where it is often associated with large changes in the basal spacing (~1 Å) but little or no change in the interlayer separations. Such subtle changes have been observed in layered double hydroxides intercalated with nitrate anions when subjected to thermal treatment at 300 °C.[39]

3.4 Reaction 2: Reaction in MEA only

A second reaction conducted using just MEA shows that at no point during the reaction were any crystalline intermediates formed, however the spinel oxide can still be seen to form and was the only material found to be present once collected from the autoclave (Figure 3.19). Unfortunately, there was not enough time during the synchrotron experiment to allow this reaction to run to completion which is why no plateau in the spinel growth is observed.

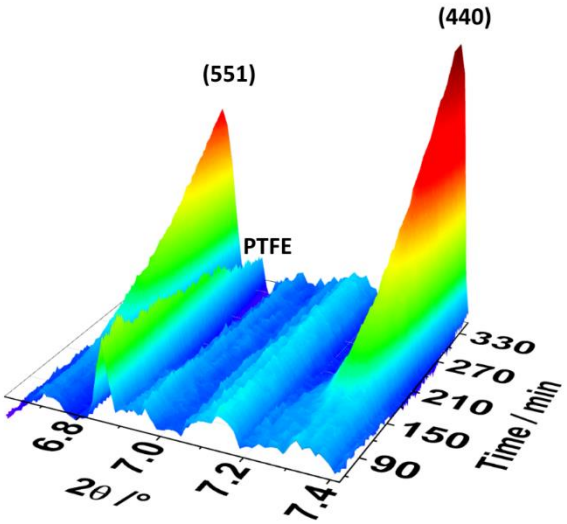

Figure 3.19 Colour map of the higher angle peaks of the cobalt gallium oxide spinel formed when only MEA is used as a solvent with Miller indices of the spinel labelled. No crystalline transient phases are observed during the reaction. The feature found around 6.85 is due to the PTFE liner.

3.5 Comparison of both reactions

The first obvious comparison is that crystalline intermediate phases are seen in the reaction with 1:1 MEA:H_2O whereas only the spinel is observed during the reaction in MEA only. Using TOPAS to integrate the intensity of the (440) reflection for both reactions and then normalising to a common baseline it was possible to compare the crystallisation curves of both spinels from the two different solvent conditions (Figure 3.20). Note that the amount of reagents were the same in both cases. The spinel formed in 1:1 H_2O:MEA crystallises at a faster rate than in MEA alone, though the onset of crystallisation occurs at a similar time (~150 minutes). The difference in the rate of spinel growth could be attributed to the greater solvent viscosity when MEA only is used,[48] which might affect either (or both) diffusion of reagents in solution or stirring

rate, rather than being necessarily directly related to the formation of the intermediate seen when a 1:1 H_2O:MEA ratio is used.

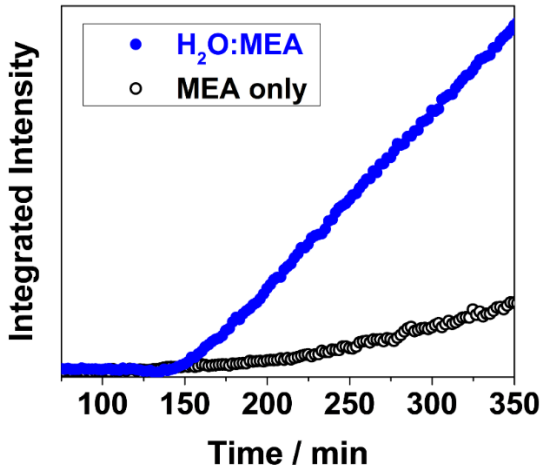

Figure 3.20 Comparison of crystallisation curves of the spinel phase.

3.6 Analysis of in situ data of both cobalt gallium oxides

Peak fitting in Origin was used to calculate the FWHM (of the (440) reflection) in order to ascertain if there was any change in the crystal/domain size of the spinel occurring throughout the reaction. In the reaction of MEA only the peaks are broader (Figure 3.21a) than in the 1:1 H_2O:MEA reaction (Figure 3.21b). However, the lack of any detectable peak sharpening during the period of crystal growth studied suggests that the crystallisation is nucleation dominated and that once crystals have formed there is little continued growth at those crystals and instead formation of new nucleation sites. Further work is needed to test this hypothesis but similar behaviour is observed in both reactions based on the change in the FWHM (Figure 3.21c and Figure 3.21d).

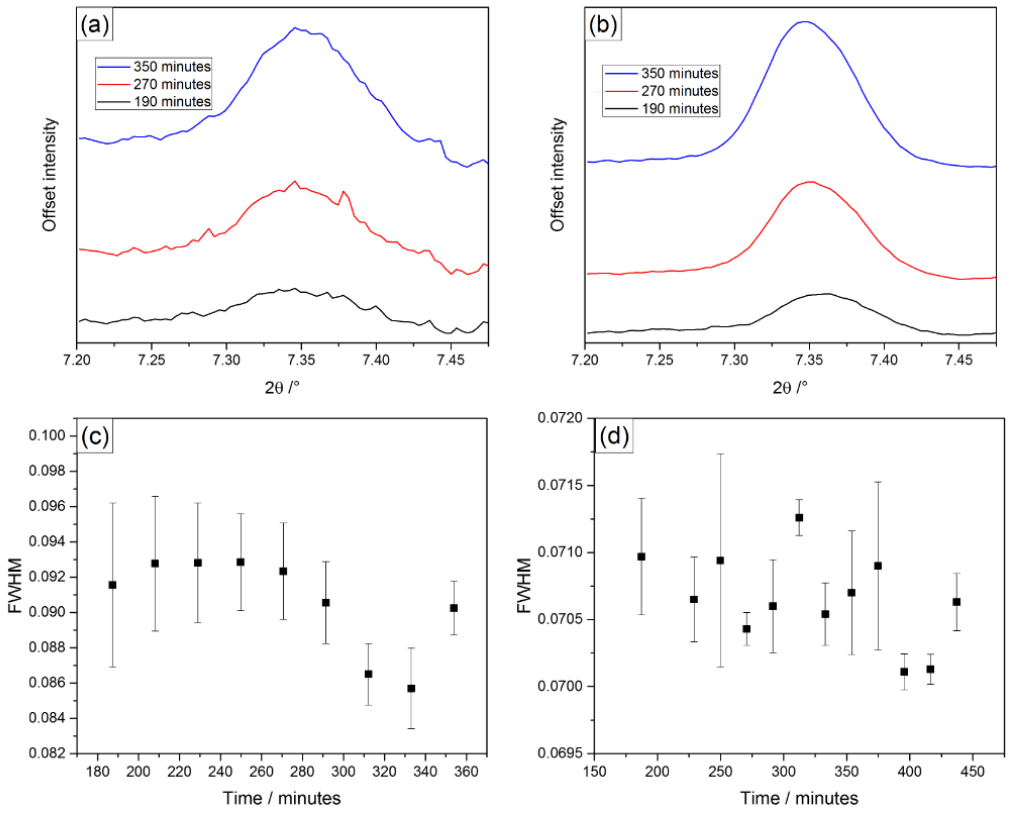

Figure 3.21 (a) *In situ* XRD of MEA only reaction showing the change in the width of the (440) reflection at different times, (b) *In situ* XRD of MEA:H_2O reaction showing the change in the width of the (440) reflection at different times, (c) FWHM of (440) reflection at different times during the MEA only reaction, and (d) FWHM of (440) reflection at different times during the MEA:H_2O reaction.

Refinement of the lattice parameter for both spinels using the *in situ* data was also attempted and the results are shown in Figure 3.22. The size of the lattice parameter was refined using only the (440) reflection in both reactions. In the reaction with 1:1 MEA:H_2O the (440) reflection can be seen to shift to low angler with time (Figure 3.22a). The refinement suggests a steady increase in the size of the cell of the spinel phase which plateaus as the reaction comes to completion (Figure 3.22b). Conversely the opposite appears to be true for the reaction in with MEA only where subtle shift to higher angle occurs (Figure 3.22c) and refinement of this reflection shows a small decrease in the cell size (Figure 3.22d). However, in the case of MEA only the size of the errors calculated are too large for this trend to be confirmed with any certainty. The size of the errors is likely due to the weak intensity of the broad (440) reflection and because only one reflection was used in refining the unit cell parameter. The more intense reflections (for example the (311)) were too often overlapped with PTFE resulting in meaningless fits, and it was not possible to extract more useful information

about the lattice parameters from the *in situ* experiment alone especially during the period where the spinel is beginning to grow in intensity. It should also be noted that although the lattice parameter of the spinel prepared in MEA only appears to get smaller this change is very small *cf.* the spinel prepared in the aqueous solution of ethanolamine where the change in lattice parameter is calculated as being much larger, (Table 3.2).

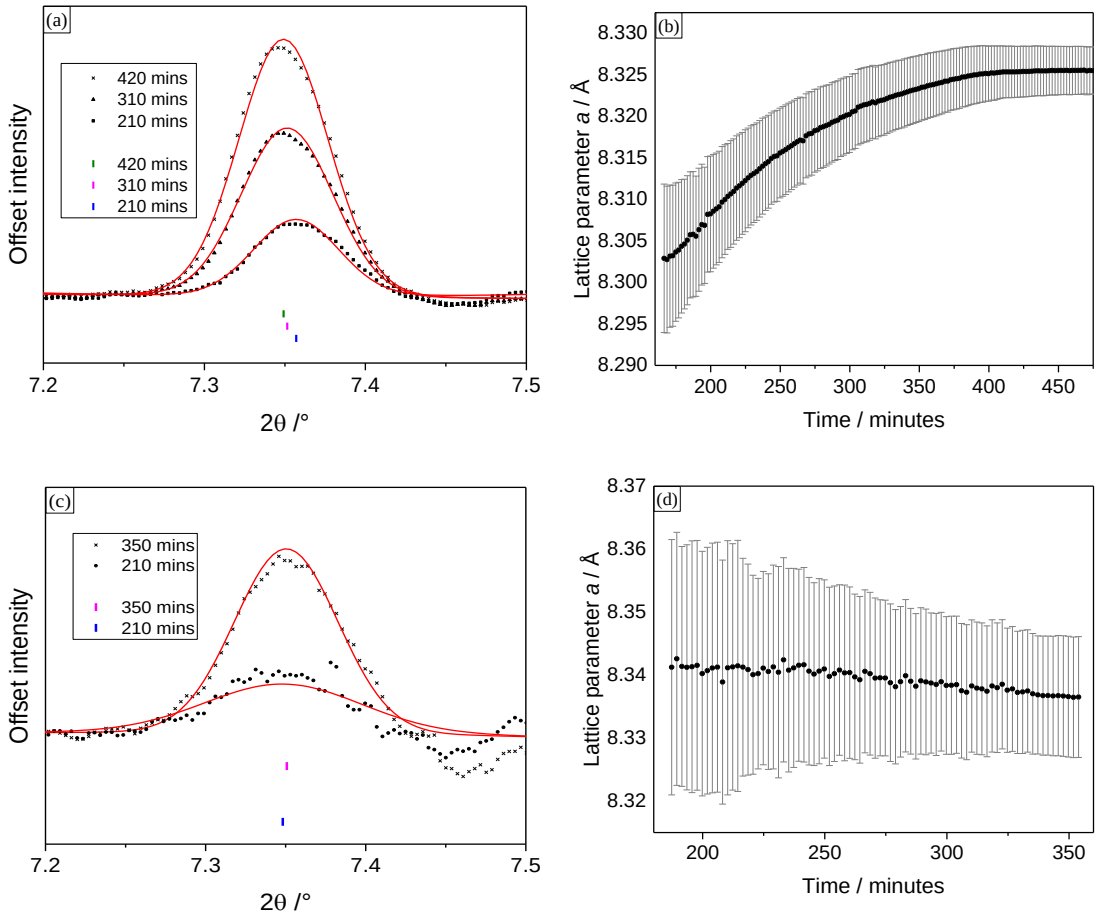

Figure 3.22 (a) (440) reflection in the Pawley refinement of the spinel prepared in H_2O:MEA, (b) change in lattice parameter of the spinel prepared in H_2O:MEA, (c) (440) reflection in the Pawley refinement of the spinel prepared in MEA only and (d) change in lattice parameter of the spinel prepared in MEA only.

Table 3.2 The change in unit cell parameter for both spinels with time and the unit cell of both spinels obtained from a Pawley refinement once isolated from the reaction vessel.

	Lattice parameter *a* / Å	
	MEA:H_2O	MEA
200 mins	8.308(7)	8.340(19)
350 mins	8.323(4)	8.337(9)
Isolated spinels (*i.e.* end of reaction)*	8.3257(2)	8.3302(15)

* *Ex situ* refinement from data obtained from Cukα_1 radiation

3.7 Ex situ Characterisation of isolated cobalt gallium oxide spinels

Both reactions yielded cobalt gallium oxide spinels as phase pure materials. PXRD of spinels from both reactions reveals that the reaction in ethanolamine only formed a poorly crystalline spinel (Figure 3.23a) whereas reaction in ethanolamine and water formed a highly crystalline spinel (Figure 3.23b). This information is confirmed from Scherrer analysis performed on all observable reflection in the PXRD patterns. The instrument broadening was taken into account using NIST ceria as a standard. Scherrer analysis using the FWHM of all observed reflections showed that the crystalline material has much sharper diffraction peaks and the domain size from Scherrer analysis was approximately 33±9 nm. The Scherrer estimated domain size of cobalt gallium oxide formed from ethanolamine only was calculated as 6±0.3 nm. Only Pawley refinements were undertaken on these oxides from which it is possible to obtain refined lattice parameters. The increased unit cell size of the less crystalline material is in keeping with nano-sized crystal domains. No Rietveld refinement was undertaken which could have provided information on the spinel composition as cobalt and gallium differ in 4 electrons meaning that they are almost indistinguishable by X-ray diffraction.

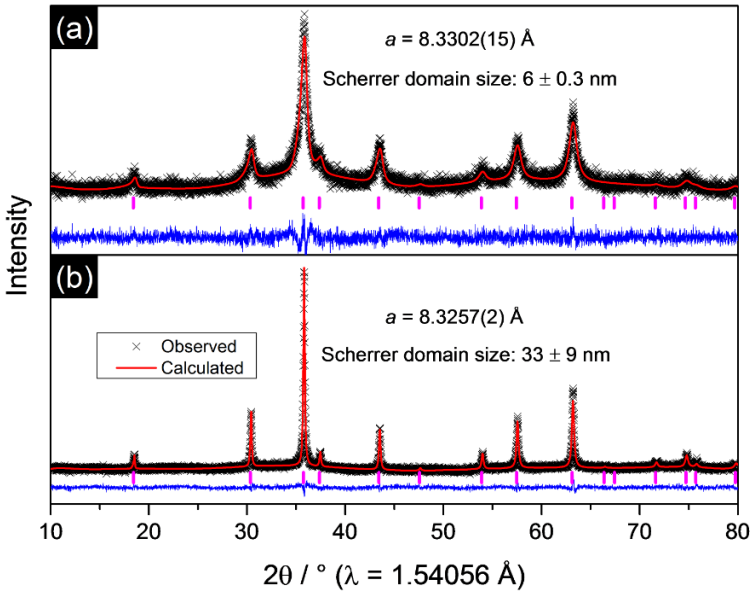

Figure 3.23. Pawley refinements of both spinels prepared from ethanolamine only and an ethanolamine water mixture. Refined lattice parameters and estimated domain size are indicated on each fit.

BET surface area measurements performed on both spinels show that the both have similar surface areas, Table 3.3, which might not be expected since the crystallinity of both spinels is markedly different.

Table 3.3. BET surface area measurements on cobalt gallium oxide synthesised in MEA:H2O and MEA only.

$CoGa_2O_4$	BET surface area / $m^2\ g^{-1}$
MEA:H_2O	32
MEA	30

Electron microscopy shows that both spinels seem to have a similar particle size (Figure 3.24) which accounts for the observed surface areas calculated for both materials. However, HRTEM suggests that the material formed in MEA and water has highly ordered domains whereas reaction is MEA only seems to form particles with disordered crystal domains. This is entirely consistent with the Scherrer analysis which provides an indication on the mean ordered domain size which is not necessarily the same as the particle size.

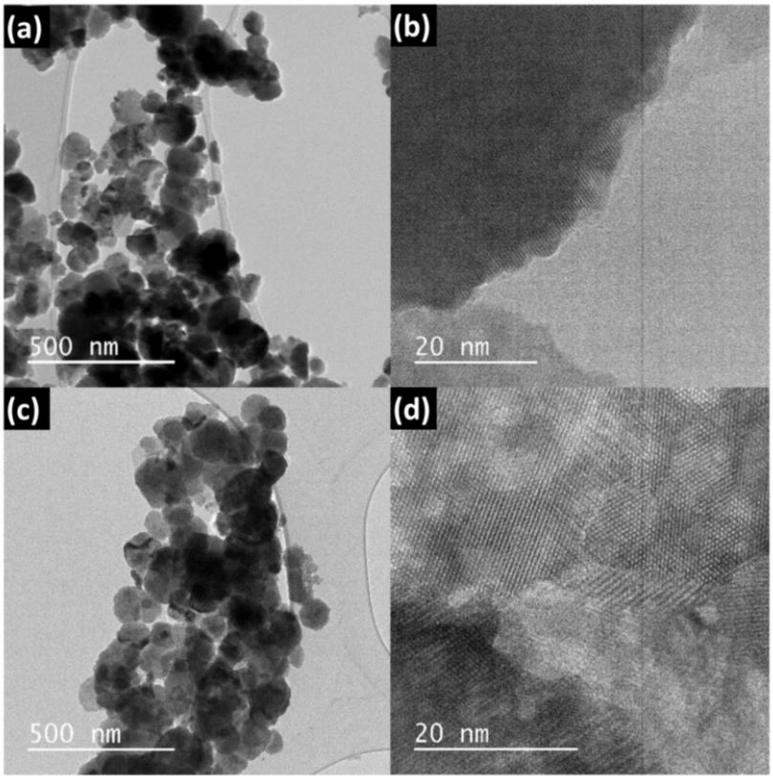

Figure 3.24 (a) TEM of $CoGa_2O_4$ prepared in MEA:H2O, (b) HRTEM showing ordered crystal domains of the same spinel, (c) TEM of $CoGa_2O_4$ prepared in MEA only showing similar crystallite size and morphology, (d) HRTEM showing that the particles are made up of disordered crystal domains.

XANES measurements were carried out in transmission mode on B18 at the Diamond Light Source at the Co-K edge on both spinels (Figure 3.25). It was found that in both cases cobalt was present almost exclusively as Co^{2+}. The small pre-edge feature is evidence that most Co^{2+} is likely in octahedral coordination meaning that cobalt gallium oxide formed in both reactions are inverse spinels (Figure 3.25 *inset*). This is in agreement with other literature reports of $CoGa_2O_4$ which show that $CoGa_2O_4$ usually has some degree of inversion.[18,19,49,50] Later in this chapter this will be illustrated further with a study of similar materials.

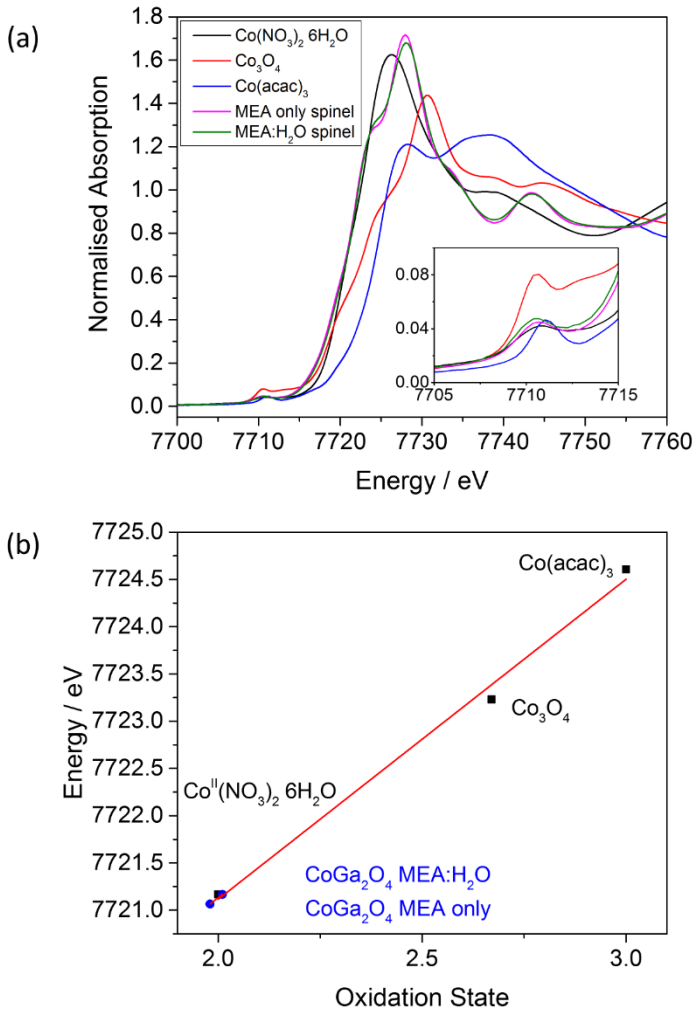

Figure 3.25. (a) Co-K edge XANES spectra normalised to the edge step, and (b) plot of edge position (defined as the energy at which normalised absorption = 0.5) as a function of oxidation state with a linear fit to reference materials providing the calculated oxidation states of $CoGa_2O_4$ spinels from the *in situ* experiment.

3.8 Summary

This study has shown that during solvothermal reactions layered double hydroxides can form as transient phases before re-dissolution and formation of metal oxides. The formation of these layered double hydroxides is dependent on the reaction media. Oxide materials, including spinels, are often prepared by firing layered double hydroxides at high temperatures (300 – 500 °C)[51–53] but the work reported here is the first study to show their formation as kinetically stable materials preceding spinel formation under solvothermal conditions. The fast acquisition time of the *in situ* XRD uniquely allowed for observation of two transient phases including one in particular

which is very short lived and unlikely to have been quenched and seen by conventional laboratory techniques.

The hydro(solvo)thermal synthesis of layered double hydroxides has been reported numerous times in the literature and remains one of the key synthetic routes to their formation.[23,53–59] Layered double hydroxides remain highly relevant in materials science and are still being developed for new technologies such as fire retardation materials and as additives for water based lubricants.[57,60–62] LDHs have even been studied as water oxidation photocatalysts.[63]

This study demonstrates the complexity of solvothermal reactions, with the presence of metastable products highlighting that predicting the pathways and outcomes of exploratory synthesis of new functional materials remains extremely challenging.

3.9 Solvothermal synthesis of cobalt gallium oxide prepared by solvothermal reaction of γ-Ga_2O_3 and $Co(NO_3)_2{\cdot}6H_2O$

3.9.1 Synthetic procedure

3.9.1.1 Synthesis of cobalt gallium oxide from γ-Ga_2O_3

As illustrated in the previous sections two solvothermal procedures may be used to synthesize cobalt gallium oxide from gallium: the use of ethanolamine alone or a 1:1 reaction of ethanolamine:water. The syntheses presented here are an adaption of this reaction but uses pre-formed γ-Ga_2O_3 instead. The synthesis of γ-Ga_2O_3 is described elsewhere (Chapter 5). 0.300 g (1.60 mmol) γ-Ga_2O_3 and 0.292 g $Co(NO_3)_2{\cdot}6H_2O$ (1.600 mmol) were added to a PTFE liner followed by the addition of 10 ml monoethanolamine (MEA). The reaction mixture was stirred for 10 minutes at room temperature before being sealed in a stainless-steel autoclave and placed in a fan assisted oven at 240 °C for 72 h. The autoclave was then removed from the oven and allowed to cool naturally to ambient temperature and the reaction mixture filtered dispersed in methanol and then collected by vacuum filtration and washed with copious amounts of methanol to isolate a bright blue powder nominally called $CoGa_2O_4$, (Figure 3.26).

Figure 3.26 γ-Ga_2O_3 *(left)* and *(right)* $CoGa_2O_4$

The reaction often resulted in a large deposition of metallic cobalt as observed by eye. Furthermore, it was often found that this reaction would form other impurity phases such as GaOOH or unreacted γ-Ga_2O_3. In an effort to optimise this reaction a solvent mixture of 10 ml 1:1 ethanolamine:H_2O was used. Although a small amount of metallic cobalt was still present most of the unreacted cobalt nitrate remained in solution probably due to the presence of water in the solvent mixture. The supernatant collected from the reaction was dark red in colour indicative of unreacted cobalt nitrate. It was found that this method was also more reliable in that no unreacted γ-Ga_2O_3 or GaOOH was found as an impurity product. It should also be noted that in the controlled reaction of γ-Ga_2O_3 and 1:1 MEA:H_2O that the oxyhydroxide $Ga_5O_7(OH)$ forms exclusively and this phase was also absent in the powder diffraction pattern of the cobalt gallium material isolated at the end of the reaction.

To remove the metallic cobalt from the sample the cobalt gallium oxide was filtered through a funnel several times surrounded by rare-earth magnets several times.

The reaction using only 10 ml deionised water always resulted in the formation of Co_3O_4 as a secondary phase with cobalt gallium oxide.

3.9.2 General characterisation

Powder X-ray diffraction shows the shift of all Bragg peaks of γ-Ga_2O_3 to lower angle for $CoGa_2O_4$ which is consistent with the incorporation of the larger Co^{2+} cation

(Figure 3.27). Furthermore, the diffraction peaks become sharper suggesting the material is more crystalline and has a bigger crystallite size than the defect spinel γ-Ga_2O_3.

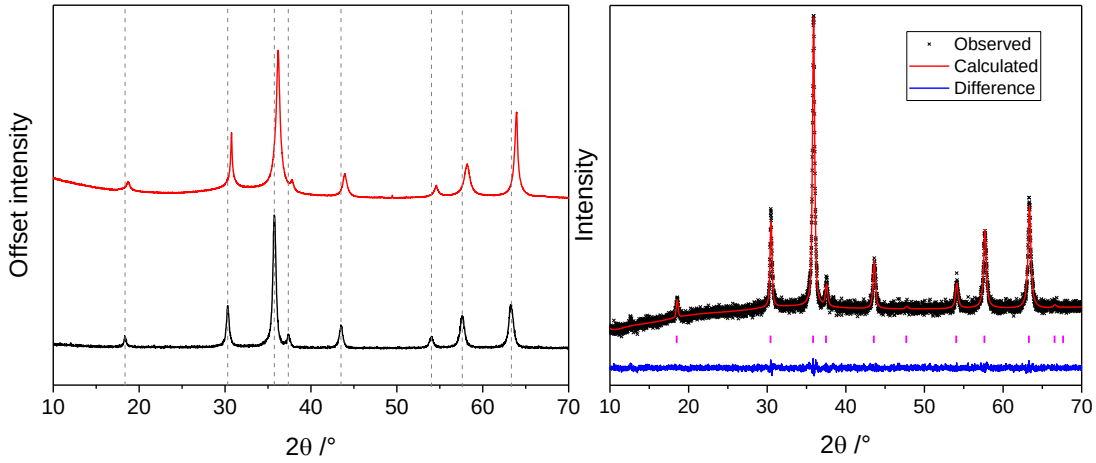

Figure 3.27 Stacked plot *(left)* of $CoGa_2O_4$ (black) with γ-Ga_2O_3 (red) with dashed lines showing shift to lower angle for $CoGa_2O_4$. Pawley refinement *(right)* of $CoGa_2O_4$ with lattice parameter a = 8.3050(13) Å *cf.* γ-Ga_2O_3 where a = 8.2376(9) Å.

TEM shows the transformation of γ-Ga_2O_3 with the flake-like plate morphology into the oval morphology of the mixed metal gallate. In both cases the material was made of small crystallites on the nano-scale range, (Figure 3.28).

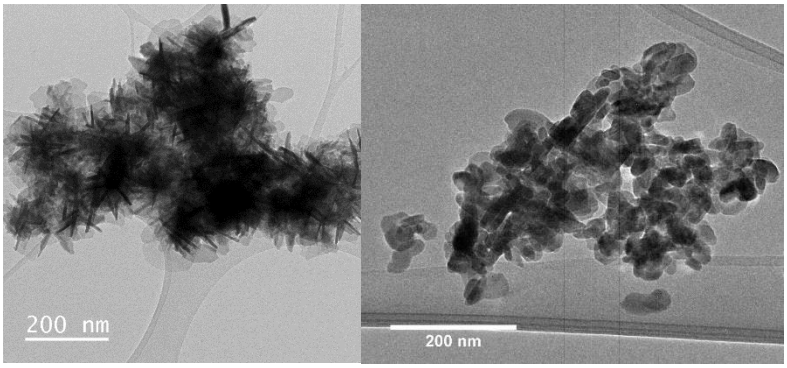

Figure 3.28 Morphology transformation of gallium oxide *(left)* into cobalt gallium oxide *(right)* after reaction with cobalt nitrate hexahydrate.

In situ X-ray thermodiffractometry (Figure 3.29) showed that the spinel was stable at 900 °C but upon closer inspection of the contour map anomalous cell contraction occurs over the temperature 250 – 500 °C. Similar negative thermal expansion through this range was also seen in cobalt gallium oxide prepared from gallium metal. A proposed explanation suggested this could be due to a redistribution the cations in the structure caused by a change in the proportion of tetrahedral and octahedral Ga-O and

Co-O bonds. Since Co-O and Ga-O distances are different between tetrahedral and octahedral sites then the amount of each will affect the average unit cell size. This is unlikely to be a straightforward correlation and some discontinuity in cell volume with changing bond distances may be expected. A metastable arrangement of cations in the as made sample may rearrange to give a transient spinel species before ultimately rearranging to form a more thermodynamically stable spinel.

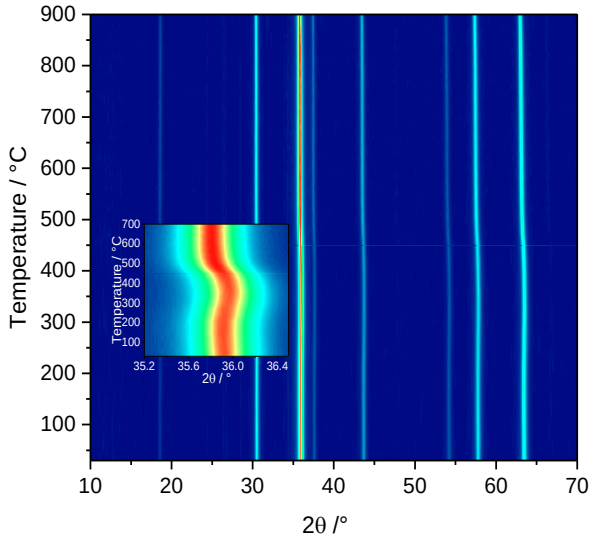

Figure 3.29 Contour plot of *in situ* heating XRD on cobalt gallium oxide. *Inset* close up on most intense spinel reflection (311) showing the non-typical thermal expansion behaviour between 250 – 500 °C.

XANES analysis confirmed only the presence of Co^{2+} (Section 3.4.5) in both the as-made sample and in a sample that had been heated in air to 600 °C suggesting that if a re-distribution of cations occurs it does so without oxidation of the Co^{2+} cation. However, this negative thermal expansion was not observed when the sample was heated under N_2, (Figure 3.30). An *in situ* XANES or XAS experiment where a sample of spinel is heated to 600 C in various atmospheres would further probe whether a redistribution of the cations is occurring.

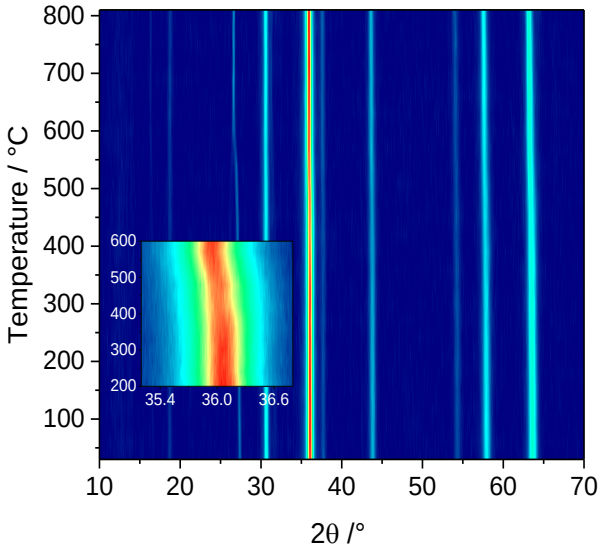

Figure 3.30 Thermodiffractometry of $CoGa_2O_4$ heated in N_2, with inset showing no contraction of the cell.

Finally, this anomalous cell contraction is also irreversible and not seen upon cooling down to room temperature from 900 °C, (Figure 3.31).

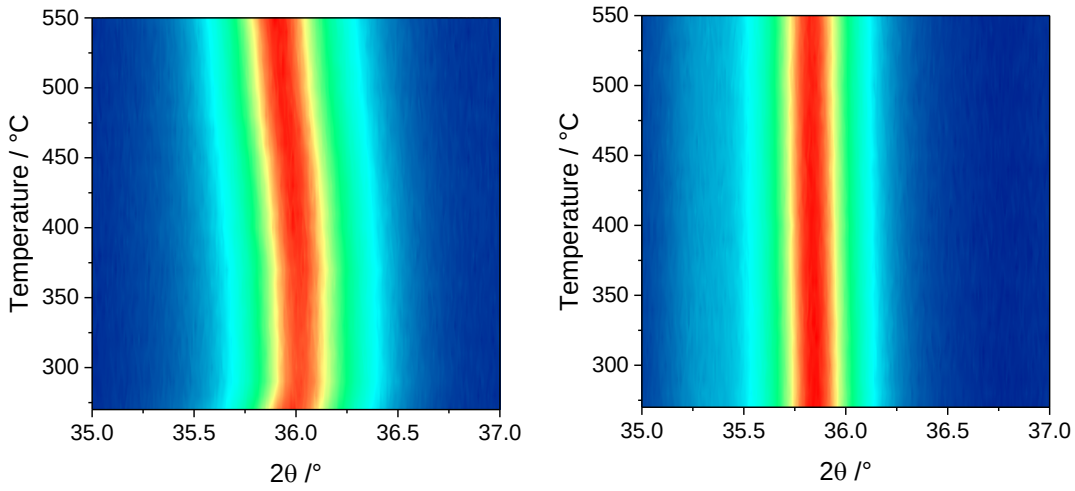

Figure 3.31 Thermodiffractometry of $CoGa_2O_4$ heating up from 30 to 900 °C showing the region 270-550 °C *(left)* and then cooling back down again *(right)* showing no anomalous behaviour.

3.9.3 Neutron diffraction study of cobalt gallium oxide

This anomalous cell contraction was then investigated by *in situ* neutron diffraction on heating. Cobalt and gallium differ in only 4 electrons and so are almost indistinguishable by X-rays and therefore structural analysis with X-rays would not be possible, however, the neutron coherent scattering cross-sections of cobalt and gallium are appreciably different (0.779 barns for cobalt and 6.675 barns for gallium) so to be

distinguishable. Neutron diffraction also allows for the oxygen position to be refined more accurately too.

The neutron diffraction data were collected on the Polaris instrument at ISIS. The sample for neutron diffraction was sealed in a vanadium can and then placed in a furnace itself in a chamber which was evacuated. A room temperature diffraction pattern was recorded and then the furnace was slowly ramped up to 600 °C and diffraction patterns were recorded at various temperature intervals.

3.9.3.1 Refinement of room temperature spinel

The refinement was carried out using the Playford model of $CoGa_2O_4$ as a starting point. The first constraint applied on the refinement was to keep the total cation site occupancy to 1. Without this constraint when the occupancies of the sites were refined it was found that unphysical results occurred with the occupancy of both metal sites exceeding 1.

The initial refinement of the room temperature spinel showed that the cobalt gallium oxide is a largely inverse spinel with an inversion parameter, $x = 0.749$, with trivalent gallium cations preferentially occupying the tetrahedral site and also that the spinel is slightly cobalt rich. Because of this the spinel must be partially deficient in the oxide anion to charge balance the excess of divalent metal. Therefore, the oxide anion occupancy was set to charge balance the cation charge and was not refined, (it was assumed all cobalt was present as Co^{2+} which was later confirmed by XANES, (Section 3.4.5)). The oxide vacancy is ~1.7% which is acceptable since cobalt gallium oxide prepared from the solvothermal oxidation directly from gallium metal has been shown to be partially deficient in oxide anion up to 6%.[12] Changing and fixing the oxide anion occupancy to charge balance the cations causes only a small increase in the wrp from 2.003 to 2.011%, which was not considered a significant result. A good fit to the data was obtained (Figure 3.32) and the refined composition is shown in Table 3.4.

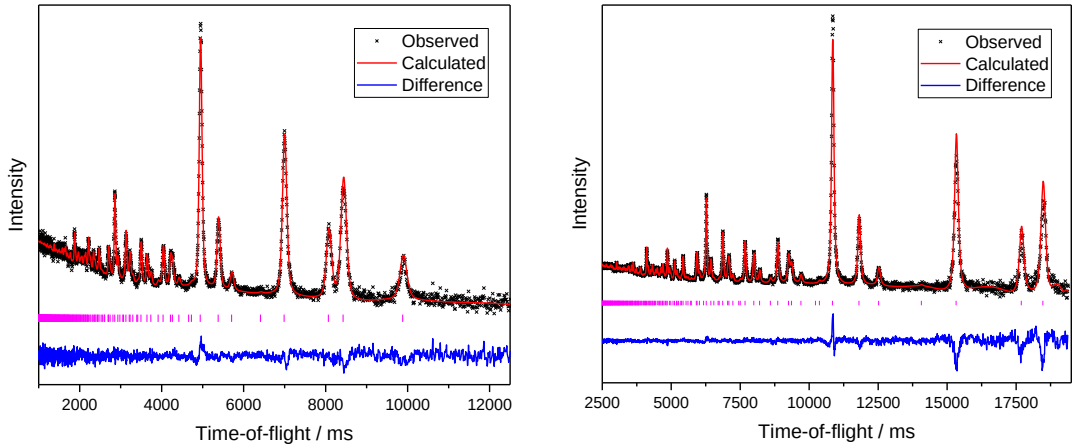

Figure 3.32 Multi bank Rietveld refinement of cobalt gallium oxide from data obtained from Polaris bank 3 *(left)* and bank 5 *(right)*.

Table 3.4 Crystal parameters for $Co_{1.146}Ga_{1.861}O_{3.932}$ at room temperature before heating. Space group $Fd\bar{3}m$, a = 8.31401(7) Å. Rp = 2.524%, wRp = 2.011%.

Wyckoff site	Atom	x	y	z	Occupancy	Beq / Å^2
8a	Ga	0.125	0.125	0.125	0.749(4)	0.205(12)
	Co	0.125	0.125	0.125	0.251(4)	0.205(12)
16d	Ga	0.5	0.5	0.5	0.556(4)	0.389(14)
	Co	0.5	0.5	0.5	0.444(4)	0.389(14)
32e	O	0.25596(5)	0.25596(5)	0.25596(5)	0.983*	0.573(1)

*O occupancy was not refined, (see text).

Another model was tested before proceeding with the refinements of the spinel at higher temperature. This was to fix the total amount of Co and Ga to be 1:2 as is the stoichiometry typically observed in many spinels. The refinement showed the spinel to be largely inverse but a poor fit was obtained compared to the cobalt rich spinel. When the oxide anion occupancy was refined in this model it also refined to a partially oxide deficient spinel, which not only does it not charge balance the cations in this model but also hints that model is indeed slightly rich in the divalent cation. The M^{2+}:M^{3+} as 1:2 spinel model was discarded.

3.9.3.2 Refinement of spinel with increasing temperature

In all the neutron diffraction refinements at higher temperatures the room temperature model was used as a starting point. Another constraint was applied, in addition to keeping the total occupancy of each site to 1, which was to keep the total amounts of cobalt and gallium in the spinel the same throughout. An initial attempt without this

constraint resulted in small changes to the overall spinel composition, such as increasing the amount of cobalt, which does not make chemical sense.

With these constraints applied the cobalt and gallium occupancies over both crystallographic sites can be refined whilst simultaneously keeping both sites fully occupied and maintaining the stoichiometric ratio found from the room temperature refinement.

Using the room temperature refinement as a starting model and the constraints mentioned above similar refinements were then undertaken for all powder patterns up to 600 °C and then a final refinement after cooling to room temperature.

A plot of lattice parameter as a function of temperature shows that there is a non-linear increase as the cell expands (Figure 3.33a). The thermal parameters also show a linear increase as temperature increases which is to be expected and supports that the refined parameters are real (Figure 3.33b). The non-linear expansion of the lattice parameter is more consistent with what is observed by X-ray thermodiffractometry when the sample is heated under nitrogen (Figure 3.33c) but not as pronounced when the sample is heated in air (Figure 3.33d). Furthermore, the onset of the cell contraction in the neutron thermodiffractometry occurs at a similar temperature for the sample measured with X-rays under nitrogen which is a higher temperature than observed in the X-ray thermodiffractometry when heated in air. This could be due to one of several reasons: the sample is placed inside a vanadium can which itself is placed inside a furnace and so the transfer of heat compared to the X-ray diffractometer is different. The chamber containing the sample is evacuated and since the sample is densely packed in the vanadium can if the negative thermal expansion is due to a reaction with oxygen this could be reduced under these conditions and thus the lattice parameter trend is more similar to the X-ray thermodiffractometry when heated under N_2 than when heated in air.

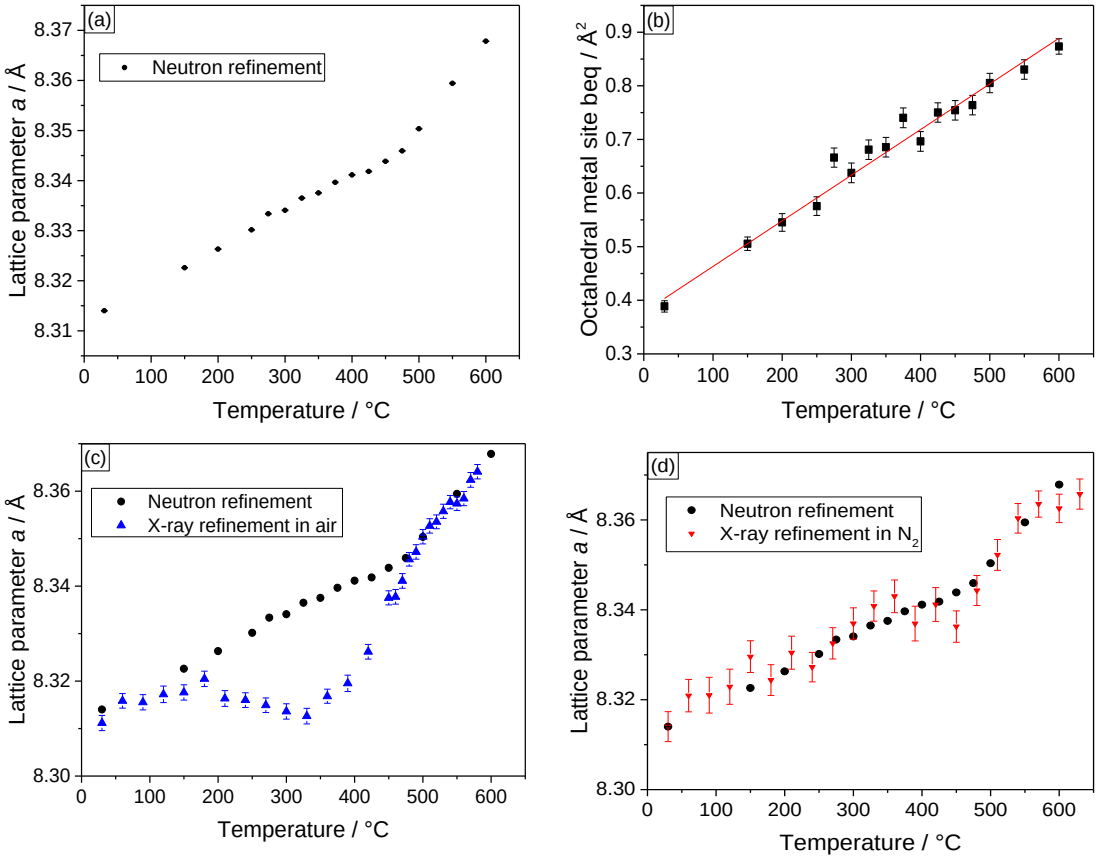

Figure 3.33 Evolution of lattice parameters for the cobalt gallium oxide spinel *(left)* obtained from separate refinements of both neutron and X-ray powder diffraction data. Linear increase in thermal parameters *(right)*.

A rearrangement of the cationic distribution occurs within the spinel with increasing temperature, (Figure 3.34). As the spinel is heated cobalt gallium oxide tends towards a more normal spinel in that gallium cations start to adopt the octahedral sites (and cobalt cations adopting the tetrahedral sites). The onset of this rearrangement occurs at around 300 °C which coincides well with the onset of the negative thermal expansion observed in the X-ray thermodiffractometry under nitrogen. A gradual rearrangement occurs between 300 and 450 °C, a similar temperature range observed by X-ray thermodiffractometry, but this is then followed by a more pronounced rearrangement of the cations up to 600 °C. It was expected that any structural change would have completed after the period of negative thermal expansion (250 – 500 °C) (from the X-ray thermodiffractometry) and as such the neutron experiment had only been performed to 600 °C. The results of the refinement of the spinel heated at 600 °C is detailed below (Table 3.5).

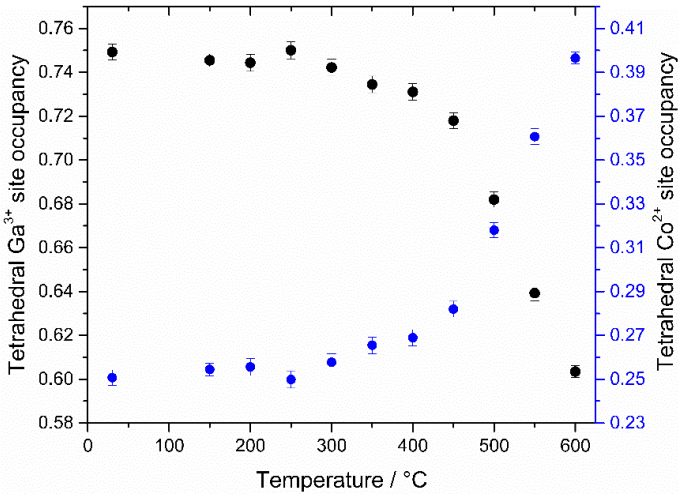

Figure 3.34 Change in the tetrahedral metal site occupancy with temperature. The spinel tends towards a normal arrangement as divalent cation tetrahedral occupancy increases with temperature.

Table 3.5 Crystal parameters for $Co_{1.146}Ga_{1.861}O_{3.932}$ at 600 °C. Space group $Fd\bar{3}m$, a = 8.36794(5) Å. Rp = 2.074%, wRp = 1.755%.

Wyckoff site	Atom	x	y	z	Occupancy	Beq / Å^2
8a	Ga	0.125	0.125	0.125	0.603(3)	0.640(14)
	Co	0.125	0.125	0.125	0.400(3)	0.640(14)
16d	Ga	0.5	0.5	0.5	0.629(1)	0.824(12)
	Co	0.5	0.5	0.5	0.373(1)	0.824(12)
32e	O	0.25675(4)	0.25675(4)	0.25675(4)	0.983*	1.214(9)

*O occupancy was not refined

The refinement of the neutron diffraction data after heating to 600 °C and cooled to room temperature shows that this rearrangement of cations is very different compared to before heating (Figure 3.35 and Table 3.6), with a larger unit cell after heating. Though the rearrangement is not irreversible only a small change in the cationic distribution difference is seen in the sample at 600 °C and the sample cooled back to room temperature compared to the as-made sample and the sample at 600 °C.

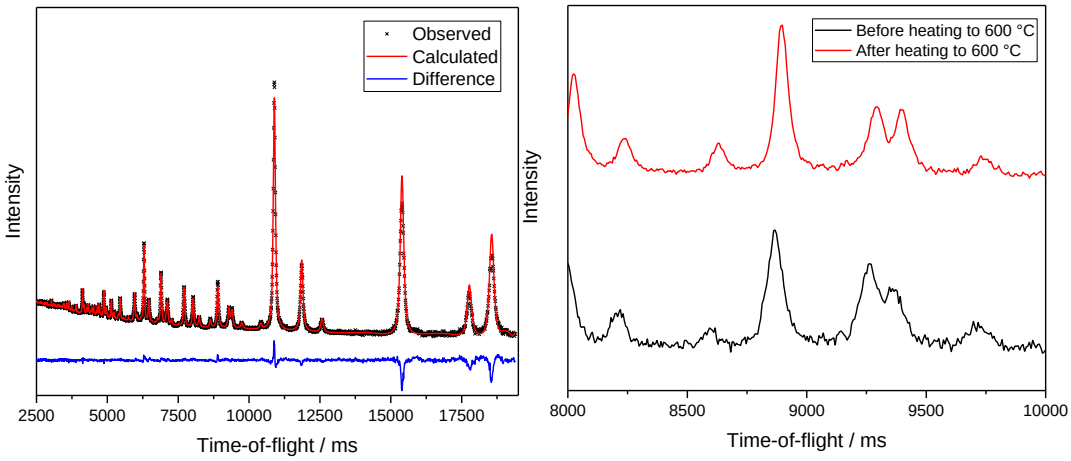

Figure 3.35 Rietveld refinement fit of spinel after heating to 600 °C from Polaris (bank 5) *(left)* and subtle relative peak intensity changes observed in before and after heating *(right)*.

Table 3.6 Crystal parameters for $Co_{1.146}Ga_{1.861}O_{3.932}$ after heating to 600 °C. Space group $Fd\bar{3}m$, a = 8.33646(5) Å. Rp = 2.003%, wRp = 1.947%.

Wyckoff site	Atom	x	y	z	Occupancy	Beq / Å^2
8a	Ga	0.125	0.125	0.125	0.611(3)	0.344(10)
	Co	0.125	0.125	0.125	0.389(3)	0.344(10)
16d	Ga	0.5	0.5	0.5	0.625(1)	0.409(9)
	Co	0.5	0.5	0.5	0.375(1)	0.409(9)
32e	O	0.25716(3)	0.25716(3)	0.25716(3)	0.983*	0.7223(7)

*O occupancy was not refined

These refinements suggest that the as-made cobalt gallium oxide synthesised at 240 °C contains a metastable arrangement of cations that rearrange to form a more thermodynamically stable spinel. The refined composition of the spinel before and after heating are given in Table 3.7.

Table 3.7 Cobalt gallium oxide spinel composition before and after heating to 600 °C.

	Lattice parameter a / Å	Structural formula
As made	8.31401(7)	$^{IV}(Co_{0.2507}Ga_{0.7493})^{VI}[Co_{0.8884}Ga_{1.1116}]O_{3.93045}$
After heating to 600 °C	8.33645(5)	$^{IV}(Co_{0.3916}Ga_{0.6084})^{VI}[Co_{0.7476}Ga_{1.2524}]O_{3.93045}$

The changes in the spinel composition are manifested in the average metal-oxygen bond length for both the tetrahedral and octahedral position as the composition of the spinel changes (Table 3.8). As expected a larger bond length on average is seen for

the tetrahedral M-O bond since more Co^{2+}, which is larger than Ga^{3+} (0.58 Å *cf.* 0.47 Å in coordination IV)[64] is present on this site after heating to 600 °C than for the as-made sample. The opposite is true for the octahedral site where a decrease in average bond length is observed since smaller Ga^{3+} now populates the octahedral site more after thermal treatment than in the as-made sample.

Table 3.8 Change in the average metal-oxygen bond length with the change in temperature and change in the degree of spinel inversion.

Temperature / °C	Coordination	Co^{2+} occupancy	Ga^{3+} occupancy	Average bond length / Å
28 (before heating)	Tetrahedral	0.251(4)	0.749(4)	1.8858
	Octahedral	0.444(4)	0.556(4)	2.0302
600	Tetrahedral	0.400(3)	0.603(3)	1.9095
	Octahedral	0.373(1)	0.629(1)	2.0371
28 (after heating)	Tetrahedral	0.389(3)	0.611(3)	1.9083
	Octahedral	0.375(1)	0.625(1)	2.0262

It is interesting to compare the post heated spinel to other cobalt gallates in the literature. The degree of inversion in the spinel is clearly sensitive to the experimental procedure. $CoGa_2O_4$ has been reported with various inversion parameters but usually described as an inverse spinel. A single crystal study reported an inversion parameter of $x = 0.575$.[18] High temperature syntheses of $CoGa_2O_4$ have been reported with an inversion parameters of $x = 0.654$, and $x = 0.72$.[65] $CoGa_2O_4$ has been synthesised from a high temperature and high pressure hydrothermal reaction between the respective nitrates and refinement of synchrotron X-ray data showed that the spinel had an inversion parameter of 1.[66] The degree of inversion, whilst never consistently reported, is always reported as being largely inverse. This is in contrast to $CoAl_2O_4$ which is almost always reported as being a completely a normal spinel.[66–68] With gallium and aluminium being similar in size and sharing similar chemistries it perhaps appears odd why cobalt gallium oxide is so frequently, as in this instance, is reported as a largely inverse spinel.

3.9.3.3 Discussion regarding the inversion in spinels containing gallium

Often it is sufficient to use crystal field theory (CFT) to predict the site preference of metals within a spinel. For example, CFT accurately predicts that Co_3O_4 is a normal spinel and Fe_3O_4 as inverse. With this knowledge it could be argued that the inversion of $CoGa_2O_4$ should be determined by the Co^{2+} cation alone. Ga^{3+} would have 0 CFSE and therefore no preference in being octahedral or tetrahedral. Were this the case then a similar degree of inversion should be seen in $CoAl_2O_4$ yet it has always been reported as being a normal spinel. It is well established that gallium shows a marked preference for tetrahedral sites in spinels and so a more thorough treatment regarding why different cations occupy different sites must require more than CFSE alone and other factors must be taken into account including the following: the Madelung constant, the size of the cations,[69,70] the polarization of the anion and the degree of covalency between the chemical bonds.[71] Synthesis conditions, in particular temperature and pressure are also important in determining the final cation distribution. Numerous studies have been undertaken in order to develop a theory into spinel site occupation.[69–75]

Furthermore, it is a general feature of d^{10} ions to adopt tetrahedral coordination due to their polarizing power.[72] A strong polarization between a cation and anion contributes to a strong covalent interaction which is favoured in tetrahedral coordination where sp^3 hybridisation is possible.[71] This is why Ga^{3+} is so commonly found in tetrahedral coordination in spinels.

Melot argued that the tetrahedral site preference of Ga^{3+} is due to the d^{10} cation tending to adopt sp^3 hybridization.[76]

Nakatsuka has argued that in the spinel itself the size of the cations in the spinel directly has an influence on the inversion parameter. Replacing the larger Co^{2+} for Al^{3+} on the tetrahedral site results in abnormally long bond lengths which are less favoured. In contrast Ga^{3+} is slightly larger and so this effect is less pronounced.[67]

3.9.3.4 Discussion regarding the change in inversion parameter with temperature

As mentioned above the experimental conditions directly affect the degree of inversion observed in cobalt gallium oxide spinels. Porta and Anichini found that with $Co(Ga_zAl_{1-z})O_4$ solid solutions a higher degree of inversion was found when prepared at a higher temperature. Not only do the experimental conditions directly influence the degree of inversion in $Co(Ga_zAl_{1-z})O_4$ but the incorporation of Ga^{3+} directly influences the inversion parameter as $CoAl_2O_4$ becomes increasingly more inverse owing the reasons regarding polarization described above.[65] Other similar experiments where a third cation is introduced in to the spinel to change its degree of inversion have been reported.[72]

The inversion parameter for cobalt gallate appears to be flexible and sensitive to the synthetic procedure whilst cobalt aluminate is usually a normal spinel. However a Rietveld study of powder XRD data of samples of $CoAl_2O_4$ quenched at different reaction temperatures (750 – 1200 °C) showed that the spinel tended towards a more inverse spinel at higher temperatures.[77] There have been studies on spinels which show a change in cation distribution when heated even though they were initially prepared at high temperature. For example, in a sample of Hercynite ($FeAl_2O_4$) prepared at 1400 °C and then rapidly quenched to room temperature also showed a change in the degree of inversion, becoming more normal at 600 °C and then rearrangement to a more inverse configuration upon heating to 1150 °C.[78]

Thermodynamic modelling of cationic ordering in spinels has been the subject of intense investigation.[69,73,79] Perhaps one contribution is due to the crystal field stabilisation energy. Co^{2+}, d^7, has more known tetrahedral complexes than any other transition element. Co^{2+} forms stable tetrahedral complexes because it has the greatest number of electrons in the lower-energy orbitals as compared with the number of electrons in the higher-energy orbitals.

Since the properties of materials are affected by the arrangement of cations the experimental conditions can often be tuned to suit a desired application. The *in situ* neutron thermodiffractometry experiment highlights perhaps another way in which a material can be designed or fine-tuned by modifying its arrangement of cations by firing the material after synthesis.

3.9.4 Total neutron scattering of cobalt gallium oxide before and after heating

The pair distribution function (PDF) obtained from the normalised total neutron scattering was calculated. The PDF for both the before and after heating samples were fitted using the crystallographic information obtained from the refinement of Bragg scattering from the neutron diffraction data. The PDF fit obtained for the as-made sample (Figure 3.36) is a result of refining only the thermal and lattice parameters. In this sample a good fit in the high-r range is consistent with the Rietveld refinement of the average structure model obtained from the neutron Bragg scattering. However as can be seen a much poorer fit in the low-r range, in particular to the first peak, is an indication of local disorder present in this material. The first PDF peak occurs around 1.9 – 2 Å which is a convolution of the metal-oxygen bonds. The poor fit to the peak is not unexpected since a previous investigation into the local structural disorder of cobalt gallium oxide involving RMC modelling suggested that local distortion around the Ga-O octahedra is the likely cause also found in the case of γ-Ga_2O_3 (also a spinel).[43,12,80] Owing to a significant presence of Co^{2+} on the octahedral sites Jahn-Teller distortion is also likely to cause some structural distortion of the M-O octahedra too. No improvement of the fit could be obtained since the model is still constrained by the parameters of the cubic spinel in space group $Fd\bar{3}m$. Previous work involving RMC has indicated this and improvement of the first PDF peak involves relaxing the symmetry constraints in order to model the Ga-O distortion.[12]

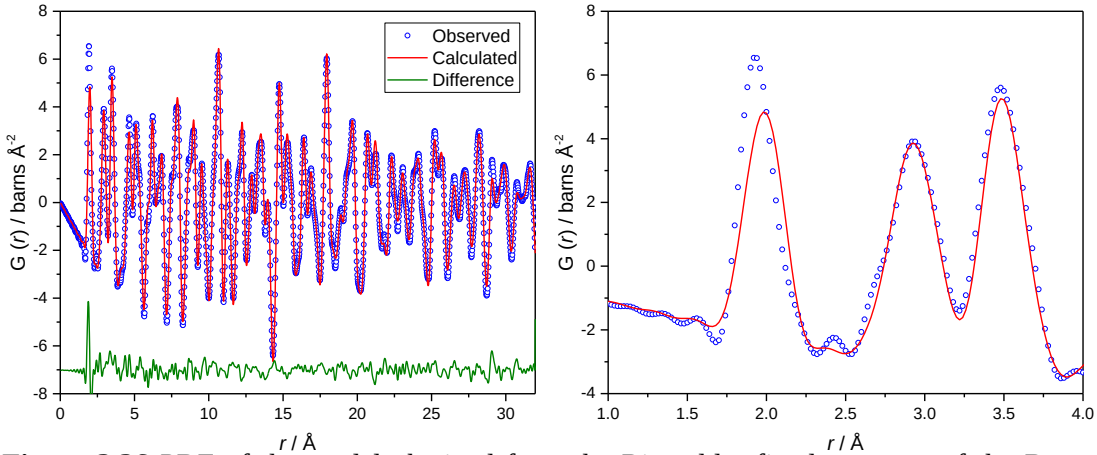

Figure 3.36 PDF of the model obtained from the Rietveld refined structure of the Bragg scattering *(red)* fitted against the measured PDF *(blue)* for cobalt gallium oxide before heating *(left)*, low r-region fit *(right)*.

The PDF of the sample after heating was similarly fitted using the average crystallographic model obtained from the Bragg diffraction from neutron data and refining the thermal and lattice parameters of the spinel (Figure 3.37). As with the as-made sample a reasonable fit to the PDF is obtained meaning that the average crystal structure is largely sufficient to describe the material but the first PDF peak is still fitted poorly which indicates that structural disorder around the metal-oxygen polyhedra remains after firing to 600 °C and is not removed after rearrangement of the spinel. This is perhaps not surprising since it has been shown that disorder around the Ga-O octahedra occurs in the high temperature gallium oxide polymorphs such as the thermodynamically stable β-Ga_2O_3 polymorph.[11]

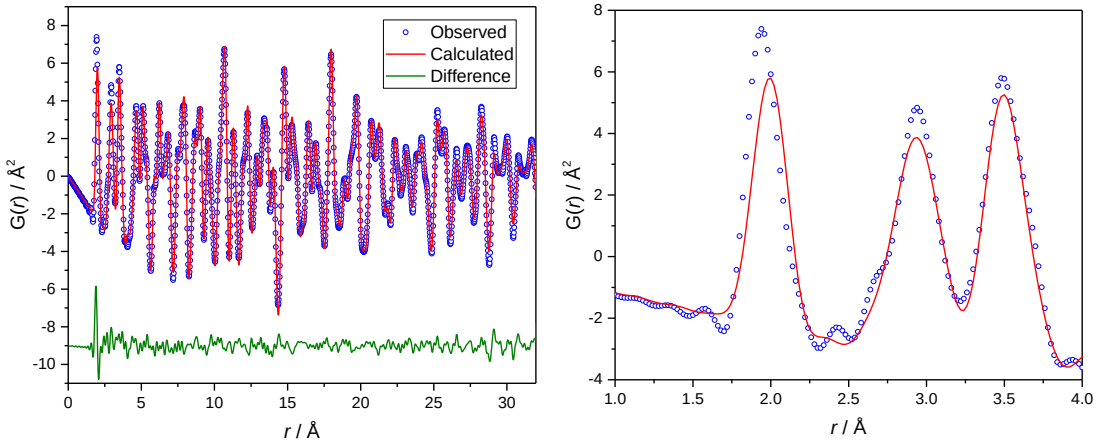

Figure 3.37 PDF of the model obtained from the Rietveld refined structure of the Bragg scattering *(red)* fitted against the measured PDF *(blue)* for cobalt gallium oxide after heating to 600 °C *(left)*, the low-r region of the PDF fit *(right)*.

If the occupancy of cobalt and gallium from the as-made sample are used in the sample after heating a slightly poorer fit is obtained, evident by the difference in the *Rw* value (13.90% *cf.* 14.74%), which is further confirmation that the rearrangement of cations is real.

3.9.5 XANES

As described above a redistribution of the gallium and cobalt cations occurs in cobalt gallium oxide as it is heated which could be attributed to the negative thermal expansion observed in the X-ray diffraction heating contour map. However, upon heating the Co^{2+} could be oxidised to Co^{3+}. A XANES experiment was conducted to

investigate whether the rearrangement of cations in cobalt gallium oxide occurs with, or without, oxidation of cobalt.

XANES was carried out on the same sample that was used for neutron diffraction (Figure 3.38a). Analysis of the Co-K edge in $CoGa_2O_4$ shows that Co remains in the +2 oxidation state in the as-made sample before and after heating to 600 °C which means that the rearrangement of cations in the spinel occurs without oxidation of cobalt (Figure 3.38b). Closer inspection of the pre-edge feature shows that there is a slight increase in intensity after firing to 600 °C similar to that observed in Co_3O_4 (Figure 3.38c). This is expected since Rietveld refinement of the neutron diffraction data showed an increase in tetrahedral cobalt with increasing temperature. The pre-edge feature in this material occurs due to the electronic transition (1s → 3d) and is forbidden in geometries that carry a centre of inversion, such as the octahedral Co^{2+}. As Co^{2+} shifts towards a tetrahedral geometry with increasing temperature the amount of Co^{2+} in a geometry with no inversion symmetry increases and thus the intensity of the pre-edge feature increases. The absence of any Co^{3+} in the post-fired sample is not surprising: more cobalt is in tetrahedral coordination and Co^{3+}, a d^6 cation would preferentially occupy an octahedral site with low spin because of the gain in crystal field stabilisation energy and so the transition to tetrahedral upon oxidation site would not be expected.

An *in situ* heating experiment using XANES was also undertaken. A sample of as-made cobalt gallium oxide was ramped at 10 °C min^{-1} to 550 °C, whilst simultaneously measuring XANES spectra, (Figure 3.38(d)). The edge position of the sample at different temperatures remains very similar to the 90 °C, and close to the Co^{2+} reference. It was concluded that no oxidation of Co^{2+} occurs in cobalt gallium oxide when heated in air. The spectra become increasingly noisy at higher temperatures and as such no analysis of the pre-edge feature intensity as a function of temperature was conducted.

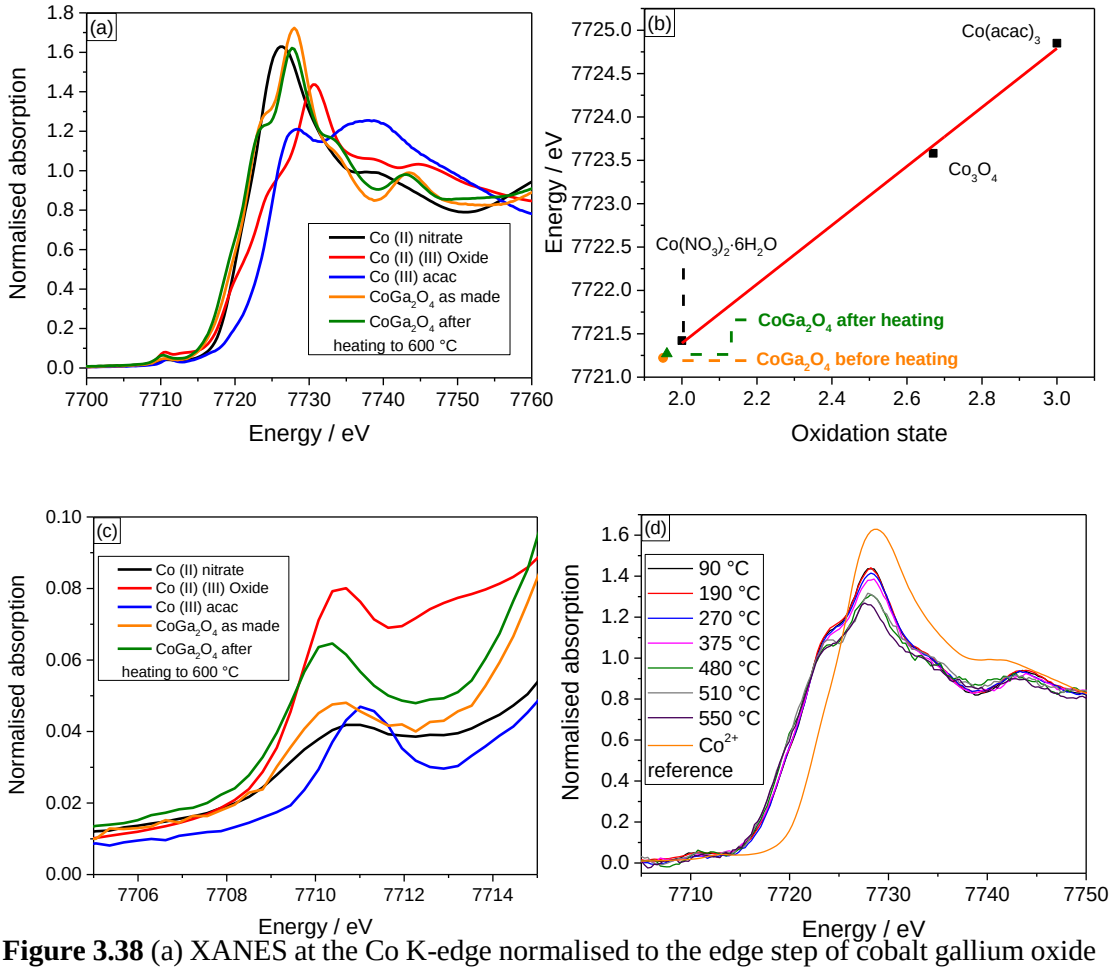

Figure 3.38 (a) XANES at the Co K-edge normalised to the edge step of cobalt gallium oxide before and after heating to 600 °C with relevant cobalt references, (b) Calculated oxidation state of cobalt gallium oxide before and after heating determined from the edge position (defined where normalised absorption = 0.5), (c) close up on pre-edge region of XANES data, and (d) *in situ* XANES of cobalt gallium oxide.

3.9.6 Magnetic behaviour

The functional applications and properties of a metal oxide material is, in part, a consequence of the arrangement of cations (especially in a spinel). Magnetometry was conducted to investigate whether the magnetic properties of the cobalt gallium oxide are changed in the as made sample and after heating to 600 °C since the cationic arrangement is altered.

The magnetic behaviour of the as made spinel and after being fired to 600 °C was studied by SQUID magnetometry. A magnetisation (M) versus temperature (T) experiment was performed over the range 5 – 300 K for both zero-field cooled (ZFC) and field cooled (FC) magnetisation. The magnetic behaviour of both samples is very similar. Both display paramagnetic behaviour above 10 K but the presence of magnetic

ordering becomes apparent at low temperatures ~10 K (Figure 3.39). This ordering has been seen in both $CoGa_2O_4$ prepared by high temperature synthesis[50] and the sample prepared by solvothermal synthesis from gallium metal[12] and was attributed to antiferromagnetic ordering in both cases though it has been argued that this is spin glass behaviour owing to competing antiferromagnetic and ferrimagnetic interactions.[49] Therefore, it was unsurprising that the antiferromagnetic ordering was also observed in the sample heated to 600 °C (*i.e.* after the cation rearrangement has occurred).

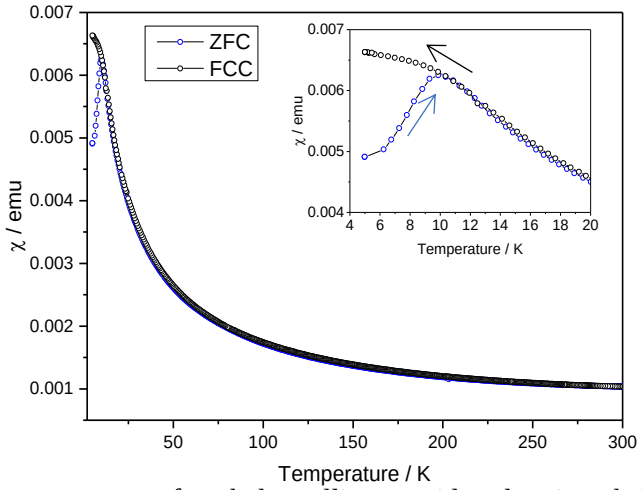

Figure 3.39 Magnetometry of cobalt gallium oxide showing behaviour of typical antiferromagnetic ordering with inset showing the Néel temperature close to 10 K.

3.10 Application of the synthetic method to other mixed metal oxides

3.10.1 Overview

The synthesis of cobalt gallium oxide from gallium oxide demonstrated above may at first seem an unnecessary step in that the γ-Ga_2O_3 must first be prepared from gallium metal before it is converted into the mixed metal oxide. As it has already been demonstrated, cobalt gallium oxide can be prepared directly from gallium metal.[12] However, gallium metal is unusual in that it has a very low melting point (29 °C) attributed to its diatomic molecular-like crystal structure with one out of seven very short Ga-Ga bond distances.[81,82] The fact that gallium melts at a low temperature is likely a key feature in why the solvothermal oxidation to gallium oxide directly from gallium metal can be effected. Similar solvothermal reactions were attempted with

both aluminium ingots and finely divided aluminium powder and yielded only unreacted aluminium. If the approach shown above to form mixed metal oxides from binary metal oxides can be achieved by this solvothermal method then perhaps this synthesis can be adapted for other metal oxides. A recent publication has already shown how galvanic replacement reactions can occur with metal oxide nanocrystals.[83] In this paper "nano-cages" of Mn_3O_4/γ-Fe_2O_3 were prepared by reacting preformed Mn_3O_4 nano-crystals with iron(II) perchlorate via a redox-couple reaction between the multivalent metallic ions. It has long been established that mixed metal hydroxides can be prepared from separate binary metal oxides in hydrothermal reactions.[84,85] The obvious candidate was to use γ-Al_2O_3 as a precursor for mixed-metal aluminates. Test reactions with zinc and cobalt salts were performed since mixed metal gallates can be prepared from these transition metal ions by reaction with γ-Ga_2O_3.

3.10.2 Synthetic procedure

0.262 g (2.57 mmol) γ-Al_2O_3 (SASOL) and 0.764 g (2.57 mmol) $Zn(NO_3)_2 \cdot 6H_2O$ (Aldrich, ≥98%) or 0.748 g (2.57 mmol) $Co(NO_3)_2 \cdot 6H_2O$ (Aldrich, ≥98%) were added to a PTFE liner followed by the addition of 5 ml mono-ethanolamine (MEA) and 5 ml H_2O. The reaction mixture was stirred for 10 minutes at room temperature before being sealed in a stainless steel autoclave and placed in a fan assisted oven at 240 °C for 72 h. The autoclave was then removed from the oven and allowed to cool naturally to ambient temperature and the reaction mixture filtered and collected by vacuum filtration and washed with copious amounts of methanol. The isolated powders were dried overnight at 70 °C.

3.10.3 Powder X-ray diffraction

The powder X-ray diffraction patterns from both reactions are shown below, (Figure 3.40). Reaction with zinc nitrate shows that formation of the spinel phase $ZnAl_2O_4$ has formed (Figure 3.40a) although there are some broader peaks apparent underneath the intense mixed metal spinel peaks which is very likely to be unreacted γ-Al_2O_3. A small boemite impurity was also detected by XRD. No reaction with cobalt nitrate occurred, instead only transformation of γ-Al_2O_3 into the aluminium oxyhydroxide boehmite, AlOOH, (Figure 3.40b). Given the propensity of boehmite to form from hydrothermal reactions using alumina and aluminium based salts this is hardly surprising.[86]

Although reaction with cobalt nitrate did not seem to work under the conditions specified above the fact that zinc can be added directly into the poorly crystalline spinel offers scope for further reactions using similar oxide precursors which could be important especially since alumina containing other metals is of vital importance for many catalytic applications.[87–89]

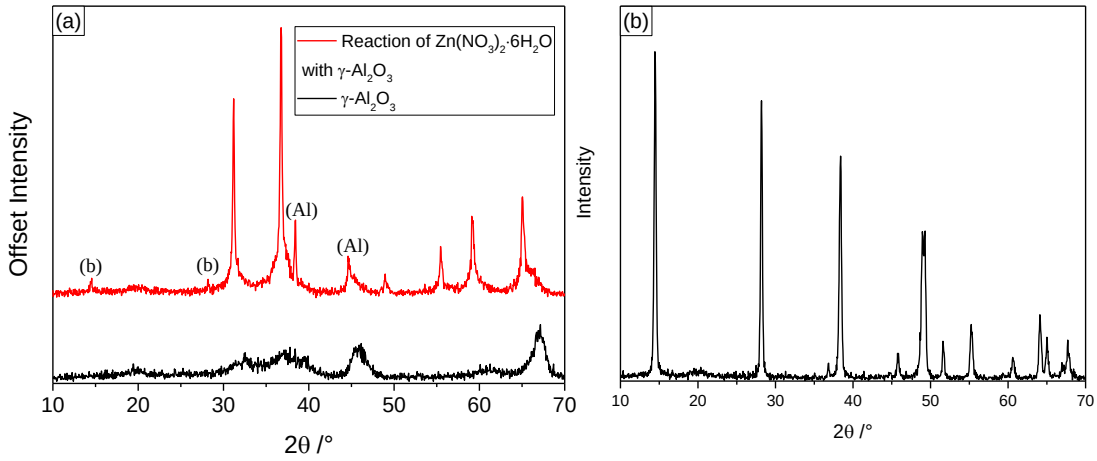

Figure 3.40 (a) Stacked PXRD plot showing poorly crystalline γ-Al_2O_3 (black), and reaction of $Zn(NO_3)_2{\cdot}6H_2O$ with γ-Al_2O_3 (red) displaying $ZnAl_2O_4$ with small a boehmite impurity (labelled (b)), and unreacted γ-Al_2O_3. Peaks labelled Al are of the aluminium sample holder. (b) PXRD showing AlOOH *(Boehmite)* formed from reaction of $Co(NO_3)_2{\cdot}6H_2O$ with γ-Al_2O_3.

3.11 Catalysis with cobalt gallium oxide spinels

3.11.1 Cobalt gallium oxide as water oxidation photocatalysts for the evolution of oxygen

The cobalt gallates used for photocatalysis were the samples prepared during the *in situ* diffraction experiment described in Section 3.32. The photocatalytic activity was studied by the well-established *tris*(bipyridine)ruthenium(II) – sodium persulfate system (Figure 3.41).[90,91] This has previously been used with the spinel Co_3O_4 as the water oxidation catalyst (WOC), so provides a useful comparison for the new cobalt gallium oxide spinels, to assess their activity.

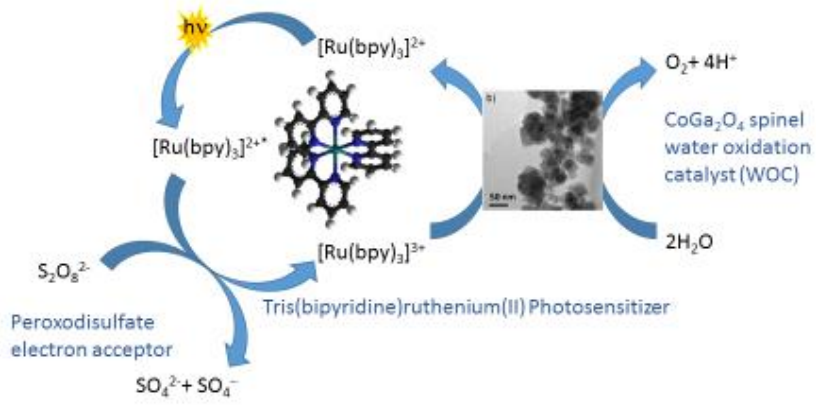

Figure 3.41 Schematic showing the photochemical water oxidation catalytic cycle using spinel catalysts, tris(bipyridine)ruthenium(II) photosensitzer and peroxodisulfate electron acceptor.

3.11.2 Synthetic procedure

Photocatalytic water oxidation was investigated with tris(bipyridine)ruthenium(II) hexahydrate (1 mM, 99.95% trace metal basis, Aldrich) as the photosensitizer and sodium persulfate (5 mM, ≥99.0%, Sigma-Aldrich) as the electron acceptor in borate buffer (80 mM, pH 8.5) with a catalyst concentration of 2 mM. First, a suspension was prepared by ultrasonic dispersion of the compounds, which was then degased with He to remove O_2 from solution and headspace. Then, the system was exposed to an LED lamp (460 nm, 30 min) and the evolved oxygen was measured by gas chromatography (Agilent Technologies, 7820A). Next, 100 ml of gas from the headspace was injected into the gas chromatograph using a gastight syringe (Hamilton 1825 RN). For increased detection sensitivity of O_2 on the thermal conductivity detector (Varian, operated at 200 °C), He was chosen as carrier gas.

3.11.3 Photocatalytic results

Labelling experiments proved water to be the source of the produced oxygen (Figure 3.42) and ICP-MS analyses indicated only minor leaching of Co and Ga during catalysis from the photocatalyst synthesized in 1:1 H_2O:MEA, while more significant leaching of 2.85% Ga was observed in the catalyst synthesized in MEA, pointing to its lower stability.

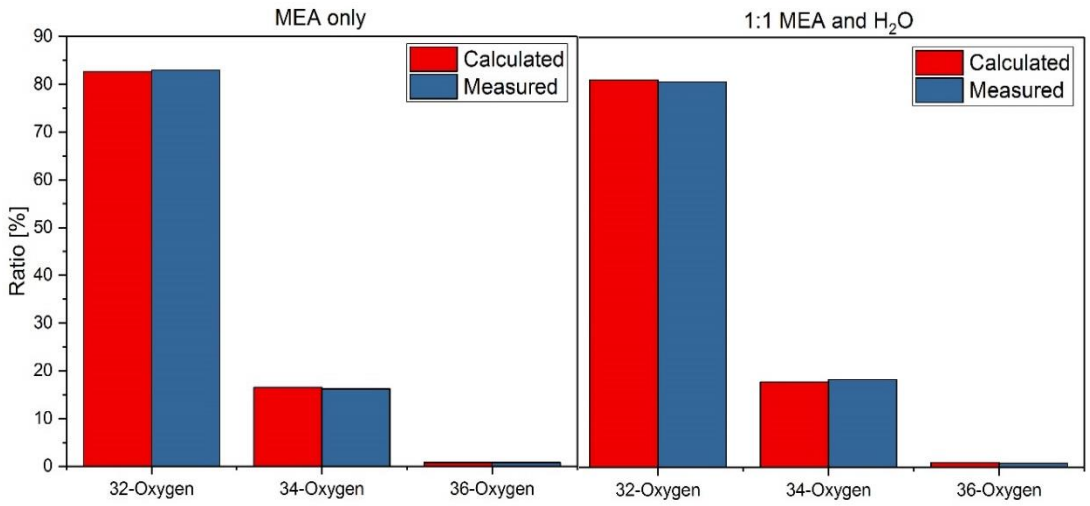

Figure 3.42 Experimental and theoretical ratios of $^{16}O^{16}O$, $^{16}O^{18}O$, and $^{18}O^{18}O$ evolved during the irradiation of a $H_2{}^{18}O$ (9.1 and 9.9 atom-% ^{18}O).

Table 3.9 summarises the catalytic activity of both cobalt gallium oxide spinels compared against two cobalt oxide photocatalysts. The new $CoGa_2O_4$ materials have similar activities to each other, but the surface-normalised activity is apparently lower than the microwave-synthesized Co_3O_4 reference (a spinel with similar surface area). It is noted that the activity of both cobalt oxide catalysts is very different. The type of catalyst is only one aspect contributing to its catalytic activity. The surface area, crystallinity and morphology of the catalysts are other important parameters to focus on when considering the photocatalytic behaviour of metal oxide catalysts.[92]

This difference in activity between the cobalt oxide and cobalt gallium oxide catalysts might arise from the presence of a lower concentration of surface cobalt in the mixed-metal materials than in the Co_3O_4 reference. Furthermore, Co_3O_4 contains a mixture of Co^{2+} and catalytically active Co^{3+},[93,94] unlike the gallate spinels that contain mainly Co^{2+}, which may also account for the differences observed. The catalysis is clearly very sensitive to the surface chemistry, since upon annealing the activity is completely removed. PXRD after catalysis revealed the stability of the material (Figure 3.43).

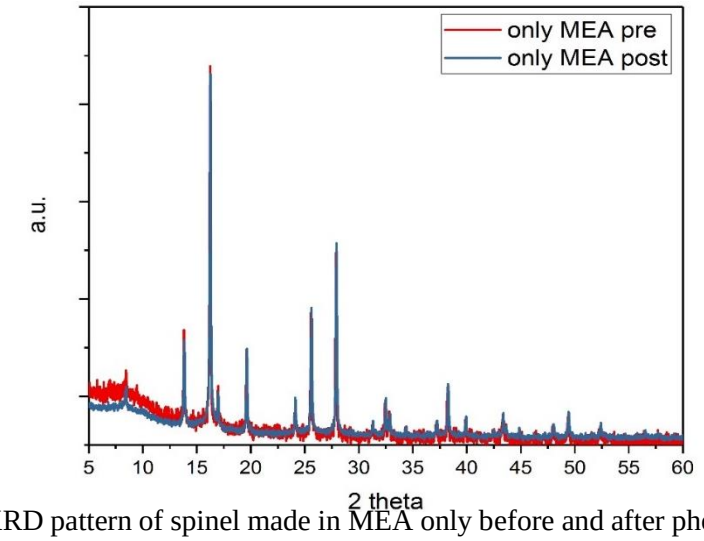

Figure 3.43 PXRD pattern of spinel made in MEA only before and after photocatalytic water oxidation.

Table 3.9 Characterisation and photocatalysis results from $CoGa_2O_4$ spinels, along with a Co_3O_4 reference material.

Material	BET surface area / m^2g^{-1}	O_2 /µmol	% Yield O_2	µmol O_2 / m^2
$CoGa_2O_4$ (MEA)	30	4.7 ± 0.2	23.3 ± 0.8	94.3 ± 12.6
$CoGa_2O_4$ (MEA:H_2O)	32	6.0 ± 1.1	30.1 ± 4	77.8 ± 2.8
Co_3O_4 (commercial)	36	2.5 ± 0.3	12.7 ± 1.6	34.7 ± 4.5
Co_3O_4 (microwave)	26	6.1 ± 1.1	30.6 ± 5.3	135.1 ± 9.9

3.12 Three-way catalysis with cobalt gallium oxide

Palladium supported aluminas are widely investigated and used as three-way catalysts and commonly the spinel γ-Al_2O_3 is used as the support.[95] A three-way catalyst attempts to oxidise carbon monoxide and any unburnt hydrocarbons whilst simultaneously reducing nitrogen oxides. This is used in automotive exhaust catalytic convertors. In contrast palladium support gallium oxides have rarely been studied for this application and for this reason palladium support on gallium oxide and cobalt gallium oxide were screened as potential candidates for three-way catalysis.

3.12.1 Catalyst preparation

γ-Al_2O_3, $CoGa_2O_4$, and γ-Ga_2O_3 were used as catalyst supports for palladium. The cobalt gallate used in the three-way catalysis was prepared from γ-Ga_2O_3 as described in Section 3.4.

Palladium was dispersed onto 0.2 g of each catalyst support by wet impregnation to add 0.2%wt Pd on to each support. After wet impregnation the catalysts were dried overnight at 110 °C followed by firing at 500 °C for 2 h.

3.12.2 Three-way catalysis conditions

The standard three-way catalysis gas conditions are tabulated below (Table 3.10). The gas flow was 5 L min^{-1}. Unreacted hydrocarbons are represented by propene (C_3H_6) and propane (C_6H_8). The catalysts were subjected to three cycles of this gas flow each cycle heating from 110 °C to 500 °C with a ramp rate of 10 °C min^{-1}. The gas flow was perturbed every three seconds during each cycle alternating between a rich and lean fuel by changing the fuel/air mixture. Lambda is used to denote whether a gas is lean or rich: when $\lambda = 1$ the mixture is stoichiometric, >1 means an air/fuel ratio which is lean, <1 an air/fuel ratio which is rich. For 2 cycles the gas feed was perturbed every 3 seconds alternating between $\lambda = 0.94$ to $\lambda = 1.04$ meaning that on average $\lambda = 0.99$ which is a slightly rich gas feed. For the third and final cycle the gas feed was perturbed every three seconds between $\lambda = 0.96$ to $\lambda = 1.06$ which on average $\lambda = 1.01$, slightly lean conditions. This was done to simulate "realistic" conditions which might be expected for a catalytic convertor in an automobile.

The effluent gases were monitored by FTIR with the exception of N_2, H_2 and O_2. N_2 and H_2 are not monitored, and O_2 is monitored by an oxygen analyser.

Table 3.10 Gas mixture composition used in the three-way catalysis testing.

Gas mixture for Three-way catalysis	Concentration
NO	2200 ppm
CO	0.78-2.78%
C_3H_6	666 ppm
C_3H_8	333 ppm
H_2	0.23-0.7%
H_2O	5%
CO_2	14%
O_2	0.7-1.9%

3.12.3Results from Three-way Catalysis

Both gallium containing oxides show poor light off temperatures (the temperature at which the gas from the feed starts to oxidise or reduce), and poor activity for carbon monoxide and total unburnt hydrocarbon conversion compared to the alumina reference (Figure 3.44). However, the cobalt gallium oxide has improved oxidation function over the gallium oxide catalyst. For the alumina reference a plateau in activity is reached by around 275 °C and any increase in activity afterwards is minimal. For both gallium catalysts the plateau is achieved around 325 °C but in both cases activity seems to increase again between 400 – 500 °C but it is unclear why.

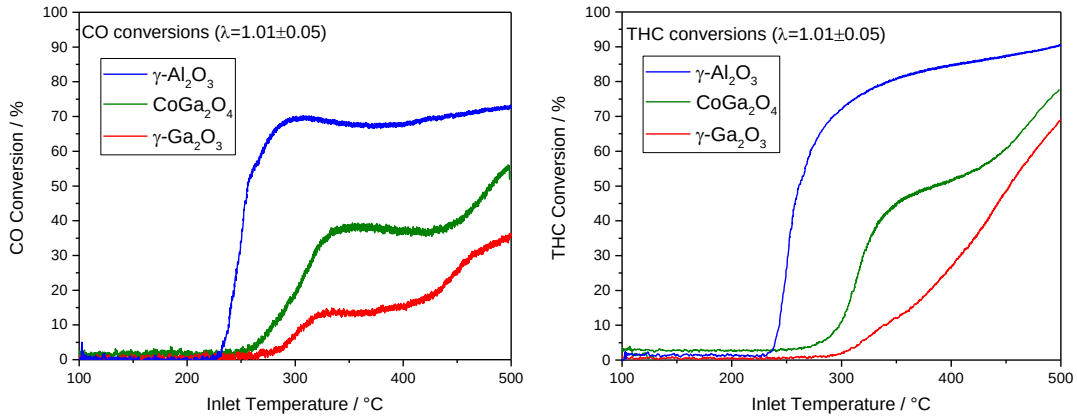

Figure 3.44 Oxidation of CO by each catalyst, *(left)* and oxidation of the total hydrocarbon content from the gas feed *(right)* showing that alumina outperforms both gallium catalysts. The presence of cobalt in the gallium oxide catalysts improves overall activity.

Similarly, in the reduction of NO_x the alumina reference outperforms both gallium

oxide catalysts, (Figure 3.45). An improved reduction function seen in the cobalt containing gallium oxide compared to pure gallium oxide is similar to the improved oxidation function observed in carbon monoxide and hydrocarbon oxidation. The cobalt gallium oxide shows a second increase in conversion above 450 °C which is attributed to the presence of cobalt in this catalyst. γ-Ga_2O_3 shows very low activity compared to the cobalt gallium oxide catalyst. The conversion of NO_x by the alumina catalyst reaches a maximum conversion at around 300 °C, after which time the catalytic activity steadily decreases.

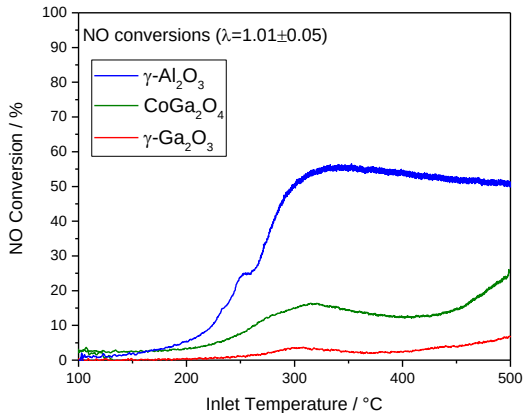

Figure 3.45 Reduction of NO_x displayed as conversion against inlet temperature.

Gallium and palladium may form intermetallic compounds when exposed to gases found in the harsh three-way catalysis gas feed and given the temperatures used in this testing (up to 500 °C) it would not be unexpected if such an intermetallic compound may have formed. Ga-Pd alloys such as GaPd, and $GaPd_2$ are finding increasing uses in certain areas of catalysis, in particular the semi-hydrogenation of acetylene.[96,97] An investigation in to palladium supported on mixed $(Ga,Al)_2O_3$ oxide supports and whether intermetallic alloys are produced forms part of Chapter 5. The formation of this intermetallic compound may then shut off activity in the three-way catalysis. No evidence of the intermetallic compound was found by electron microscopy or powder XRD but this is likely due to the very low loading of palladium on the support.

3.14 Summary

This work has shown that high energy X-rays can follow *in situ* the synthesis of dense metal oxides mimicking real laboratory synthesis conditions. Though data quality may be compromised by using a large volume steel autoclave the reaction pathway of the

solvothermal reaction could still be mapped. In aqueous ethanolamine, the solvothermal reaction of gallium metal and cobalt nitrate forms two layered double hydroxides before the formation of the spinel, one which is short lived and likely would have been undetected without this *in situ* experiment. The LDHs themselves could be useful materials so optimising their synthesis would also be useful to do, especially if they contain non-conventional Co:Ga ratios as expected in this study. This experiment shows that designing and predicting the outcome of solvothermal reactions of mixed metal oxides remains extremely challenging.

The cobalt gallium oxide material prepared by solvothermal synthesis from gallium oxide is a largely inverse spinel which upon heating rearranges to form a more thermally stable and slightly less inverse spinel. The synthetic method of this mixed metal oxide could be applicable to the synthesis of other oxides such as shown in this work with preliminary results from mixed metal aluminium oxides.

Aluminium oxide outperforms cobalt gallate and gallium oxide in three-way catalysis screening experiments, which might be due to the formation of intermetallic compounds on the gallium containing oxides impeding the overall activity. The cobalt gallium oxide showed improved activity over the pure gallium oxide catalyst which could be related directly to the presence of cobalt, the difference in distribution of cations, or on the crystallinity and the morphology of the sample which may affect palladium dispersion. Cobalt gallate spinels show potential in the photocatlytic oxygen evolution reaction showing improved activity over commercial cobalt oxide but lower activity than a microwave synthesised cobalt oxide sample. Catalytic activity is not dependent on the type of catalyst alone: morphology, crystal size and crystallinity, surface area are all important parameters which need to be considered during photocatalysis experiments. The *in-situ* X-ray diffraction experiment shows how small changes in the reaction affords catalysts with different crystal domain sizes which may then be relatable to the observed photocatalytic activity.

3.15 References

1 S. J. Moorhouse, Y. Wu, H. C. Buckley and D. O'Hare, *Chem. Commun.*, 2016, **52**, 13865–13868.

2 M. Staniuk, O. Hirsch, N. Kra, R. Bo, W. van Beek, P. M. Abdala and D. Koziej, *Chem. Mater.*, 2014, **26**, 2086–2094.

3 Y. Wu, M. I. Breeze, G. J. Clarkson, F. Millange, D. O'Hare and R. I. Walton, *Angew. Chemie - Int. Ed.*, 2016, **55**, 4992–4996.

4 H. H. M. Yeung, Y. Wu, S. Henke, A. K. Cheetham, D. O'Hare and R. I. Walton, *Angew. Chemie - Int. Ed.*, 2016, **55**, 2012–2016.

5 Y. Wu, S. Henke, G. Kieslich, I. Schwedler, M. Yang, D. A. X. Fraser and D. O'Hare, *Angew. Chemie - Int. Ed.*, 2016, **55**, 14081–14084.

6 R. I. Walton, F. Millange, R. I. Smith, T. C. Hansen and D. O'Hare, *J. Am. Chem. Soc.*, 2001, **123**, 12547–12555.

7 D. Croker, M. Loan and B. K. Hodnett, *Cryst. Growth Des.*, 2009, **9**, 2207–2213.

8 Y. Zhou, L. Yuanhua and G. R. Patzke, *Prog. Chem.*, 2012, **24**, 1583–1591.

9 G. Philippot, E. D. Boejesen, C. Elissalde, M. Maglione, C. Aymonier and B. B. Iversen, *Chem. Mater.*, 2016, **28**, 3391–3400.

10 S.-W. Kim, S. Iwamoto and M. Inoue, *Ceram. Int.*, 2009, **35**, 1603–1609.

11 H. Y. Playford, A. C. Hannon, E. R. Barney and R. I. Walton, *Chem. Eur. J*, 2013, **19**, 2803–2813.

12 H. Y. Playford, A. C. Hannon, M. G. Tucker, M. R. Lees and R. I. Walton, *J. Phys. Condens. Matter*, 2013, **25**, 454212.

13 M. Drakopoulos, T. Connolley, C. Reinhard, R. Atwood, O. Magdysyuk, N. Vo, M. Hart, L. Connor, B. Humphreys, G. Howell, S. Davies, T. Hill, G. Wilkin, U. Pedersen, A. Foster, N. De Maio, M. Basham, F. Yuan and K. Wanelik, *J. Synchrotron Radiat.*, 2015, **22**, 828–838.

14 N. Pienack and W. Bensch, *Angew. Chemie.*, 2011, **50**, 2014–2034.

15 K. M. Ø. Jensen, C. Tyrsted, M. Bremholm and B. B. Iversen, *ChemSusChem*, 2014, **7**, 1594–1611.

16 E. D. Bøjesen and B. B. Iversen, *CrystEngComm*, 2016, **18**, 8332–8353.

17 R. I. Walton and F. Millange, in *The Chemistry of Metal–Organic Frameworks*, Wiley-VCH Verlag GmbH & Co. KGaA, 2016, pp. 729–764.

18 A. Nakatsuka, Y. Ikeda, N. Nakayama and T. Mizota, *Acta Crystallogr. Sect. E Struct. Reports Online*, 2006, **62**, 109–111.

19 F. Leccabue, C. Pelosi, E. Agostinelli, V. Fares, D. Fiorani and E. Paparazzo, *J. Cryst. Growth*, 1986, **79**, 410–416.

20 S. J. Moorhouse, N. Vranje, A. Jupe, M. Drakopoulos and D. O'Hare, *Rev. Sci. Instrum.*, 2012, **83**, 84101.

21 M. Basham, J. Filik, M. T. Wharmby, P. C. Y. Chang, B. El Kassaby, M. Gerring, J. Aishima, K. Levik, B. C. A. Pulford, I. Sikharulidze, D. Sneddon, M. Webber, S. S. Dhesi, F. Maccherozzi, O. Svensson, S. Brockhauser, G. Náray and A. W. Ashton, *J.*

Synchrotron Radiat., 2015, **22**, 853–858.

22 V. Rives, *Layered Double Hydroxides: Present and Future*, Nova Science Publishers, Illustrate., 2001.

23 G. V. Manohara and P. Vishnu Kamath, *Bull. Mater. Sci.*, 2010, **33**, 325–331.

24 A. V. Radha, G. S. Thomas, P. V. Kamath and C. Shivakumara, *J. Phys. Chem. B*, 2007, **111**, 3384–3390.

25 D. G. Evans and R. C. T. Slade, *Struct. Bond.*, 2006, **119**, 1–87.

26 H.-P. Boehm, J. Steinle and C. Vieweger, *Angew. Chemie.*, 1977, **16**, 489–496.

27 A. Álvarez, R. Trujillano and V. Rives, *Appl. Clay Sci.*, 2013, **80**–**81**, 326–333.

28 F. Thevenot, R. Szymanski, P. Chaumette, I. Fran, A. D. B. Prrau and R. Cedex, *Clays Clay Miner.*, 1989, **37**, 396–402.

29 Y. Q. Xiao, M. F. Thorpe and J. B. Parkinson, *Phys. Rev. B*, 1999, **59**, 277–285.

30 C. Ruby, M. Abdelmoula, S. Naille, A. Renard, V. Khare, G. Ona-Nguema, G. Morin and J. M. R. Génin, *Geochim. Cosmochim. Acta*, 2010, **74**, 953–966.

31 I. G. Richardson, *Acta Crystallogr. Sect. B Struct. Sci. Cryst. Eng. Mater.*, 2013, **69**, 629–633.

32 S. Arias, J. G. Eon, R. A. S. San Gil, Y. E. Licea, L. A. Palacio and A. C. Faro, *Dalt. Trans.*, 2013, **42**, 2084–2093.

33 K. Jayanthi, S. Nagendran and P. V. Kamath, *Inorg. Chem.*, 2015, **54**, 8388–8395.

34 M. Vucelic, W. Jones and G. D. Moggridge, *Clays Clay Miner.*, 1997, **45**, 803–813.

35 I. Pausch, *Clays Clay Miner.*, 1986, **34**, 507–510.

36 A. J. Dent, G. Cibin, S. Ramos, A. D. Smith, S. M. Scott, L. Varandas, M. R. Pearson, N. A. Krumpa, C. P. Jones and P. E. Robbins, *J. Phys. Conf. Ser.*, 2009, **190**, 12039.

37 A. A. Coelho, *J .Appl. Crystallogr.*, 2000, **33**, 899–908.

38 F. Millange, R. I. Walton and D. O. Hare, *J. Mater. Chem.*, 2000, **10**, 1713–1720.

39 Z. P. Xu and H. C. Zeng, *Chem. Mater.*, 2001, **13**, 4564–4572.

40 R. Ma, Z. Liu, K. Takada, K. Fukuda, Y. Ebina, Y. Bando and T. Sasaki, *Inorg. Chem.*, 2006, **45**, 3964–3969.

41 Z. Liu, R. Ma, M. Osada, K. Takada and T. Sasaki, *J. Am. Chem. Soc.*, 2005, **127**, 13869–13874.

42 F. Cavani, F. Trifirò and A. Vaccari, *Catal. Today*, 1991, **11**, 173–301.

43 G. Mascolo and O. Marino, *Miner. Mag.*, 1980, **43**, 619.

44 S. Miyata, *Clays Clay Miner.*, 1983, **31**, 305–311.

45 S. Marappa and P. Vishnu Kamath, *Z. Anorg. Allg. Chem*, 2015, **641**, 927–934.

46 G. R. Williams, A. I. Khan and D. O'Hare, *Struct. Bond.*, 2005, **119**, 161–192.

47 N. Iyi, K. Fujii, K. Okamoto and T. Sasaki, *Appl. Clay Sci.*, 2007, **35**, 218–227.

48 T. G. Amundsen, L. E. Øi and D. A. Eimer, *J. Chem. Eng. Data*, 2009, **54**, 3096–

3100.

49 J. L. Soubeyroux, D. Fiorani and E. Agostinelli, *J. Magn. Magn. Mater.*, 1986, **54**–**57**, 83–84.

50 D. Fiorani and S. Viticoli, *Solid State Commun.*, 1978, **25**, 155–157.

51 E. Kanezaki, *J. Chem. Soc. Faraday Trans.*, 1998, **106**, 279–284.

52 V. Rives, *Mater. Chem. Phys.*, 2002, **75**, 19–25.

53 G. S. Thomas and P. V. Kamath, *Mater. Res. Bull.*, 2005, **40**, 671–681.

54 P. X. Zhi and Q. L. Guo, *Chem. Mater.*, 2005, **17**, 1055–1062.

55 U. Unal, *J. Solid State Chem.*, 2007, **180**, 2525–2533.

56 S. Britto, A. V. Radha, N. Ravishankar and P. V. Kamath, *Solid State Sci.*, 2007, **9**, 279–286.

57 Y. Gao, Y. Zhang, G. R. Williams, D. O'Hare and Q. Wang, *Sci. Rep.*, 2016, **6**, 35502.

58 G. G. C. Arizaga, K. G. Satyanarayana and F. Wypych, *Solid State Ionics*, 2007, **178**, 1143–1162.

59 G. R. Williams and D. O'Hare, *J. Mater. Chem.*, 2006, **16**, 3065.

60 H. Wang, Y. Liu, Z. Chen, B. Wu, S. Xu and J. Luo, *Sci. Rep.*, 2016, **6**, 22748.

61 P. Xiong, X. Ji, X. Zhao, W. Lv, T. Liu and W. Lu, *Chemom. Intell. Lab. Syst.*, 2015, **144**, 11–16.

62 G. Fan, F. Li, D. G. Evans and X. Duan, *Chem. Soc. Rev.*, 2014, **43**, 7040–7066.

63 C. G. Silva, Y. Bouizi, V. Fornés and H. García, *J. Am. Chem. Soc.*, 2009, **131**, 13833–13839.

64 R. D. Shannon and C. T. Prewitt, *Acta Crystallogr. Sect. B*, 1969, **25**, 925–946.

65 P. Piero and A. Anichini, *J.C.S. Faradat I*, 1980, **76**, 2448–2456.

66 A. N. Christensen, P. Norby and J. C. Hanson, *Powder Diffr.*, 1995, **10**, 185–188.

67 A. Nakatsuka, Y. Ikeda, Y. Yamasaki, N. Nakayama and T. Mizota, *Solid State Commun.*, 2003, **128**, 85–90.

68 L. Gama, M. A. Ribeiro, B. S. Barros, R. H. A. Kiminami, I. T. Weber and A. C. F. M. Costa, *J. Alloys Compd.*, 2009, **483**, 453–455.

69 H. S. C. O'Neill and A. Navrotsky, *Am. Mineral.*, 1983, **68**, 181–194.

70 T. Yokoyama and T. Meguro, *Jpn. J. Appl. Phys.*, 2005, **44**, 6201–6203.

71 J. B. Goodenough and A. L. Loeb, *Phys. Rev.*, 1955, **98**, 391–408.

72 C. Otero Arean and E. Garcia Diaz, *Mater. Chem.*, 1982, **7**, 675–683.

73 A. Navrotsky and O. J. Kleppa, *J. Inorg. Nucl. Chem.*, 1968, **30**, 479–498.

74 A. Miller, *J. Appl. Phys.*, 1959, **30**, S24–S25.

75 D. S. McClure, *J. Phys. Chem. Solids*, 1957, **3**, 311–317.

76 B. C. Melot, K. Page, R. Seshadri, E. M. Stoudenmire, L. Balents, D. L. Bergman

and T. Proffen, *Phys. Rev. B*, 2009, **80**, 1–8.

77 H. S. C. O'Neill, *Eur. J. Mineral.*, 1994, **6**, 603–609.

78 R. J. Harrison, *Am. Mineral.*, 1998, **83**, 1092–1099.

79 M. A. Carpenter and E. K. H. Salje, *Am. Mineral.*, 1994, **79**, 1068–1083.

80 H. Y. Playford, A. C. Hannon, M. G. Tucker, D. M. Dawson, S. E. Ashbrook, R. J. Kastiban, J. Sloan and R. I. Walton, *J. Phys. Chem. C*, 2014, **118**, 16188−16198.

81 D. Sharma B and J. Donohue, *Zeitschrift fur Krist.*, 1962, **117**, 293–300.

82 A. R. Williams, D. Weaire and J. E. Inglesfield, *J. Phys. C Solid State PHys*, 1968, **1**, 222–231.

83 M. H. Oh, T. Yu, S.-H. Yu, B. Lim, K.-T. Ko, M.-G. Willinger, D.-H. Seo, B. H. Kim, M. G. Cho, J.-H. Park, K. Kang, Y.-E. Sung, N. Pinna and T. Hyeon, *Science.*, 2013, **340**, 964–968.

84 E. Morán-Miguélez, M. A. Alario-Franco and J. C. Joubert, *Mater. Res. Bull.*, 1986, **21**, 107–113.

85 G. Li, S. Feng, L. Li, X. Li and W. Jin, *Chem. Mater.*, 1997, **9**, 2894–2901.

86 T. S. Kannan, P. K. Panda and V. A. Jaleel, *J. Mater. Sci. Lett.*, 1997, **16**, 830–834.

87 J. Han, L. Jia, B. Hou, D. Li, Y. Liu and Y. Liu, *Ranliao Huaxue Xuebao*, 2015, **43**, 846–851.

88 L. Ji, J. Lin and H. C. Zeng, *J. Phys. Chem. B*, 2000, **104**, 1783–1790.

89 M. Trueba and S. P. Trasatti, *Eur. J. Inorg. Chem.*, 2005, **2005**, 3393–3403.

90 F. Evangelisti, R. Moré, F. Hodel, S. Luber, G. R. Patzke, P. Wang, S. Shannigrahi, N. L. Yakovlev and T. S. A. Hor, *J. Am. Chem. Soc.*, 2015, **137**, 11076–11084.

91 H. Liu, R. Moré, H. Grundmann, C. Cui, R. Erni and G. R. Patzke, *J. Am. Chem. Soc.*, 2016, **138**, 1527–1535.

92 H. Liu and G. R. Patzke, *Chem. Asian J*, 2014, **9**, 2249–2259.

93 D. A. Lutterman, Y. Surendranath and D. G. Nocera, *J. Am. Chem. Soc.*, 2009, **131**, 3838–3839.

94 Y. Surendranath, M. W. Kanan and D. G. Nocera, *J. Am. Chem. Soc.*, 2010, **132**, 16501–16509.

95 J. Wang, H. Chen, Z. Hu, M. Yao and Y. Li, *Catal. Rev.*, 2015, **57**, 79–144.

96 C. Wannek and B. Harbrecht, *J. Alloys Compd.*, 2001, **316**, 99–106.

97 M. Armbrüster, G. Wowsnick, M. Friedrich, M. Heggen and R. Cardoso-Gil, *J. Am. Chem. Soc.*, 2011, **133**, 9112–9118.

Chapter 4: Polymorphism of $Ga_{2-x}Al_xO_3$

4. Polymorphism of $Ga_{2-x}Al_xO_3$

4.1 Introduction

4.1.1 Polymorphism of Al_2O_3

Polymorphism in the Al-O, Al-(OH) and Al-O-(OH) systems is well established and accepted and has been researched extensively in part owing to the huge importance of aluminium oxide polymorphs as supports for precious metals and other reactive species in many areas of catalysis.[1] These alumina polymorphs (in particular γ-Al_2O_3) are not only used as catalyst carriers but also as adsorbents, coatings, soft abrasives or as catalysts themselves owing to their usually high surface areas and surface activity.[2] At least 11 oxides, hydroxides and oxyhydroxides of aluminium are known (Figure 4.1(a)).[3] The thermodynamically stable polymorph of alumina, at room temperature and pressure, is α-Al_2O_3, corundum (Figure 4.1(b)), and all metastable aluminas (defined herein as phases that are only stable at lower temperatures), commonly referred to as transition aluminas in industry, convert to this polymorph at a high enough temperature. α-Al_2O_3 has a very high thermal stability making it very useful as use as a coating or as a crucible in high temperature applications. These transition aluminas and α-Al_2O_3 can be categorised into two main groups depending on whether the oxide anion lattice is face centred cubic or hexagonal close packed. Figure 4.1a shows the interconversion of all known polymorphs but it must be stressed that although the transition aluminas can be accessed via thermal decomposition of hydroxide and oxyhydroxide precursors there are many other synthetic routes to the different polymorphs including sol-gel and hydro(solvo)thermal synthesis.[4,5] The structure of the spinel γ-Al_2O_3 was solved by single crystal diffraction and found to contain a small amount of Al^{3+} ions occupying non-spinel positions as well as the expected positions.[6]

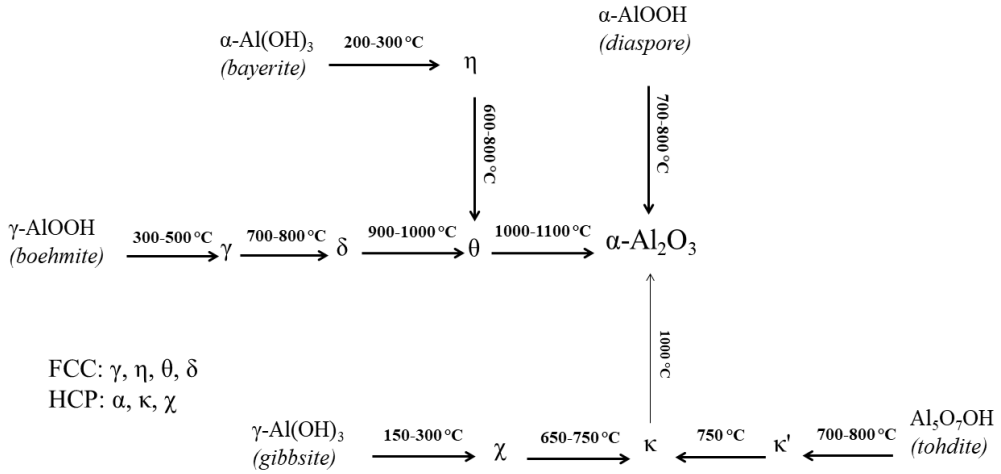

Figure 4.1(a) Interconversion of aluminium oxides, hydroxides, and oxyhydroxides.[3] The Greek letters alone denote Al_2O_3 polymorphs.

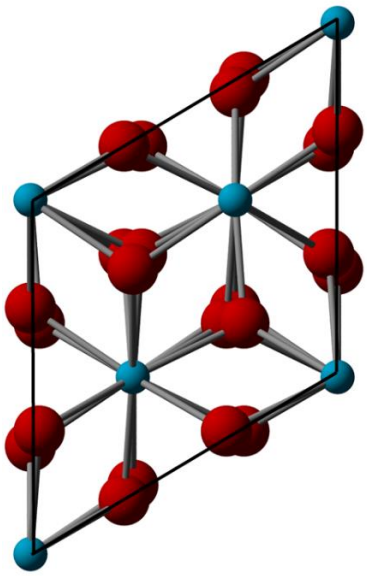

Figure 4.1(b) α-Al_2O_3 (corundum); the thermodynamically stable polymorph of alumina. Blue spheres represent trivalent aluminium cations in octahedral coordination.

4.1.2 Polymorphism of Ga_2O_3

Gallium oxide polymorphism had received comparatively little attention until the work by Roy and co-workers in 1952,[7] and up until recently the polymorphism in the Ga-O, Ga-(OH) and Ga-O-(OH) systems remained highly contested despite a large number of publications on the structural characterisation of gallium oxide.[8–13] The structures of the alpha and beta polymorphs have been well characterised. The thermodynamically stable polymorph is the monoclinic beta polymorph (in contrast to the alpha polymorph for aluminium oxide). The structure of beta gallium oxide has

been studied by single crystal diffraction and contains a 1:1 ratio of octahedral:tetrahedral cations both in distorted coordination.[14,15] α-Ga_2O_3, structurally analogous to α-Al_2O_3, is metastable but β-Ga_2O_3 irreversibly converts to this polymorph at a high pressure because α-Ga_2O_3 has a smaller molar volume.[16] γ-Ga_2O_3 can be prepared by oxidation directly from gallium metal in an aminoalcohol. This synthesis was first discovered by Kim and coworkers,[17] and later developed by Playford *et al.* for lower temperatures.[18] A similar solvothermal synthesis published in a short communication by Pohl in 1967 showed how metallic gallium could be oxidised to γ-Ga_2O_3 at 150 °C using an aqueous solution of ethylenediamine,[19] though the material formed from this synthesis is not as crystalline as that prepared by Kim and Playford. It is now known that the structure of γ-Ga_2O_3, is structurally analogous to γ-Al_2O_3 having a disordered spinel structure containing small amounts of Ga^{3+} occupying non-spinel sites in the $Fd\bar{3}m$ space group. Analysis of the pair distribution function and reverse Monte Carlo simulations were required in order to fully understand and characterise the structure of γ-Ga_2O_3.[18,20]

During the investigation into the synthesis and structural characterisation of γ-Ga_2O_3 the existence of two other Ga_2O_3 polymorphs and a new oxyhydroxide was revealed: ε, and κ-Ga_2O_3, and also the oxyhydroxide $Ga_5O_7(OH)$ (Figure 4.2). All three are based on an hexagonal close packed oxide lattice, and, whilst κ-Ga_2O_3 and $Ga_5O_7(OH)$ are structural analogues of κ-Al_2O_3 and $Al_5O_7(OH)$ (tohdite/akdalaite) no known polymorph of ε-Al_2O_3 has yet been discovered. The existence of a kappa polymorph of gallium oxide had been postulated previously but little work had been carried out on determining its crystal structure. κ-Ga_2O_3 remains to this day elusive and difficult to synthesise phase pure but recent work has been reported to understand its structure in more detail and its structural relation to ε-Ga_2O_3.[21,22] The delta-polymorph, which had previously been described as adopting the cubic bixbyite structure,[9,13] is in fact a nano-crystalline version of ε-Ga_2O_3. The Greek symbols in front of the Ga_2O_3 and Al_2O_3 polymorphs denote the same crystal chemistry (except β-Ga_2O_3 which is isostructural with θ-Al_2O_3) and so it can be seen that gallium oxide and aluminium share very similar oxide chemistry though there are still fewer known polymorphs of gallia than alumina polymorphs.

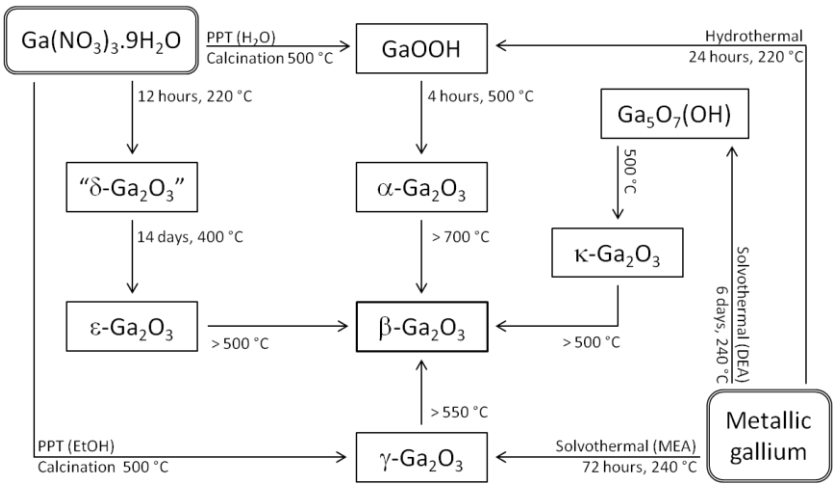

Figure 4.2 Synthesis and interconversion of Ga_2O_3 polymorphs reproduced from Playford *et al*.[18]

4.1.3 Chemical similarity between Ga and Al in oxides

Gallium is immediately below aluminium in Group 13 in the Periodic Table and so some similarities between their chemistries should be expected. However certain trends are not as expected and are briefly outlined here. Owing to the scandide contraction gallium is only slightly larger than aluminium. Their similar size means that gallium and aluminium can often be found together in oxide materials and minerals as indeed they frequently are in Nature. A secondary effect of this contraction is that gallium has a more polarizable electron cloud, which means that in certain systems, such as in spinels, gallium often occupies the tetrahedral site where greater covalency with the oxide anion can occur with the sp^3 hybridized configuration.[8,23]

4.1.4 Polymorphism in Ga-Al-O

Since Ga^{3+} and Al^{3+} are of a similar size and can be mixed in oxides some research into the polymorphism of $Ga_{2-x}Al_xO_3$ has been conducted, yet an in-depth discussion is lacking. Roy began researching on the polymorphism in the system Ga-Al-O in the 1950s following the success of his research with Ga_2O_3 polymorphism.[24,25] Similar to his work with Ga_2O_3, the starting point was with freshly precipitated gels containing both Ga and Al followed by thermal treatment to isolate different phases. Heating at high temperature was found to yield the monoclinic β-$Ga_{2-x}Al_xO_3$ phase. Wartenberg

and Reusch had previously shown in 1932 that solid solutions of β-$Ga_{2-x}Al_xO_3$ could be prepared, one of the earliest papers detailing polymorphism in the Ga-Al-O system.[26] Roy advanced on this and proposed that in the mixed oxide up to 67% Al^{3+} could be substituted into β-Ga_2O_3. The α-Al_2O_3 structure could be substituted with up to 25% Ga at high temperature, whilst metastable solid-solutions containing as much as 100% Ga could be prepared at low temperature.[24] At the time at which those studies were conducted powder crystallography was in its infancy, and solid state NMR just being developed, and so little structural analysis on these mixed oxides was undertaken. Only lattice spacings and relative intensities of Bragg peaks were usually reported much the same for his report on the polymorphism with pure Ga_2O_3. The limit of metal substitution likely depends on the method of fabrication, and whether the material is a thin film or polycrystalline powder: recently a study into a polycrystalline sample of β-$Ga_{2-x}Al_xO_3$ prepared by solution combustion synthesis revealed that up to 40% Al^{3+} can be incorporated by this method. A linear increase in the band-gap of the material was observed suggesting the potential of β-$Ga_{2-x}Al_xO_3$ as power devices.[27] A novel metastable $GaAlO_3$ was also reported by Roy from hydrothermal synthesis between 400-800 °C though it was frequently contaminated with the thermodynamically stable polymorphs of gallium and aluminium. This metastable oxide was claimed to decompose into ε-Ga_2O_3 (it should be noted that the nomenclature for gallium oxide polymorphs has since changed and epsilon has been renamed to kappa since κ-Ga_2O_3 is structurally analogous to κ-Al_2O_3).[18] The $GaAlO_3$ compound first described by Roy has also been the subject of another paper by MacDonald *et al*.[28] Unit cell lattice parameters were provided and a range of hexagonal space groups were selected based on systematic absences. High temperature hydrothermal synthesis >700 °C was used for the reaction. Two new phases, designated X and Y, were also reported by MacDonald and co-workers. A monoclinic unit cell was found for material X from single crystal work. Y was prepared from a 7-day hydrothermal synthesis at 710 °C but no further details were provided on this phase only that, like X, it was unlike any other reported phase of aluminium and gallium oxide or hydrate. Analogies between gallium and aluminium oxide chemistry has also been reported on by others.[29]

The Inoue group in Japan have contributed and furthered the understanding of polymorphism in Ga-Al-O. In a series of papers, they detailed how solvothermal

synthesis at 300 °C could be used to prepare solid solutions of the $Ga_{2-x}Al_xO_3$ defect spinel from use of $Ga(acac)_3$ and $Al(O\text{-}i\text{-}Pr)_3$.[30–35] A variety of solvents were tested with emphasis on using the diols as the reaction media. Different solvents resulted in differing total amounts of aluminium to be incorporated, and the particle size (and surface areas) were affected by the choice of solvent. The reaction supposedly proceeds by formation of γ-Ga_2O_3 first which then incorporates aluminium. $Ga(acac)_3$ alone in the diol solvent forms a poorly crystalline but phase pure Ga_2O_3 spinel whilst $Al(O\text{-}iPr)_3$ forms a boehmite-derivative. A proposed mechanism for the reaction with diols suggests that heterolytic cleavage of the C-O bond occurs. The reaction was found to be optimal when 4, 5 or 6 carbon chain diols were used. It was suggested that the participation of an intramolecular hydroxyl group on the diol is the reason for the high activity owing to the formation of a 5,6 or 7 membered ring respectively, though there was no direct evidence to support this claim. With an increase in the aluminium concentration in the spinel it is generally found that the spinels become less crystalline owing to an increase in the overall static disorder in the material. A ^{27}Al MAS NMR study found that aluminium and gallium preferentially adopted octahedral and tetrahedral coordination in the spinel respectively. No further structural analysis was undertaken. These spinels were also found to decompose into the thermodynamically stable monoclinic beta polymorph at higher temperatures if more aluminium was present. Mixed oxides containing gallium and aluminium have been studied by various other research groups.

Very recently a paper was published describing how these mixed metal spinels can be prepared by a low temperature hydrothermal synthesis using citric acid to chelate the metals. The photoluminescence properties of the materials were investigated in this paper.[36]

With regards to other polymorphs little work has been carried out. The alpha and beta mixed oxides have never been consistently reported on with regards to how much aluminium can be incorporated but it is generally agreed that above a certain aluminium content in the defect spinel the spinel transforms into the alpha corundum structure. Again, little, if any, structural analysis has been undertaken on these polymorphs and the general polymorphism of these oxides remains poorly understood. Excluding X and Y reported by MacDonald only 4 polymorphs have been reported:

corundum-type α-$Ga_{2-x}Al_xO_3$, monoclinic β-$Ga_{2-x}Al_xO_3$, spinel-type γ-$Ga_{2-x}Al_xO_3$ (Figure 4.3), and a hexagonal $GaAlO_3$ for which no structure type has been provided.

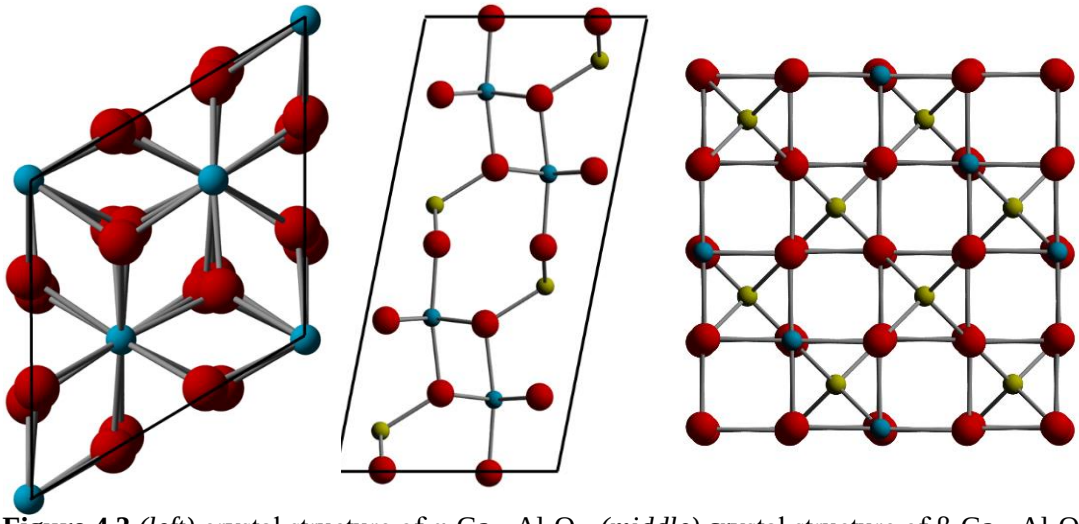

Figure 4.3 *(left)* crystal structure of α-$Ga_{2-x}Al_xO_3$, *(middle)* crystal structure of β-$Ga_{2-x}Al_xO_3$, *(right)* crystal structure of γ-$Ga_{2-x}Al_xO_3$, blue spheres are octahedral trivalent cations and yellow spheres tetrahedral trivalent cations.

4.1.5 Catalysis with $Ga_{2-x}Al_xO_3$

Gallium oxide polymorphs, like aluminas, have been investigated for catalysis but to a much lesser extent. α, β and γ-Ga_2O_3 have been found to outperform TiO_2 in the decomposition of volatile aromatics.[37] They have also been investigated for application in the dehydrogenation of propane to propene,[38] recently as water splitting photocatalysts[39] and as power devices since β-Ga_2O_3 is a wide-band semi-conductor with a band gap of ~4.7 eV.[40] The mixed metal gallium aluminium oxides have also received interest for their application as catalysts, whilst the works of Roy and MacDonald *et al.* in the 1950s was mainly a study for academic interest. Extensive study has been reported on the mixed metal defect spinel for its use in the selective catalytic reduction (SCR) of NO,[30–34,41] dehydrogenation of propane,[35,42] dimethyl ether steam reforming,[43] and Ga_2O_3 supported on Al_2O_3 has been applied for photocatalysis.[44] A mixed oxide composite of γ-Ga_2O_3/α-Al_2O_3 has been reported to have great potential as a support for NiW catalysts for hydrocarbon sulfur removal catalysis.[45] Recently the spinel-type γ-Ga_2O_3-Al_2O_3 mixed system has been investigated as a support for palladium for liquid-phase hydrogenation of acetylene to ethylene.[46]

4.2 Scope of this chapter

In this chapter, a synthesis of defect spinel γ-$Ga_{2-x}Al_xO_3$ using a low temperature solvothermal method is presented. The polymorphism of the $Ga_{2-x}Al_xO_3$ system is investigated by solvothermal and high temperature experiments, and the structures of the polymorphs in the Ga-Al-O system investigated by analysis of the Bragg scattering of X-ray diffraction, and other techniques including solid-state ^{27}Al and ^{71}Ga MAS NMR.

A novel oxyhydroxide containing both Ga and Al was obtained from extended solvothermal reaction in 1,4-butanediol. This material was found to have a similar crystal structure to the mineral tohdite (also akdalaite). The thermal decomposition of this material was investigated showing the formation of a polymorph related to the recently elucidated structure of ε-Ga_2O_3. Diesel oxidation, and acetylene semi-hydrogenation catalysis using Ga_2O_3 polymorphs, and mixed metal β-$Ga_{2-x}Al_xO_3$ as supports for palladium is presented towards the end of this chapter.

4.3 γ-$Ga_{2-x}Al_xO_3$

4.3.1 Synthetic procedure

4.3.1.1 Synthesis of γ-$Ga_{2-x}Al_xO_3$ from 1,4-butanediol

This synthesis was based on the work of Inoue *et al.*[31,32,34] but optimised for lower temperatures. 0.4 g (1.01 mmol) of $Ga(acac)_3$ (Aldrich, 99.99%) and an appropriate amount *(x)* of $Al(O\text{-}i\text{-}Pr)_3$ (Aldrich, ≥98%) to give a (2-*x*):*x* molar ratio, where ($0 \leq x \leq 0.6$), were added to a PTFE liner followed by the addition of 8 ml 1,4-butanediol. The reaction mixture was stirred at room temperature for 10 minutes to ensure the reagents were well mixed before being sealed inside a stainless-steel autoclave and placed inside a preheated fan assisted oven at 240 °C for 48 hours. After this time the autoclave was allowed to cool naturally to ambient temperature and the vessel opened to reveal a white opaque gel. This gel was dispersed by magnetic stirring in the mother liquor followed by addition of acetone to reduce the viscosity of the diol. The gel was then collected by suction filtration and air was pulled through for thirty

minutes until the gel had partially dried followed by drying at 70 °C overnight to yield a white powder.

4.3.1.2 Synthesis of γ-$Ga_{2-x}Al_xO_3$ from 2-propanol

0.4 g (1.01 mmol) $Ga(acac)_3$ (Aldrich, 99.99%) and an appropriate amount *(x)* of $Al(O\text{-}i\text{-}Pr)_3$ (Aldrich, ≥98%), to give a (2-*x*):*x* molar ratio of Ga:Al, where ($0 \leq x \leq 1.8$), of Ga:Al precursors were added to a PTFE liner followed by the addition of 10 ml 2-propanol. The reaction mixture was stirred at room temperature for 5 minutes before being sealed inside a stainless-steel autoclave and placed inside a preheated fan assisted oven at 240 °C for 24 hours. After this time the autoclave was allowed to cool naturally to ambient temperature and the vessel opened to reveal a white solid powder. The powder was collected by suction filtration and then washed with copious amounts of acetone before being dried at 70 °C overnight.

4.3.2 General Characterisation

4.3.2.1 Experimental considerations

The synthesis in 1,4-butanediol at 240 °C was found to be rather unreliable often forming unwanted by-products such as AlOOH (boemite) and diaspore-type GaOOH (tsumgallite). Extensive work was reported by Inoue using this method and found no such phases forming in their reaction and it was reported that up to 75% Al^{3+} could be incorporated into the Ga_2O_3 spinel structure.[31] However, their synthesis was conducted at 300 °C for 2 h. The boiling point of 1,4-butanediol is 235 °C and so at 240 °C the solvothermal conditions have only just been reached which could be the cause of the lack of reproducibility. It was found that the synthesis at 240 °C allowed a maximum of 30% Al^{3+} to be incorporated into the spinel structure, $x = 0.6$. Addition of more aluminium precursor only formed AlOOH, (boehmite), as an impurity product. In fact, it was found that many of the solvents that were used in the work by Inoue *et al.*[34] for crystallising γ-$Ga_{2-x}Al_xO_3$ under solvothermal conditions at 300 °C did not work at 240 °C. A further complicating matter is that some solvents, in particular those containing both –OH and $–NH_3$ functional groups or solely amino groups, were incompatible with aluminium salts forming only a thick gel at the end of the reaction.

Table 4.1 lists the solvents investigated and any crystalline materials formed from the reaction.

The alcohol 2-propanol with a lower boiling point and viscosity compared to 1,4-butanediol was found to be optimal in the preparation of mixed metal aluminium gallium spinels at 240 °C. The use of 2-propanol halved the reaction time compared to the 1,4-butanediol synthesis and the reactions were also reproducible. Furthermore, solid solutions of up to 90% Al^{3+} could be obtained. The reaction is a one-pot synthesis and does not require any further steps such as calcination. 2-propanol also has a much lower toxicity than pernicious amino-based solvents such as triethylenediamine, which is fatal by inhalation, and is cheaper and more easily available than 1,4-butanediol which is a controlled substance owing to its being a precursor to the recreational drug γ-hydroxybutyrate.

Aluminium isopropoxide has been widely used as a reagent in sol-gel reactions where water is used to induce hydrolysis to form an amorphous network that is then fired to produce a crystalline solid.[33] In these solvothermal reactions the presence of a small amount of water present in either solvent may drive the hydrolysis of the reaction with the composition of the material obtained (*i.e.* oxide, hydroxide) governed by the choice of solvent used in the reaction.

The use of other aluminium salts, in particular $Al(acac)_3$ and $Al(NO_3)_3{\cdot}9H_2O$, were found to give unreliable results compared to $Al(O\text{-}iPr)_3$. Whenever a hydrated aluminium (or gallium) salt was used there was always formation of a small GaOOH impurity phase present observed by X-ray diffraction.

Table 4.1 Summary of solvothermal reactions of $Ga(acac)_3$ and $Al(O\text{-}iPr)_3$ in a variety of tested solvents. Reactions were all performed at 240 °C.

Solvent	Crystalline materials	Extent of Al^{3+} substitution	Other notes
1,4-butanediol	$\gamma\text{-}Ga_{2-x}Al_xO_3$, AlOOH, GaOOH	30%	AlOOH forms above 30%. Reaction of $Al(O\text{-}iPr)_3$ forms AlOOH. Unreliable reaction of yielding mixed phases.
Ethylenediamine	$\gamma\text{-}Ga_2O_3$	0%	No reaction between Ga and Al salts. Amorphous Al-O phase assumed to form.
Triethylenediamine	None	0%	No reaction at 240 °C, thick gel obtained.
Monoethanolamine	None	0%	Al^{3+} salts incompatible with aminoalcohols. Thick gel obtained when Al salts introduced.
Ethylacetate	$\gamma\text{-}Ga_{2-x}Al_xO_3$	30%	Bright yellow powders obtained. Unreliable reaction often forming mixed phases.
2-propanol	$\gamma\text{-}Ga_{2-x}Al_xO_3$	90%	Cheap, low toxicity, reliable reaction. Shorter reactions times. Reaction of $Al(O\text{-}i\text{-}Pr)_3$ forms an unknown phase unidentifiable by X-ray diffraction.
Toluene	None	0%	Amorphous materials formed
2-methylaminoalcohol	None	0%	Thick gel isolated from reaction vessel

4.3.2.2 Powder X-ray Diffraction

Powder X-ray diffraction shows that the spinel structure is retained for the solid-solution up to a 90% Al^{3+} incorporation, (*i.e.* x = 1.8) (Figure 4.4(f)). The profiles show that these materials have very broad Bragg reflections indicative of a poorly crystalline material likely consisting of nano-sized crystallites. BET surface area measurements confirmed that these materials had a very high surface area ~200 m^2g^{-1}. The profiles could be fitted to a cubic crystal system with space group $Fd\bar{3}m$, typical for spinel oxides, and Pawley refinements allowed the unit cell lattice parameter to be refined and shows a linear decrease with the increase in Al^{3+} content (Figure 4.5). The peak shapes of the observed reflections become broader with increasing Al^{3+} substitution suggesting an increase in static disorder present in the material. A spurious peak emergent around 42.5 °2θ is quite prominent in the 90% Al^{3+} substituted spinel indicating that 90% has likely reached the limit of substitution in this solid-solution. No Rietveld analysis was undertaken owing to the broadness of the peaks.

Control reactions of $Ga(acac)_3$ in either 1,4-butanediol or 2-propanol always formed γ-Ga_2O_3, whilst controlled reactions of $Al(O\text{-}i\text{-}Pr)_3$ formed AlOOH, (boehmite), in 1,4-butanediol, and an unknown phase which was unidentifiable by X-ray diffraction when 2-propanol was the solvent (Figure 4.5). Whilst some reflections did agree with the positioning of reflections from boehmite (JCPDS number 21-1307) no good match was found nor to the defect aluminium oxide spinel, or pseudoboehmite and the identity of this material remains speculative. Given the difference in peak shapes it likely a mixed phase material. The initial formation of γ-Ga_2O_3 can be proposed to control the crystal structure and growth of the gallium and aluminium mixed metal spinels Without the nucleation of γ-Ga_2O_3 there is no formation of γ-Al_2O_3 and so other, likely more stable, Al-O or Al-O-H phases form from the reaction.[34]

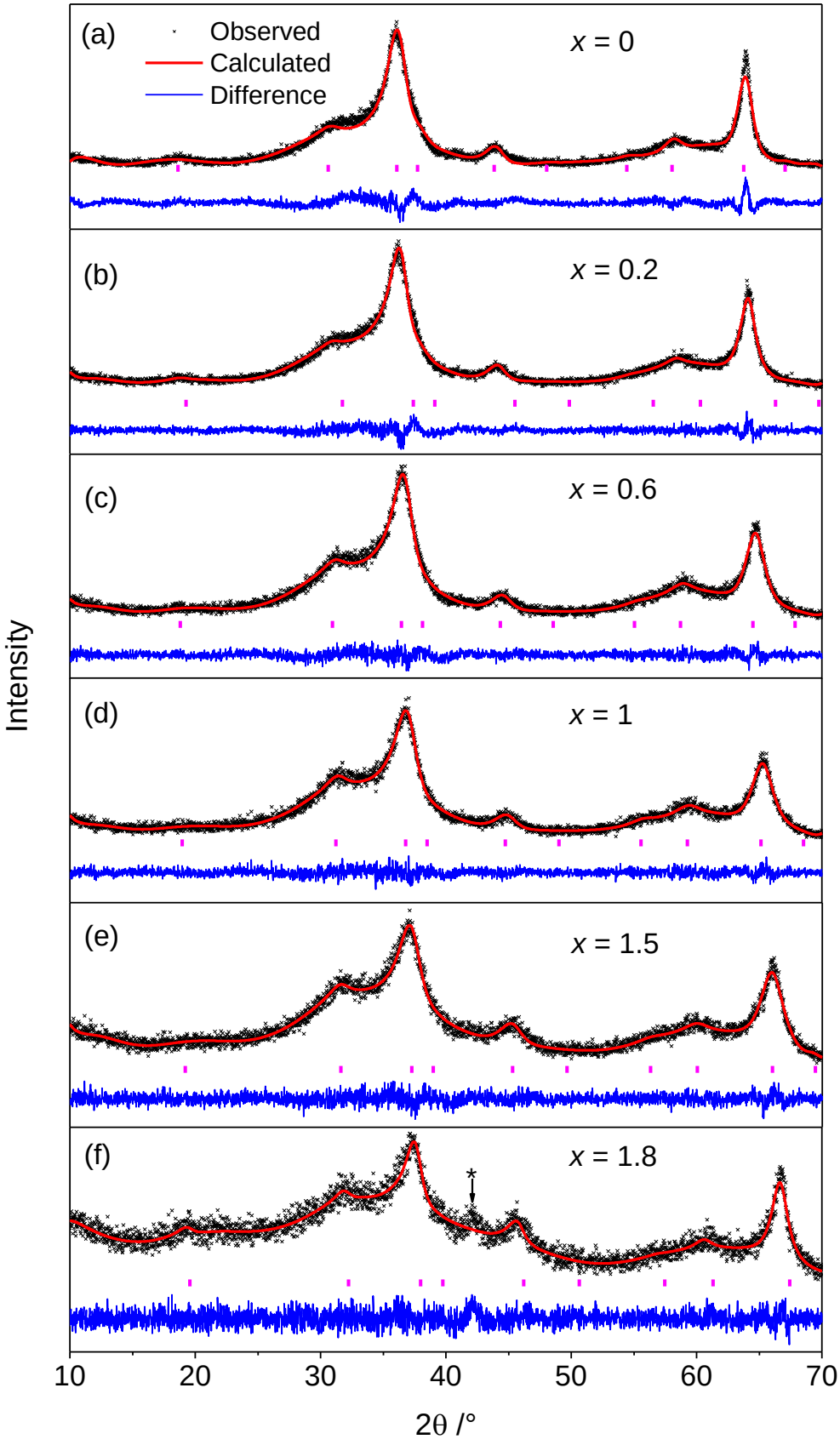

Figure 4.4 Pawley refinements against powder XRD data (λ = 1.54056 Å) for spinels γ-$Ga_{2-x}Al_xO_3$, ($0 \leq x \leq 1.8$). * denotes impurity phase.

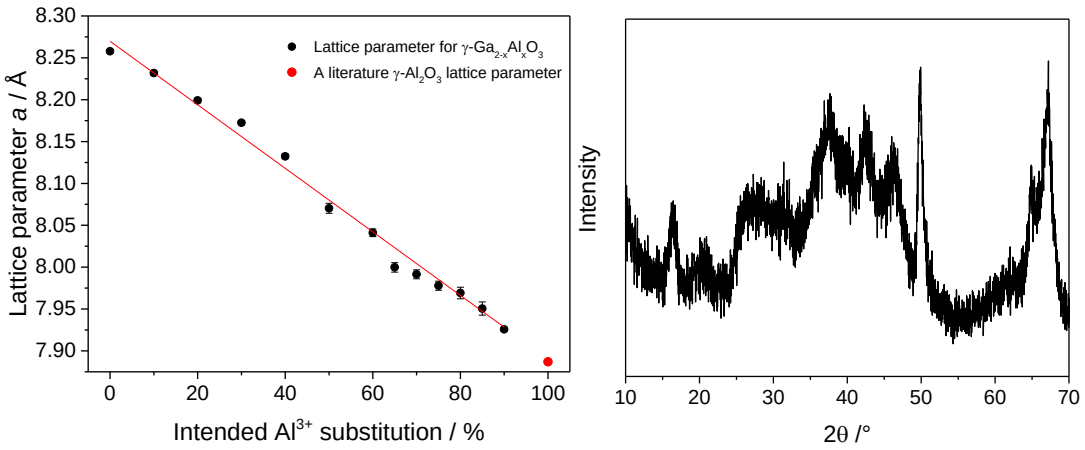

Figure 4.5 *(left)* change in the spinel lattice parameter with increasing aluminium substitution with a reference γ-Al_2O_3 material,[47] *(right)* powder XRD pattern of the unidentifiable material formed from solvothermal reaction of $Al(O\text{-}iPr)_3$ with 2-propanol.

4.3.2.3 Electron microscopy

TEM reveals that these materials are indeed composed of nano-sized crystallites (3 – 10 nm diameter) (Figure 4.6). SEM shows that these crystallites agglomerate with an almost spherical morphology whilst EDX confirms the expected Ga:Al ratio (Table 4.2).

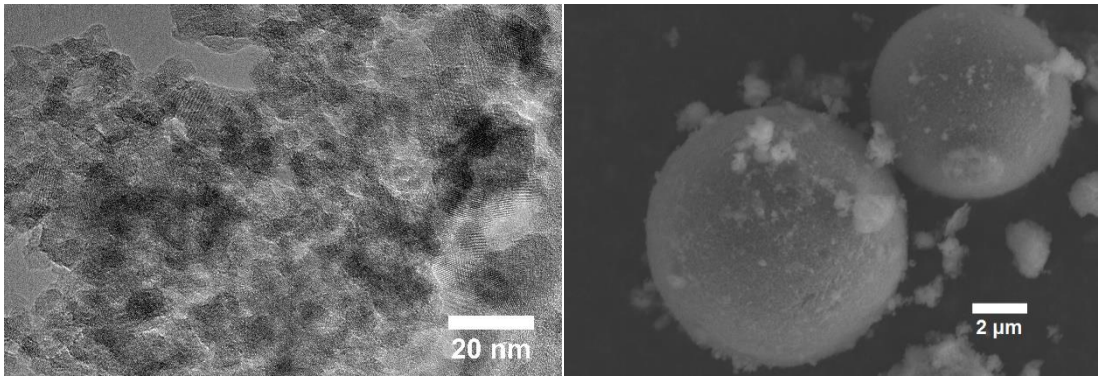

Figure 4.6 Electron microscopy on a sample of γ-$Ga_1Al_1O_3$ *(left)* HR-TEM and *(right)* SEM.

Table 4.2 EDX measurements from scanning electron microscopy averaged from 6 different areas of each sample.

Sample	Average Ga At%	Average Al At%
γ-$Ga_{1.4}Al_{0.6}O_3$	68	32
γ-$Ga_1Al_1O_3$	53	47
γ-$Ga_{0.5}Al_{1.5}O_3$	21	79

4.3.2.4 In situ thermodiffractometry

Substitution of aluminium for gallium in the spinel enhances the thermal stability of the spinel phase (Figure 4.7). Pure nano-crystalline γ-Ga_2O_3 transforms directly into the thermodynamically stable polymorph β-Ga_2O_3 at around 750 °C, whilst a higher temperature is required for the transformation of aluminium substituted samples. This agrees favourably with previous literature results.[31]

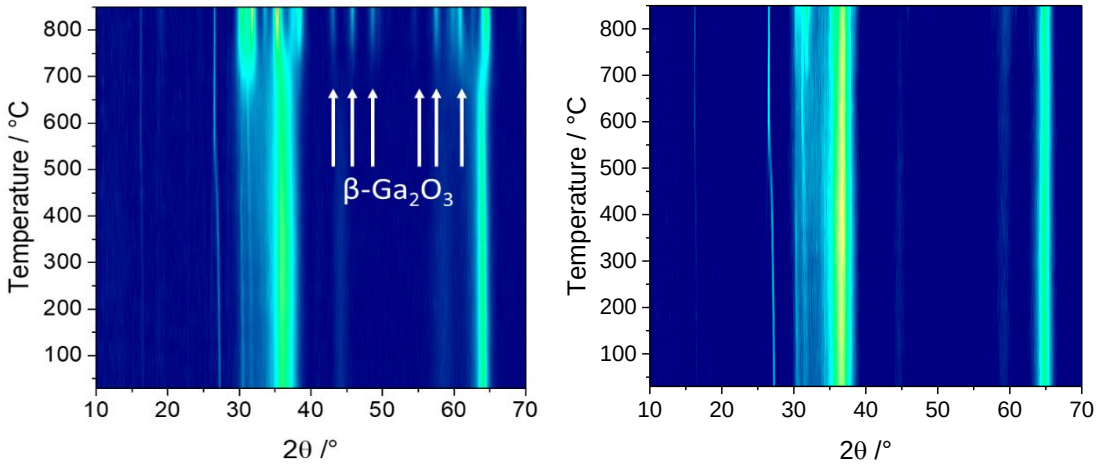

Figure 4.7 *In situ* thermodiffractometry of γ-$Ga_{2-x}Al_xO_3$ spinels *(left) x* = 0 *(right) x* = 0.6.

Transformation into phase pure β-$Ga_{2-x}Al_xO_3$ occurs up to 65% Al^{3+} substitution, while the spinel phase separates into β-$Ga_{2-x}Al_xO_3$ and α-$Ga_{2-x}Al_xO_3$ at higher substitutions. At a 90% Al substitution, the spinel converts directly into α-$Ga_{0.2}Al_{1.8}O_3$. Further discussion on these high temperature phases is found in Section 4.6.

The mixed-metal spinels become increasingly more crystalline as the temperature is raised. A good example is found in the 75% Al substituted γ-Ga_2O_3 sample. Whilst a temperature above 1000 °C is required to bring about phase transformation and separation, PXRD of a sample heated to 1000 °C shows that the crystallinity of the spinel is markedly different to the as-prepared sample (Figure 4.8).

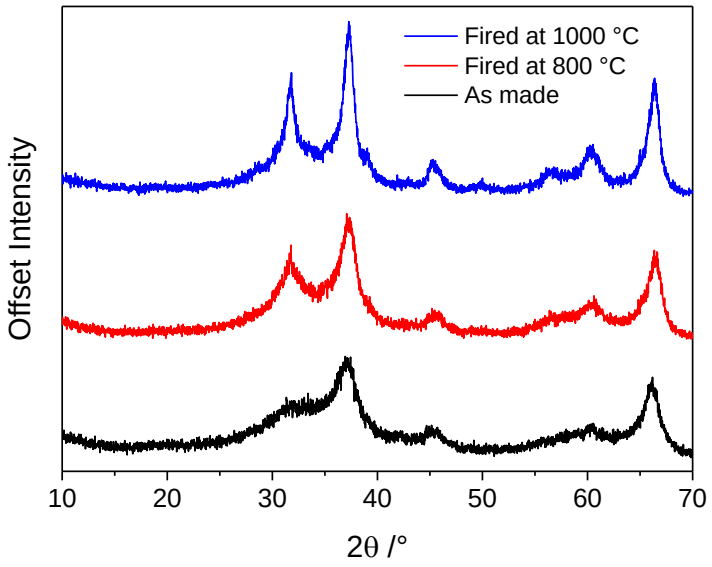

Figure 4.8 Change in the crystallinity of γ-$Ga_{0.5}Al_{1.5}O_3$ when fired at different temperatures.

4.3.2.5 ^{27}Al and ^{71}Ga NMR

A combined ^{27}Al and ^{71}Ga MAS NMR study was undertaken in order to probe the coordination environment of the metals in three mixed metal spinels of composition γ-$Ga_{1.4}Al_{0.6}O_3$, γ-$Ga_{1.0}Al_{1.0}O_3$, and γ-$Ga_{1.5}Al_{0.5}O_3$.

The ^{27}Al NMR spectra for all samples show a well resolved signal between 0-20 ppm characteristic of 6-coordinate aluminium[48] (Figure 4.9(a)). A very weak signal between 60-80 ppm, the region typical for 4-coordinate aluminium,[48] is observed in γ-$Ga_{1.6}Al_{0.4}O_3$ which suggests very little tetrahedral Al^{3+} is present in this sample. A more intense signal is observed in γ-$Ga_{1.0}Al_{1.0}O_3$ in this region and an even more intense signal for γ-$Ga_{0.5}Al1_{1.5}O_3$ meaning that tetrahedral aluminium is now quite prevalent. From the relative intensities of the signals it was possible to make a quantitative analysis about the aluminium coordination (Table 4.3). Owing to the presence of only 30% Al^{3+} in γ-$Ga_{1.4}Al_{0.6}O_3$ the aluminium can selectively occupy the octahedral site, or is directed to the octahedral by the tetrahedral favouring Ga^{3+}, however when Al^{3+} becomes the dominant metal as in γ-$Ga_{0.5}Al_{1.5}O_3$, Al^{3+} must occupy more tetrahedral sites.

The octahedral signal can be seen to shift to slightly lower ppm with increasing Al^{3+} as has been observed previously and ascribed to the increase of the more electronegative tetrahedral Ga^{3+} nearest neighbours deshielding the Al nucleus resulting in a lower magnetic field shift of the octahedral Al^{3+} peak.[31]

The ^{71}Ga MAS NMR spectra (Figure 4.9(b)) show noticeably broader signals but are well resolved enough to be able to show two separate signals present between -100 and 200 ppm and clearly the signals become weaker with increasing Al^{3+} content. In both γ-$Ga_{1.4}Al_{0.6}O_3$ and γ-$Ga_{1.0}Al_{1.0}O_3$ the Ga^{3+} occupies the tetrahedral:octahedral sites in an approximately 1:2 ratio, however there is much less Ga^{3+} in γ-$Ga_{0.5}Al_{1.5}O_3$ meaning that it can selectively occupy the tetrahedral site and the ratio of tetrahedral:octahedral Ga^{3+} reverses to a 2:1 ratio (Table 4.3). A small shift to higher ppm is observed for the 4-coordinate Ga^{3+} in the ^{71}Ga MAS NMR spectra with increasing Al^{3+} substitution because of the incorporation of less electronegative Al^{3+}.

Table 4.3 Relative occupation of tetrahedral and octahedral sites as determined by ^{27}Al and ^{71}Ga MAS NMR.

Sample	^{27}Al MAS NMR		^{71}Ga MAS NMR	
	Tetrahedral	Octahedral	Tetrahedral	Octahedral
γ-Ga_2O_3	-	-	26.8	73.2
γ-$Ga_{1.4}Al_{0.6}O_3$	5.2	94.8	33.6	66.4
γ-$Ga_{1.0}Al_{1.0}O_3$	7.7	92.3	39.3	60.7
γ-$Ga_{0.5}Al_{1.5}O_3$	14.7	85.3	63.5	36.5
γ-$Ga_{0.2}Al_{1.8}O_3$	19.4	80.6	61.8	38.2

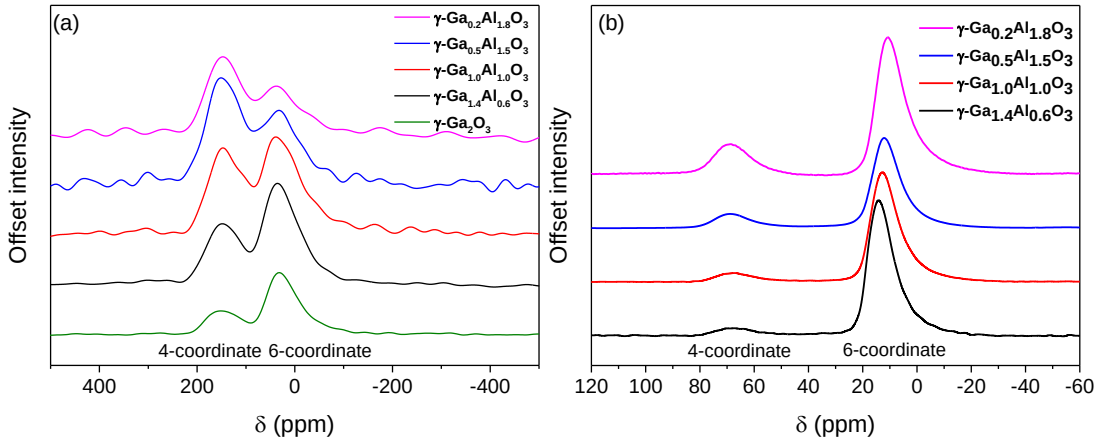

Figure 4.9 (a) ^{71}Ga MAS NMR spectra of 5 γ-$Ga_{2-x}Al_xO_3$ solid solutions, normalised to equal 6-coordinate peaks height. 20 T, 75 kHz MAS, 8192(0%, 30% Al) 16384(50%,75%, 90% Al) transients, 0.5 s recycle delay, 1.5 μs pulse, (b) ^{27}Al MAS NMR spectra of 4 γ-$Ga_{2-x}Al_xO_3$ solid solutions, normalised to equal 6-coordinate peaks height. 14.1 T, 20 kHz MAS, 2048 transients, 0.5 s recycle delay, 0.1 μs excitation pulse.

From the relative intensities of both ^{27}Al and ^{71}Ga MAS NMR spectra it was possible to propose chemical formula for the spinels in terms of relative amounts of tetrahedral and octahedral site occupation and thus postulate if the metal vacancies in the defect

spinel are on tetrahedral or octahedral sites assuming the ideal spinel structure (Table 4.4).

Table 4.4 Proposed chemical formula of spinel based on the intended Al^{3+} substitution and results from ^{27}Al and ^{71}Ga MAS NMR data.

Sample	Defect spinel formula	AB_2O_4 type spinel formula
γ-Ga_2O_3	γ-$(Ga_{0.535})^{tet}[Ga_{1.465}]^{oct}O_3$	(□-$Ga_{0.713}$)^{tet}[$Ga_{1.953}$]^{oct}O_4
γ-$Ga_{1.4}Al_{0.6}O_3$	γ-$(Ga_{0.470}Al_{0.031})^{tet}[Ga_{0.930}Al_{0.569}]^{oct}O_3$	(□-$Ga_{0.626}Al_{0.0419}$)^{tet}[$Ga_{1.24}Al_{0.759}$]^{oct}O_4
γ-$Ga_{1.0}Al_{1.0}O_3$	γ-$(Ga_{0.393}Al_{0.077})^{tet}[Ga_{0.607}Al_{0.923}]^{oct}O_3$	(□-$Ga_{0.524}Al_{0.103}$)^{tet}[$Ga_{0.809}Al_{1.23}$]^{oct}O_4
γ-$Ga_{0.5}Al_{1.5}O_3$	γ-$(Ga_{0.318}Al_{0.221})^{tet}[Ga_{0.183}Al_{1.28}]^{oct}O_3$	(□-$Ga_{0.424}Al_{0.295}$)^{tet}[$Ga_{0.244}Al_{1.706}$]^{oct}O_4
γ-$Ga_{0.2}Al_{1.8}O_3$	γ-$(Ga_{0.124}Al_{0.349})^{tet}[Ga_{0.076}Al_{1.45}]^{oct}O_3$	(□-$Ga_{0.165}Al_{0.465}$)^{tet}[$Ga_{0.101}Al_{1.935}$]^{oct}O_4

□ denotes a vacant site.

In all five materials, the octahedral sites are almost fully occupied meaning that the vacancies are located mainly on the tetrahedral sites. In the pure gallium oxide sample the tetrahedral:octahedral ratio is ~1:2.7 which is substantially larger than the ratio found in disordered gallium oxide prepared from amorphous gels (1:2.1).[20] These NMR and structural formula data are also plotted graphically below (Figure 4.10) to show how the change in relative octahedral:tetrahedral proportion for each metal and the change in site occupancy changes with the composition of the spinel. Of course, this is an oversimplification since the occupation of non-spinel sites, which were found to be partially occupied in both the crystalline pure γ-Al_2O_3 and γ-Ga_2O_3 structures[6,18,20] has been neglected throughout this treatment. These extra sites are also tetrahedral and octahedral but the disordered nature of these materials would cause significant broadening of the NMR signals and so it was not possible to resolve additional 4 and 6-coordinate signals. It has also been proposed that the occupancy of extra sites is greater in the poorly crystalline samples of γ-Ga_2O_3[20] and so it is likely that these additional sites are likely present in these new materials.

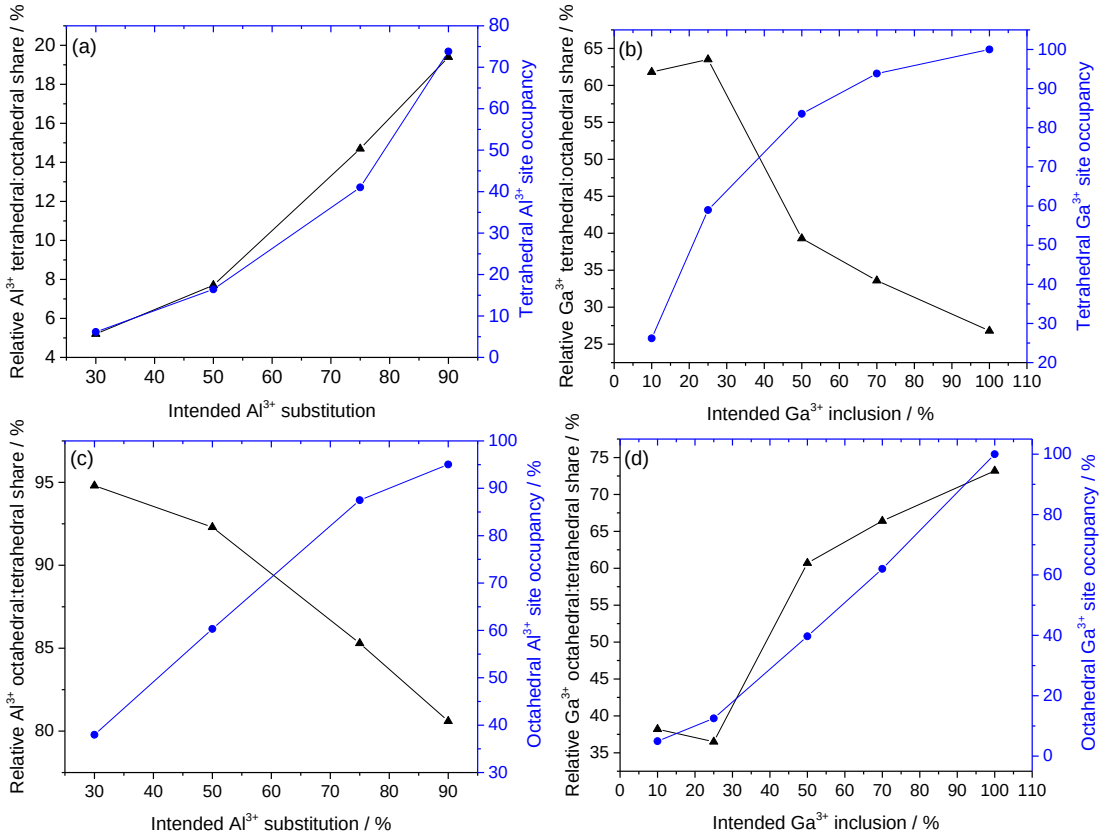

Figure 4.10 Plots showing the change in the relative Al and Ga occupation with the change in real site occupation by Al and Ga: (a) tetrahedral Al, (b) tetrahedral Ga, (c) octahedral Al, (d) octahedral Ga.

4.4 The gallium aluminium oxyhydroxide system:

$Ga_{5-x}Al_xO_7(OH)$, $(0.5 \leq x \leq 1.5)$

4.4.1 Synthetic procedure

It was found that if the reaction of $Ga(acac)_3$ and $Al(O\text{-}iPr)_3$ in 1,4-butanediol was extended to 96 hours a new crystalline phase was formed. The crystallinity and reproducibility of this phase was found to be optimal however if the aluminium alkoxide was replaced with aluminium acetylacetonate. Instead of the formation of a gel, as with the spinels, a white powder was obtained directly from the synthesis.

In a typical synthesis 0.4 g (1.01 mmol) of $Ga(acac)_3$ (Sigma, 99.99%) and an appropriate amount of $Al(acac)_3$ (Merck, ≥98%) was added to a PTFE liner followed by the addition of 8 ml 1,4-butanediol. The reaction mixture was stirred at room

temperature for 10 minutes before being sealed inside a stainless-steel autoclave and placed inside a preheated fan assisted oven at 240 °C for 96 hours. After this time, the autoclave was allowed to cool naturally to ambient temperature and the vessel opened to reveal a white powder. This solid was dispersed by magnetic stirring in the mother liquor followed by addition of acetone to reduce the viscosity of the diol. The material was then filtered by suction filtration and dried overnight at 70 °C.

4.4.2 General characterisation

4.4.2.1 Experimental considerations

The long reaction time of 96 hours is a necessary requirement of the synthesis as shorter reaction times can yield either γ-Ga_2O_3 present with AlOOH, γ-$Ga_{2-x}Al_xO_3$, or GaOOH. The reaction is reproducible and no other crystalline phases were observed by X-ray diffraction. The reaction can also take place in 1,5-pentanediol but the synthesis time is longer requiring a minimum of 7 days.

Attempts to synthesise this material by using 2-propanol were unsuccessful even after extended reaction times of 7 days. Playford *et al.* describe the synthesis of $Ga_5O_7(OH)$ (the pure gallium analogue of this material) by solvothermal reaction of Ga metal in H_2O:MEA in a 1:6 (volume) ratio.[18] Attempts to prepare $Ga_{5-x}Al_xO_7(OH)$ by this method by addition of an aluminium salt into the mixture were not successful. This is likely because, as aforementioned, aluminium salts are generally incompatible with an aminoalcohol solvent. It was found that this material could only incorporate up to a maximum of 30% Al^{3+}. Attempts to synthesis a material with a higher amount of Al^{3+} yielded only the mixed-metal spinel γ-$Ga_{2-x}Al_xO_3$ and AlOOH (boehmite). A control reaction using $Ga(acac)_3$ in 1,4-butanediol for 24 hours formed the thermodynamically stable polymorph β-Ga_2O_3 and it was not possible to isolate the pure gallium analogue, $Ga_5O_7(OH)$, by the 1,4-butanediol method.

4.4.2.2 Powder X-ray diffraction

Early attempts to identify this material found that it matched closely with a material on the JCPDS database (number 00-020-0412). This material reported by MacDonald *et al.*[28] was given the chemical formula $GaAlO_3$ and cited as crystallising in an

hexagonal cell. Lattice parameters and a list of their observed reflections matched well with the observed reflections in this work as is discussed below.

A polymorph denoted $GaAlO_3$ had also been reported by Roy and co-workers[24] earlier than the report by MacDonald. It is clear by examination of both papers that the same material is being described, which MacDonald acknowledges, and both also report that $GaAlO_3$ decomposes first into ε-Ga_2O_3 (now referred to as κ-Ga_2O_3) with gentle heating and then into β-Ga_2O_3 at higher temperatures.

Incidentally, κ-Ga_2O_3, or κ-Al_2O_3 are also obtained when $Ga_5O_7(OH)$, or $Al_5O_7(OH)$ (tohdite, or akdalaite) is heated prior to phase transformation into β-Ga_2O_3. Furthermore, the observed reflections of the new material in this work were comparable with those published for $Ga_5O_7(OH)$ (Figure 4.11) and it was therefore decided that this material is most likely $Ga_{5-x}Al_xO_7(OH)$, as opposed to $GaAlO_3$, assumed in the 1950s and 1960s.

Pawley refinement against powder XRD data of samples containing 10, 20 and 30% Al^{3+} (Figure 4.12) were conducted in space group $P6_3mc$ with initial lattice parameters obtained from the $Ga_5O_7(OH)$ structure. Clear evidence for anisotropic peak broadening was found in all three samples, though with increasing Al^{3+} content there is an increase in the overall static disorder within the material and so all reflections are broadened resulting in the anisotropic peak broadening being less pronounced (Figure 4.12(d)). The use of Stephens' phenomenological model of anisotropic peak broadening[49] was essential in order to obtain a good profile fit as Figure 4.12(a) without Stephens' and Figure 4.12(b) which included the Stephens' parameters shows.

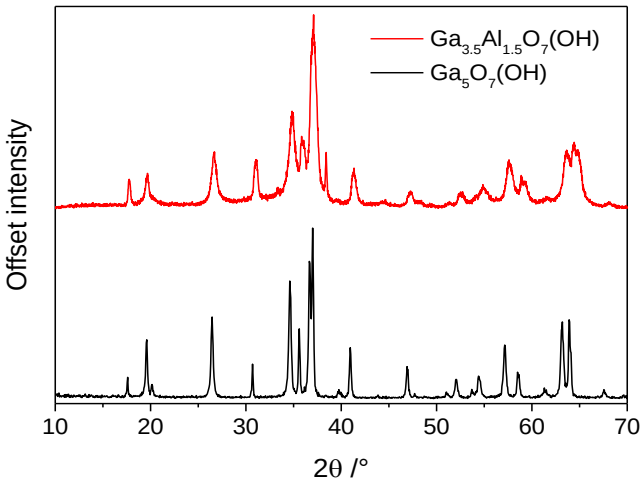

Figure 4.11 Powder XRD pattern of $Ga_5O_7(OH)$ *(black)* and 30% Al^{3+} substituted $Ga_5O_7(OH)$ *(red)*.

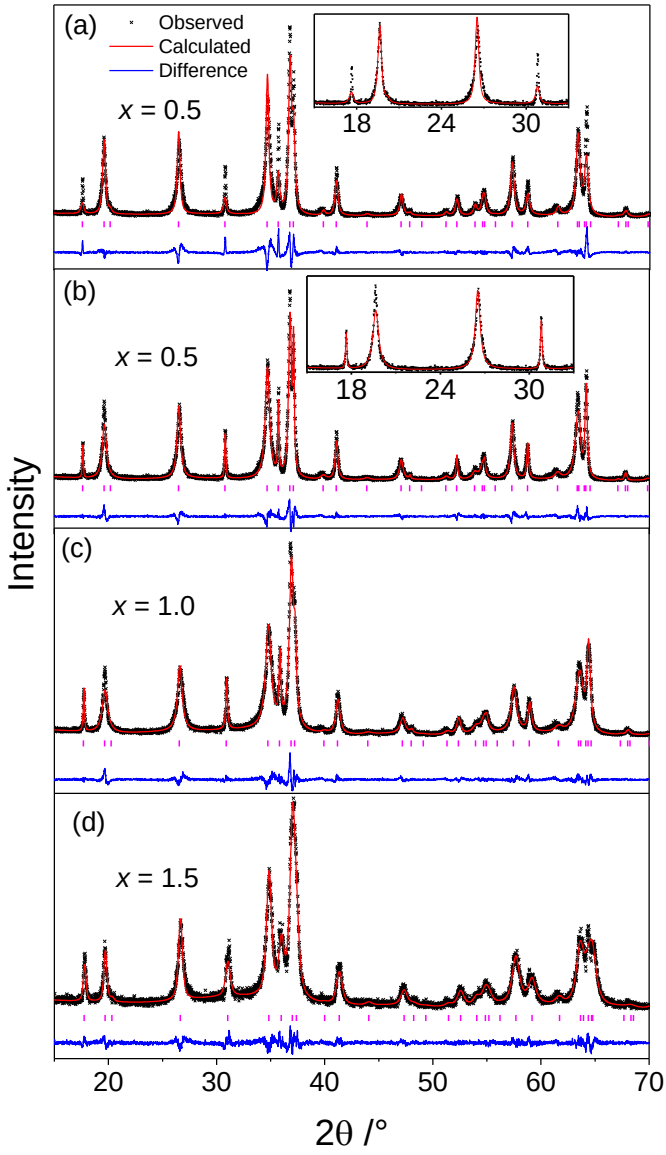

Figure 4.12 Pawley refinements against powder XRD data (λ = 1.54056 Å) for $Ga_{5-x}Al_xO_7(OH)$, ($0 \leq x \leq 1.5$), with inset showing difference in fit depending on whether Stephens' parameters are used or not.

The refined lattice parameters are provided in Table 4.5: the material obeys Vergard's law and the volume of the material linearly decreases with increasing aluminium substitution (Figure 4.13). These refined lattice parameters are similar to those reported by MacDonald *et al.* (a = 5.70 Å, c = 8.92 Å) for their supposed $GaAlO_3$.[28]

Table 4.5 List of refined lattice parameters in the system $Ga_{5-x}Al_xO_7(OH)$, ($0 \leq x \leq 1.5$).

	Lattice parameters			
Material	***a* / Å**	***c* / Å**	**Volume / Å^3**	**Reference**
$Ga_5O_7(OH)$	5.82107(8)	9.0662(2)	266.05	[18]
$Ga_{4.5}Al_{0.5}O_7(OH)$	5.8037(3)	9.0386(8)	263.66(11)	This work
$Ga_{4.0}Al_{1.0}O_7(OH)$	5.7855(4)	9.0262(10)	261.65(9)	This work
$Ga_{3.5}Al_{1.5}O_7(OH)$	5.7605(5)	9.0121(14)	258.99(14)	This work
$Al_5O_7(OH)$	5.576	8.768	236.09	[50]

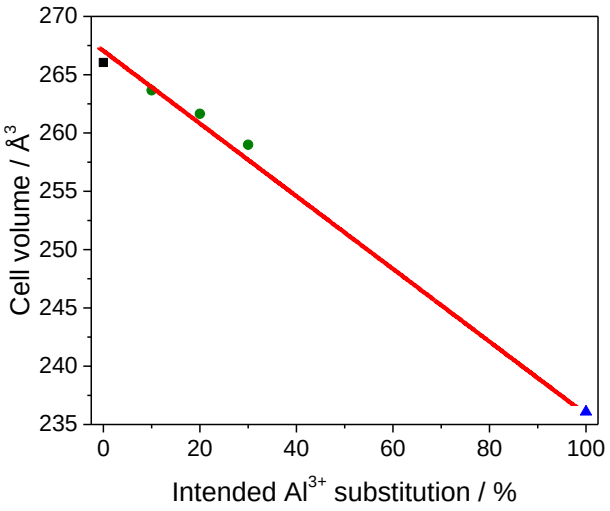

Figure 4.13 Linear decrease in cell volume for $Ga_{5-x}Al_xO_7(OH)$ with increasing Al^{3+} substitution.

4.4.2.3 Infrared Spectroscopy

Infrared spectroscopy shows an intense O-H stretching mode observed at 3300 cm^{-1} (Figure 4.14). The mode at 850 cm^{-1} is attributed to a (Ga,Al)-O-H bending mode as a mode at a similar wavenumber was assigned this in both $Ga_5O_7(OH)$[18] and in a computational study on $Al_5O_7(OH)$.[51] From this it can clearly be deduced that the $GaAlO_3$ material, originally discovered independently by the groups of Roy, and MacDonald, can be formerly identified as $Ga_{5-x}Al_xO_7(OH)$.

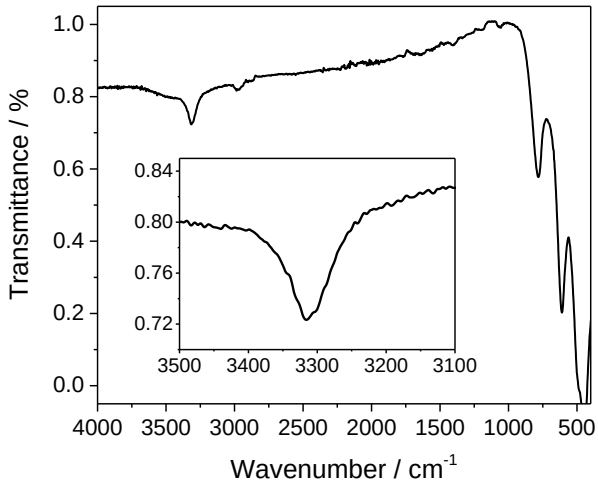

Figure 4.14 IR spectrum of $Ga_{3.5}Al_{1.5}O_7(OH)$ showing a stretching mode at 3300 cm^{-1} and Ga-O-H bending mode at 850 cm^{-1}.

4.4.2.4 Thermogravimetric analysis

TGA of $Ga_{3.5}Al_{1.5}O_7(OH)$ showed that a gradual mass loss of 1.5% occurred immediately upon heating until ~400 °C followed by a larger mass loss of 2.5% occurring between the region 400 – 600 °C (Figure 4.15). This second mass loss is consistent with the dehydration of $Ga_{3.5}Al_{1.5}O_7(OH)$ since it occurs over the temperature range which $Ga_{3.5}Al_{1.5}O_7(OH)$ is observed to decompose in the thermodiffractometry experiment (Section 4.5.5). The mass loss of 2.5% occurring between 400 – 600 °C is consistent with the expected mass loss on conversion to $Ga_{1.4}Al_{0.6}O_3$ ~2.2% (Scheme 4.1). The first observed gradual mass loss could possibly be attributed to loss of surface diol on the material.

$$2Ga_{3.5}Al_{1.5}O_7(OH) \rightarrow 5Ga_{1.4}Al_{0.6}O_3 + H_2O$$

Scheme 4.1

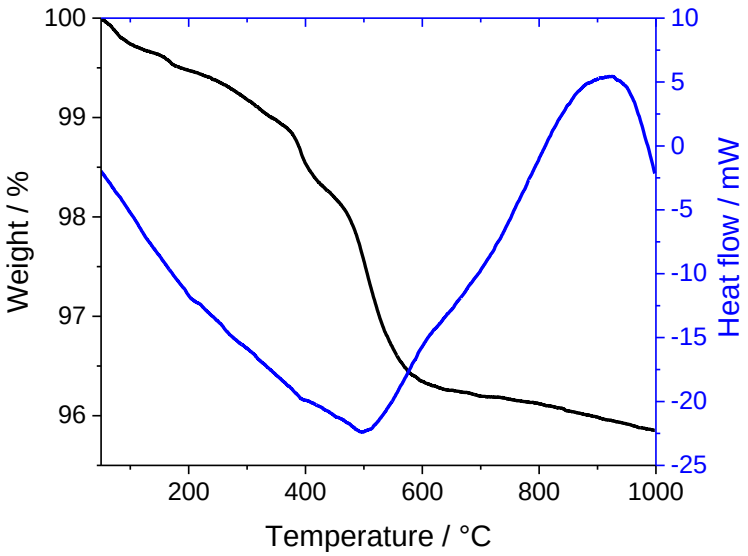

Figure 4.15 TGA/DSC-trace of $Ga_{3.5}Al_{1.5}O_7(OH)$.

4.4.2.5 Electron Microscopy

TEM shows that $Ga_{3.5}Al_{1.5}O_7(OH)$ consists of large, thin hexagonal plates (Figure 4.16). The anomalous peak broadening observed by X-ray diffraction is a likely consequence of the large yet thin plate-like morphology displayed by this material causing internal strain within the crystallite, as was also reported for the pure gallium analogue.[18]

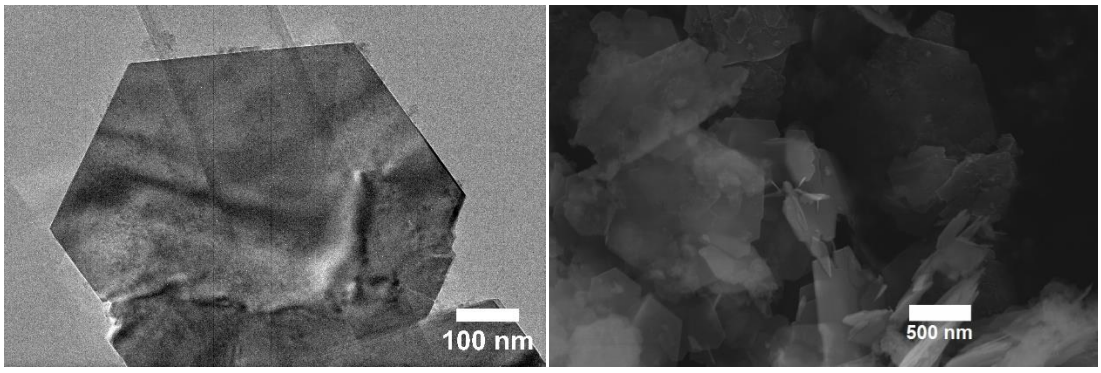

Figure 4.16 *(left)* TEM image of $Ga_{3.5}Al_{1.5}O_7(OH)$ and *(right)* corresponding SEM image.

4.4.2.6 ^{27}Al and ^{71}Ga NMR

Solid-state ^{27}Al MAS NMR was performed on a sample of $Ga_{3.5}Al_{1.5}O_7(OH)$ which showed that ~98% of the available Al^{3+} preferentially occupies the octahedral sites (Figure 4.17(a)). Only 20% of available sites in the tohdite structure are tetrahedral and given the tetrahedral preference of Ga^{3+} it is hardly surprisingly that in a sample containing 30% Al^{3+} that there should be any tetrahedrally coordinated Al^{3+}.

Solid-state ^{71}Ga MAS NMR of $Ga_{3.5}Al_{1.5}O_7(OH)$ shows a signal for both 6 and 4-coordinate geometries further confirming that the tetrahedral site must be occupied by gallium (Figure 4.17(b)).

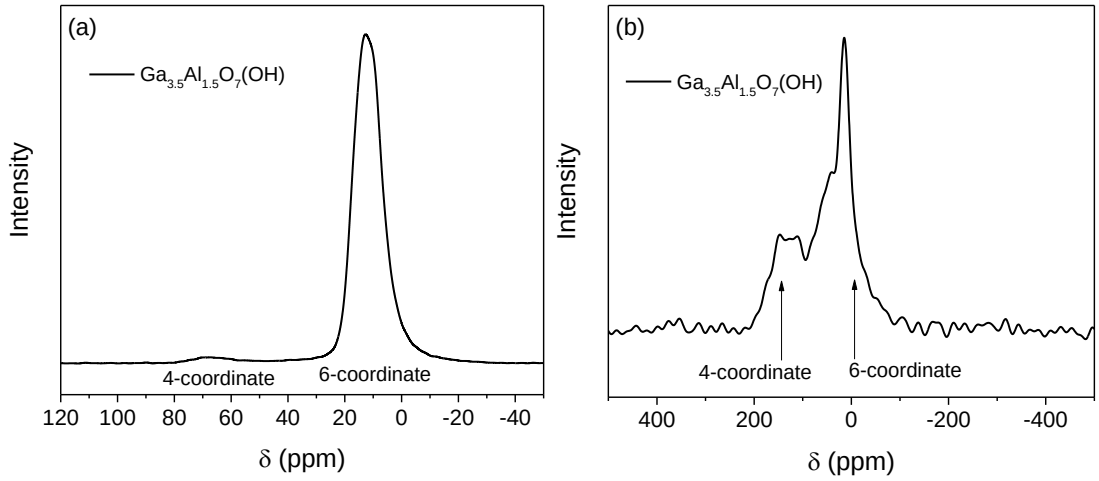

Figure 4.17 (a) ^{27}Al MAS NMR spectrum of $Ga_{3.5}Al_{1.5}O_7(OH)$ (tohdite), 14.1 T, 20 kHz MAS, 2048 transients, 0.5 s recycle delay, 0.1 μs excitation pulse, (b) ^{71}Ga MAS NMR spectra of $Ga_{3.5}Al_{1.5}O_7(OH)$. 20 T, 75 kHz MAS, 13568 transients, 0.5 s recycle delay, 1.5 μs excitation pulse.

4.4.3 Discussion of structure and comparison to other similar oxyhydroxide phases

It is clear that materials in the $Ga_{5-x}Al_xO_7(OH)$ system are mixed-metal aluminium gallium oxyhydroxides based on the tohdite/akdalaite structure, $Al_5O_7(OH)$.[3,50,52,53] The gallium analogue has only recently been reported.[18] There are no known solvothermal syntheses of $Al_5O_7(OH)$ and it is usually synthesised by reacting aluminium salts, or aluminium oxides hydrothermally at temperatures in excess of 240 °C usually with some external pressure applied. The $Al_5O_7(OH)$ analogue could not be prepared by reaction of either $Al(O\text{-}iPr)_3$ or $Al(acac)_3$ in 1,4-butanediol at 240 °C with reaction times of 4 days to 7 days. Other materials that crystallise in this space group with similar lattice parameters are nolanite, which has a formula typically $(Fe,V)_5O_7(OH)$ or $(Fe,V)_5O_8$[54–56] and some ternary molybdates both containing transition metals.[57] The structure of the former has been reported as both oxide and oxyhydroxide, and the latter is always oxide.

It has been proposed that the mineral $Fe_2O_3{\cdot}0.2H_2O$, (ferrihydrite) is analogues to akdalaite, though this remains controversial.[58,59] Ferrihydrite is ubiquitous in soil on

Earth and expected to be present in extra-terrestrial materials. Despite its ubiquity the internal atomic arrangement of this material has been subject to extensive debate and research as natural and synthetic preparations of this material usually show some degree of structural disorder. Therefore, it has only been recently, owing to advances in local structure analysis techniques, *i.e.* the pair-distribution function, that its structure was probed and in that study reported to be analogous to tohdite/akdalaite.[60] Ferrihydrite is usually described and reported as 2-line or 6-line ferrihydrite depending on how well resolved the diffraction peaks are in the powder pattern. No other analogous binary oxyhydroxides have been reported with this structure. It is interesting to note that incomplete miscibility of Al^{3+} incorporation into ferrihydrite has been observed with a limit of 25% Al^{3+} substitution.[61] The saturation limit of 25% is likely controlled by Al-Al avoidance conforming to Pauling's distortion rule.[62] Given the similar size of Ga^{3+} and Fe^{3+} it is quite reasonable to suggest that the limit of Al^{3+} in $Ga_5O_7(OH)$ of 30% is also a consequence of this avoidance. Attempts to introduce a portion of Fe^{3+} into $Ga_5O_7(OH)$ using the 1,4-butanediol synthesis was unsuccessful and instead formed a mixed metal spinel even after extended reaction times.

4.5 Thermal decomposition of $Ga_5O_7(OH)$ and synthesis of κ-Ga_2O_3

4.5.1 Synthesis of $Ga_5O_7(OH)$

The synthesis of $Ga_5O_7(OH)$ was optimised from the original synthesis of Playford *et al*.[18] This was achieved by using a ratio of MEA:H_2O to 1:1 as opposed to the reported 1:6. This resulted in reduced reaction times (2 days as opposed to 6 days) and a highly crystalline material free from any impurity phases such as γ-Ga_2O_3.

0.4 g (5.74 mmol) of liquid Ga metal (Alfa-Aesar, 99.9%) was added to a PTFE liner with addition of 5 ml H_2O and 5 ml MEA. The mixture was vigorously stirred for 2 minutes before being sealed inside a stainless-steel autoclave and placed in a pre-heated fan-assisted oven at 240 °C for 48 hours. After the reaction, the autoclave was removed from the oven and cooled naturally to room temperature. The white solid was collected by vacuum filtration and washed with copious amounts of methanol and then dried overnight at 70 °C. The material can be scaled up by reacting 3 g liquid Ga metal

with 25 ml H_2O and 25 ml MEA in a 100 ml PTFE lined autoclave. The reaction temperature and time are the same. The yield is ~4.1 g (~100%).

4.5.2 Powder X-ray diffraction of $Ga_5O_7(OH)$

PXRD confirmed the presence of a highly crystalline $Ga_5O_7(OH)$ and no other crystalline impurities were seen in the powder X-ray pattern. The structure of $Ga_5O_7(OH)$ was described above in Section 4.4.3. Anisotropic peak broadening was observed in this sample (Figure 4.18 (inset)) but less pronounced than in the aluminium substituted samples. This anisotropic peak broadening was observed previously in $Ga_5O_7(OH)$ which reportedly led to difficulty in fitting the observed X-ray diffraction pattern.[18]

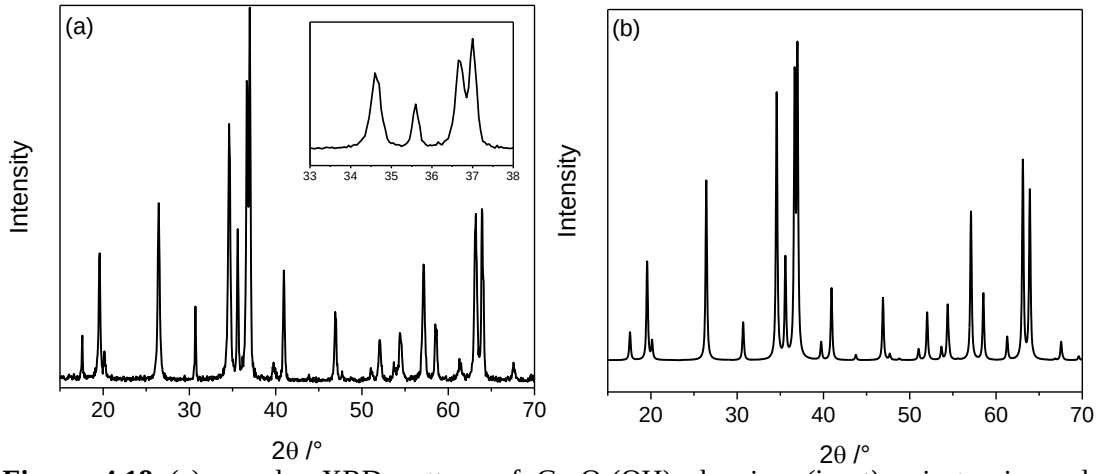

Figure 4.18 (a) powder XRD pattern of $Ga_5O_7(OH)$ showing *(inset)* anisotropic peak broadening, (b) simulated pattern of $Ga_5O_7(OH)$ without anisotropic peak broadening.

4.5.3 Thermal decomposition of $Ga_5O_7(OH)$

The thermal decomposition of $Ga_5O_7(OH)$ was followed by X-ray diffraction (Figure 4.19) and showed that the oxyhydroxide is stable until around 450 °C, then emergence of a crystalline transient phase begins to occur. This transient phase is stable until around 800 °C whereupon phase transformation into β-Ga_2O_3 commences. The transient phase was initially identified as κ-Ga_2O_3, an orthorhombic polymorph analogous to κ-Al_2O_3,[52,53] both of which have been reported as being formed from the $M_5O_7(OH)$ structure (M = Al, Ga). The phase transformation pathway reported here is slightly different to the reported thermal decomposition of $Ga_5O_7(OH)$ where the formation of β-Ga_2O_3 always coincided with the formation of κ-Ga_2O_3.[18] This suggests

that the heating rate and/or precursor crystallinity may influence the temperature and course of its decomposition.

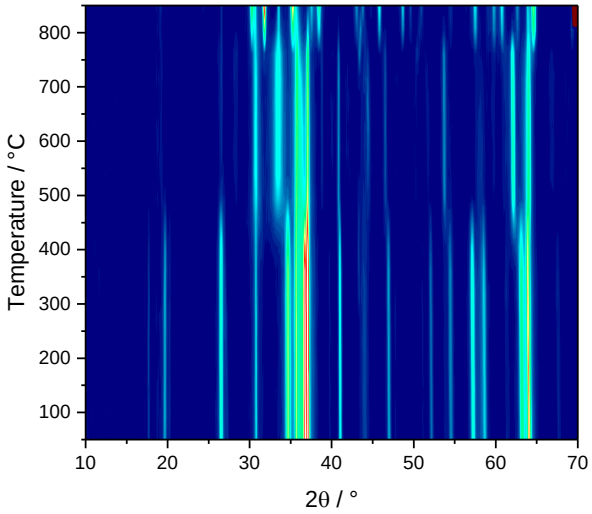

Figure 4.19 *In situ* thermodiffractometry of $Ga_5O_7(OH)$ showing formation of κ-Ga_2O_3 between 450 – 800 °C.

The transient phase in this work, initially assigned as κ-Ga_2O_3, can be isolated without the presence of β-Ga_2O_3 at any temperature between 550 – 800 °C. Though this contradicts with what is published in the literature, the difference in results (*i.e.* κ-Ga_2O_3 with, or without formation of β-Ga_2O_3) is probably a direct result of the heating conditions.

Figure 4.20(b) shows some reflections are immediately sharp and intense after the decomposition of $Ga_5O_7(OH)$ at 550 °C whilst other reflections grow in intensity up until 800 °C after when the structure collapses into β-Ga_2O_3. The sharp crystalline peaks can be readily indexed to an hexagonal cell (a = 2.895 Å, c = 9.250 Å), which is very similar to the ε-Ga_2O_3 polymorph previously synthesised by thermal decomposition of $Ga(NO_3)_3 \cdot 9H_2O$ by heating at 220 °C for 12 hours followed by firing at 400 °C for 14 days, (a = 2.9036(2) Å, c = 9.2554(9) Å).[18] It seems likely that the thermal decomposition of $Ga_5O_7(OH)$ forms a biphasic mixture of crystalline ε-Ga_2O_3 and a poorly crystalline κ-Ga_2O_3 phase which steadily becomes more crystalline at higher temperatures. A Pawley refinement of this biphasic mixture is shown in Figure 4.20(a). The refined lattice parameters of κ-Ga_2O_3 and ε-Ga_2O_3 are found in Table 4.6.

The reflections of κ-Ga_2O_3 overlap with the reflections in the powder pattern for ε-Ga_2O_3 and indeed the two structures are very closely related both having hexagonal close packed oxide layers.

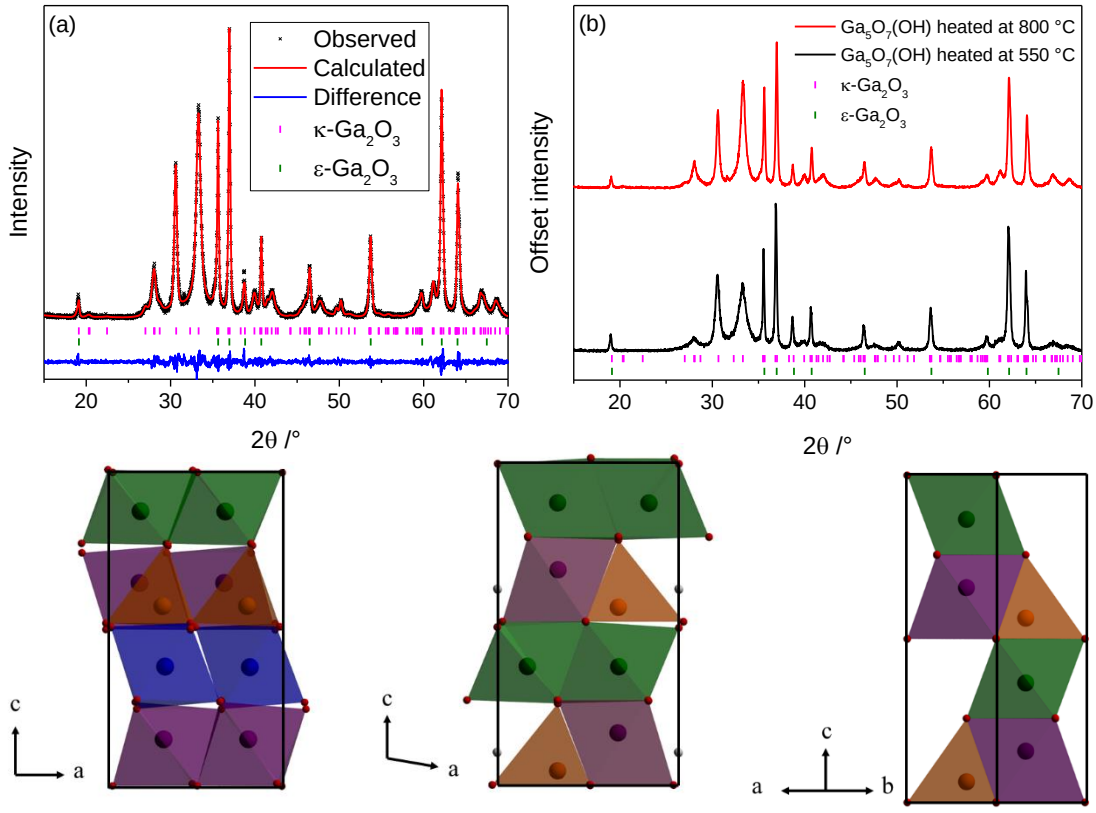

Figure 4.20 (a) Pawley refinement showing both κ-Ga_2O_3 and ε-Ga_2O_3, with κ-Ga_2O_3 reflections overlapping with ε-Ga_2O_3 reflections, (b) stacked plot showing the change in the κ-Ga_2O_3 reflection intensities with temperature, (c) crystal structures of *(left)* κ-Ga_2O_3, *(middle)* $Ga_5O_7(OH)$, and *(right)* ε-Ga_2O_3.

Table 4.6 Refined lattice parameters from a Pawley refinement against powder XRD data for a biphasic sample of κ-Ga_2O_3 and ε-Ga_2O_3.

Polymorph	*a*	*b*	*c*	Space group
ε-Ga_2O_3	2.9053(3)	2.9053(3)	9.2797(8)	$P6_3mc$
κ-Ga_2O_3	5.0388(7)	8.6887(9)	9.2848(9)	$Pna2_1$

The structure of $Ga_5O_7(OH)$ can be considered a super-structure of ε-Ga_2O_3 so it is unsurprising that both polymorphs are found in the decomposition of $Ga_5O_7(OH)$ and the material formed could possibly be a disordered intergrowth of the two materials as has been postulated for the structure of θ-Al_2O_3, which was considered to be a disordered intergrowth of two crystallographic variants at the unit cell level.[63] One

variant was based on β-Ga_2O_3 and a second was a monoclinic variant closely related to δ-Al_2O_3. Iron oxide also has similar polymorphs: ε-Fe_2O_3 is known to crystallise in an ordered (ε-Fe_2O_3) and a disordered (ε-Fe_2O_3) polymorph,[64,65] though little has been published on the disordered polymorph, and a greater amount of focus concerns the ordered polymorph.[66,67] ε-Ga_2O_3 is considered structurally analogous to the disordered ε-Fe_2O_3, whilst κ-Ga_2O_3 is structurally analogous to the ordered polymorph.[18]

κ-Ga_2O_3 remains a poorly studied and elusive polymorph notably difficult to isolate as a phase pure material but there has been a recent study whereby claims to prepare phase pure thin films of κ-Ga_2O_3 with potential ferroelectric properties have been reported.[68]

4.5.4 Hydrothermal decomposition of $Ga_5O_7(OH)$

It was found that a mixture of κ-Ga_2O_3 and ε-Ga_2O_3 could also be synthesised when $Ga_5O_7(OH)$ was treated hydrothermally at 480 °C for 4 hours followed by firing in a box furnace at 800 °C for 5 minutes. κ-Ga_2O_3 formed from the hydrothermal synthesis is more crystalline than when heated in air. This is indicated by the sharpness of the Bragg reflections in the powder XRD pattern (Figure 4.21(a)). A Pawley refinement shows an excellent fit to the observed data when using a model including lattice parameters for both the orthorhombic κ-Ga_2O_3 polymorph, and ε-Ga_2O_3 (Figure 4.21(b)). Rietveld refinement was precluded by the presence of some β-Ga_2O_3.

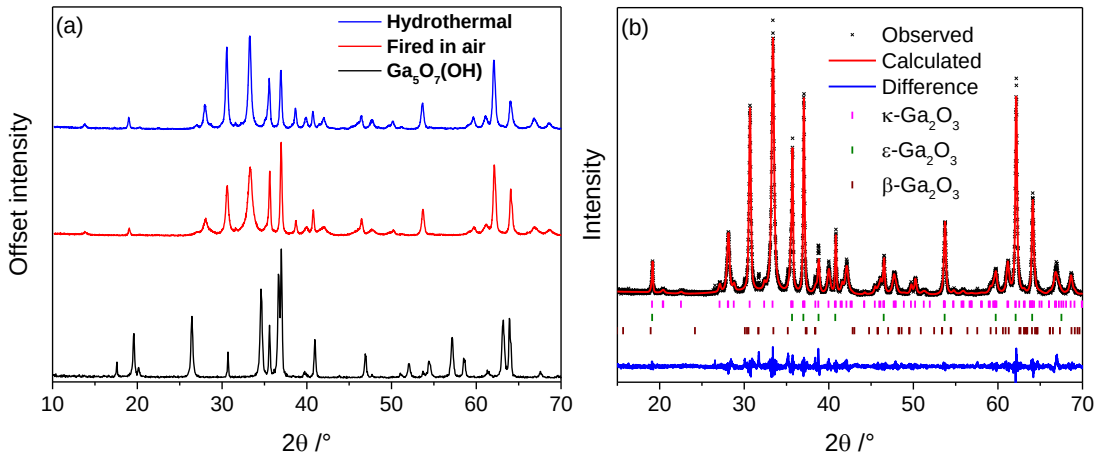

Figure 4.21 (a) as-made $Ga_5O_7(OH)$ *(black)*, $Ga_5O_7(OH)$ fired to 800 °C in air *(red)*, $Ga_5O_7(OH)$ hydrothermally treated at 480 °C *(blue)*, (b) Pawley refinement against observed powder XRD data for κ-Ga_2O_3 and ε-Ga_2O_3 obtained from a hydrothermal decomposition of $Ga_5O_7(OH)$, λ = 1.5406 Å.

Table 4.7 Refined lattice parameters for a mixture of ε-Ga_2O_3, κ-Ga_2O_3 and β-Ga_2O_3.

Polymorph	*a*	*b*	*c*	*β*	Space group
β-Ga_2O_3	11.960(9)	3.0333(12)	5.793(3)	103.81(6)	$C2/m$
κ-Ga_2O_3	5.0363(3)	8.6793(6)	9.2741(5)	90	$Pna2_1$
ε-Ga_2O_3	2.90074(15)	2.90074(15)	9.2786(9)	90	$P6_3mc$

4.5.5 Thermal decomposition of $Ga_{5-x}Al_xO_7(OH)$

The mixed metal $Ga_{5-x}Al_xO_7(OH)$ phases also decompose into mixtures of epsilon and kappa polymorphs (Figure 4.22(a)), but their decomposition materials are too poorly crystalline for Rietveld analysis of the Bragg scattering. The temperature required to dehydrate $Ga_{5-x}Al_xO_7(OH)$ increases slightly with higher aluminium substitution, as was the case for the aluminium substituted gallium oxide spinels.

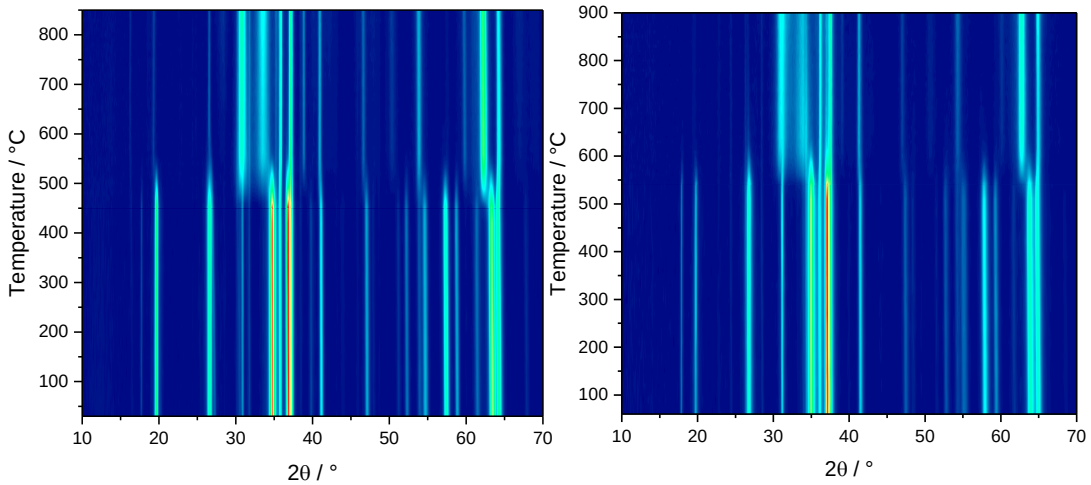

Figure 4.22 Thermodiffractometry of *(left)* $Ga_{4.5}Al_{0.5}O_7(OH)$, and *(right)* $Ga_{3.5}Al_{1.5}O_7(OH)$ which decomposes at a higher temperature.

A Pawley refinement of a sample of $Ga_{3.5}Al_{1.5}O_7(OH)$ fired to 900 °C (Figure 4.23) provided refined lattice parameters for the ε-$Ga_{1.4}Al_{0.6}O_3$: a = 2.8617(18) Å, c = 9.179(6) Å, space group $P6_3mc$, *cf.* ε-Ga_2O_3 a = 2.90074(15) Å, c = 9.2786(9) Å. The decrease in the lattice parameters is evidence for Al^{3+} incorporation as opposed to phase separating into binary oxides.

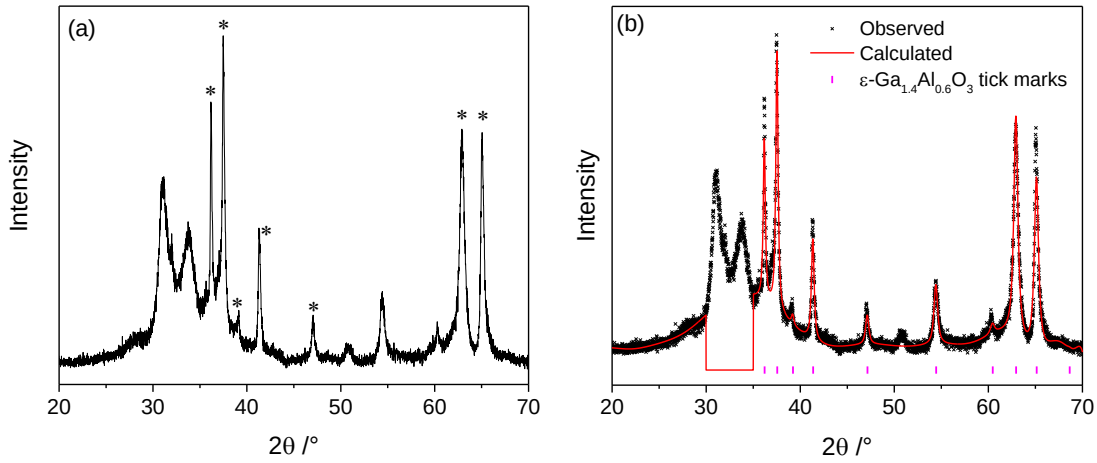

Figure 4.23 (a) Measured data for $Ga_{3.5}Al_{1.5}O_7(OH)$ after heating to 900 °C forming ε and κ-$Ga_{2-x}Al_xO_3$ phases (*) denotes ε phase, (b) Pawley refinement to measured data for ε-$Ga_{2-x}Al_xO_3$, the region 30-35 °2θ was not calculated.

4.6 High temperature polymorphs of $(Ga,Al)_2O_3$

4.6.1 α-$Ga_{0.2}Al_{1.8}O_3$

4.6.1.1 Synthesis

Typically, 0.2 g of γ-$Ga_{0.2}Al_{1.8}O_3$ was placed in an alumina crucible and set inside a box furnace and heated within a temperature range of 1000 °C – 1400 °C for 4 hours. For the sample used in Rietveld analysis a temperature of 1400 °C was used.

4.6.1.2 Rietveld analysis against powder XRD data

It was discussed above in Section 4.3.2.4 that when the 90% Al^{3+} substituted γ-Ga_2O_3 polymorph is heated above 1000 °C it transforms directly into α-$Ga_{0.2}Al_{1.8}O_3$. No prior phase transformation into the beta polymorph occurs first and phase transformation occurs directly into the alpha polymorph (Figure 4.24(a)). Rietveld analysis of a sample of α-$Ga_{0.2}Al_{1.8}O_3$ shows that the occupancy of the metal site for Ga and Al refined to 0.09 and 0.91 respectively indicating around 9% gallium in agreement with what is expected (Figure 4.24(b)). ^{27}Al MAS NMR is consistent with the presence of only 6-coordinate Al^{3+} in this material (Figure 4.25).

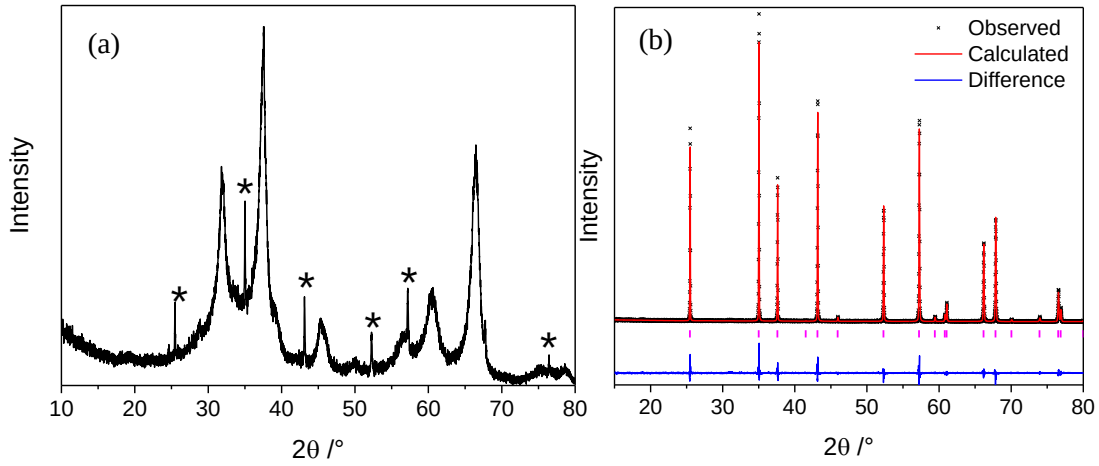

Figure 4.24 (a) 90% Al^{3+} substituted γ-Ga_2O_3 fired at 900 °C showing formation of the corundum phase (denoted *) from the spinel, (b) Rietveld plot of α-$Ga_{0.2}Al_{1.8}O_3$ against X-ray diffraction data (λ = 1.4506 Å).

Table 4.8 Refined crystal parameters for α-$Ga_{0.2}Al_{1.8}O_3$. Lattice parameters a = 4.78281(5) Å, c = 13.04096(15) Å, space group $R\bar{3}cH$. Rp = 12.5%, wRp = 19.0%, GoF = 1.247.

Atom	Wyckoff site	x	y	z	Occupancy	Beq / Å^2
Ga	12c	0	0	0.35289(8)	0.09(6)	0.22(5)
Al	12c	0	0	0.35289(8)	0.91(6)	0.22(5)
O	18e	0.3057(3)	0	0.25	1.0	0.22

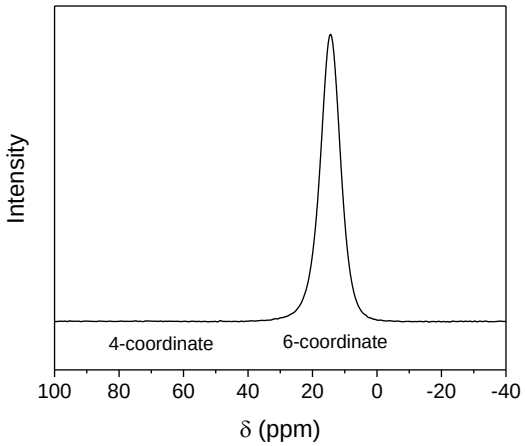

Figure 4.25 ^{27}Al MAS NMR spectrum of α-$Ga_{0.2}Al_{1.8}O_3$, 14.1 T, 20 kHz MAS, 2048 transients, 0.5 s recycle delay, 0.1 μs excitation pulse

At higher levels of gallium incorporation, such as 15% (Figure 4.26), only a mixed phase of beta and alpha is obtained, and this agrees with some literature work regarding this composition.[27]

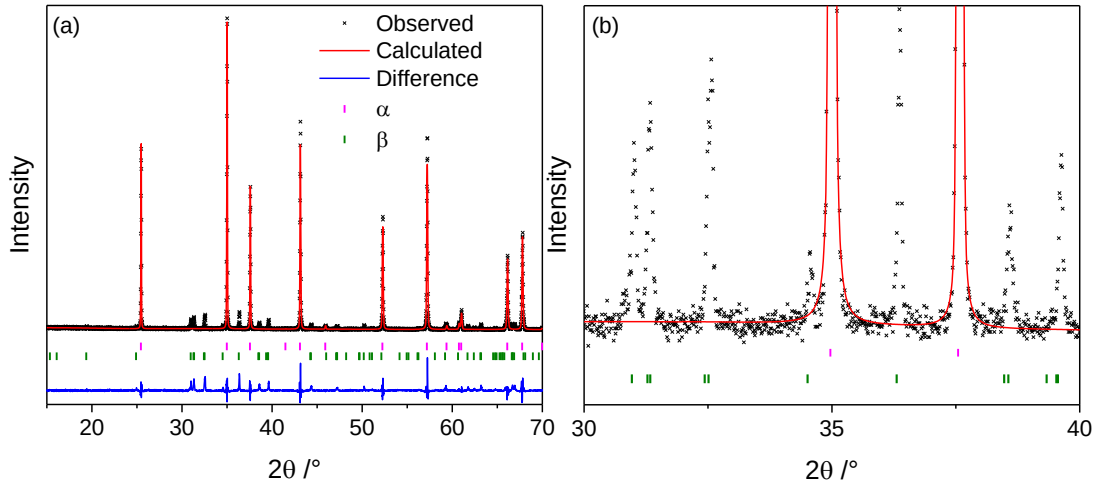

Figure 4.26 (a) Rietveld fit to a sample of 85% Al^{3+} substituted γ-Ga_2O_3 fired to 1400 °C, (b) close-up of Rietveld fit showing unfitted intensity for beta phase reflections.

A higher concentration of Al^{3+} in the spinels required a higher temperature to bring about its transformation into the beta polymorph. This is in contrast to the alpha polymorph where the spinel transforms into the corundum structure-type at a temperature of 1000 °C.

That the alpha phase forms only when ~10% of the material is gallium containing is likely a consequence of the tetrahedral preference of gallium which is accommodated in the beta polymorph. Corundum-type α-$Ga_{0.2}Al_{1.8}O_3$ contains only one metal site with octahedral coordination. It is possible to synthesise the alpha corundum type polymorph with higher amounts of gallium (25-100%), which has been described in the literature by first synthesising amorphous diaspore gels and then gently firing them at 150 °C. These materials, as would be expected, are metastable and decompose above 600 °C.[24]

4.6.2 β-$Ga_{2-x}Al_xO_3$

Section 4.3.2.4 showed that the mixed-metal beta polymorph is readily accessible by heating the mixed metal spinels and that higher temperatures are required for phase transformation with the spinels containing higher aluminium content.

4.6.2.1 Synthesis

0.2 g of γ-$Ga_{2-x}Al_xO_3$ was placed in an alumina crucible and placed inside a box furnace and heated to a temperature within the range (1000 – 1500 °C) for 4 hours and allowed to cool naturally to room temperature.

For the materials used in the Rietveld refinement study all spinels were subjected to a temperature of 1400 °C for 4 hours to produce highly crystalline oxides. Two further samples were prepared containing $x = 0.6$ and $x = 1$ by firing to 1200 °C to compare against the materials prepared at 1400 °C.

4.6.2.2 Powder X-ray diffraction

Phase pure β-$Ga_{2-x}Al_xO_3$ was obtained for samples with a $0 \leq x \leq 1.3$. Above $x = 1.3$ there was always formation of some α-$Ga_{2-x}Al_xO_3$

Rietveld refinement against powder XRD data showed that a good fit to β-$Ga_{2-x}Al_xO_3$ was obtained throughout the range of $0 \leq x \leq 1.3$ (Figure 4.27). All profiles show sharp and intense reflections indicative of highly crystalline material. No other crystalline phases were observed during the refinement indicating the purity of the materials.

Two constraints were placed on the refinement: i) the total site occupancy was fixed at 1.0 to maintain the charge balance against the oxide, ii) refinements were fixed to maintain the intended Al:Ga ratio from the reaction.

Refinement statistics for all samples can be found in Appendix A; select tables of results are provided here for the purpose of discussion (Tables 4.9-4.12)

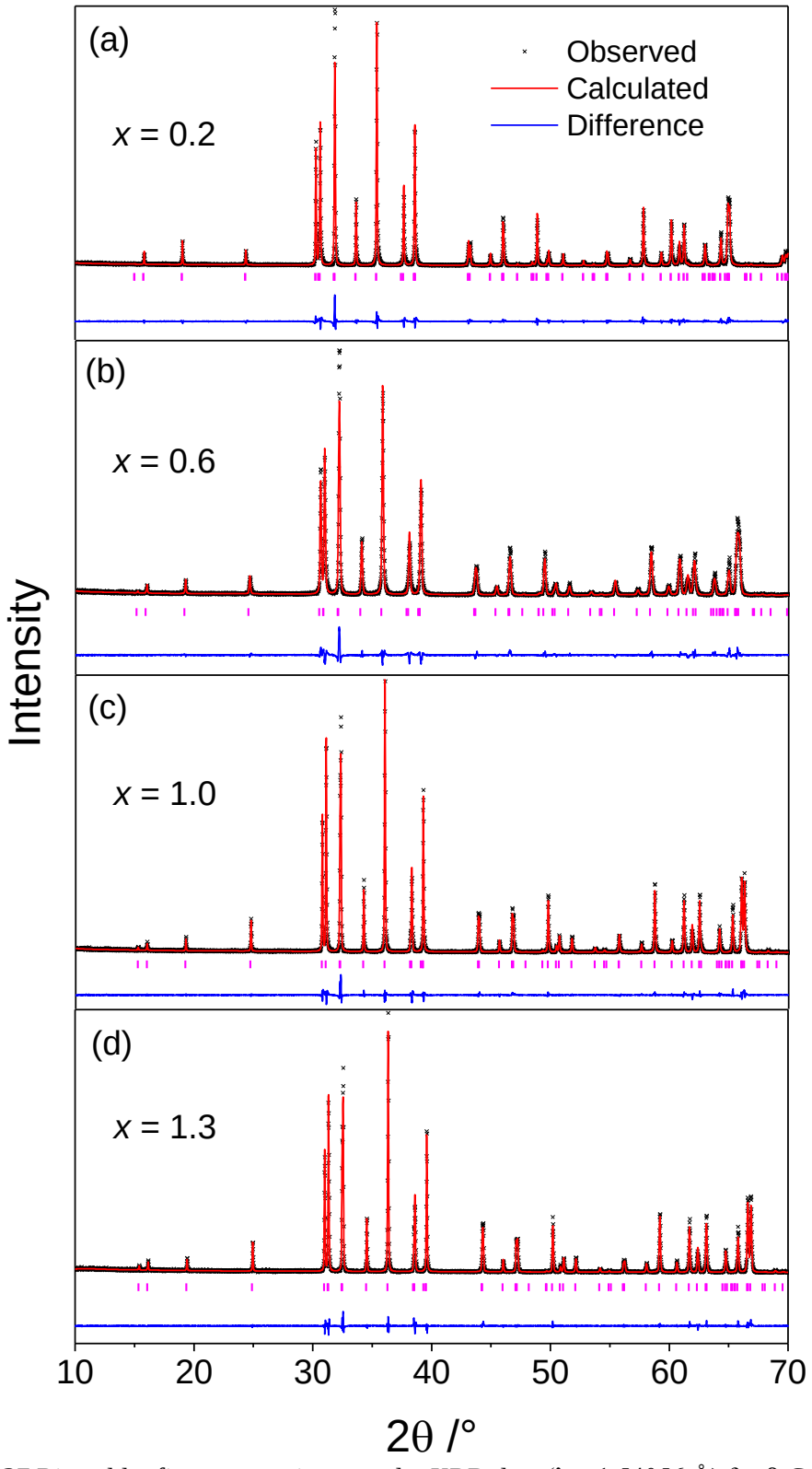

Figure 4.27 Rietveld refinement against powder XRD data (λ = 1.54056 Å) for β-$Ga_{2-x}Al_xO_3$ throughout the range of $0 \leq x \leq 1.3$.

Table 4.9 Refined crystal parameters for β-$Ga_{1.8}Al_{0.2}O_3$ a = 12.17969(16) Å, b = 3.02652(4) Å, c = 5.79034(8) Å, β = 103.8996(11) °, Space group $C2/m$, Rp = 15.1%, wRp = 21.6%

Atom	Wyckoff site	*x*	*y*	*z*	Occupancy	Beq / Å^2
Ga1	4i	0.09020(19)	0	-0.2068(5)	0.923(7)	0.20(11)
Al1	4i	0.09020(19)	0	-0.2068(5)	0.071(7)	0.20(11)
Ga2	4i	0.34139(17)	0	-0.3129(4)	0.871(7)	0.75(13)
Al2	4i	0.34139(17)	0	-0.3129(4)	0.129(7)	0.75(13)
O1	4i	0.1619(7)	0	0.107(2)	1	0.2(3)
O2	4i	0.4963(7)	0	0.2551(12)	1	0.2(3)
O3	4i	0.8277(6)	0	0.425(2)	1	0.3(3)

Table 4.10 Refined crystal parameters for β-$Ga_{1.4}Al_{0.6}O_3$ a = 12.0711(2) Å, b = 2.99309(5) Å, c = 5.74510(11) Å, β = 103.9722(16) °, Space group $C2/m$, Rp = 13.7%, wRp = 17.7%

Atom	Wyckoff site	*x*	*y*	*z*	Occupancy	Beq / Å^2
Ga1	4i	0.09149(19)	0	-0.2059(4)	0.788(5)	0.77(9)
Al1	4i	0.09149(19)	0	-0.2059(4)	0.212(5)	0.77(9)
Ga2	4i	0.34206(16)	0	-0.3125(4)	0.612(5)	0.6(1)
Al2	4i	0.34206(16)	0	-0.3125(4)	0.388(5)	0.6(1)
O1	4i	0.1607(5)	0	0.1120(16)	1	0.2(19)
O2	4i	0.4971(5)	0	0.2581(9)	1	0.2(19)
O3	4i	0.8273(5)	0	0.4262(17)	1	0.2(19)

Table 4.11 Refined crystal parameters for β-$Ga_{1.0}Al_{1.0}O_3$ a = 11.99483(11) Å, b = 2.97101(25) Å, c = 5.71499(5) Å, β = 104.0448(7) °, Space group $C2/m$, Rp = 11.1%, wRp = 15.1%

Atom	Wyckoff site	*x*	*y*	*z*	Occupancy	Beq / Å^2
Ga1	4i	0.09117(14)	0	-0.2047(3)	0.618(3)	0.54(6)
Al1	4i	0.09117(14)	0	-0.2047(3)	0.382(3)	0.54(6)
Ga2	4i	0.34169(14)	0	-0.3139(3)	0.382(3)	0.52(8)
Al2	4i	0.34169(14)	0	-0.3139(3)	0.618(3)	0.52(8)
O1	4i	0.1623(4)	0	0.108(1)	1	0.2(13)
O2	4i	0.4967(4)	0	0.2570(7)	1	0.2(14)
O3	4i	0.8261(4)	0	0.433(1)	1	0.2(13)

Table 4.12 Refined crystal parameters for β-$Ga_{0.7}Al_{1.3}O_3$, a = 11.90851(10) Å, b = 2.94608(3) Å, c = 5.67840(5) Å, β = 104.0810(8) °, Space group $C2/m$, Rp = 11.4%, wRp = 15.5%

Atom	Wyckoff site	*x*	*y*	*z*	Occupancy	Beq / Å^2
Ga1	4i	0.0907(14)	0	-0.2052(3)	0.463(3)	0.73(7)
Al1	4i	0.0907(14)	0	-0.2052(3)	0.537(3)	0.73(7)
Ga2	4i	0.31483(14)	0	-0.3150(3)	0.237(3)	0.64(8)
Al2	4i	0.31483(14)	0	-0.3150(3)	0.763(3)	0.64(8)
O1	4i	0.1614(3)	0	0.1098(9)	1	0.8
O2	4i	0.4970(4)	0	0.2580(6)	1	0.57(4)
O3	4i	0.8268(3)	0	0.4315(9)	1	0.47(9)

The change in the cell volume upon increasing aluminium content follows a linear relationship obeying Vergard's law (Figure 4.28). A decrease in the cell parameters with increasing aluminium content is expected owing to the smaller size of the Al^{3+} cation, whilst there is also an increase in the β bond angle.

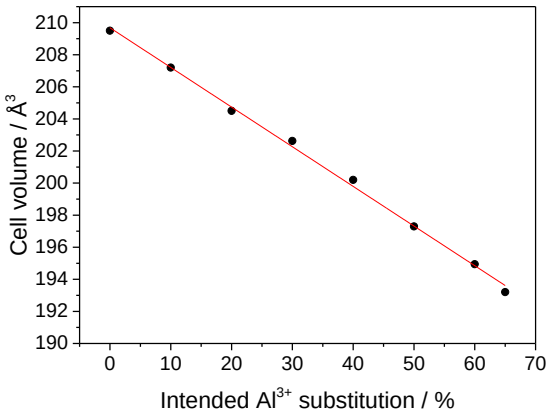

Figure 4.28 Plot of cell volume against intended aluminium substitution showing a linear decrease in accordance with Vergard's law.

Refinements show that for all samples there is a significant amount of aluminium on the tetrahedral site. The spinel and tohdite polymorphs also contain tetrahedral sites but it was found in these polymorphs that Al^{3+} selectively occupied octahedral coordination due to the tetrahedral preference of Ga^{3+}. This is not observed in the beta polymorph. The sample containing 10% aluminium also showed a significant presence of tetrahedral Al^{3+}. In this sample, it might be expected that owing to gallium being the predominant metal that it would occupy the tetrahedral site exclusively forcing the small amount of aluminium onto the octahedral site but this is not observed by the Rietveld analysis. The tetrahedral:octahedral ratio of aluminium in the beta polymorph

remains close to 1:2 but shows a small increase in tetrahedral occupation with increasing aluminium substitution over the values of x between x = 0.2 to x = 1.3 (Figure 4.29). There is also very little difference between samples fired at 1200 °C and 1400 °C (Table 4.14) implying that the tetrahedral occupation occurs immediately upon phase transformation rather than forming an initial beta polymorph with a low tetrahedral aluminium site occupancy followed by rearrangement at a higher temperature.

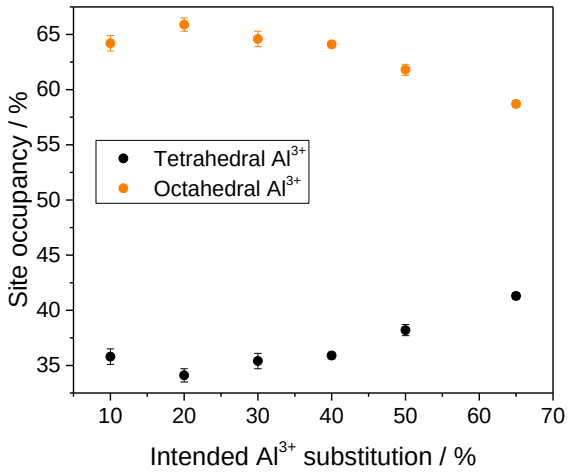

Figure 4.29 Change in the Al^{3+} tetrahedral and octahedral site occupancy with increasing Al^{3+} substitution in β-$Ga_{2-x}Al_xO_3$.

As would be expected the average bond length becomes smaller with increasing aluminium substitution (Table 4.13). Pure β-Ga_2O_3 shows a significant octahedral distortion which is present in all aluminium substituted beta polymorphs in this work (Figure 4.30). The angles around the tetrahedron fall in the range of ~104 – 120 ° for all samples indicating the presence of significant tetrahedral distortion too, something also observed in the single crystal reinvestigation of β-Ga_2O_3 by Albertsson *et al.*[15]

Table 4.13 Change in tetrahedral and octahedral bond length with increasing Al^{3+} substitution.

Al^{3+} substitution / %	**Tetrahedral average bond length / Å**	**Octahedral average bond length / Å**
0 [15]	1.8303	2.0123
10	1.8162	2.0051
30	1.8094	1.9769
50	1.8034	1.9587
65	1.7892	1.9440

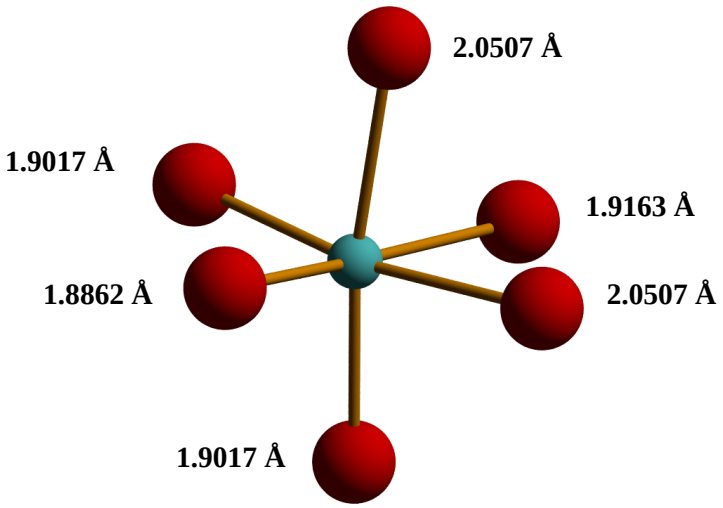

Figure 4.30 Distorted (Ga,Al)-O octahedra in β-$Ga_{1.0}Al_{1.0}O_3$ with bond lengths labelled.

4.6.2.3 ^{27}Al MAS NMR

^{27}Al MAS NMR was performed on all samples used throughout the range $0 \leq x \leq 1.3$ (Figure 4.31). A clear signal over the range 0-20 ppm is characteristic of 6-coordinate Al^{3+}, and the signal between 60-80 ppm is characteristic of 4-coordinate Al^{3+}. A shift of the 6-coordinate signal to lower ppm occurs with increasing Al^{3+} content is likely a result of nearest neighbour effects. No obvious shift in the 4-coordinate signal is observed with increasing Al^{3+} content. The NMR results show that both tetrahedral and octahedral sites are occupied by aluminium in these materials showing that although an octahedral preference is observed the occupancy ratio of tetrahedral:octahedral is very similar to that obtained through Rietveld analysis of the powder XRD data.

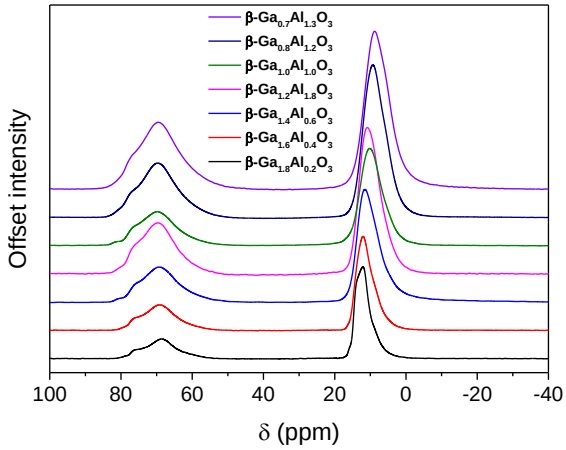

Figure 4.31 ^{27}Al MAS NMR spectra of β-$Ga_{2-x}Al_xO_3$ solid solutions, normalised to equal 6-coordinate peaks height. 14.1 T, 20 kHz MAS, 4096 (10% Al), 2048 (20%, 30%, 40% Al), 1024 (50%, 60%, 65% Al) transients, 3 s recycle delay, 0.1 μs excitation pulse.

The integrated intensity of the tetrahedral site shows a linear increase (and therefore a linear decrease in the octahedral site occupation) as the intended Al^{3+} substitution increases. A comparison of the site occupancies obtained through Rietveld analysis of PXRD data and ^{27}Al MAS NMR are shown Figure 4.32 and Table 4.14.

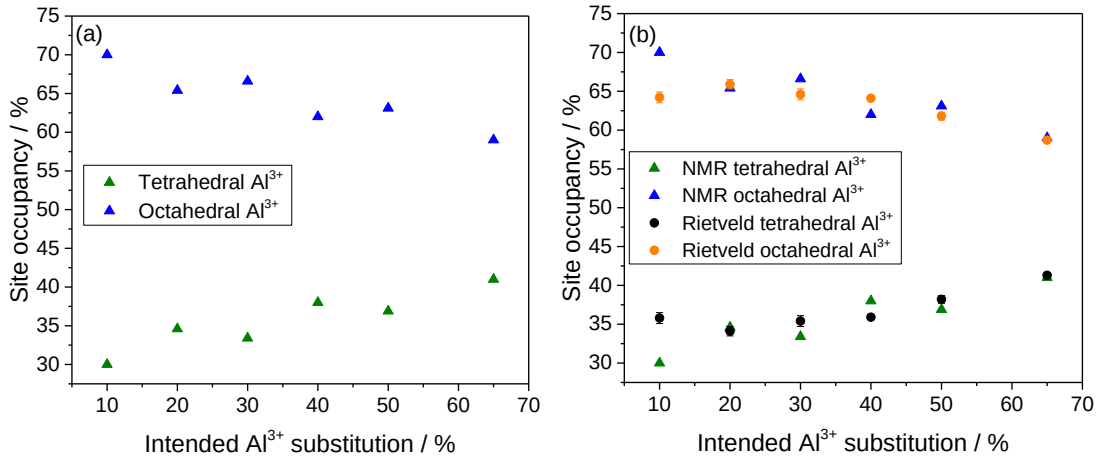

Figure 4.32 (a) ^{27}Al MAS NMR plot of Al^{3+} site occupancy changes in β-$Ga_{2-x}Al_xO_3$, (b) Al^{3+} site occupancy comparison between the ^{27}Al MAS NMR and Rietveld analysis of XRD data.

Table 4.14 Comparison in change in tetrahedral and octahedral occupation of Al^{3+} and Ga^{3+} in β-$Ga_{2-x}Al_xO_3$ by Rietveld analysis of powder XRD data and ^{27}Al MAS NMR.

Sample	Rietveld		^{27}Al NMR	
	Al^{3+} Occupancy		Al^{3+} Occupancy	
	Tet / %	Oct / %	Tet / %	Oct / %
β-$Ga_{1.8}Al_{0.2}O_3$ (1400 °C)	35.8	64.2	30.0	70.0
β-$Ga_{1.6}Al_{0.4}O_3$ (1400 °C)	34.1	65.9	34.6	65.4
β-$Ga_{1.4}Al_{0.6}O_3$ (1200 °C)	35.1	64.9	-	-
β-$Ga_{1.4}Al_{0.6}O_3$ (1400 °C)	35.4	64.6	33.4	66.6
β-$Ga_{1.2}Al_{0.8}O_3$ (1400 °C)	35.9	64.1	38.0	62.0
β-$Ga_{1.0}Al_{1.0}O_3$ (1200 °C)	39.8	60.2	-	-
β-$Ga_{1.0}Al_{1.0}O_3$ (1400 °C)	38.2	61.8	36.9	63.1
β-$Ga_{0.7}Al_{1.3}O_3$ (1400 °C)	41.3	58.7	41.0	59.0

The maximum amount of Al^{3+} that can be incorporated into the β-Ga_2O_3 structure, when spinel precursors are fired at high temperature, appears to fall in the range of 65%-70%. A recent study found that a solution combustion synthesis of the same material could incorporate up to 40% Al^{3+}.[69]

A spinel sample containing 70% Al^{3+} substituted γ-Ga_2O_3 was fired at 1200 °C, 1400 °C and finally 1500 °C. Figure 4.33(a) shows that a mixture of both α and β-$Ga_{2-x}Al_xO_3$ forms but that high temperatures favours formation of the beta polymorph. Even when heated to 1500 °C for 4 hours there is still the presence of a small amount of α-Ga_2O_3. The phase fraction was estimated by Rietveld analysis (Figure 4.33(b)). It is noted that at 1500 °C there is the possibility of the mixed-metal material reacting with the alumina crucible.

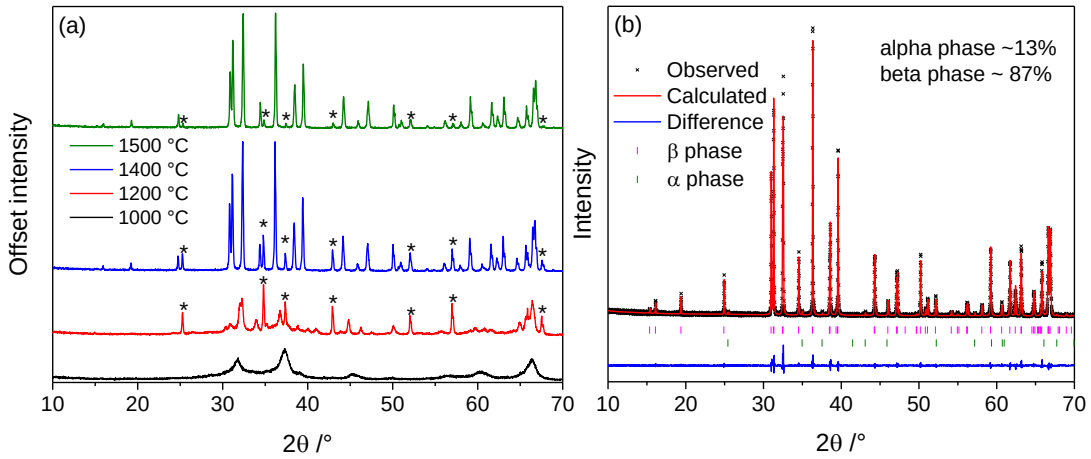

Figure 4.33 (a) γ-$Ga_{0.6}Al_{1.4}O_3$ fired at increasing temperature * denotes α-corundum phase, (b) estimation of phase fraction by Rietveld refinement results of α and β-$Ga_{1.5}Al_{0.5}O_3$ prepared from firing the corresponding spinel at 1500 °C. λ = 1.54056 Å

4.7 Catalysis

4.7.1 Diesel oxidation

Three gallium oxides were selected for study in diesel oxidation catalysis as supports and one aluminium oxide catalyst, a catalyst support typical for diesel oxidation catalysis,[70,71] was also tested to compare against the gallium oxide catalysts. Table 4.15 lists the catalysts and their respective surface areas. Palladium was deposited on the surface of each catalysts by the wet impregnation method. 0.5% Pd was used on alumina whilst 0.27% Pd was used on the gallia catalysts maintaining the same molar weight percent of palladium. TEM imaging (Figure 4.34) shows the morphology of each catalyst.

Table 4.15 Details of each catalyst, its surface area and method of preparation.

Catalyst	Coordination	Surface area / m^2g^{-1}	Preparation
0.5% Pd / γ-Al_2O_3	1:2 tet.:oct.	>150	Industry standard
0.27% Pd / α-Ga_2O_3	Oct. only	24	Heating amorphous GaOOH* at 400 C for 4 hours
0.27% Pd / β-Ga_2O_3	1:1 tet.:oct.	15	Heating amorphous GaOOH at 1000 C for 4 hours
0.27% Pd / γ-Ga_2O_3	1:2 tet:oct.	70	Solvothermal oxidation of Ga

* GaOOH was prepared by reaction of aqueous $Ga(NO_3)_3 \cdot 9H_2O$ with conc. ammonia solution.

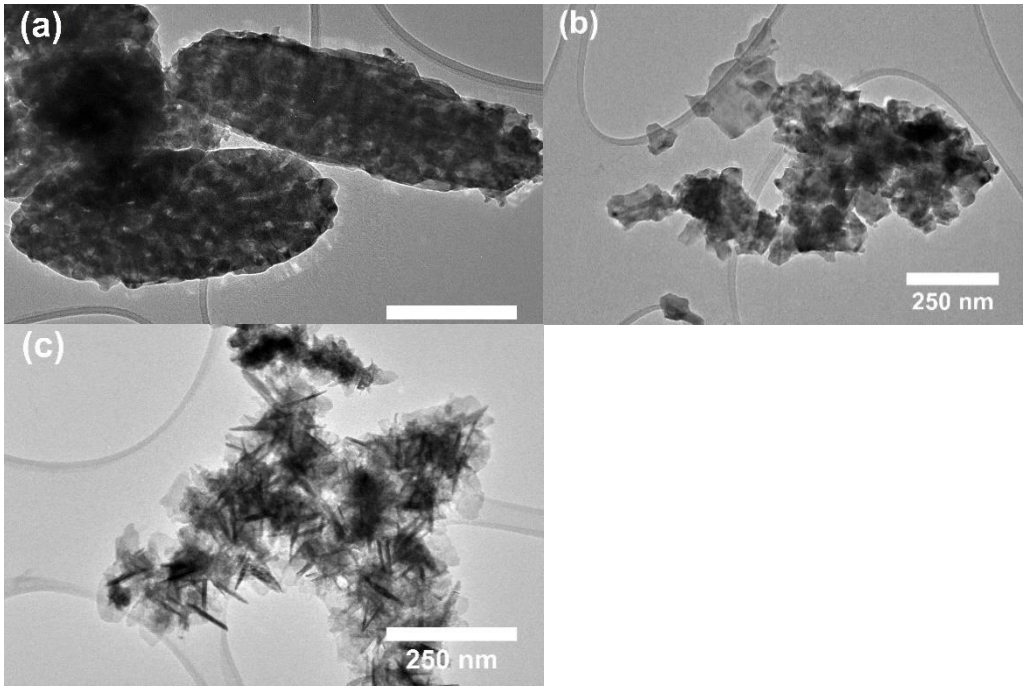

Figure 4.34 TEM images of gallium oxide catalysts (a) alpha, (b) beta, (c) gamma.

After the wet impregnation of palladium each catalyst was subjected to a 500 °C heat treatment in order to dry the catalyst. The catalysts were then pelletised to within a particle range of 255-355 μm prior to testing. A portion of each catalyst was fired to 750 °C for 10 hours to mimic a catalyst part-way through its performance lifetime. The catalysts were then loaded onto the testing rig one at a time and heated to 500 °C whilst a gas mixture (Table 4.16) was passed over the catalyst. The effluent gases were monitored by FTIR.

Table 4.16 Gas mixture used in the diesel 4HC catalytic testing. The flow rate was 4 litres per minute.

Diesel 4HC Gas Mixture	Concentration
CO	500 ppm
NO	150 ppm
C_3H_6	37 ppm
CH_4	40 ppm
Decane	26 ppm
Toluene	10 ppm
H_2O	5%
CO_2	5%
O_2	12-13%

4.7.1.1 CO oxidation

γ-Al_2O_3 outperforms all polymorphs of the Ga_2O_3 materials as catalyst supports in terms of having a lower light-off temperature (the temperature at which catalytic reactions are initiated within a catalytic convertor; here the reactor), and the T_{50} (the temperature at which 50% conversion has been achieved) (Figure 4.35). All gallium oxide supports show a higher light-off temperature and reach the maximum conversion at a higher temperature. The alpha polymorph has better activity than the beta polymorph which has better activity than the gamma polymorph. This is surprising given that the gamma polymorph is not only structurally analogous to the alumina standard support used in this work, but it also has the highest surface area of all three gallium oxide supports. Ageing the catalysts shows a slightly improved oxidation function in all three catalysts except for the beta polymorph where a marked increase in light-off temperature is observed trailing the performance of the gamma polymorph. It is important to note that ageing the gamma polymorph at 750 °C for 10 hours will have a phase transformation into a poorly crystalline beta polymorph. The light-off and T_{50} values for all catalysts is provided in Table 4.17.

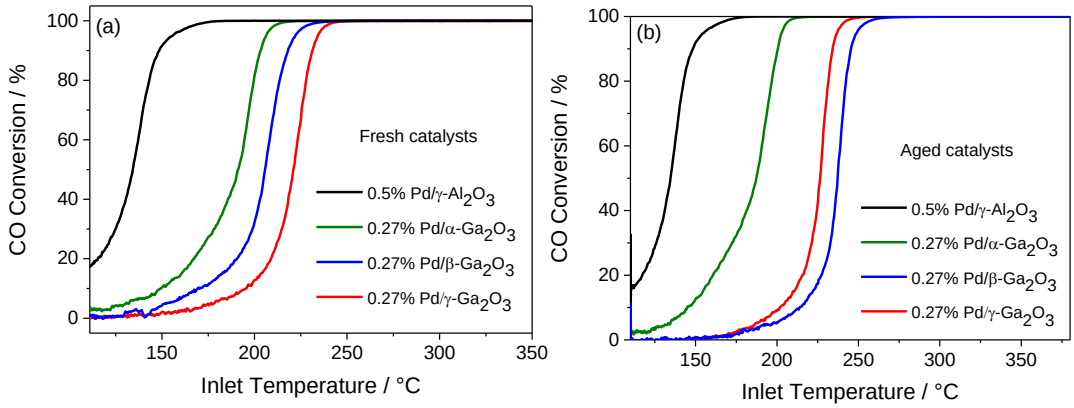

Figure 4.35 (a) CO oxidation achieved by all fresh catalysts and (b) CO oxidation by all aged catalysts

Table 4.17 CO conversion temperatures for all catalysts.

Support	Light-off temperature / °C	T_{50} / °C
γ-Al_2O_3 (Fresh)	< 111	134
γ-Al_2O_3 (Aged)	< 111	135
α-Ga_2O_3 (Fresh)	129	191
α-Ga_2O_3 (Aged)	125	187
β-Ga_2O_3 (Fresh)	148	205
β-Ga_2O_3 (Aged)	170	238
γ-Ga_2O_3 (Fresh)	170	220
γ-Ga_2O_3 (Aged)	170	226

4.7.1.2 Total hydrocarbon conversion

Total hydrocarbon conversion, (*i.e.* consisting of both the gas and liquid hydrocarbon components), is very similar to the activity observed in the CO conversion. γ-Al_2O_3 outperforms all Ga_2O_3 polymorphs with respect to the light-off and T_{50}, and the Ga_2O_3 polymorphs show better activity in the order α > β > γ (Figure 4.36). Though the light-off temperature is much lower for the alumina catalyst its activity for THC conversion only gradually increases initially before increasing at a higher rate around 200 °C. This is in contrast to the gallium oxide polymorphs which show a faster conversion rate similar to the CO conversion and results in the alpha gallium oxide polymorph having a T_{50} very similar to the alumina catalyst and their conversion activity above 200 °C is comparable reaching a maximum conversion at almost the same temperature (Table 4.18). Ageing the catalysts shows that very little has changed in the activity of the catalysts with the exception of the beta polymorph which, as for the CO conversion, has become less active lighting off at a higher temperature.

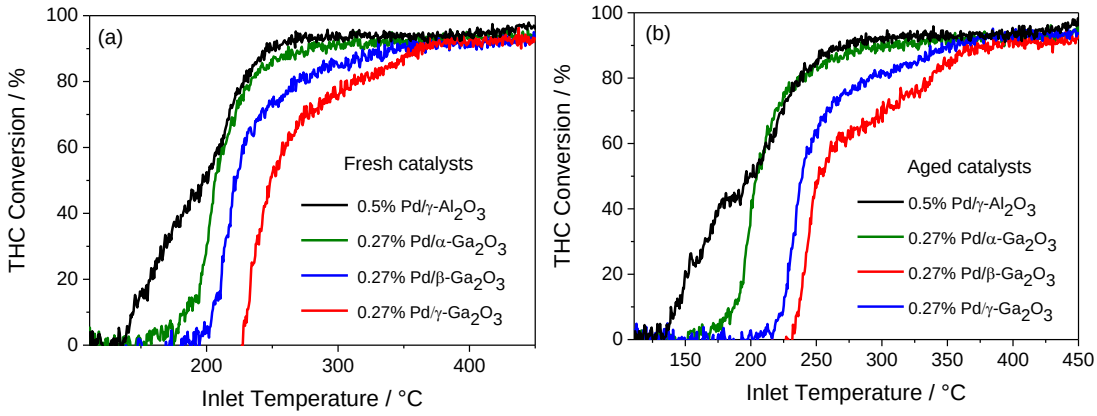

Figure 4.36 (a) THC conversion by fresh catalysts and (b) THC conversion by aged catalysts.

Table 4.18 THC conversion temperatures for all catalysts.

Catalyst	Light-off temperature / °C	T_{50} / °C
γ-Al_2O_3 (Fresh)	137	198
γ-Al_2O_3 (Aged)	135	200
α-Ga_2O_3 (Fresh)	159	205
α-Ga_2O_3 (Aged)	163	205
β-Ga_2O_3 (Fresh)	194	222
β-Ga_2O_3 (Aged)	215	250
γ-Ga_2O_3 (Fresh)	<227	249
γ-Ga_2O_3 (Aged)	<230	239

4.7.1.3 NO oxidation

In the fresh samples, a similar trend is observed but the beta polymorph has greater activity than the alpha polymorph (Figure 4.37(a)). No catalyst is particularly effective in NO oxidation which is to be expected with a palladium based catalyst.[70] All catalysts reach a maximum NO conversion between 400 - 450 °C before the activity begins to decrease. The palladium supported gamma gallia polymorph is notably ineffective again this time as a catalyst for oxidation of NO. Ageing the catalysts serves to enhance the activity of the alpha and gamma polymorphs whilst severely inhibiting the activity of the beta polymorph (Figure 4.37(b)).

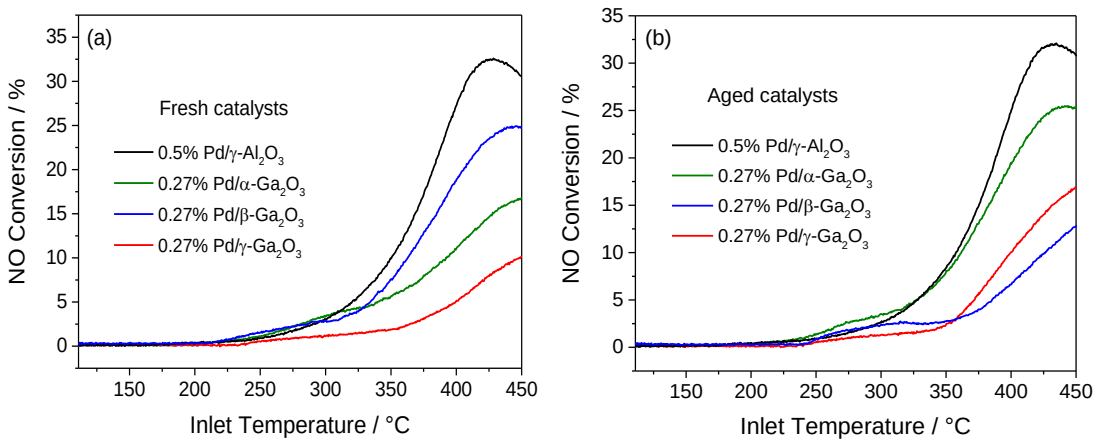

Figure 4.37 (a) NO oxidation by fresh catalysts, (b) NO oxidation by aged catalysts.

That all Ga_2O_3 polymorphs are poorer supports for diesel oxidation is unclear. However, it is widely known that formation of gallium-palladium intermetallic compounds occurs readily especially under gases[46,72] such as CO observed here in the diesel oxidation tests. Given that the palladium present on these catalysts is in such a small amount it is unlikely that the formation of intermetallic species would be detected and indeed no crystalline intermetallic compounds were detected by XRD, TEM or X-ray photoelectron spectroscopy (XPS), but its presence could make the materials less effective for the catalysis reactions tested here given that Pd^{2+} is more catalytically active in diesel oxidation than metallic Pd, as found in the alloy.

During the course of this work it was found that the intermetallic species $GaPd_2$ could be synthesised via solvothermal reaction of either Ga metal, or γ-Ga_2O_3 and $PdCl_2$ in ethanolamine at 240 °C, and was detected as low as 10% Pd in a 1:9 Pd:Ga reaction and was also observed by TEM (Figure 4.38). Given that in the solvothermal reaction palladium can extrude gallium from the oxide it is not unlikely that formation of this species could form upon heating the palladium impregnated gallium oxide catalysts to 500 °C in the presence of the reducing gas CO and therefore be responsible for retarding the catalytic activity of the spinel catalyst.

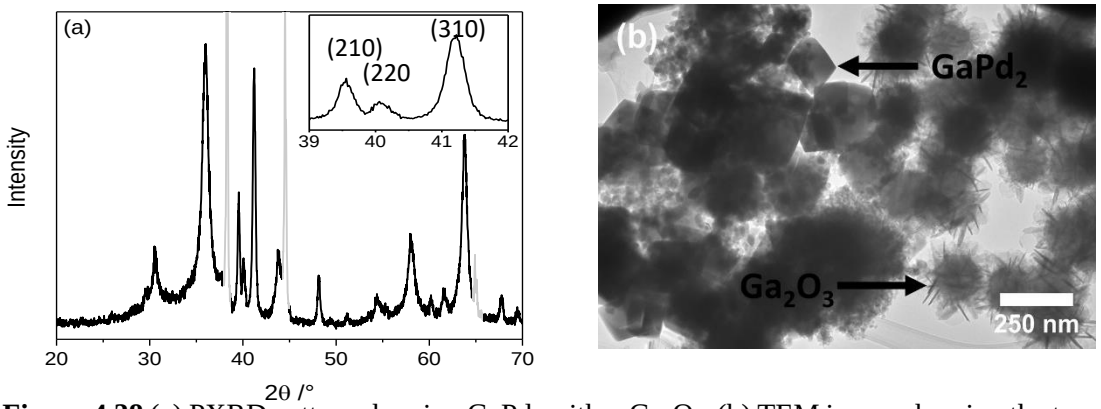

Figure 4.38 (a) PXRD pattern showing $GaPd_2$ with γ-Ga_2O_3, (b) TEM image showing the two distinct particle morphologies: $GaPd_2$ and γ-Ga_2O_3. The inset shows a close-up on $GaPd_2$ reflections. Faded peaks are of the aluminium sample holder.

4.7.2 Semi-hydrogenation of acetylene

Since there is a possibility that the formation of some intermetallic compound had formed by reaction of palladium with the gallium oxide support, some gallium oxides loaded with Pd were tested as catalysts for the semi-hydrogenation of acetylene. There is a growing interest in using $GaPd_2$ supported on Ga_2O_3 by *in situ* reduction in this area of catalysis.[73,74]

$GaPd_2$ as well as other Ga-Pd intermetallic species have received and continue to receive great interest in their potential as catalysts for methanol steam reforming[72,75] and in particular for the semi-hydrogenation of ethylene, having superior activity, stability, and selectivity for ethene over ethane.[76–80] The formation of isolated active sites by the presence of gallium impedes and prevents over-hydrogenation to ethane.[80]

In this work two catalysis experiments were performed:

Experiment 1: An investigation using high surface area γ-Al_2O_3, and γ-Ga_2O_3, which have been pre-reacted with $PdCl_2$, and where the formation of $GaPd_2$ is known to form during the synthesis from Ga_2O_3.

Experiment 2: An investigation using Pd loaded onto low surface area β-Ga_2O_3, β-$Ga_{1.4}Al_{0.6}O_3$ β-$Ga_1Al_1O_3$, and α-Al_2O_3.

4.7.2.1 Experiment 1

4.7.2.1.1 Catalyst synthesis

$GaPd_2$ / gallium oxide catalyst

5 g of γ-Ga_2O_3 and 500 ppm (wt%) of $PdCl_2$ were added to a 100 ml PTFE liner followed by addition of 50 ml ethanolamine. The liner was placed inside a stainless-steel autoclave and placed in a pre-heated fan-assisted oven at 240 °C for 72 hours. After the reaction, the autoclave was cooled naturally to room temperature and the grey coloured solid isolated by vacuum filtration and washed with methanol. The material was dried overnight at 70 °C.

Pd / aluminium oxide catalyst

5 g of γ-Al_2O_3 and 500 ppm (wt%) of $PdCl_2$ were added to a 100 ml PTFE liner followed by addition of 50 ml ethanolamine. The liner was placed inside a stainless-steel autoclave and placed in a pre-heated fan-assisted oven at 240 °C for 72 hours. After the reaction, the autoclave was cooled naturally to room temperature and the grey coloured solid isolated by vacuum filtration and washed with methanol. The material was dried overnight at 70 °C.

4.7.2.1.2 Catalyst preparation

Catalysts were pelletised to within a 250 – 355 μm particle size range prior to testing and approximately 500 mg catalyst was used for each reaction. The catalyst was tested on fixed-bed reactor located inside an oven in order to reach the desired temperature. The catalyst was held inside the reactor between two layers of glass wool. The outlet gases were analysed by gas chromatography.

The catalyst was subjected to an *in situ* pre-reduction step heating at 140 °C with hydrogen. The samples were flushed with nitrogen while cooling to room temperature. Then, the catalyst was tested for acetylene hydrogenation under ethylene rich conditions. The testing conditions are summarised in Table 4.19. The temperature was varied within the range detailed in Table 4.19, with the purpose of obtaining data through the whole range of conversion.

Table 4.19 Testing conditions during experiment 1.

Catalyst mass / mg	Flow of 1% acetylene, 1.1% H_2 in ethylene / ml min^{-1}	Pressure / bar	Oven temperature / °C
500	50	4	20.8 – 144.8

4.7.2.1.3 Results

The experiment showed that the gallium oxide catalyst achieved a higher overall conversion of acetylene than the aluminium oxide (Figure 4.39(a)), but more importantly showed that less ethane was produced compared to the Pd/alumina catalyst (Figure 4.39(b)) suggesting that the Pd/gallia catalyst shows a higher selectivity. The production of ethane with increasing acetylene conversion is also different for both catalysts as alumina shows that a plateau in ethane concentration is reached around 120 °C (when ~50% acetylene conversion is achieved) and then a decrease in ethane concentration is observed whereas the gallium oxide polymorph shows a gradual, linear increase in ethane concentration with increasing acetylene conversion.

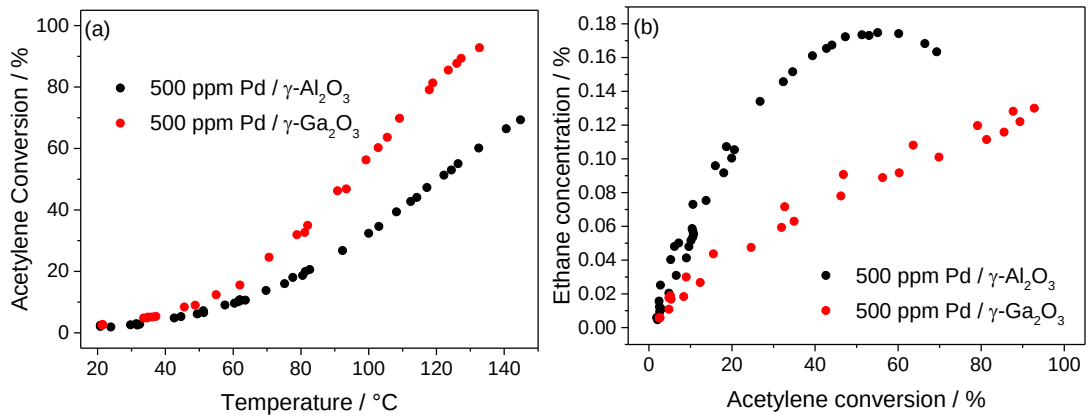

Figure 4.39 (a) acetylene conversion *vs* temperature, (b) ethane concentration *vs* acetylene conversion by both catalysts.

It is worth noting here that use of the high surface area alumina is not standard practice in this area of catalysis as the high surface area polymorph is associated with higher levels of surface bound hydroxyl groups leading to over-hydrogenation of acetylene. Lower surface area polymorphs are desired in acetylene semi-hydrogenation. Experiment 2 explores the catalysis with some lower surface area polymorphs.

4.7.2.2 Experiment 2

4.7.2.2.1 Catalyst synthesis

Pd / β-Ga_2O_3 catalysts

Three gallium oxide containing catalysts were used in this experiment: β-Ga_2O_3, β-$Ga_{1.4}Al_{0.6}O_3$, and β-$Ga_{1.0}Al_{1.0}O_3$. These catalysts were prepared in two steps: the first step was to prepare 5 g of the spinel oxides first by the solvothermal 2-propanol synthesis route detailed in Section 4.3.1.2 and the second step firing at 1400 °C for 4 hours was done to yield highly crystalline, low surface area beta polymorphs. 3500 ppm Pd was loaded onto the surface of each support by wet impregnation maintaining the same mass % Pd on each support.

Pd / α-Al_2O_3 catalyst

The low surface area alpha alumina catalyst was obtained from Johnson Matthey. 3500 ppm was loaded onto the surface of the catalyst by wet impregnation to maintain the same mass % Pd as the gallium oxide catalysts.

4.7.2.2.2 Catalysts preparation

0.1 g of each powdered material was used for each reaction. The catalysts were tested on a fixed bed reactor located inside an oven in order to reach the desired temperature. The catalyst was held inside the reactor between two layers of glass wool. The outlet gases were analysed by gas chromatography.

The catalysts were pre-reduced in the same way as detailed in experiment 1. Then, the catalysts were tested for acetylene hydrogenation under ethylene rich conditions. The testing conditions are summarised in Table 4.20. The temperature was varied within the range detailed in Table 4.20, with the purpose of obtaining data through the whole range of conversion.

Table 4.20 Testing conditions during experiment 2.

Catalyst mass / mg	Flow of 1% acetylene, 1.1% H_2 in ethylene / ml min^{-1}	Pressure / bar	Oven temperature / °C
100	50	4	28.4 – 104.4

4.7.2.2.3 Results

The mixed-metal oxides show a greater overall acetylene conversion than the pure alumina or pure gallia support with the gallium oxide catalyst showing the lowest activity for all catalysts (Figure 4.40(a)). The β-$Ga_{1.0}Al_{1.0}O_3$ catalyst reaches the highest overall conversion and at a lower temperature than the other three catalysts. In terms of how much ethane is produced in the experiment the catalysts are all very similar, though the β-$Ga_{1.0}Al_{1.0}O_3$ catalyst shows the lowest amount of ethane produced between 50-70 °C (Figure 4.40(b)).

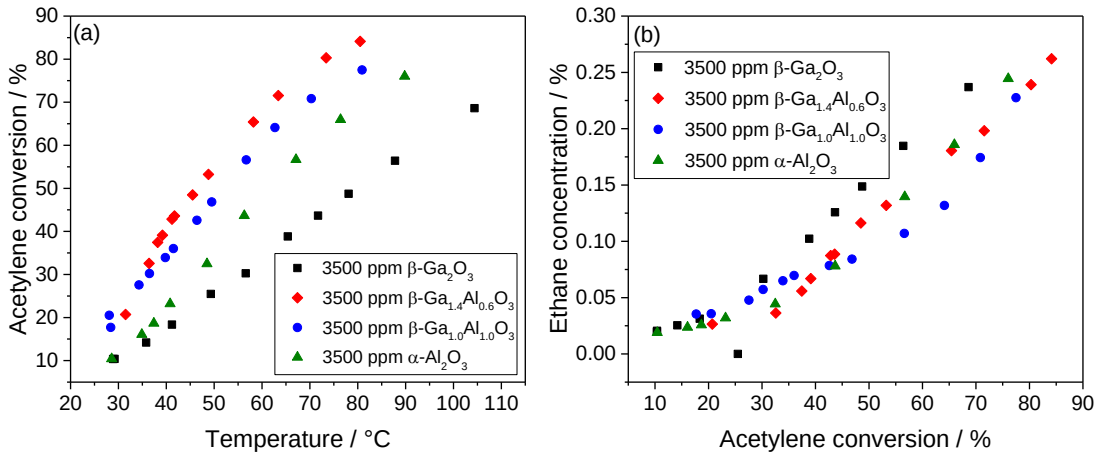

Figure 4.40 (a) acetylene conversion *vs* temperature for all catalysts, (b) selectivity curve showing ethane concentration *vs* acetylene conversion for all catalysts.

Attempts to identify the formation of any $GaPd_2$ by XRD, XPS and electron microscopy were unsuccessful. Infrared spectroscopy analysis of CO chemisorbed on to Pd was used to investigate any differences between the catalysts in an attempt to elucidate any intermetallic species formation. In the alumina-only catalyst no intermetallic species would be expected to form and therefore many IR active modes of CO should be expected including terminal, bridging and tri-coordinated CO on Pd (Table 4.21). IR spectroscopy of the alumina catalyst reveals the presence of all bridging and tri-coordinated CO adsorbed on Pd but very little linearly adsorbed CO

(Figure 4.41(a)). The same is true for both β-$Ga_{1.4}Al_{0.6}O_3$, and β-$Ga_{1.0}Al_{1.0}O_3$ suggesting the presence of only Pd and not $GaPd_2$ on the surface of the catalyst. It would typically be expected that the presence of $GaPd_2$ would lower the intensity of bridged and tri-coordinated adsorbed CO owing to the isolated Pd atoms and show high intensities of the linearly adsorbed CO. Recent work by Föttinger *et al.* has shown that CO adsorption on $GaPd_2$ has a detrimental effect on $GaPd_2$ causing it to degrade within the time of the measurement (60 minutes).[75,81] It is likely that in this work, the formation of any $GaPd_2$ could also have been degraded by the CO experiment: the infrared spectroscopy collection time was ~30 minutes, which could be long enough to degrade any intermetallic Ga-Pd species into their monometallic counterparts. The IR experiment may therefore be inconclusive as to the presence of $GaPd_2$.

Table 4.21 Expected IR CO adsorption bands[82]

CO band	Wavenumber / cm^{-1}
Linear adsorption	2020-2110
Bridge-bonded defective species	1950-2010
Bridge-bonded on (111) terraces	1900-1940
Tri-coordinated CO on (111) terraces	1800-1890

The total intensity for the CO adsorption band is similar in sets of samples with same Pd loading which translates into comparable available Pd sites for CO adsorption thus similar particle size.

From the shift in the band position and similar total area it can be concluded that in the mixed gallium aluminium oxide samples the morphology of the particles is different.

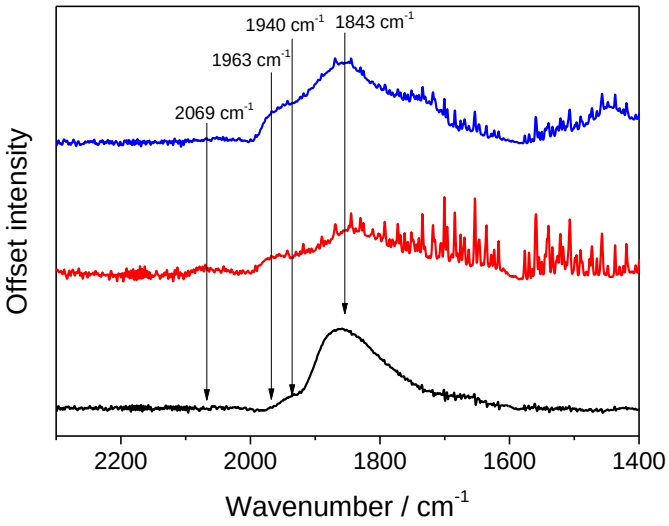

Figure 4.41 IR spectra of CO adsorbed on 3500ppmPd/α-Al_2O_3 *(black)*, 3500ppmPd/β-Ga_2O_3 *(red)*, 3500ppmPd/β-$Ga_1Al_1O_3$ *(blue)*.

In conclusion, there is still lacking evidence for any intermetallic Ga-Pd species forming during the either the diesel oxidation or semi-hydrogenation of acetylene catalysis experiments. However, importantly, the current results suggest that the mixed-metal $(Ga,Al)_2O_3$ oxides show evidence for improvement over the pure alumina or pure gallia catalysts and should be investigated further.

4.8 Conclusions and summary

An investigation into the polymorphism of the system $Ga_{2-x}Al_xO_3$ has been presented and summarised in the scheme below (Figure 4.42).

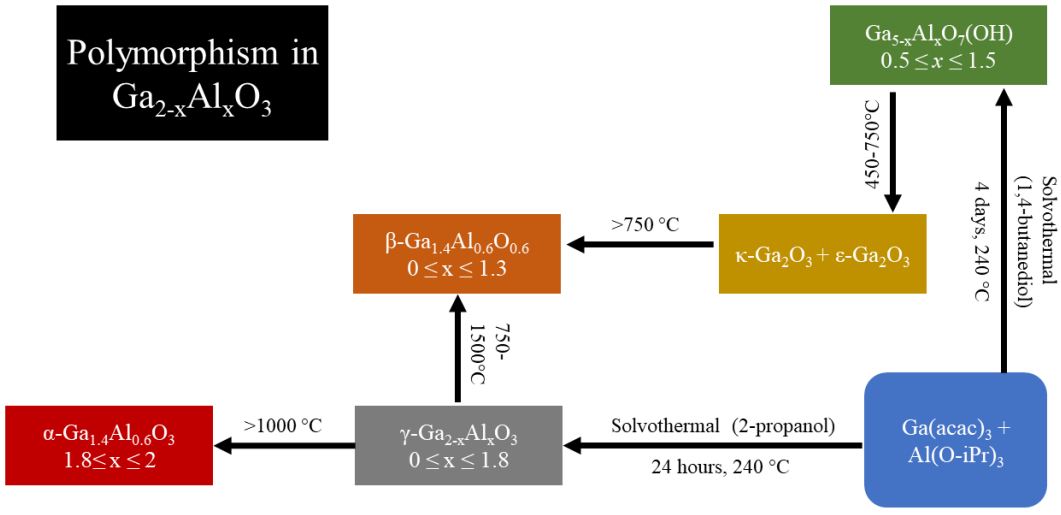

Figure 4.42 Synthesis and interconversion of $Ga_{2-x}Al_xO_3$ polymorphs.

The interconversion of the polymorphs is similar to the interconversion of gallium oxide polymorphs (Figure 4.43). γ-$Ga_{2-x}Al_xO_3$ and $Ga_{5-x}Al_xO_7(OH)$ can be prepared by solvothermal methods as can pure γ-Ga_2O_3 and $Ga_5O_7(OH)$, though different reagents and solvents are required for the oxyhydroxide.

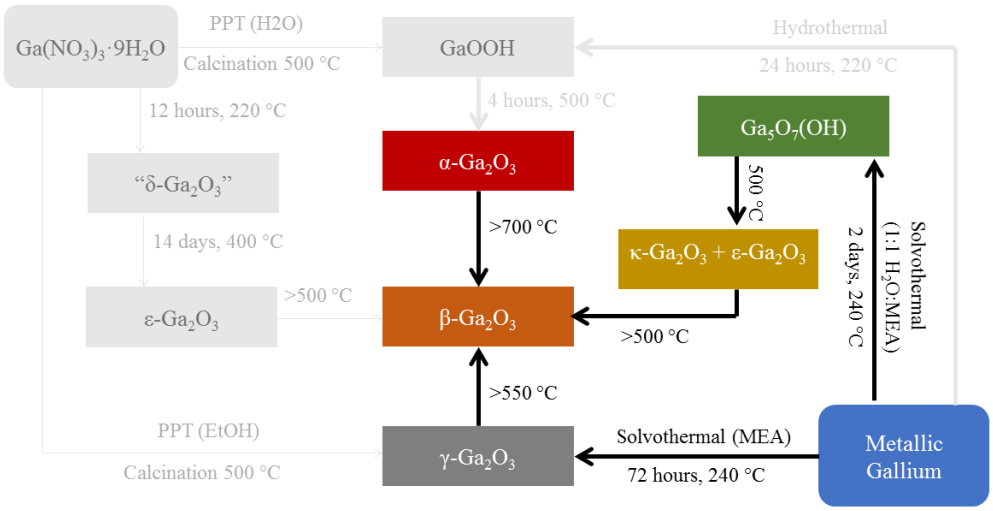

Figure 4.43 Interconversion of gallium oxide polymorphs devised by Playford *et al*. Some phases are faded grey to highlight the similar interconversion between Ga_2O_3 and $Ga_{2-x}Al_xO_3$ polymorphs.

Gallium aluminium oxide spinels can be accessed via a solvothermal route but optimised for lower temperature than previously. Up to 90% Al^{3+} can be incorporated into the spinel structure. Solid state MAS NMR shows that gallium and aluminium preferentially occupy the tetrahedral and octahedral sites respectively but this is not exclusive and mixed site occupation was observed for all spinels throughout the solid solution γ-$Ga_{2-x}Al_xO_3$ where $0.2 \leq x \leq 1.8$.

The thermal decomposition of $Ga_5O_7(OH)$ was re-investigated and found that it decomposes into a mixture of ε-Ga_2O_3 and κ-Ga_2O_3 at 450 °C, though further work is needed to determine if this is a biphasic mixture or a disordered intergrowth of the polymorphs.

During this investigation, the synthesis of a new gallium aluminium oxyhydroxide was discovered, though it had likely been discovered independently by Roy and by MacDonald first but incorrectly identified as $GaAlO_3$. It is metastable, decomposing into ε-$Ga_{2-x}Al_xO_3$ and κ-$Ga_{2-x}Al_xO_3$ following the same dehydration pathway as the

isostructural $Ga_5O_7(OH)$, prior to formation of the thermodynamically stable β-$Ga_{2-x}Al_xO_3$.

The limit of solubility of Al^{3+} into β-Ga_2O_3 has been contested widely in the literature. Rietveld refinement in this work shows that the solubility limit appears to be between 65-70%. Mixed phases formed at higher levels of aluminium, with higher temperatures favouring formation of the beta polymorph.

Some preliminary studies of the use of gallium oxide and mixed gallium aluminium oxides in catalysis were reported. Aluminium oxide outperforms three gallium oxide polymorphs when used as supports for palladium in diesel oxidation. This had been attributed to the possible formation of the intermetallic species $GaPd_2$. On the other hand, palladium supported on mixed-metal β-$Ga_{2-x}Al_xO_3$ shows improved activity over α-Al_2O_3 and β-Ga_2O_3 in the semi-hydrogenation of acetylene, although the presence of $GaPd_2$ needs further work to prove that it has formed.

4.9 References

1 M. Trueba and S. P. Trasatti, *Eur. J. Inorg. Chem.*, 2005, **2005**, 3393–3403.

2 K. Wefers and C. Misra, *Alcoa Tech. Pap.*, 1987, **19**, 1–100.

3 I. Levin and D. Brandon, *J. Am. Ceram. Soc.*, 1998, **81**, 1995–2012.

4 Y. D. Ivakin, M. N. Danchevskaya and G. P. Muravieva, *Moscow Univ. Chem. Bull.*, 2005, **45**, 4–7.

5 O. V Al'myasheva, E. N. Korytkova, A. V Maslov and V. V Gusarov, *Inorg. Mater.*, 2005, **41**, 540–547.

6 Ľ. Smrčok, V. Langer and J. Křesťan, *Acta Crystallogr. Sect. C Cryst. Struct. Commun.*, 2006, **62**, 83–84.

7 R. Roy, V. G. Hill and E. F. Osborn, *J. Am. Chem. Soc.*, 1952, **74**, 719–722.

8 J. C. Lavalley, M. Daturi, V. Montouillout, G. Clet, C. Otero Areán, M. Rodríguez Delgado and A. Sahibed-dine, *Phys. Chem. Chem. Phys.*, 2003, **5**, 1301–1305.

9 S. Penner, C. Zhuo, R. Thalinger, M. Grünbacher, C. Hejny, S. Vanicek and M. Noisternig, *Monatsh Chem.*, 2016, **147**, 289–300.

10 M. Rodríguez Delgado and C. Otero Areán, *Mater. Lett.*, 2003, **57**, 2292–2297.

11 A. E. Romanov, S. I. Stepanov, V. I. Nikolaev and V. E. Bougrov, *Rev. Adv. Mater. Sci*, 2016, **44**, 63–86.

12 L. Shi, J. Zhang, S. Wu, Y. Li, L. Jiang and Q. Cui, *J. Am. Ceram. Soc.*, 2014, **97**, 2607–2614.

13 S. Yoshioka, H. Hayashi, A. Kuwabara, F. Oba, K. Matsunaga and I. Tanaka, *J. Phys. Condens. Matter*, 2007, **19**, 346211–11.

14 R. H. Fenn, *J. Chem. Soc. A*, 1960, **33**, 676–684.

15 J. Åhman, G. Svensson and J. Albertsson, *Acta Cryst*, 1996, **C52**, 1336–1338.

16 H. Wang, Y. He, W. Chen, Y. W. Zeng, K. Stahl, T. Kikegawa and J. Z. Jiang, *J. Appl. Phys.*, 2010, **107**, 33520.

17 S.-W. Kim, S. Iwamoto and M. Inoue, *Ceram. Int.*, 2009, **35**, 1603–1609.

18 H. Y. Playford, A. C. Hannon, E. R. Barney and R. I. Walton, *Chem. Eur. J*, 2013, **19**, 2803–2813.

19 K. Pohl, *Naturwissenschaften*, 1968, **55**, 82.

20 H. Y. Playford, A. C. Hannon, M. G. Tucker, D. M. Dawson, S. E. Ashbrook, R. J. Kastiban, J. Sloan and R. I. Walton, *J. Phys. Chem. C*, 2014, **118**, 16188−16198.

21 Y. Oshima, Y. Matsushita and S. Yamamoto, *J. Appl. Phys.*, 2015, **118**, 85301.

22 F. Boschi, M. Bosi, T. Berzina, E. Buffagni, C. Ferrari and R. Fornari, *J. Cryst. Growth*, 2016, **443**, 25–30.

23 D. S. McClure, *J. Phys. Chem. Solids*, 1957, **3**, 311–317.

24 V. G. Hill, R. Rustum and E. F. Osborn, *J. Am. Ceram. Soc.*, 1952, **35**, 136–142.

25 R. Roy and V. G. Hill, *Ind. Eng. Chem.*, 1953, **45**, 819–820.

26 H. V. Wartenerg and H. J. Reusch, *Z. Anorg. Allg. Chem*, 1932, **207**, 1–20.

27 B. W. Krueger, C. S. Dandeneau, E. M. Nelson, S. T. Dunham, F. S. Ohuchi and M. A. Olmstead, *J. Am. Ceram. Soc*, 2016, **99**, 2467–2473.

28 J. Macdonald, J. Gard and F. Glasser, *J. Inorg. Nucl. Chem.*, 1967, **29**, 661–671.

29 L. M. Foster and H. C. Stumpf, *J. Am. Chem. Soc.*, 1951, **73**, 1590–1595.

30 T. Masuda, T. Watanabe, Y. Miyahara, H. Kanai and M. Inoue, *Top. Catal.*, 2009, **52**, 699–706.

31 M. Takahashi, N. Inoue, T. Takeguchi, S. Iwamoto, M. Inoue and T. Watanabe, *J. Am. Ceram. Soc.*, 2006, **89**, 2158–2166.

32 T. Nakatani, T. Watanabe, M. Takahashi, Y. Miyahara, H. Deguchi, S. Iwamoto, H. Kanai and M. Inoue, *J. Phys. Chem. A*, 2009, **113**, 7021–7029.

33 T. Masuda, T. Watanabe, Y. Miyahara, S. Iwamoto, H. Kanai and M. Inoue, *J. Mol. Catal. A Chem.*, 2009, **307**, 71–76.

34 M. Takahashi, T. Nakatani, S. Iwamoto, T. Watanabe and M. Inoue, *Appl. Catal. B Environ.*, 2007, **70**, 73–79.

35 M. Chen, J. Xu, F. Z. Su, Y. M. Liu, Y. Cao, H. Y. He and K. N. Fan, *J. Catal.*, 2008, **256**, 293–300.

36 M. Hirano, K. Sakoda, K. Souma, H. Nishimoto, K. Jinno and Y. Hirose, *Ceram. Int.*, 2015, **41**, 14285–14292.

37 Y. Hou, L. Wu, X. Wang, Z. Ding, Z. Li and X. Fu, *J. Catal.*, 2007, **250**, 12–18.

38 B. Zheng, W. Hua, Y. Yue and Z. Gao, *J. Catal.*, 2005, **232**, 143–151.

39 S. Jin, X. Wang, X. Wang, M. Ju, S. Shen, W. Liang, Y. Zhao, Z. Feng, H. Y. Playford, R. I. Walton and C. Li, *J. Phys. Chem. C*, 2015, **119**, 18221–18228.

40 M. Higashiwaki, K. Sasaki, H. Murakami, Y. Kumagai, A. Koukitu, A. Kuramata, T. Masui and S. Yamakoshi, *Semicond. Sci. Technol.*, 2016, **31**, 34001.

41 M. Haneda, Y. Kintaichi, H. Shimada and H. Hamada, *Chem. Lett.*, 1998, 27, 181–182.

42 Z. Zhang and Y. Tan, *Catal. Sci. Technol.*, 2016, **6**, 5183–5195.

43 T. Mathew, Y. Yamada, A. Ueda, H. Shioyama and T. Kobayashi, *Appl. Catal. A Gen.*, 2005, **286**, 11–22.

44 T. Honma, H. Mori, K. M. Kemner, S. D. Kelly, H. Kageyama, T. Asanuma, A. Mishra and S. Mishra, *J. Phys. Conf. Ser.*, 2016, **712**, 12056.

45 J. N. Díaz de León, *Appl. Catal. B Environ.*, 2016, **181**, 524–533.

46 T. N. Afonasenko, N. S. Smirnova, V. L. Temerev, N. N. Leont, T. I. Gulyaeva and P. G. Tsyrul, *Kinet. Catal.*, 2016, **57**, 490–496.

47 G. Gutie, A. Taga and B. Johansson, *Phys. Rev. B*, 2001, **65**, 12101.

48 D. Muller, W. Gessner, J. Behrens, H and G. Scheler, *Chem. Phys. Lett.*, 1981, **79**, 59–62.

49 P. W. Stephens, *J. Appl. Cryst*, 1999, **32**, 281–289.

50 B. Goro, *Bull. Chem. Soc. Jpn.*, 1964, **37**, 1555–1557.

51 R. Demichelis, Y. Noel and C. Marcelo, *J. Phys. Conf. Ser.*, 2008, **117**, 12013.

52 M. Okumiya, G. Yamaguchi, O. Yamada and S. Ono, *Bull. Chem. Soc. Jpn.*, 1971, 44, 418–423.

53 M. Okumiya and G. Yamaguchi, *Bull. Chem. Soc. Jpn.*, 1971, 44, 1567–1570.

54 S. C. Robinson, H. T. Evans, W. T. Schaller and J. J. Fahey, *Am. Mineral.*, 1957, **42**, 619–628.

55 B. M. Gatehouse, I. E. Grey and E. H. Nickel, *Am. Mineral.*, 1983, **68**, 833–839.

56 A. W. Hanson, *Acta Cryst*, 1957, **11**, 703–709.

57 C. Ma and J. Beckett, *Am. Mineral.*, 2016, **101**, 1161–1170.

58 A. Manceau, S. Skanthakumar and L. Soderholm, *Am. Mineral.*, 2014, **99**, 102–108.

59 V. Barron, J. Torrent and F. M. Michel, *Am. Mineral.*, 2012, **97**, 253–254.

60 F. M. Michel, L. Ehm, S. M. Antao, P. L. Lee, P. J. Chupas, G. Liu, D. R. Strongin, M. A. A. Schoonen, B. L. Phillips and J. B. Parise, *Science.*, 2007, **316**, 1726–1730.

61 A. Manceau and W. P. Gates, *Clay Miner.*, 2013, **48**, 481–489.

62 L. Pauling, *J. Am. Chem. Soc.*, 1929, **51**, 1010–1026.

63 L. Kovarik, M. Bowden, D. Shi, N. M. Washton, A. Andersen, J. Z. Hu, J. Lee, J. Szanyi, J. H. Kwak and C. H. F. Peden, *Chem. Mater.*, 2015, **27**, 7042–7049.

64 E. Tronc, C. Chanéac and J. P. Jolivet, *J. Solid State Chem.*, 1998, **139**, 93–104.

65 I. Dézsi and J. M. D. Coey, *Phys. stat. sol*, 1973, **15**, 681–685.

66 L. Machala, J. Tucek and R. Zbořil, *Chem. Mater.*, 2011, **23**, 3255–3272.

67 J. López-Sánchez, A. Muñoz-Noval, A. Serrano, M. Abuín, J. de la Figuera, J. F. Marco, L. Pérez, N. Carmona and O. Rodríguez de la Fuente, *RSC Adv.*, 2016, **6**, 46380–46387.

68 I. Cora, F. Mezzadri, F. Boschi, M. Bosi, M. Čaplovičová, G. Calestani, I. Dódony, B. Pécz and R. Fornari, *CrystEngComm*, 2017, **19**, 1509–1516.

69 C. Kranert, M. Jenderka, J. Lenzner, M. Lorenz, H. Von Wenckstern, R. Schmidt-Grund and M. Grundmann, *J. Appl. Phys.*, 2015, **117**, 125703.

70 A. Russell and W. S. Epling, *Catal. Rev.*, 2011, **53**, 337–423.

71 J. A. Kurzman, L. M. Misch and R. Seshadri, *Dalton Trans.*, 2013, **42**, 14653–67.

72 H. Lorenz, R. Thalinger, E.-M. Köck, M. Kogler, L. Mayr, D. Schmidmair, T. Bielz, K. Pfaller, B. Klötzer and S. Penner, *Appl. Catal. A Gen.*, 2013, **453**, 34–44.

73 M. Armbrüster, R. Schlögl and Y. Grin, *Sci. Technol. Adv. Mater*, 2014, **15**, 34803.

74 L. Li, B. Zhang, E. Kunkes, K. Fçttinger and M. Armbrüster, *ChemCatChem*, 2012, **4**, 1764–1775.

75 A. Haghofer, K. Föttinger, F. Girgsdies, D. Teschner, A. Knop-Gericke, R. Schlögl and G. Rupprechter, *J. Catal.*, 2012, **286**, 13–21.

76 A. J. Mccue and J. A. Anderson, *Front. Chem. Sci. Eng*, 2015, **9**, 142–153.

77 M. Armbru, K. Kovnir, M. Behrens, D. Teschner, Y. Grin and R. Schlo, *J. Am. Chem. Soc.*, 2010, **132**, 14745–14747.

78 A. Ota, M. Armbru, M. Behrens, D. Rosenthal, M. Friedrich, I. Kasatkin, F. Girgsdies, W. Zhang, R. Wagner and R. Schlo, *J. Phys. Chem. C*, 2011, **115**, 1368–1374.

79 J. Osswald, K. Kovnir, M. Armbrüster, R. Giedigkeit, R. E. Jentoft, U. Wild, Y. Grin and R. Schlögl, *J. Catal.*, 2008, **258**, 219–227.

80 J. Osswald, R. Giedigkeit, R. E. Jentoft, M. Armbrüster, F. Girgsdies, K. Kovnir, T. Ressler, Y. Grin and R. Schlögl, *J. Catal.*, 2008, **258**, 210–218.

81 K. Föttinger, *Catal. Today*, 2013, **208**, 106–112.

82 F. M. Hoffman and A. M. Bradshaw, *J. Catal.*, 1976, **44**, 328–331.

Chapter 5: Solvothermal Reactions of Gallium Precursors and Early First Row Transition Metals Salts

5. Solvothermal Reactions of Gallium Precursors and Early First Row Transition Metals Salts

5.1 Introduction on mixed-metal gallium oxides synthesis

Gallium is known to form oxides with metals from all over the Periodic Table. For example, gallium can form delafossites and oxides having the $NaFeO_2$ structure with some metals in Group I and first row transition metals,[1–3] a variety of different structures with some Group II metals,[4–10] spinels with the later first row transition elements,[11–16] and garnet-type oxides with some rare-earth metals.[17] This chapter focusses on the synthesis and characterisation of mixed metal gallium oxide materials where the metal is an early first row transition metal (vanadium, chromium, manganese). Much work has been undertaken on understanding gallium spinels, in particular spinels of gallium with the later first row transition metals, but in contrast there is very little on the oxides formed from gallium and the earlier transition metals. Few oxides containing gallium and vanadium have been reported on in the scientific literature. The mixed valent vanadium material V_2GaO_5 was prepared by high temperature synthesis at 1423 K.[18] Its structure, solved from single crystal X-ray diffraction, contains β-gallia-like columns of tetrahedral GaO_4, and VO_6 octahedral chains parallel to the *c*-axis (Figure 5.1). It was reported that vanadium usually adopts octahedral geometry in oxides and indeed the structure solution of this oxide confirmed that both V^{3+} and V^{4+} occupied the octahedral sites in the structure, whilst tetrahedral sites are solely occupied by gallium. At lower temperatures, 1273 K, a different material in the V_2O_3-VO_2-Ga_2O_3 system, $V_6Ga_2O_{13}$, was found to be stable.[18] Both V_2GaO_5 and $V_6Ga_2O_{13}$ are stable at room temperature and pressure in air. V^{3+} is usually unstable oxidising to V^{4+} or V^{5+}. For example, this is found in corundum-type V_2O_3 which gradually oxidises to monoclinic (distorted rutile) VO_2 in the presence of air at room temperature.[18] Bixbyite V_2O_3 has only recently been discovered by reaction of VF_3 in a water-saturated stream of 10vol% hydrogen in argon. The material is stable to 823 K and then transforms to V_2O_3.[19] Most aqueous V^{3+} cations oxidise to the vanadyl cation, with $V_2(SO_4)_3$ being the notable dry-air-stable exception.[20]

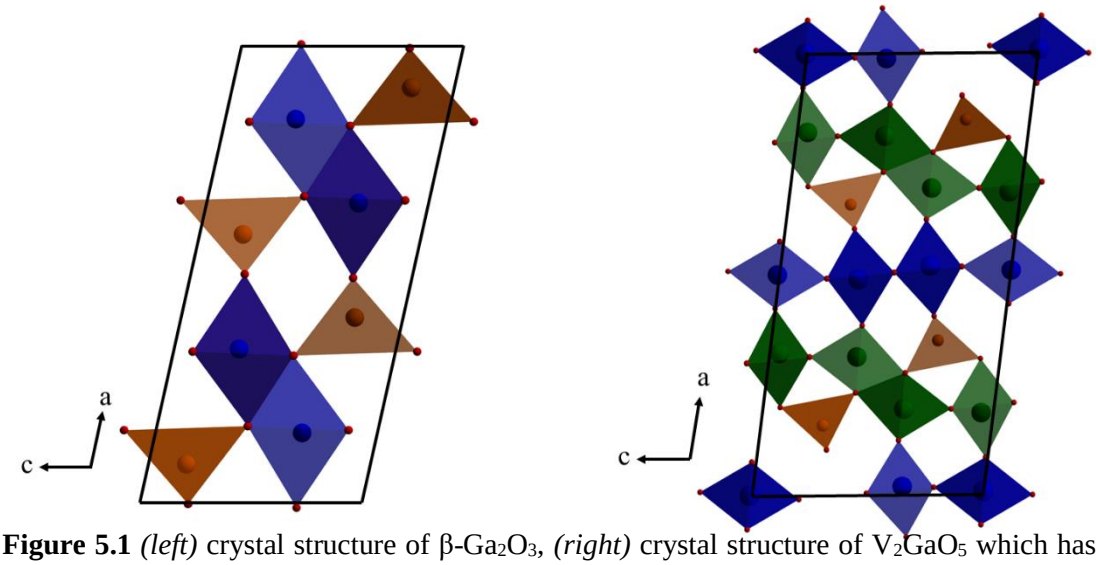

Figure 5.1 *(left)* crystal structure of β-Ga_2O_3, *(right)* crystal structure of V_2GaO_5 which has similar beta-gallia-like columns: GaO_4 *(orange)*, VO_6 *(blue)*, and (Ga, V)O_6 *(green)*.

A mixed metal aluminium vanadium oxide defect spinel, $AlVO_3$, is known and can be prepared by reduction in hydrogen at 1000 °C. An X-ray, neutron and electron diffraction study showed that Al^{3+} randomly occupies two-thirds of available tetrahedral sites. The spinel is antiferromagnetic with a Néel temperature of 270 K.[21]

The geometrically frustrated AlV_2O_4 spinel is also known. This oxide features vanadium in oxidation states +2 and +3, which is unusual. This is an interesting material for it displays a charge-ordering state below 700 K.[22–24] Since aluminium and gallium are of a similar size it seems likely that gallium analogues of these spinels can be prepared, and indeed was the original motive behind some of the work in this chapter.

With regards to other early transition metals, there are no known oxides containing both chromium and gallium with the exception of a Cr^{3+} doped $MgGa_2O_4$-Ga_2O_3 system,[25] but both manganese and iron form spinels with gallium at high temperature[26–28] There are few reports on iron gallium oxide prepared from low temperature hydro(solvo)thermal[29] chemistry but, aside from microwave-hydrothermal,[30] manganese gallium oxides have not been reported from any hydro(solvo)thermal reactions in the literature.

5.1.1 Catalysis by mixed-metal oxides

V_2O_5 is employed as the catalyst in the Contact process: an industrial process to manufacture H_2SO_4 and is employed worldwide. V_2O_5, in combination with hydrogen peroxide, also finds use in the oxidative esterification of aldehydes employed by some organic chemists.[31] Vanadium containing oxides have also been widely explored for application in other areas of catalysis, such as in the oxidative propane dehydrogenation reaction as vanadium containing oxides have been found to outperform most other catalysts.[32,33] Currently one of the best catalysts in this reaction is a vanadium molybdenum based catalyst.[34] Oxidative propane dehydrogenation is an important reaction for the production of olefins, in particular ethylene and propylene, with the demand expected to increase substantially in the near future. Steam cracking is also used for olefin production but the reaction favours ethylene over propylene, whereas the problems with dehydrogenation lies within its thermodynamic constraints and coking leading to catalyst deactivation. Oxidative dehydrogenation overcomes most of these issues and therefore intense research is taking place to develop better catalysts for the oxidative dehydrogenation of alkanes.[35] The vanadium gallium oxides described above have not yet been investigated for potential catalytic applications.

Supported chromium oxides have found use in alkane dehydrogenation reactions[36] and in olefin polymerisation reactions,[37] however one potential disadvantage of chromium oxides and their application in catalysis is the possibility of forming Cr^{6+} which is toxic. Chromium oxide was used as an additive in the water-gas shift reaction but research now focusses on using other metals as additives instead for this very reason.[38]

Chromium oxides, however, have found other important applications other than catalysis. Cr_2O_3 has found application as a pigment and recently reinvestigated as such,[39] whilst CrO_2 is famous for its use in recording tape in the mid-20th century owing to it being ferromagnetic.[40]

Manganese containing water oxidation catalysts are closed related to photosystem II, a light dependent reaction step in oxygenic photosynthesis. Manganese substituted cobalt gallium oxide, prepared by a microwave-hydrothermal method, was found to outperform both cobalt gallium oxide and manganese gallium oxide as a water oxidation catalyst.[30,41]

5.2 Scope of this chapter

In this chapter, synthesis and structural analysis of new materials formed from the reaction of gallium precursors and some of the early first row transition metal salts (*i.e.* of V, Cr, and Mn) are presented. The reactions used were based, in part, on reactions discussed in earlier chapters such as for the synthesis of cobalt gallium oxide (Chapter 3) and aluminium substituted gallium oxides (Chapter 4). The synthesis and characterisation of a novel vanadium substituted gallium oxyhydroxide is presented and later in the chapter the results regarding the synthesis and characterisation of a new chromium substituted gallium oxide, and a manganese gallium oxide is presented. Catalysis studies with the gallium vanadium oxyhydroxide material is presented at the end of the chapter.

5.3 A new gallium vanadium oxyhydroxide: $Ga_{5-x}V_xO_{8-y}(OH)_y$

5.3.1 Synthesis

In a typical synthesis, 0.150 g (2.15 mmol) of Ga metal (Alfa-Aesar, 99.9%) and 0.396 g (2.15 mmol) Na_3VO_4 (Alfa-Aesar, 99.9%) were added to a 10 ml mixture of 1:1 water:ethanolamine (MEA) with stirring. The mixture was sealed in a 23 ml PTFE-lined steel autoclave and heated at 240 °C for 96 hours in a preheated fan-assisted oven. The autoclave was cooled to room temperature naturally and the solid isolated by suction filtration. The black solid was then washed with methanol and dried overnight at 70 °C.

An alternative synthesis was to mix 0.40 g (1.09 mmol) of $(Ga(acac)_3$ (Aldrich, 99.99%) and 0.380 g (1.09 mmol) $V(acac)_3$ (Aldrich, 97%) in 10 ml 1,4-butanediol with stirring. This mixture was sealed in a 23 ml PTFE lined autoclave and placed in a preheated fan-assisted oven at 240 °C for 96 hours. Upon cooling naturally to room temperature, the slurry was collected via centrifugation followed by washing in acetone and isolated by further centrifugation. The slurry was dried overnight at 70 °C which yielded a black powder. The material prepared by this synthesis is less crystalline than the method in 1:1 MEA:H_2O.

Control reactions using either only $Ga(acac)_3$ or $V(acac)_3$ under the same reaction conditions yielded β-Ga_2O_3 or corundum-type V_2O_3, respectively. Typically a flow of

H_2 or CO is required to reduce V_2O_5 to V_2O_3[42] though it has been prepared solvothermally[43] or by refluxing in an organic template.[44] This shows that trivalent vanadium containing oxides may be prepared directly by solvothermal synthesis.

5.3.2 General characterisation

5.3.2.1 Powder X-ray diffraction

The room temperature powder XRD pattern of the material formed in MEA:H_2O shows reflections with two clearly different peak shapes. It was assumed, at first, that this was a mixed phase material. However, upon indexing an hexagonal unit cell, analogous to the $5Al_2O_3{\cdot}H_2O$-type structure (tohdite),[45–51] was found (space group $P6_3mc$), with lattice parameters a = 5.78 Å, c = 9.28 Å. The pure gallium analogue, $5Ga_2O_3{\cdot}H_2O$, with lattice parameters a = 5.82107(8) Å, c = 9.0662(2) Å, has only recently been synthesised and a detailed structural refinement found that the formula of these materials is better represented as $M_5O_7(OH)$, (M = Al or Ga).[52] The two distinct peak shapes found in the powder pattern of the new vanadium material are a clear example of anisotropic peak broadening often found for materials composed of plate morphology. The intense sharp peaks however indicate that the material has a large crystallite size.

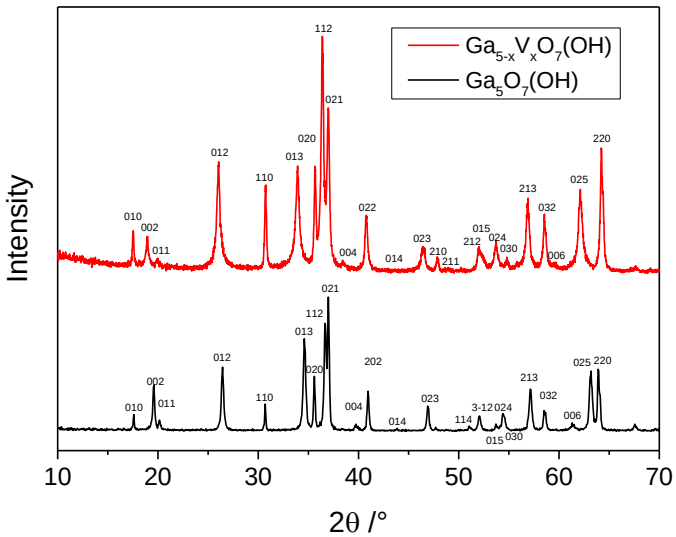

Figure 5.2 Powder XRD patterns of $Ga_5O_7(OH)$ (tohdite) *(black),* and vanadium substituted gallium tohdite *(red).*

A Pawley refinement against room temperature powder X-ray diffraction data was carried out on this material and it was found that Stephens' phenomenological model of anisotropic peak broadening was essential in order to model both peak shapes (Figure 5.3).[53] A large value on the (00l) reflection indicates the direction of the cell where the large anisotropic peak broadening is found (Table 5.1). At this stage, the material was described as $Ga_{5-x}V_xO_7(OH)$ with the assumption that the vanadium is present only as V^{3+}. Even with the Stephens' model applied the (112) reflection remains poorly fitted.

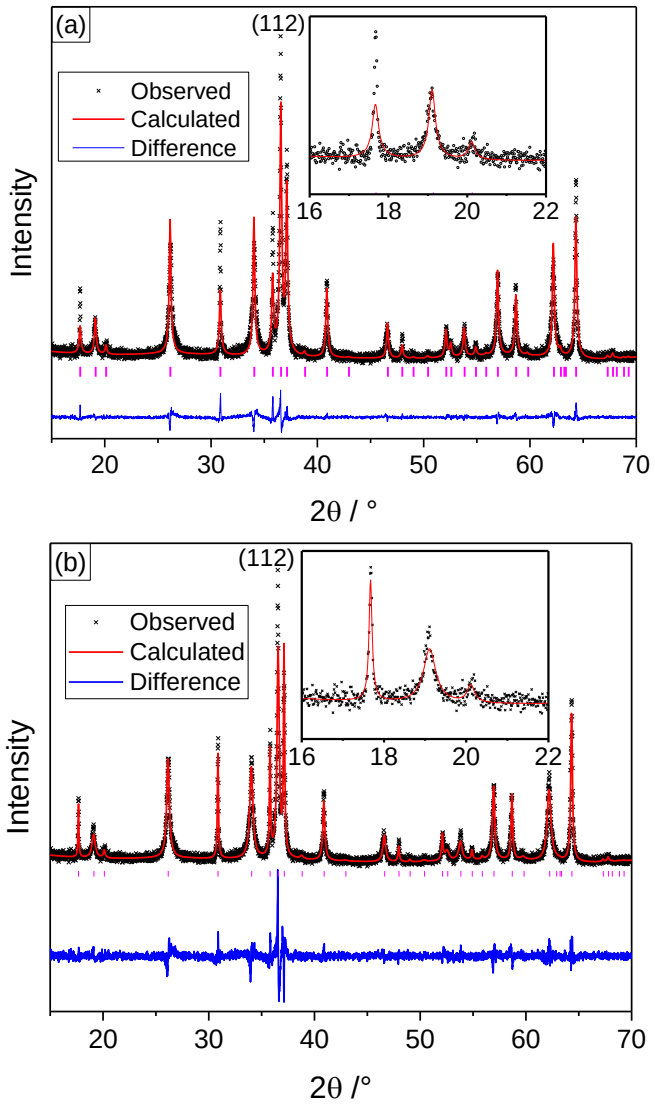

Figure 5.3 (a) Pawley refinement without the Stephens' model of anisotropic peak broadening with *(inset)* showing a close up of the fit, (b) Pawley refinement using the Stephens' mode with *(inset)* showing that both broad and sharp peaks are reasonably well fitted.

Refined lattice parameters were calculated as: a = 5.78824(3) Å and c = 9.2785(8) Å in the refinement including the Stephens' parameters.

Table 5.1 Refined Stephens' parameters.

Parameter	Value
S400	-639.7
S202	62.9
S004	3957

5.3.2.2 Further experimental details and characterisation by PXRD

The long reaction time of 96 hours is necessary in order to obtain a phase pure material. A 48-hour reaction shows an impurity phase apparent at around 13 °2θ (Figure 5.4(a)). An even shorter reaction time of 24 hours forms only an unidentifiable material(s) (Figure 5.4(b)). The intense peak around 13 °2θ is also observed as in Figure 5.4(a) but other peaks are clearly observed in Figure 5.4(b). The position of the second peak around 26 °2θ and its intensity relative to the first peak tentatively suggests the formation of a layered double hydroxide (LDH) with the first and second peak being the (003) and (006) reflections respectively. The formation of LDHs preceding the formation of metal oxides in solvothermal reactions was presented in Chapter 3.[54]

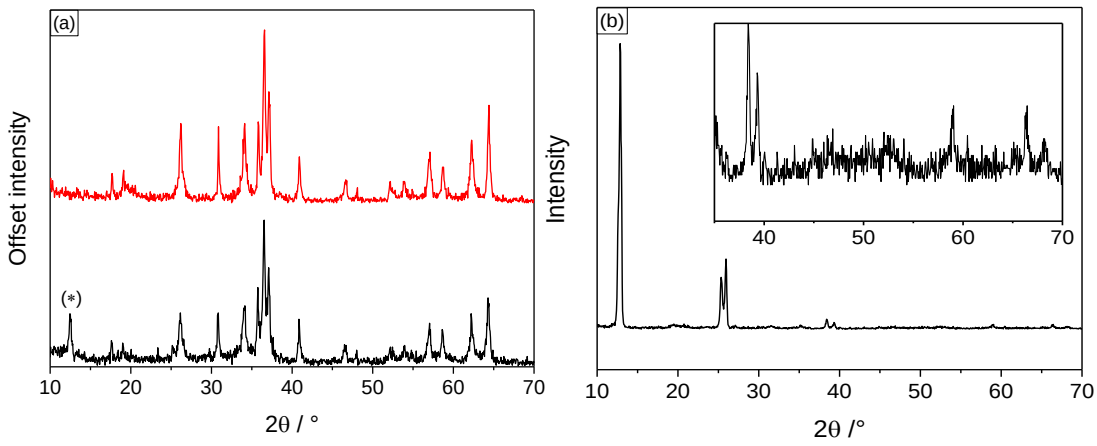

Figure 5.4 Powder XRD patterns of (a) 48 h reaction of Na_3VO_4 and Ga in 1:1 MEA:H_2O *(black)* showing an impurity phase (denoted *), a 96 h reaction of Na_3VO_4 and Ga in 1:1 MEA:H_2O *(red)* showing single phase $Ga_{5-x}V_xO_7(OH)$, and (b) a 24 hour reaction of Na_3VO_4 and Ga in 1:1 MEA:H_2O showing no formation of the tohdite-like material with *(inset)* close up of higher angle peaks.

The 1:1 ratio of metals appears to be fixed as addition of too little Na_3VO_4 forms $Ga_5O_7(OH)$ as a secondary phase whilst addition of too much Na_3VO_4 forms the unidentifiable material described above (Figure 5.5(a)) even after 96 hours. This dependency on the stoichiometric ratio contrasts with the Al^{3+} substituted $Ga_5O_7(OH)$ material described in Chapter 4, which could incorporate between 10 – 30% aluminium. No oxyhydroxide material formed at higher substitutions of aluminium but the material showed flexibility in the level of aluminium substitution.

Control reactions using only Ga metal or Na_3VO_4 under the same reaction conditions yielded either phase pure $Ga_5O_7(OH)$, or an unidentifiable material in the case of Na_3VO_4 (Figure 5.5(b)).

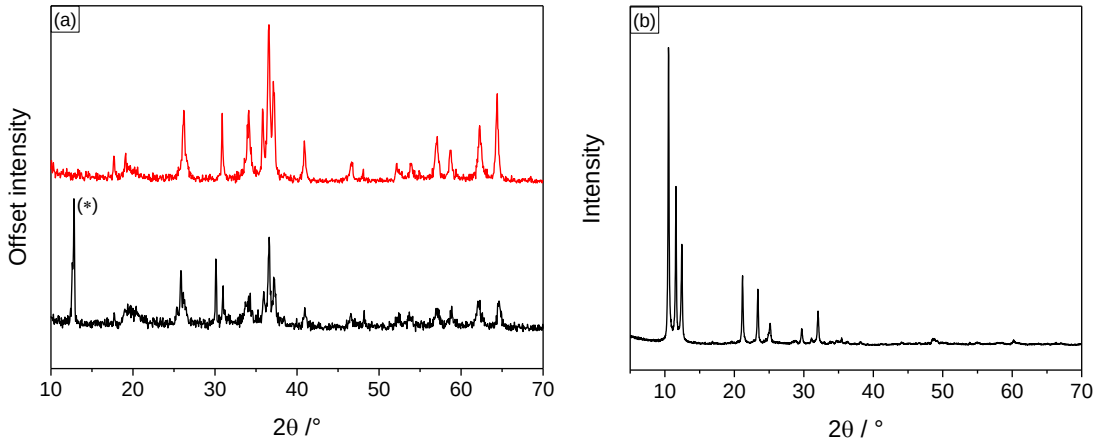

Figure 5.5 Powder XRD of materials (a) made with a 2:1 V:Ga stoichiometry *(black)* showing an impurity phase (*), which is absent in the reaction with 1:1 ratio *(red)*, (b) control reaction of Na_3VO_4 showing an unidentifiable material.

The room temperature powder XRD pattern of the material formed in 1,4-butanediol from acetylacetonate precursors also showed significant anisotropic peak broadening (Figure 5.6) however in this material all reflections are much broader indicating nano-sized crystallites. This was expected since the material formed in a slurry which cannot be obtained from filtration but instead must be collected by centrifugation. Since all peaks are much broader Pawley refinements proved challenging even with the Stephens' model applied. Furthermore, often the broadened peaks in the pattern showed a shoulder as if indicating a secondary phase. Though this was not always apparent it was observed in numerous diffraction patterns of different samples and so the material formed in the MEA:H_2O mixture was used for further structural analysis and characterisation.

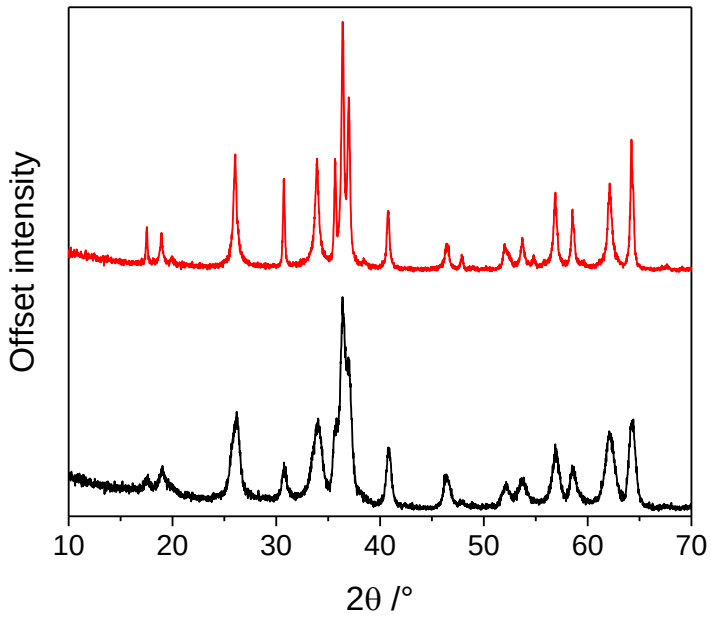

Figure 5.6 Powder XRD of materials prepared from a 96 hour reaction of gallium and vanadium acetylacetonates in 1,4-butanediol *(black)* (note the shoulder on the peak at ~26 °2θ), and a 96 hour reaction of gallium metal and sodium orthovanadate in 1:1 MEA:H_2O *(red)*.

The mineral tohdite, or akdalaite which is the name commonly given to natural tohdite, is isostructural with nolanite (further discussion is found in Section 5.3.4), which was reported to contain iron and vanadium. Attempts to substitute Ga^{3+} for Fe^{3+} using the 1,4-butanediol method were unsuccessful forming only $FeGa_2O_4$ or Fe_3O_4. A high-pressure phase where Ti^{4+} was doped into $Al_5O_7(OH)$ has also been reported[55] but again attempts to substitute a portion of Ga^{3+} for Ti^{4+}, which would require the loss of some of the hydroxy group such that the formula be written $Ga_{5-x}Ti_xO_{8-y}(OH)_y$, or instead would require a vacant Ga^{3+} site, was also not possible to prepare solvothermally by either the 1,4-butanediol or 1:1 H_2O:MEA method.

Reactions where $Ga(acac)_3$ was fully or partially substituted for $Al(acac)_3$ were unsuccessful in incorporating Al^{3+} into the structure of this material. It is surprising that no Al^{3+} can be included and yet it can form a mixed oxyhydroxide with gallium only (Chapter 4).

5.3.3 Time-of-Flight Powder Neutron Diffraction

5.3.3.1 Refinement of neutron data only

Time-of-flight powder neutron diffraction data were collected on the Polaris instrument, at ISIS, at room temperature.

An initial model using the $Ga_5O_7(OH)$ structure was used to fit the data,[52] and vanadium was added to the structure so that the gallium and vanadium had a half share of each site initially to give a Ga:V ratio of 1:1, (Table 5.2), as expected from the ratio used in the synthesis and inferred from the metal ratios obtained from EDX, (SEM) and EELS, (TEM). The initial lattice parameters were taken from Pawley refinement of the room temperature X-ray diffraction data.

Table 5.2 The initial crystal parameters used prior to the refinement of vanadium gallium oxyhydroxide based on the $Ga_5O_7(OH)$ model. Space group $P6_3mc$. Initial lattice parameters: a = 5.78824 Å, c = 9.27859 Å.

Wyckoff site	Atom	x	y	z	Occupancy	Beq / Å^2
6c	Ga1	0.1654	0.3308	0.3633	0.5	0.3
	V1	0.1654	0.3308	0.3633	0.5	0.3
2b	Ga2	2/3	1/3	0.1598	0.5	0.3
	V2	2/3	1/3	0.1598	0.5	0.3
2b	Ga3	1/3	2/3	0.0439	0.5	0.3
	V3	1/3	2/3	0.0439	0.5	0.3
2a	O1	0	0	-0.0173	1.0	0.3
6c	O2	0.5133	0.0265	0.0004	1.0	0.3
6c	O3	0.8334	0.6668	0.2594	1.0	0.3
2b	O4	1/3	2/3	0.2503	1.0	0.3
2a	H1	0	0	0.100	1.0	0.3

The structure of akdalaite/tohdite has been scrutinised in a paper using computational methods to confirm that the space group $P6_3mc$ is adequate.[56] The two subgroups of $P6_3mc$ are $P31c$ and $Cmc2_1$, which offer additional degrees of freedom. It was found that these extra degrees of freedom are not exploited in akdalaite with minimal energy differences between all three space groups and concluded that $P6_3mc$ is appropriate for the structure. Based on this and the structural refinement of $Ga_5O_7(OH)$, also refined in $P6_3mc$, this space group was chosen for the current work.

Two constraints were applied to the refinement. The first was to keep the metal sites fully occupied (*i.e.* so that the total site occupancy equals 1), to ensure the result did not become unphysical with sites exceeding 1. The second was to keep the thermal parameter for each mixed metal site the same. Since the coherent scattering cross section of vanadium is 0.018 barns the structural information of the metal sites will be dominated by gallium. As the refinement is a representation of the average crystal structure it would be expected that two metals sharing the same site would have the same thermal parameters and fractional coordinates and so although these refined parameters are refined for the gallium the values obtained can be applied to vanadium too.

The anisotropic peak broadening was not so pronounced in the neutron data, likely due to the lower resolution obtained from the instrument, but it was found that the Stephens' phenomenological model of anisotropic peak broadening was required in order to obtain a satisfactory fit. With the Stephens' parameters included the refinement proceeded smoothly to an wRp of 2.026%, and the refined crystal parameters are shown in Table 5.3 and the fit to the data from banks 3 and 5 shown in Figure 5.7.

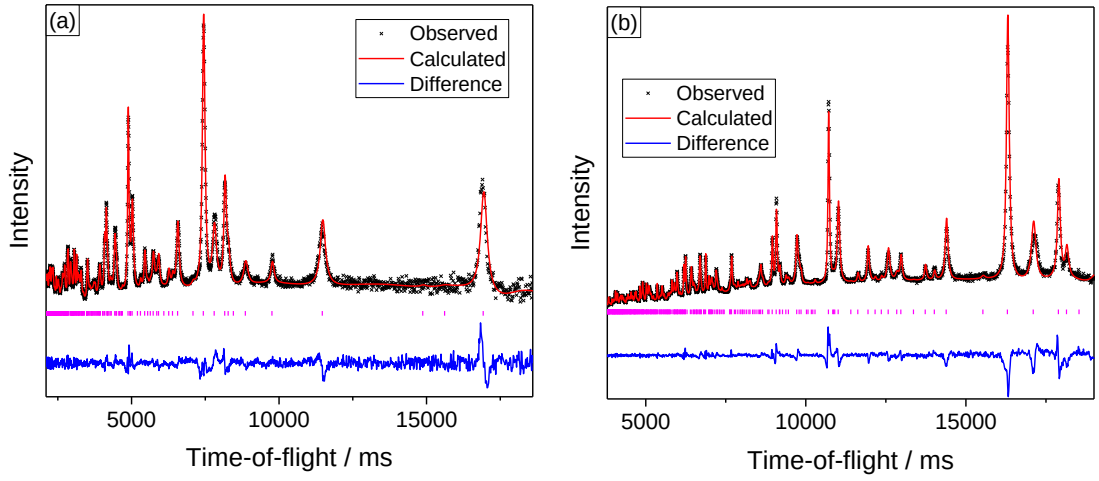

Figure 5.7 (a) Results of Rietveld refinement of vanadium substituted gallium tohdite using neutron diffraction from Polaris bank 3 and (b) bank 5.

Table 5.3 Refined crystal parameters for $Ga_{2.52}V_{2.48}O_{7.33}(OH)_{0.67}$. Space group $P6_3mc$, a = 5.7906(2) Å, c = 9.2550(5) Å. Rp = 1.955%, wRp = 2.026%.

Wyckoff site	Atom	x	y	z	Occupancy	Beq / Å^2
6c	Ga1	0.1674(7)	0.3348(14)	0.3440(5)	0.284(7)	0.23(9)
	V1	0.1674(7)	0.3348(14)	0.3440(5)	0.716(7)	0.23(9)
2b	Ga2	2/3	1/3	0.1358(5)	0.671(1)	0.26(7)
	V2	2/3	1/3	0.1358(5)	0.329(1)	0.26(7)
2b	Ga3	1/3	2/3	0.0353(2)	1.0	0.08(2)
	V3	1/3	2/3	0.0353(2)	0	0.08(2)
2a	O1	0	0	-0.0196(5)	1.0	0.382(12)
6c	O2	0.5127(1)	0.0253(3)	-0.0125(4)	1.0	0.382(12)
6c	O3	0.8310(4)	0.6619(8)	0.2456(4)	1.0	0.382(12)
2b	O4	1/3	2/3	0.2400(5)	1.0	0.382(12)
2a	H1	0	0	0.070(16)	0.67(4)	1.2(2)

During the refinement, it was found that the Ga3 (2b) site occupancy refined slightly above 1, to 1.019, which was a strong indication that this site was occupied only by gallium and later in the refinement this parameter was fixed at 1.0 to give a meaningful interpretation to the refinement.

A good fit to data was determined especially for the shorter time-of-flight reflections (Figure 5.8(a)), though a noticeable 2θ offset was observed in longer time-of-flight reflections (Figure 5.8(b)) possibly due to micro-strain within the crystallites.

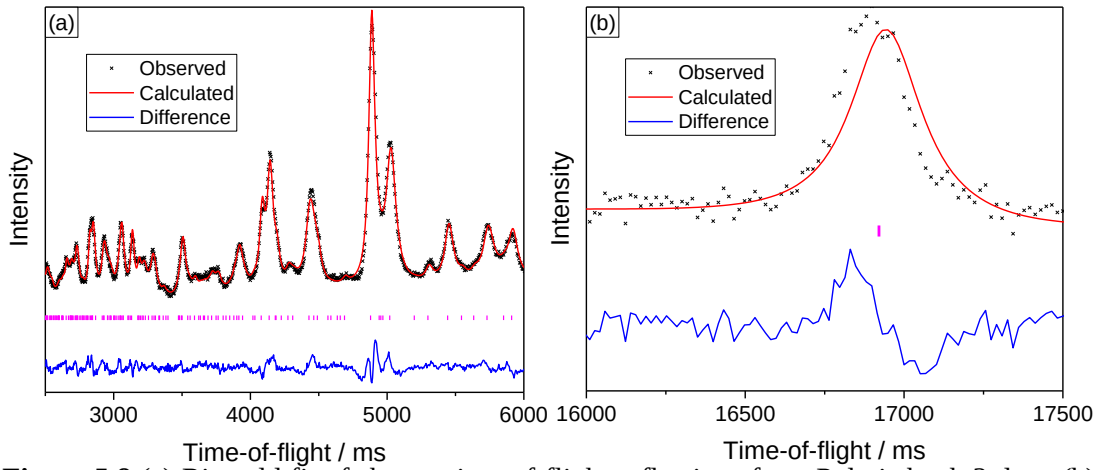

Figure 5.8 (a) Rietveld fit of shorter time-of-flight reflections from Polaris bank 3 data, (b) longer time-of-flight reflection showing 2θ offset.

Occasionally false structure refinements are obtained owing to the high correlation between the thermal parameters and the site occupancies. In this refinement, the thermal parameters were the last structural parameters to be refined. It is believed in this structural model that the refined occupancy parameters and thermal parameters are physical since the thermal parameters for the site containing only gallium is much smaller than for the sites containing a portion of vanadium which makes sense. Furthermore, the refined chemical composition is $Ga_{2.52}V_{2.48}O_{7.33}(OH)_{0.67}$ which gives a refined composition close to Ga:V as 1:1 which is in good agreement with both the stoichiometry of the reaction and the metal ratio as inferred from both EDX and EELS determined from electron microscopy. In addition to this, gallium exclusively occupies the tetrahedral site which is not unexpected owing to the tetrahedral site preference shown by gallium in many oxide materials. Similar tetrahedral preference by gallium was found by ^{71}Ga MAS NMR in the Al^{3+} substituted $Ga_5O_7(OH)$ materials (Chapter 4). The occupancy of the hydrogen refined to 0.67 which is acceptable so long as a small portion of the vanadium is oxidised to V^{4+}. The average oxidation state of vanadium in this model is $V^{3.13+}$ *i.e.* most of the vanadium is trivalent. V^{3+} will preferentially adopt octahedral coordination owing to its size and crystal field stabilisation energy such as is found in many spinels for the $3d^3$ configuration.[57] Tetrahedral vanadium usually is often found in the pentavalent state such as found in Na_3VO_4 and NH_4VO_3, but is still often too large for tetrahedral coordination and in V_2O_5 vanadium adopts distorted trigonal bipyramids. V^{3+} is even larger than V^{5+} rendering a tetrahedral geometry highly unlikely. This is in contrast to refined nolanite crystal structures which have similar crystal structures to tohdite and where V^{3+} has been found distributed over both the octahedral and tetrahedral sites *(vide infra)*.[58,59]

5.3.3.2 Simultaneous Neutron Time-of-Flight and X-ray Refinement

A second refinement simultaneously refined models against both neutron and X-ray data. The reasons for this were twofold. Firstly, it would be further evidence for a correct refinement of the structural parameters if the structure from neutron data agrees with the X-ray data. Secondly, since the scattering cross section of vanadium is *ca* 0 the atomic coordinates, site occupancy and thermal parameters of the metal sites are derived only from the gallium. Introducing X-ray diffraction data into the refinement allows for the vanadium structure parameters to be refined. The atomic number

difference between vanadium and gallium is 8 and so is large enough for the two metals to be distinguished.

The neutron data from banks 3, 4 and 5 were fitted simultaneously with lab X-ray radiation of wavelength 1.54056 Å, and the refined crystal parameters are given in Table 5.4 and the fit to the data in Figure 5.9. So as to not introduce any bias into the refinement, the same initial structure model used in the time-of-flight only refinement was used in the simultaneous neutron and X-ray refinement.

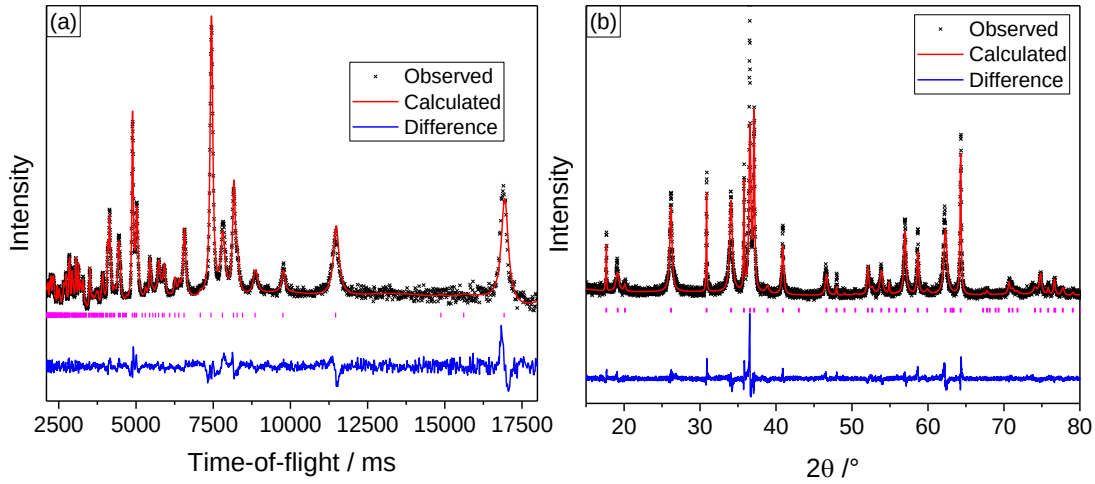

Figure 5.9 (a) Result of Rietveld refinement of vanadium substituted gallium tohdite, using neutron diffraction data from Polaris bank 3, (b) Rietveld refinement of XRD data λ = 1.54056 Å.

Table 5.4 Refined crystal parameters for $Ga_{2.52}V_{2.48}O_{7.31}(OH)_{0.69}$. Space group $P6_3mc$, a = 5.79044(17) Å, c = 9.2570(4) Å. Rp = 12.675%, wRp = 2.265%.

Wyckoff site	Atom	x	y	z	Occupancy	Beq / Å^2
6c	Ga1	0.1644(4)	0.3288(8)	0.3743(4)	0.286(5)	0.24(7)
	V1	0.1644(4)	0.3288(8)	0.3743(4)	0.714(5)	0.24(7)
2b	Ga2	2/3	1/3	0.1647(2)	0.666(11)	0.30(6)
	V2	2/3	1/3	0.1647(2)	0.334(11)	0.30(6)
2b	Ga3	1/3	2/3	0.0645(5)	1.0	0.094(17)
	V3	1/3	2/3	0.0645(5)	0	0.094(17)
2a	O1	0	0	0.0096(5)	1.0	0.38(1)
6c	O2	0.5129(1)	0.0258(2)	0.0162(3)	1.0	0.38(1)
6c	O3	0.8306(3)	0.6611(6)	0.2745(3)	1.0	0.38(1)
2b	O4	1/3	2/3	0.2688(4)	1.0	0.38(1)
2a	H1	0	0	0.103(2)	0.69(4)	1.43(19)

Clearly, a very similar structural model was obtained when the powder X-ray diffraction was included in the refinement.

Most of the Bragg reflection intensities in the X-ray data are fitted well though it is acknowledged that there is an appreciable 2θ-offset with regards to the peak positions (Figure 5.10). This was also found in the X-ray refinement for $Ga_5O_7(OH)$ and was attributed to strain in the crystallites.[52] Though the intensities of most reflections are reasonably well accounted for the most intense reflection in the X-ray data, the (112) reflection found at ~37.5 °2θ, remains poorly fitted and attempts to refine the X-ray structure further in order to better fit this peak were not successful (Figure 5.10(a)).

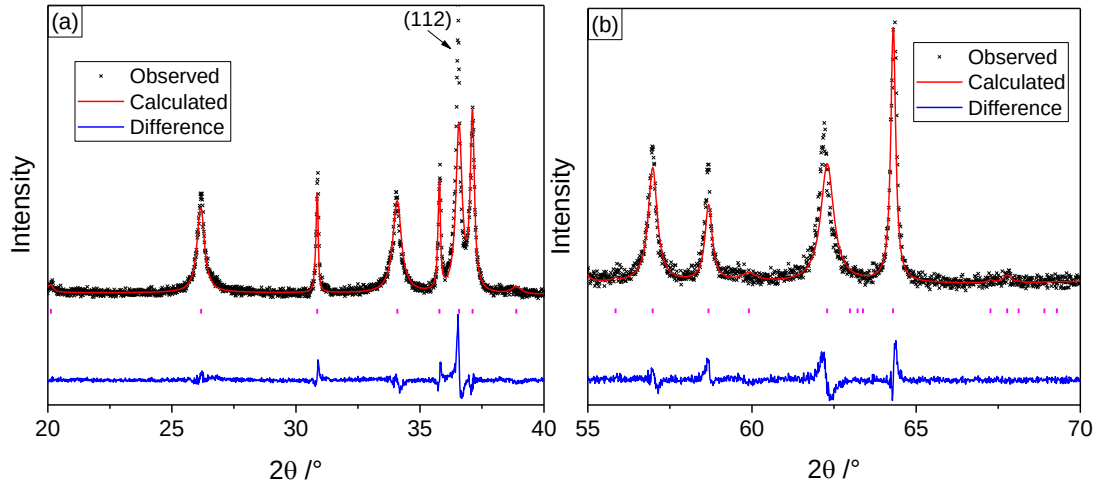

Figure 5.10 (a) Rietveld refinement of the lower angle fit showing good fit to data with the Stephens' model but poor fit to (112) reflection, (b) Rietveld refinement showing higher angle peaks but noticeable 2θ offset.

The fit to both sets of data are shown again in Figure 5.11 to highlight the quality of the fit and difference in reflection intensities between the X-ray and neutron data.

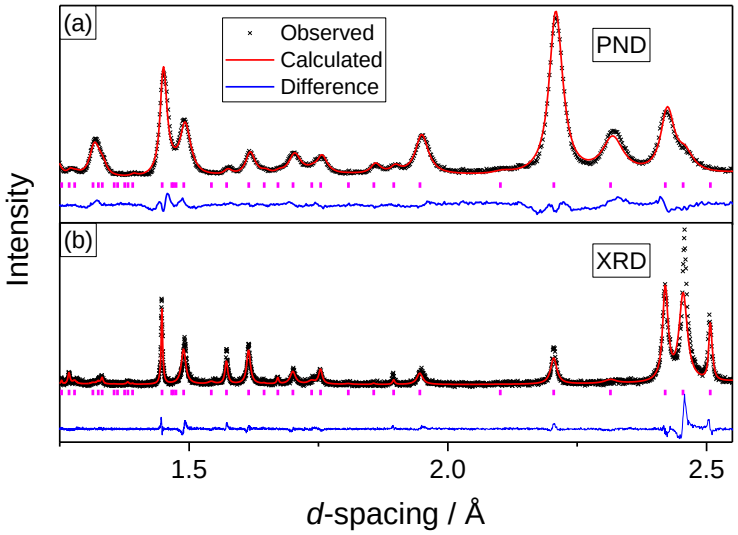

Figure 5.11 (a) Powder neutron diffraction refinement (Polaris bank 3) refined simultaneously with (b) powder X-ray diffraction refinement and plotted in *d*-spacing.

Although the Rietveld refinement does not fit the *(112)* reflection very well, the simulated powder pattern using the model obtained from the simultaneous neutron time-of-flight and X-ray refinement does show that an intense *(112)* reflection should be expected which compares favourably with the measured data (Figure 5.12).

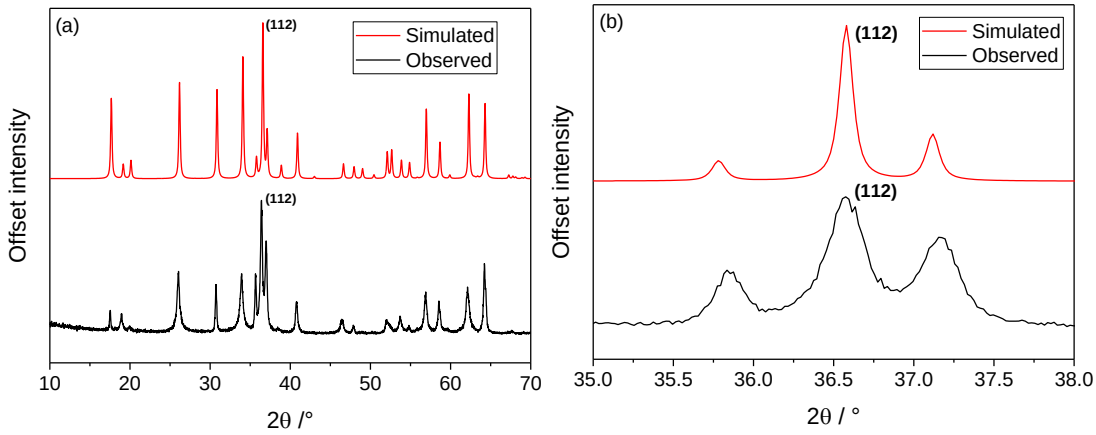

Figure 5.12 (a) observed powder pattern of $Ga_{2.52}V_{2.48}O_{7.31}(OH)_{0.69}$ *(black)* compared against a simulated powder pattern *(red)* using the refined model from simultaneous PXRD and PND data showing the PXRD pattern expected without the anomalous peak broadening, (b) close-up of the *(112)* reflection.

5.3.4 Discussion about the structure of $Ga_{2.52}V_{2.48}O_{7.31}(OH)_{0.69}$ and comparison between tohdite, nolanite and some hexagonal ternary molybdates

The structure of $Ga_{2.52}V_{2.48}O_{7.31}(OH)_{0.69}$ has been described above as being based on the tohdite structure. The tohdite structure consists of hexagonal close packed oxide layers, a layer of MO_6 octahedra and a layer containing MO_6 octahedra and MO_4 tetrahedra. The layers of edge-sharing MO_6 octahedra also share edges with the MO_6 octahedra in the layer above and below, and corner-share with the tetrahedra in the layer above and below (Figure 5.13). Nolanite is a material with a similar crystal structure.

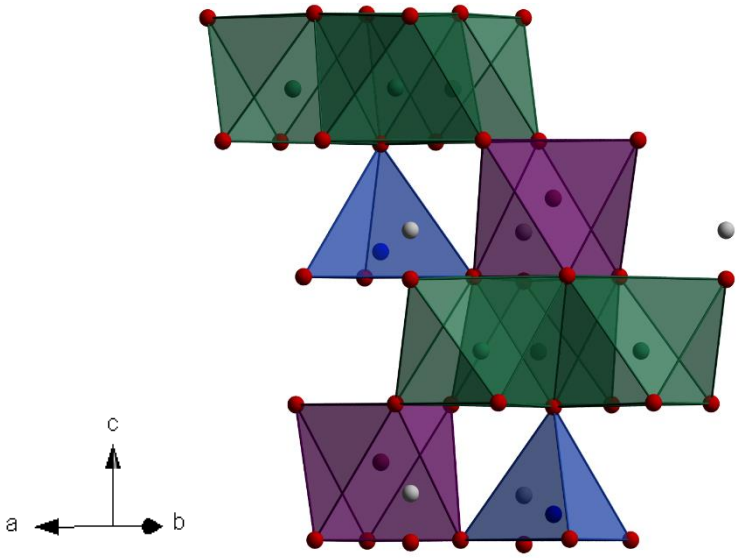

Figure 5.13 Crystal structure of tohdite which is shared by other minerals such as nolanite, ternary molybdates and also likely the structure adopted by ferrihydrite.

The tohdite/nolanite structure seems to be quite flexible in what cations it can accommodate; a variety of oxidation states and the coordination of the cations may vary according to different samples. However, from this work it would appear that solvothermal synthesis alone can only afford certain variations of nolanite and synthesis of other new materials containing different cations, such as an iron substituted $Ga_5O_7(OH)$ material may have to be prepared by alternative preparative techniques.

Nolanite, $(Fe, V)_5O_7(OH)$ and $(Fe, V)_5O_8$, was first described in papers by Barnes *et al.*[60] and also by Robinson.[59] In the latter paper the authors discussed that the sample

contains both tri and tetravalent vanadium and divalent iron. A chemical formula $Fe_{2.5}^{2+}V_{1.7}^{3+}V_{5.5}^{4+}O_{16}$ was proposed based on chemical analyses of the mineral. A single crystal structure of nolanite was described in 1958 by Hanson[61] and concluded that the trivalent vanadium had a strong but not exclusive preference for the tetrahedral site and tetravalent vanadium to take the octahedral sites. Its formula was given as $Fe_{2.5}V_{7.11}O_{16}$. It was noted that the metal centres are displaced from their centre of gravity in the octahedra and this displacement was also observed in the refined structure for vanadium gallium oxyhydroxide octahedra in this work, Table 5.6 and Figure 5.14.

Hanson concluded that at the time it was not possible to write a valid chemical formula based on X-ray data alone but noted that it had a similar structure to the ternary oxides of tetravalent molybdenum, $A_2^{2+}Mo_3^{4+}O_8$, but without the V^{4+}-V^{4+} bonding seen between the tetravalent molybdenum.

Another sample of nolanite, this time from Kalgoorlie in Western Australia, was investigated in 1983.[58] The sample contained iron and vanadium but also small amounts of titanium and aluminium. The formula given was $Al_{0.3}Fe_{2.2}Ti_{0.6}V_{6.9}O_{14}(OH)_2$, which is the tohdite formulation (*i.e.* it is an oxyhydroxide). The vanadium was assigned as being entirely trivalent based on bond valence sums but the structure refinement was hindered because the 3 transition metals present are virtually indistinguishable by X-rays. Since aluminium can be incorporated in to this structure, a tohdite/nolanite structure based entirely on Ga and V does not seem impossible since aluminium and gallium are similar in size. The fact that nolanite has been reported as being both oxide and oxyhydroxide also fits with the observed data for the material described in this work in that the hydrogen sites can be partially occupied, *i.e.* mixtures of hydroxide and oxide can be present. In the Hanson model of nolanite, $Fe_{2.5}V_{7.11}O_{16,}$ the tetrahedral site is occupied by both vanadium and iron unlike in the structure refinement of the gallium vanadium oxyhydroxide in this work, which suggested full occupancy of the tetrahedral site by gallium. Instead in $Fe_{2.5}V_{7.11}O_{16}$ the octahedral 6c site is cited to be fully occupied by vanadium.

Solvothermal reactions to synthesise a pure iron vanadate with the nolanite structure were attempted using the 1,4-butanediol method described above by substituting $Ga(acac)_3$ for $Fe(acac)_3$. This was to allow further comparison of the gallium vanadium

tohdite material against nolanite. All attempts were unsuccessful yielding a material with a diffraction pattern resembling that of a spinel. It is possible that longer reaction times may eventually bring about the formation of a nolanite material. The synthesis of an aluminium substituted gallium oxide spinel to a tohdite material using 1,4-butanediol as a solvent was presented in Chapter 4. Nolanite minerals obtained from different regions can contain cations other than iron and vanadium, but there has been a published study into synthetic nolanite synthesised by solvothermal synthesis,[62] which is the first published example of synthetic nolanite. The material was prepared using the iron and vanadium acetylacetonate salts with a benzyl alcohol and oleyl amine mixture as the solvent and reacted at 220 °C for 24 hours. XANES of the material showed it to contain only divalent iron and mixed tri and tetravalent vanadium cations. No mention on the coordination of any cation is given and the structure was not refined. The material displays room temperature ferromagnetism and is a semi-conductor, which, the authors claimed, offers scope of the material being used in data storage devices.

A Ti^{4+} substituted $Al_5O_7(OH)$ material has been prepared at high temperature and pressure (500 °C; 1.5 kbar) from an amorphous gel containing both Ti and Al. Up to 18% Ti^{4+} was reportedly included in the material. Reportedly, 3 Ti^{4+} cations replace 4 Al^{3+} cations leaving one Al site vacant in the structure.[55]

$Ga_{2.52}V_{2.48}O_{7.31}(OH)_{0.69}$ may also be isostructural with ferrihydrite. The structure of ferrihydrite was elaborated upon in Chapter 4 but in summary it has been proposed that it is an oxyhydroxide containing Fe^{3+} cations and is usually very poorly crystalline. A model suggesting that ferrihydrite is analogous to akdalaite was proposed based on analysis of its pair distribution function.[63]

Table 5.5 lists some materials that share similar crystal chemistry with $Ga_{2.52}V_{2.48}O_{7.31}(OH)_{0.69}$.

Table 5.5 Some materials analogous to $Ga_{2.52}V_{2.48}O_{7.31}(OH)_{0.69}$ and their lattice parameters, and space group.

		Lattice parameters		
Material	**Space Group**	***a***	***c***	**Reference**
$Ga_{2.52}V_{2.48}O_{7.31}(OH)_{0.69}$	$P6_3mc$	5.79044(17)	9.25704(4)	This work
$Al_5O_7(OH)$ (tohdite/akdalaite)	$P6_3mc$	5.8238(2)	9.0634(3)	[45]
$Ga_5O_7(OH)$	$P6_3mc$	5.82107(8)	9.0662(2)	[52]
$(Fe_{1.25}^{2+}V_{0.85}^{3+})V_{2.75}^{4+}O_8$, (nolanite)	$P6\,?$	5.85	9.29	[61]
Ti^{4+} substituted $Al_5O_7(OH)$	$P6_3mc$	5.571	8.759	[55]
$(Fe_{0.3}^{2+}Fe_{0.7}^{3+})(Ti_{0.55}^{4+}Al_{0.1}^{3+}V_{2.6}^{3+}Fe_{0.5}^{3+}Fe_{0.25}^{2+})O_7(OH)$, (nolanite)	$P6_3mc$	5.897(2)	9.256(3)	[58]
$Fe_{2.5}V_{1.5}V_{5.6}O_{16}$ (synthetic nolanite)	$P6_3mc$	5.854	9.295	[62]
$Fe_5O_7(OH)$ (ferrihydrite) (usually reported as $Fe_2O_3{\cdot}0.5H_2O$)	$P6_3mc$	5.958	8.965	[63]
$Fe_2Mo_3O_8$, (kamiokite)	$P6_3mc$	5.791(5)	9.945(5)	[64]
$(Mg_{1.57}Fe_{0.43})Mo_3O_8$ (Majindeite)	$P6_3mc$	5.778	9.904	[65]

Table 5.6 provides the average bond lengths in $Ga_{2.52}V_{2.48}O_{7.31}(OH)_{0.69}$ as obtained from the simultaneous refinement of X-ray and neutron data. As can be seen the O-H bond length of 0.863 Å is shorter than a typical O-H bond length of approximately 1 Å as was found in the $Ga_5O_7(OH)$ structure refinement.[52] In the crystal structure of $Al_5O_7(OH)$ the O-H bond length was reported as 0.876 Å[46] which is closer to the length seen in this gallium vanadium oxyhydroxide material, 0.863 Å. In the nolanite model reported by Gatehouse *et al.,* the position of the hydrogen was not refined since it was an X-ray study. That the bond lengths are similar to those in the pure gallium-tohdite material is unsurprising given the similarity in ionic radii between Ga^{3+} and V^{3+} in an octahedral environment, (0.62 Å and 0.64 Å respectively).[52,66] Bond valence sums (Table 5.7) agree well with the expected oxidation states of the metals present in $Ga_{2.52}V_{2.48}O_{7.31}(OH)_{0.69}$.

Table 5.6 List of bond lengths in the structure of $Ga_{2.52}V_{2.48}O_{7.31}(OH)_{0.69}$

	$Ga_{2.52}V_{2.48}O_{7.31}(OH)_{0.69}$		**$Ga_5O_7(OH)$**		
Wyckoff site	**Bond type**	**Bond Length / Å**	**Bond type**	**Bond Length / Å**	**Multiplicity**
6c	$(Ga_{0.29}, V_{0.71})$1-O1	2.070(5)	Ga1-O1	1.989(4)	1
Octahedral	$(Ga_{0.29}, V_{0.71})$1-O2	2.089(5)	Ga1-O2	2.046(4)	2
	$(Ga_{0.29}, V_{0.71})$1-O3	1.912(6)	Ga1-O3	1.921(5)	2
	$(Ga_{0.29}, V_{0.71})$1-O4	1.956(6)	Ga1-O4	1.979(4)	1
2b	$(Ga_{0.67}, V_{0.33})$2-O2	2.065(4)	Ga2-O2	2.117(5)	3
Octahedral	$(Ga_{0.67}, V_{0.33})$2-O3	1.933(4)	Ga2-O3	1.908(7)	3
2b	Ga3-O2	1.856(2)	Ga3-O2	1.856(3)	3
Tetrahedral	Ga3-O4	1.891(5)	Ga3-O4	1.871(6)	1
2a	O1-H1	0.863(18)	O1-H1	1.063(19)	

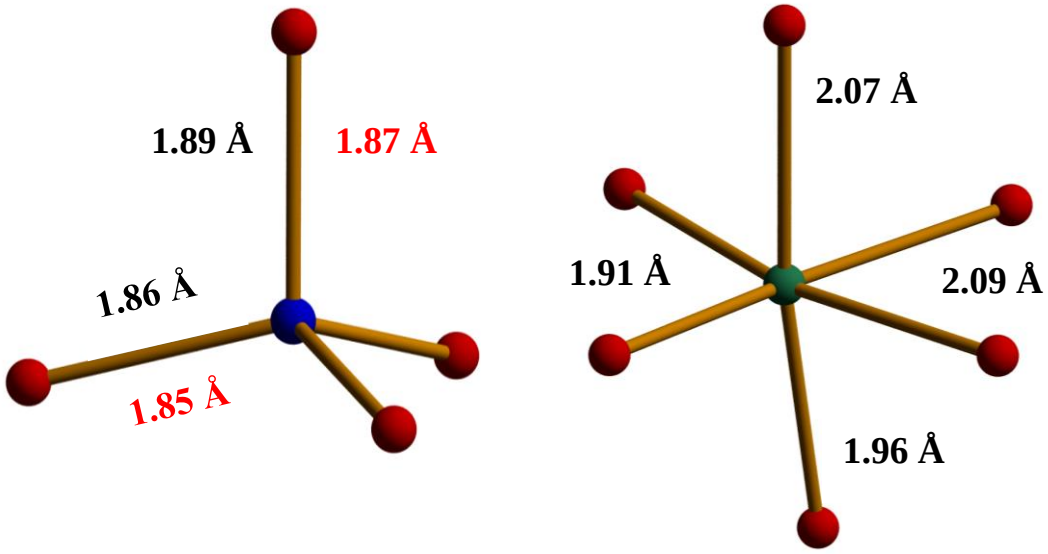

Figure 5.14 Tetrahedral bond lengths for $Ga_{2.52}V_{2.48}O_{7.31}(OH)_{0.69}$ *(black) cf.* tetrahedral bond lengths for pure tohdite *(red)*, and octahedral bond lengths showing metal displacement from centre of gravity in $Ga_{2.52}V_{2.48}O_{7.31}(OH)_{0.69}$.

Table 5.7 Bond valence sums (BVS) calculated for Ga and V in $Ga_{2.52}V_{2.48}O_{7.31}(OH)_{0.69}$.

Wyckoff site	Bond type	Ga BVS / vu	V BVS / vu
6c Octahedral	$(Ga_{0.29}, V_{0.71})$1-O	2.92	3.03
2b Octahedral	$(Ga_{0.67}, V_{0.33})$2-O	2.95	3.05
2b Tetrahedral	Ga3-O	2.78	-

5.3.5 Further characterisation

5.3.5.1 Electron microscopy

Electron microscopy was used to both image the material and to estimate the ratio of gallium and vanadium in the material. EDX by SEM and EELS by TEM both suggest that the metal ratio is close to 1:1 (Table 5.8).

Table 5.8 Metal ratio obtained from electron microscopy

Metal	EDX (SEM)	EELS (TEM)
Ga	50.2	48.9
V	48.8	51.1

Imaging by SEM reveals two distinct particle sizes: large clusters of thin plates, or isolated regions of very large plates (Figure 5.15). It is very likely that the anisotropic peak broadening observed in the powder diffraction data is a consequence of this large plate like nature. The plate morphology is also observed by TEM and atomic resolution imaging of this material was possible (Figure 5.16).

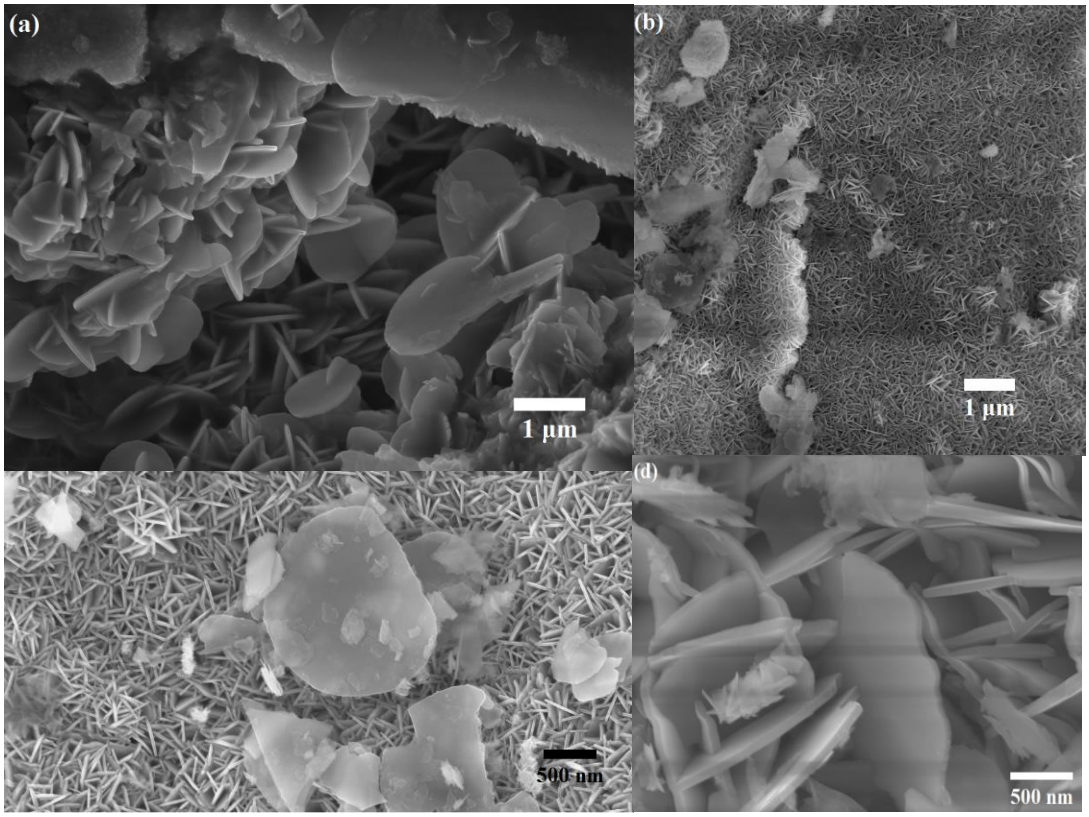

Figure 5.15 (a-d) SEM of $Ga_{2.52}V_{2.48}O_{7.31}(OH)_{0.69}$ showing both clusters of plates of varying size.

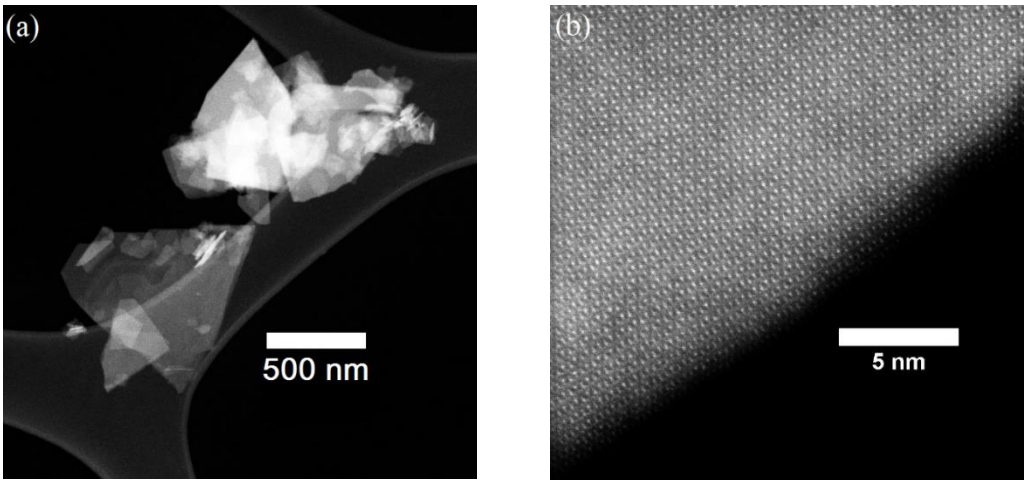

Figure 5.16 (a) TEM of $Ga_{2.52}V_{2.48}O_{7.31}(OH)_{0.69}$ revealing plate-like morphology, (b) HR-TEM showing atomic resolution of a $Ga_{2.52}V_{2.48}O_{7.31}(OH)_{0.69}$ plate.

5.3.5.2 Infrared spectroscopy

A simple but effective method to ascertain whether a material has a structurally bound hydroxyl group is to use infrared spectroscopy. This was successfully implemented in showing that $Ga_5O_7(OH)$ and $Ga_{5-x}Al_xO_7(OH)$ have hydroxyl groups (Chapter 4). The infrared spectra collected on $Ga_5O_7(OH)$ and $Ga_{2.52}V_{2.48}O_{7.31}(OH)_{0.69}$ are shown in Figure 5.17. The peak at ~3365 cm^{-1} corresponds to a (O-H) stretching mode, whilst the peak at ~740 cm^{-1} can be assigned to a (Ga,V)-O-H bending mode. Aside from the change in relative peak intensities the IR spectra of $Ga_5O_7(OH)$ and $Ga_{2.52}V_{2.48}O_{7.31}(OH)_{0.69}$ are quite similar, as expected.

Only a small weakly intense peak is found for $Ga_{2.52}V_{2.48}O_{7.31}(OH)_{0.69}$ in stark contrast to the sharp and strong intense peak for the O-H stretching mode in $Ga_5O_7(OH)$. The inset showing a close up of the O-H stretching mode confirms the presence of a hydroxyl group, as expected from the neutron refinement.

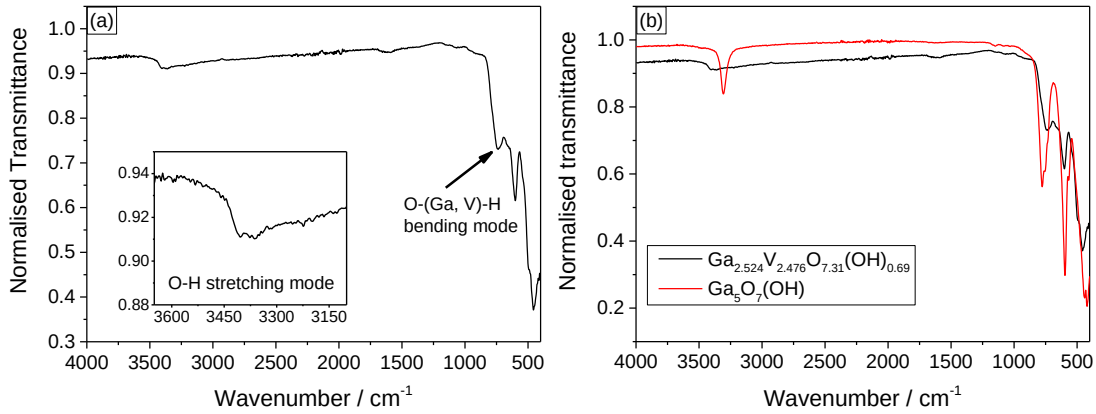

Figure 5.17 (a) Infrared spectroscopy showing an (O-H) stretching mode around 3365 cm^{-1} with *(inset)* showing a close up of the stretching mode, a (Ga,V)-O-H bending mode at ~740 cm^{-1} is also present, (b) comparison between the infrared spectrum of $Ga_{2.52}V_{2.48}O_{7.31}(OH)_{0.69}$ and $Ga_5O_7(OH)$.

A reaction carried out in a 1:1 mixture of MEA:D_2O attempted to deuterate the sample, which was partly successful. When H is substituted for its isotope D the wavenumber of the (O-D) should become smaller by a factor of $\sqrt{2}$ and therefore it is possible to predict the wavenumber of the O-D stretching mode, which in this material should be expected around 2380 cm^{-1} and indeed a small but real peak is observed in the infrared spectrum at around 2490 cm^{-1}, further evidence that the material has some bound hydroxyl group associated with it (Figure 5.18).

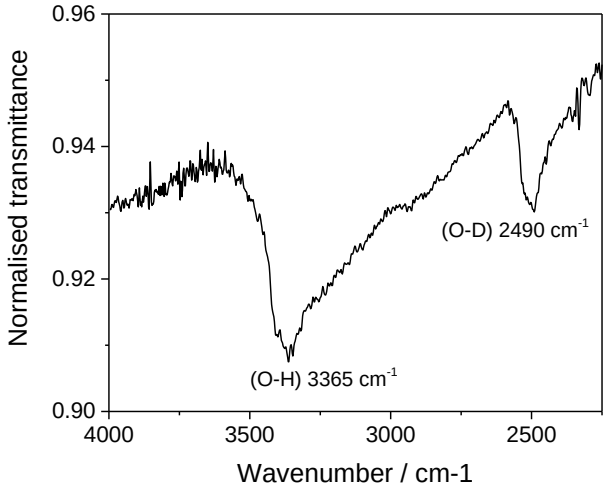

Figure 5.18 Infrared spectrum of a sample of $Ga_{2.52}V_{2.48}O_{7.31}(OH)_{0.69}$ with H partially substituted for D.

5.3.5.3 In situ thermodiffractometry

In situ powder XRD with heating reveals that upon heating to 300 °C several peaks suddenly shift to higher angle indicating a contraction of the cell which very slowly expands again (likely due to thermal expansion which is expected) up until 600 °C at which point the structure begins to collapse with expulsion of other phase(s) (Figure 5.19). Kappa and beta gallium oxide are likely candidates for the decomposition phases. Kappa is especially likely since in the contour map a transient phase lasting between 550 – 800 °C is observed which is expected from the thermal decomposition of $Ga_5O_7(OH)$.[52] It is not possible to identify any vanadium decomposition phases with any certainty in the room temperature pattern after firing to 810 °C. One possible explanation for the contraction of the cell is removal of the hydroxyl group which would require the vanadium to be oxidised in order to charge balance the structure giving a proposed formula of $Ga_{2.52}V_{2.48}O_8$. V^{4+} would be expected to have shorter bonds than V^{3+} and hence could explain the observed contraction in the cell. That this material is metastable and decomposes around 600 °C suggests that it is unlikely that it could be prepared by conventional high temperature synthesis.

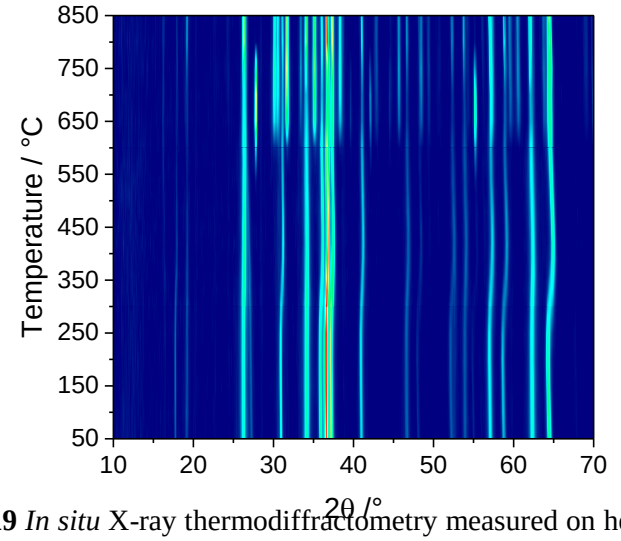

Figure 5.19 *In situ* X-ray thermodiffractometry measured on heating $Ga_{2.52}V_{2.48}O_{7.31}(OH)_{0.69}$ showing a contraction of the cell occurring around 250 °C – 450 °C. Phase separation occurs around 600 °C and transient phases are observed between 550 °C – 750 °C.

Refinement of the lattice parameters of this material with temperature shows that both the *a* and *c* lattice parameters decrease in size (Figure 5.20). The *a* parameter increases initially, likely due to thermal expansion, but then starts to gradually decrease after 150 °C and continues to get smaller upon heating to 300 °C. This is in contrast to the *c* parameter, which shows that although a sudden decrease occurs at 200 °C the *c* lattice parameter begins to expand once more immediately after the contraction.

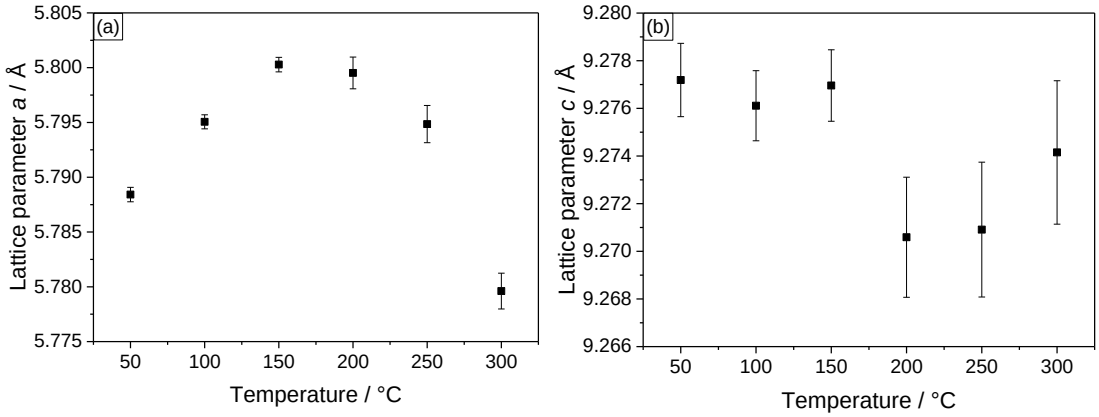

Figure 5.20 (a) Change in lattice parameter *a* with temperature, (b) change in lattice parameter *c* with temperature.

A separate sample was heated to 300 °C for 4 hours and then cooled to room temperature in order to analyse the structure of this material after the period of cell contraction. Infrared spectroscopy confirms that the O-H stretching mode has gone (Figure 5.21).

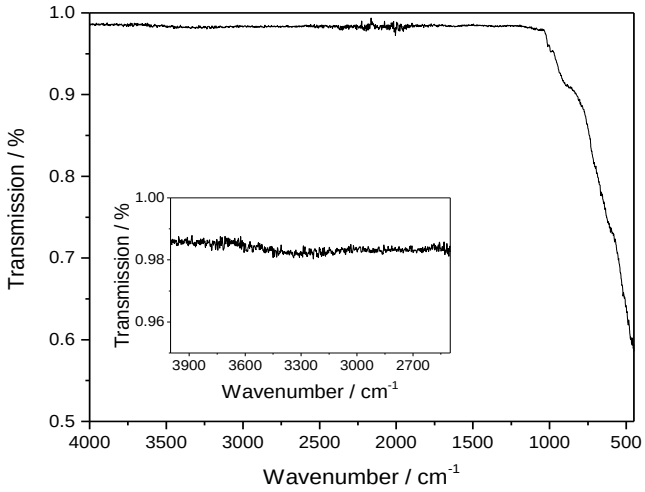

Figure 5.21 IR spectroscopy of a sample of $Ga_{2.52}V_{2.48}O_{7.31}(OH)_{0.69}$ fired at 300 C showing that the O-H stretching band has disappeared.

The room temperature powder XRD pattern after firing to 300 °C of this material shows that although the peaks present can all be indexed to a single phase there appears to be a broad feature in the background of the powder pattern between 25 – 40 °2θ, which could possibly be due to an amorphous phase beginning to form during or after the period of cell contraction (Figure 5.22). The broader peaks in the as-made sample have become noticeably sharper upon heat treatment.

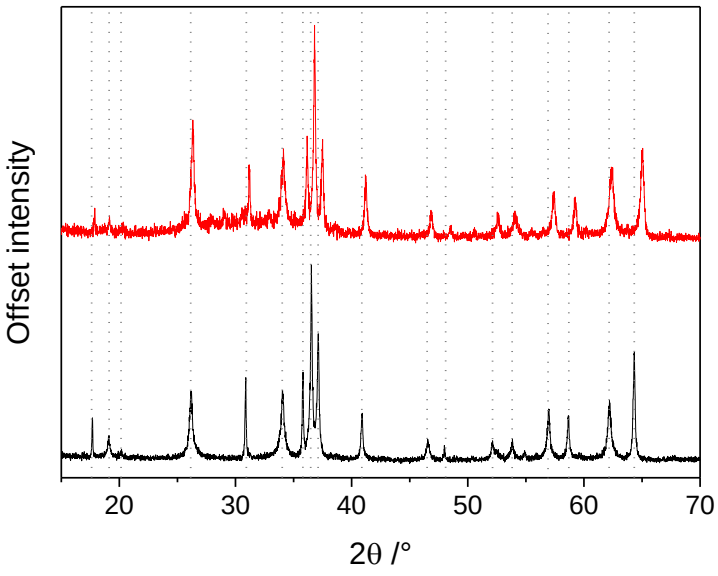

Figure 5.22 PXRD of as-made $Ga_{2.52}V_{2.48}O_{7.31}(OH)_{0.69}$ *(black)* and after firing to 300 °C *(red)* with a possible broad feature between 25-40 °2θ. Grey dotted lines highlight the shift to lower angle after firing.

A Pawley refinement of this phase yielded lattice parameters which shows that a contraction is occurring in both the *a* and *c* parameters (Table 5.9).

Table 5.9 Lattice parameters of $Ga_{2.52}V_{2.48}O_{7.31}(OH)_{0.69}$ before and after heating to 300 °C by *in situ* thermodiffractometry or box furnace.

	Lattice parameters from Pawley refinement of XRD data	
	***a* / Å**	***c* / Å**
As-made sample	5.78824(3)	9.2786(8)
After firing to 300 °C	5.7492(12)	9.260(3)
***In situ* 300 °C**	5.7796(16)	9.274(3)

The difference in the size of the lattice parameters of the sample between the *in situ* heating experiment and the XRD data after firing to 300 °C is likely due to added complexity of the thermal expansion of the cell acting against the cell contraction for the sample measured *in situ*.

A similar X-ray diffraction *in situ* heating experiment was also performed in flowing N_2 as to prevent any possible oxidation of vanadium should this be occurring (Figure 5.23). The contraction of the cell still occurred but at a much higher temperature (~500 °C), and the structure remains a phase pure material after heating to 810 °C and no crystalline decomposition materials are observed suggesting that heating in air causes collapse of the structure due to oxidation of the vanadium which leads to formation of other materials.

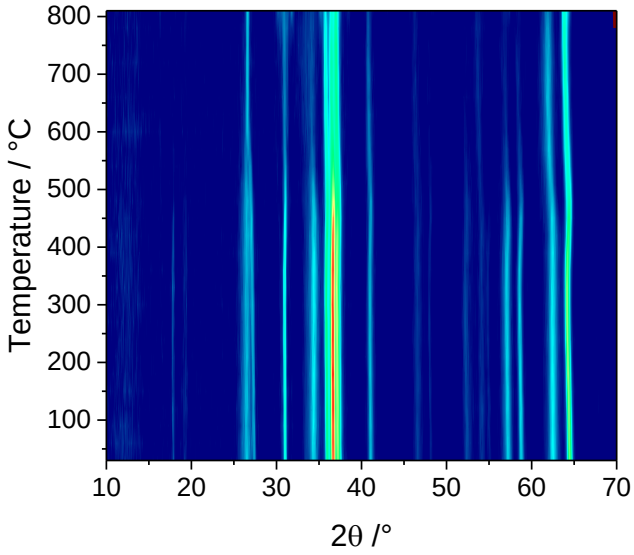

Figure 5.23 *In situ* thermodiffractometry of $Ga_{2.52}V_{2.48}O_{7.31}(OH)_{0.69}$ whilst heated in flowing N_2.

5.3.5.4 TGA-MS

In order to probe whether hydroxide loss meant that water was being evolved at 300 °C TGA-MS was carried out on a sample of $Ga_{2.52}V_{2.48}O_{7.31}(OH)_{0.69}$ (Figure 5.24). The sample was heated rapidly to 300 °C in air. A gradual mass loss occurs upon heating to 250 °C which was followed by a second steeper period of mass loss up to around 350 °C. A mass loss of 1.2% is observed which is close to the mass loss expected for the proposed formula above which would be 1.4%. Mass spectrometry clearly indicates the presence of H_2O at around 200 °C which continues to increase in intensity up to around 375 °C. At this temperature this is unlikely to be surface bound water and is further evidence for a structural O-H group. When compared alongside the X-ray *in situ* heating experiment this suggests that the contraction in the cell (between 300 – 400 °C) is due to removal of the structural O-H groups.

In the TGA a mass increase occurs around 350 °C up to 400 °C and during this time the intensity of the H_2O signal decreases. The increase in mass seen in the TGA could be due to oxidation and uptake of oxygen due to formation of other phases. Though crystalline phases do not present themselves until 600 °C (as observed by *in situ* thermodiffractometry), in the powder XRD pattern after heating to 300 °C the broad feature in the XRD pattern is indicative of an amorphous material forming which could be due to the onset of phase separation.

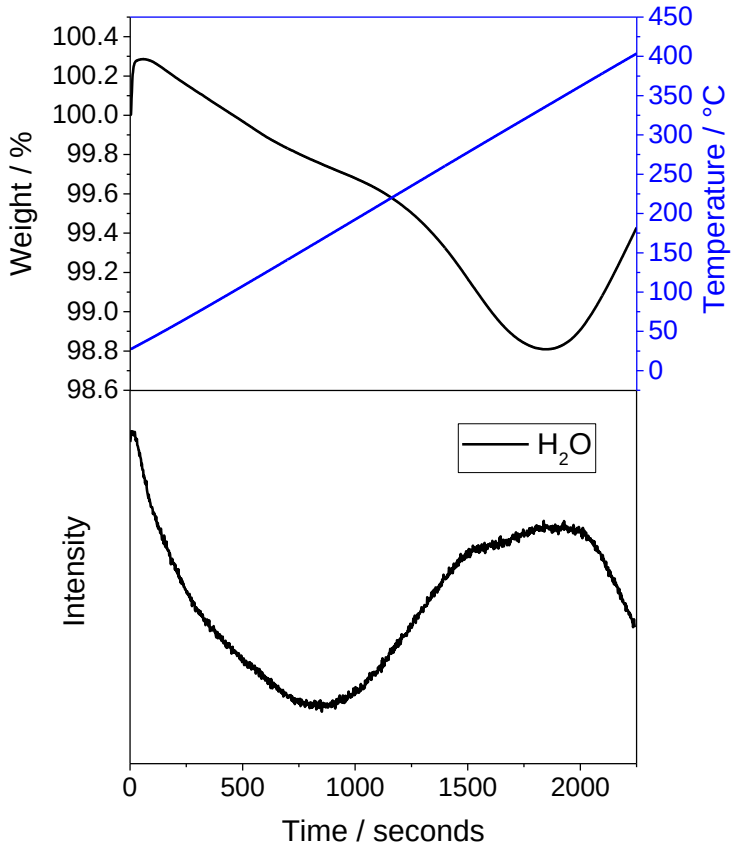

Figure 5.24 TGA-MS of $Ga_{2.52}V_{2.48}O_{7.31}(OH)_{0.69}$ showing the presence of H_2O being evolved from the structure between 200-350 °C.

5.3.5.5 XANES

XANES at the vanadium K-edge was measured at the B18 beamline at the Diamond Light Source. V_2O_3 and $VO(acac)_2$ references were prepared by reactions described in Appendix A.

Analysis of the data showed that in the as-made sample the calculated oxidation state of vanadium is $V^{3.11+}$ (Figure 5.25). This agrees excellently with the expected oxidation state of vanadium in the structural model obtained by Rietveld refinement of powder neutron and X-ray diffraction data which required vanadium to be $V^{3.13+}$. The presence of a small amount of V^{4+} is hardly surprising: V^{3+} compounds are typically unstable in air (V_2O_3 oxidises slowly in air to VO_2; most aqueous V^{3+} cations oxidise to the stable diatomic VO^{2+} species). XANES was also measured on a sample which had been heated to 300 °C for 1 hour in air, which showed a higher oxidation state of $V^{3.40+}$. This is in agreement with observed data from IR, *in situ* thermodiffractometry and TGA-MS that at an elevated temperature the oxyhydroxide is dehydrated requiring the vanadium to be partially oxidised in order to charge

balance the structure before it collapses at the higher temperature of 600 °C. Using the refined formula for vanadium gallium oxyhydroxide as $Ga_{2.52}V_{2.48}O_{7.31}(OH)_{0.69}$ the expected formula of the sample when dehydrated should be $Ga_{2.52}V_{2.48}O_8$, which assumes an oxidation state of vanadium as being $V^{3.40+}$.

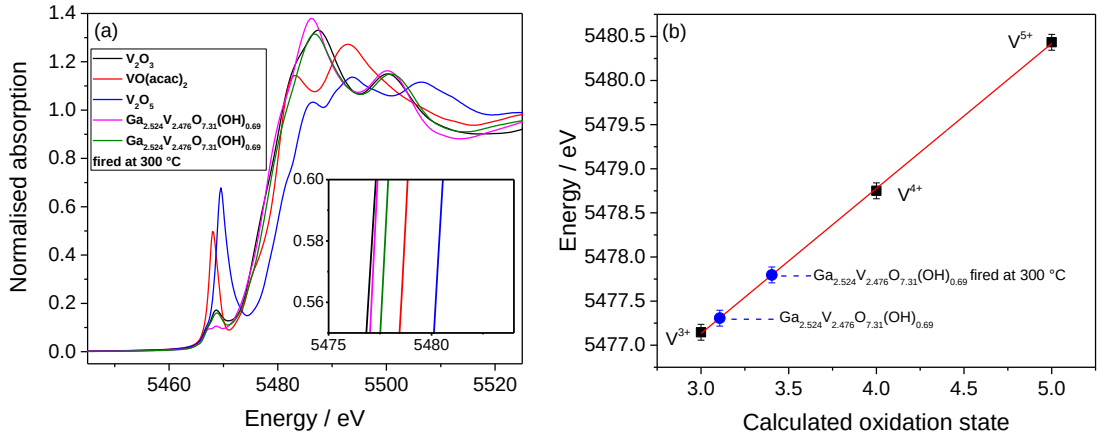

Figure 5.25 (a) V K-edge XANES spectra normalised to the edge step of $Ga_{2.52}V_{2.48}O_{7.31}(OH)_{0.69}$ and relevant references (inset shows a close up of the edge position for all materials), (b) plot of edge position (defined as the energy at which normalised absorption = 0.5) as a function of oxidation state with a linear fit to reference materials providing the calculated oxidation of vanadium in $Ga_{2.52}V_{2.48}O_{7.31}(OH)_{0.69}$ and $Ga_{2.52}V_{2.48}O_{7.31}(OH)_{0.69}$ fired at 300 °C (both in blue).

5.3.5.6 Magnetometry

The *M vs T* curve measured with an applied field of 1000 Oe, suggests that $Ga_{2.52}V_{2.48}O_{7.31}(OH)_{0.69}$ is paramagnetic in both the zero-field cooled (ZFC) and field cooled (FC) measurements (Figure 5.26). An inverse susceptibility plot shows that linear Curie-Weiss behaviour, typical for paramagnetic materials, is observed during the temperature range 200-300 K, and an effective magnetic moment can be calculated from these data as 4.77 μ_B. This does not agree with the spin only magnetic moment were vanadium to be present in only the trivalent state, which the spin only formula calculates as 2.83 μ_B. Deviation from the spin only calculation was expected since XANES and the refined composition from XRD and PND data suggest a small amount of V^{4+} to be present.

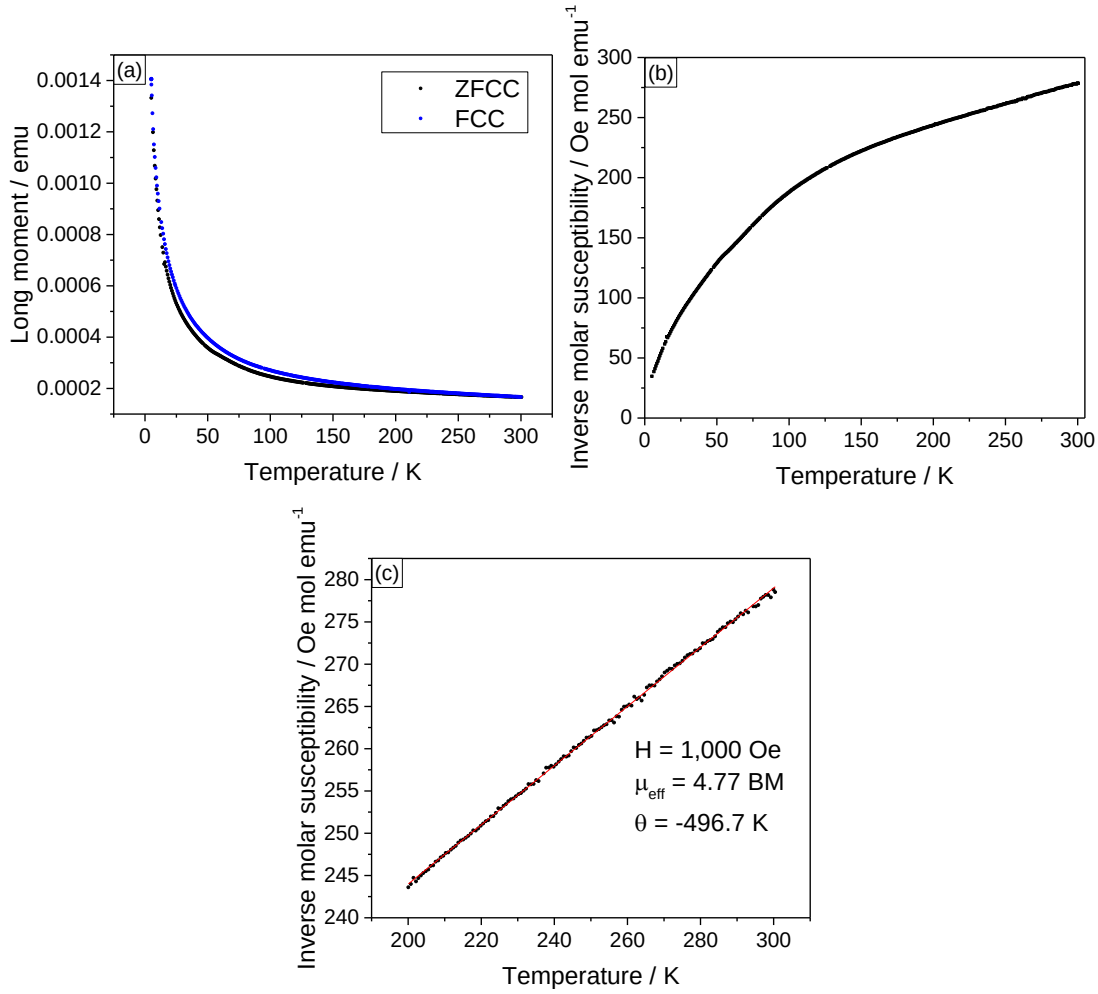

Figure 5.26 (a) ZFC and FC *M vs T* plot of $Ga_{2.52}V_{2.48}O_{7.31}(OH)_{0.69}$ (b) inverse susceptibility over the entire temperature range measured, (c) linear Curie-Weiss behaviour between 200 – 300 K and calculation of the effective magnetic moment.

ZFC magnetometry of a sample fired at 300 °C also shows similar paramagnetic behaviour (Figure 5.27). Linear Curie-Weiss behaviour is again only observed in the temperature range 200 – 300 K. Below 200 K the inverse susceptibility deviates from this relationship and this is likely due to weak interactions with the V cations in the material. The presence of an amorphous impurity phase as suggested by XRD cannot be ruled out and so an effective magnetic moment was not calculated for this material.

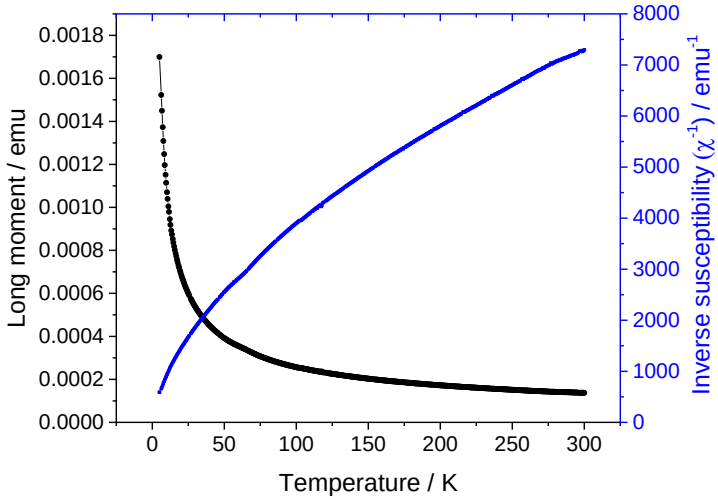

Figure 5.27 ZFC *M* vs *T (black)* curve and inverse susceptibility *(blue)* for $Ga_{2.52}V_{2.48}O_{7.31}(OH)_{0.69}$ fired at 300 °C displaying paramagnetic behaviour.

5.4 Synthesis of a new Cr substituted γ-Ga_2O_3

5.4.1 Synthesis

0.3 g (0.82 mmol) of $Ga(acac)_3$, (Sigma, 99.99%), and 0.093 g (0.35 mmol) of $CrCl_3 \cdot 6H_2O$ (Aldrich, 96%) were added to a 23 ml PTFE lined steel autoclave followed by addition of 10 ml 1,4-butanediol. The ratio of metals for this reaction is therefore 0.7:0.3 Ga:Cr. Other ratios were tried higher than 30% but there was always formation of GaOOH present in the isolated polycrystalline material. The mixture was stirred vigorously for 15 minutes at room temperature before being sealed and placed into a fan-assisted oven pre-heated to 240 °C for 72 hours. The autoclave was then removed from the oven and left to cool naturally to ambient temperature. The crystallised material was stirred in its mother liquor, aided by addition of acetone to reduce the viscosity of the solvent. The material was collected by vacuum filtration and washed with copious amounts of acetone to yield a green coloured solid. The material was then dried overnight at 70 °C prior to characterisation. Longer reaction times did not yield the oxyhydroxide (tohdite) phase as seen with $V(acac)_3$ and $Al(acac)_3$.

72-hour solvothermal reactions of either $Ga(acac)_3$ or $CrCl_3 \cdot 6H_2O$ in 1,4-butanediol formed γ-Ga_2O_3 (usually contaminated with some GaOOH) and α-CrOOH (grimaldiite) respectively.

A separate control solvothermal reaction using $Cr(acac)_3$ in 1,4-butanediol instead of $CrCl_3 \cdot 6H_2O$ formed an amorphous phase instead. This could be γ-CrOOH, which has been reported in the literature as being amorphous when prepared hydrothermally.[67] $Cr(acac)_3$ was prepared by the method described by Fernelius *et al*.[68] 2.66 g (0.01 mol) of $CrCl_3 \cdot 6H_2O$ (Aldrich, 96%) was dissolved in 20 g (0.3 mol) $CO(NH_2)_2$ (Aldrich, 99.0%) followed by addition of 6 g (0.06 mol) of acetylacetone (Fisher, 99%). The mixture was heated to reflux and left for 1 hour. As the reaction progressed CO_2 and NH_3 were released as the urea was hydrolysed and maroon coloured crystals began to form. The reaction was concluded upon termination of CO_2 effervescence and the crystals collected by vacuum filtration. The crude product was recrystallized in hot toluene and forced out of solution by the petroleum ether anti-solvent whilst cooling in ice to ~0 °C.

The reaction of $Ga(acac)_3$ with $Cr(acac)_3$ also made a spinel with no other crystalline impurity phases present but since the control reaction of $Cr(acac)_3$ yields an amorphous material it was the spinel produced when $CrCl_3 \cdot 6H_2O$ was used that was studied for further analysis.

5.4.2 Powder X-ray diffraction

The powder XRD pattern of chromium substituted gallium oxide can be indexed and its profile fitted to a cubic spinel group (space group $Fd\bar{3}m$) (Figure 5.28). The refined lattice parameter a = 8.233(2) Å is very similar to nano-crystalline pure γ-Ga_2O_3 where the refined lattice parameter a = 8.2440(2) Å.[52] This is unsurprising given that the Cr^{3+} cation is very similar in size to the Ga^{3+} cation in an octahedral environment (0.615 Å for Cr^{3+} and 0.62 Å for Ga^{3+}).[66] The extremely broad Bragg reflections suggest a poorly crystalline material consisting of very small particles.

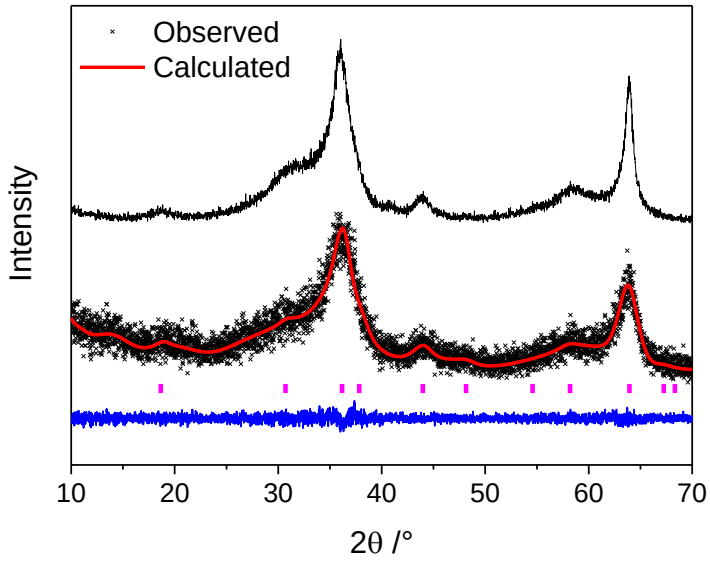

Figure 5.28 Pawley refinement of the profile of a chromium substituted γ-Ga_2O_3 showing pure γ-Ga_2O_3 above the Pawley refinement as a comparison.

Owing to the broad Bragg reflections of this poorly crystalline material, Rietveld refinement against the X-ray diffraction was not possible.

The powder XRD data of α-CrOOH shows a distinctly different powder pattern to that of the spinel but it matches well to a simulated pattern of α-CrOOH[69] (Figure 5.29). This also contains broad Bragg reflections indicating that the material also consists of small particles.

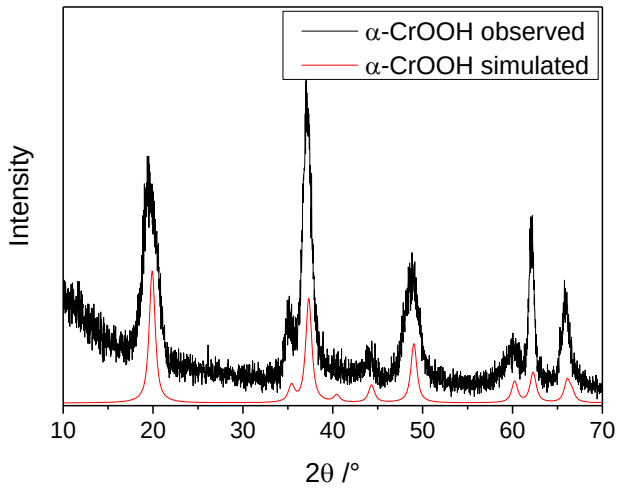

Figure 5.29 Powder XRD pattern of synthesised α-CrOOH against a simulated pattern.

5.4.3 Further characterisation

5.4.3.1 XANES

XANES was measured at the Cr K-edge to obtain information on the local environment of the chromium. XANES was measured on B18 at the Diamond Light Source on a sample of 30% Cr substituted γ-Ga_2O_3 with appropriate chromium reference materials to calibrate the oxidation state.

Figure 5.30 shows that the chromium is present exclusively in the trivalent oxidation state. Examination of the pre-edge region shows the lack of any significant pre-edge feature, which is indicative of chromium substituting gallium for the octahedral sites in the spinel. This material should then be described as a defect spinel, with the formula γ-$Ga_{1.4}Cr_{0.6}O_3$ as it remains lacking in the divalent cation required for the spinel structure of type AB_2O_4. The formula may be written as □$Ga_{1.867}Cr_{0.8}O_4$, where □ represents a vacant metal site in the spinel.

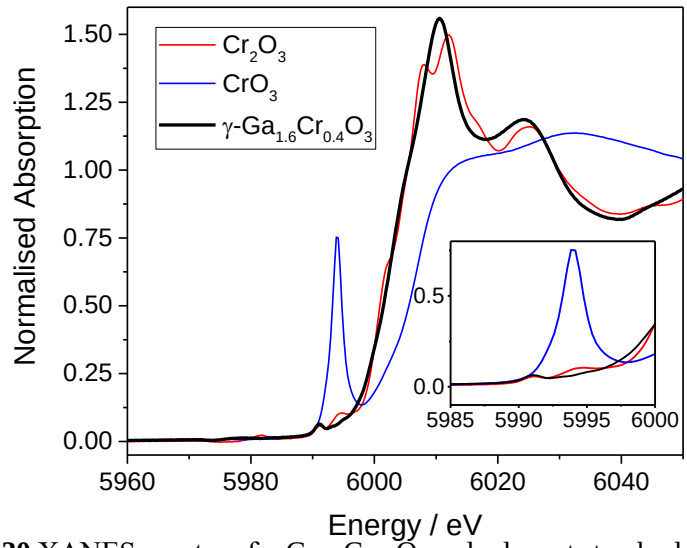

Figure 5.30 XANES spectra of γ-$Ga_{1.4}Cr_{0.6}O_3$ and relevant standards with *(inset)* showing the lack of pre-edge feature.

5.4.3.2 Electron microscopy

5.4.3.2.1 Transmission electron microscopy (TEM)

HR-TEM imaging confirms the small particle size with individual particles having a size around ~10 - 25 nm in diameter. Atomic resolution images show that the material

has ordered crystalline lattice fringes (Figure 5.31). EELS confirmed the ratio of chromium to gallium in the spinel as approximately 0.3:0.7.

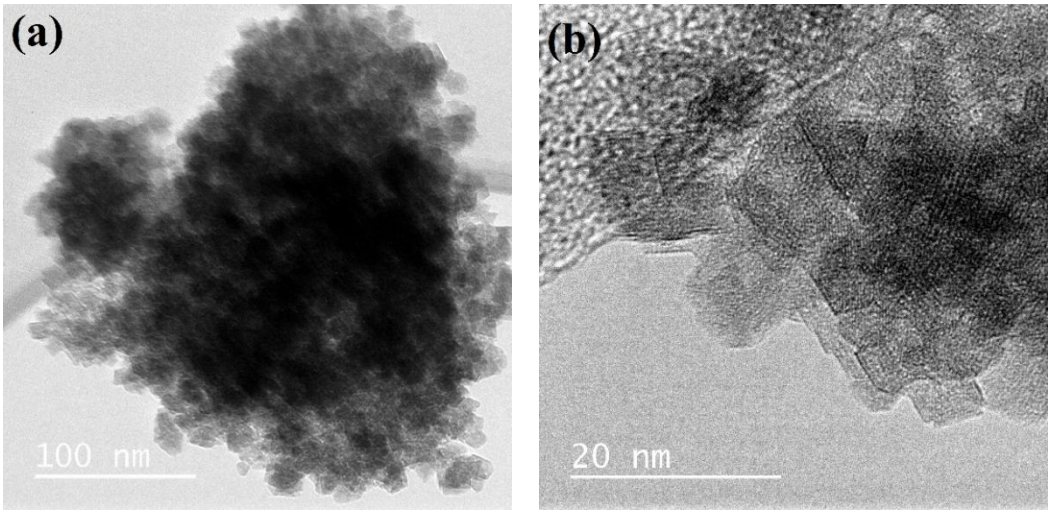

Figure 5.31 (a) TEM of γ-$Ga_{1.4}Cr_{0.6}O_3$, (b) HR-TEM displaying crystalline lattice fringes.

5.4.3.3 X-ray thermodiffractometry

X-ray diffraction was measured as a sample of γ-$Ga_{1.4}Cr_{0.6}O_3$ was heated to 900 °C at 50 °C temperature intervals (Figure 5.32(a)). The spinel structure is stable up to ~850 °C before phase separation begins to occur indicated by the appearance of reflections at 50 and 55 °2θ in Figure 5.32(b). Although some phase separation has occurred the spinel structure is still present at 900 °C. No β-Ga_2O_3, the thermodynamically stable polymorph of Ga_2O_3, is observed at 900 °C.

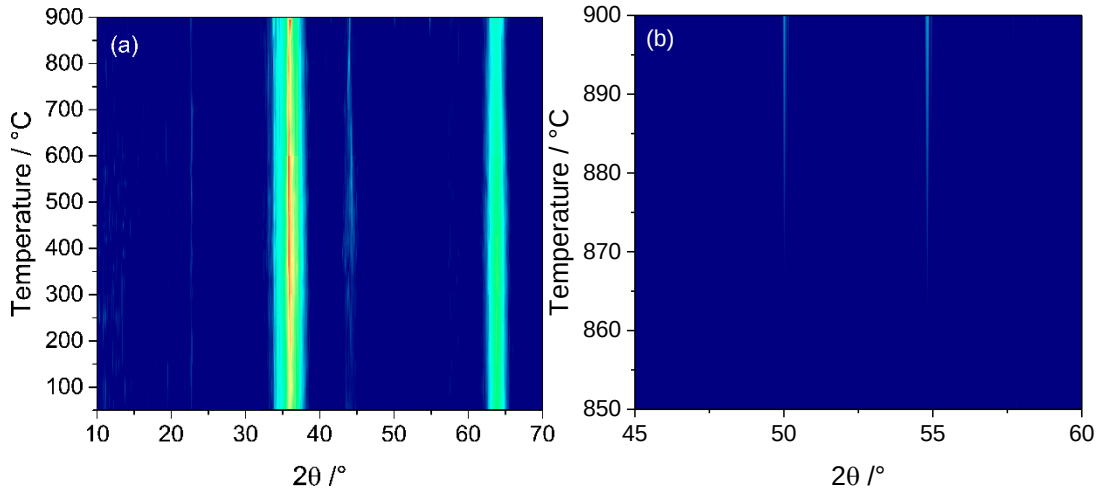

Figure 5.32 (a) *In situ* thermodiffractometry of γ-$Ga_{1.4}Cr_{0.6}O_3$ (b) close up on the region where phase separation begins to occur.

The substitution of chromium for gallium into this material enhances the thermal stability of the spinel as pure γ-Ga_2O_3 transforms into β-Ga_2O_3 above 700 °C (Figure 5.33(a)). XRD of α-CrOOH was also measured whilst heated to 900 °C and can be seen to be stable up to 350 °C before transformation into Cr_2O_3 (Figure 5.33(b)). Inspection of the powder XRD pattern of Cr_2O_3 in Figure 5.33(b) shows reflections at 50 and 55 °2θ, which are also present in the decomposition of γ-$Ga_{1.4}Cr_{0.6}O_3$ suggesting that Cr_2O_3 is a strong candidate for the material into which the mixed metal defective spinel starts to phase separate. The phase separation into Cr_2O_3 at ~850 °C but retention of the spinel structure could also be an example of Zener pinning. This is where particles of one phase prevent the sintering or collapse of a second phase

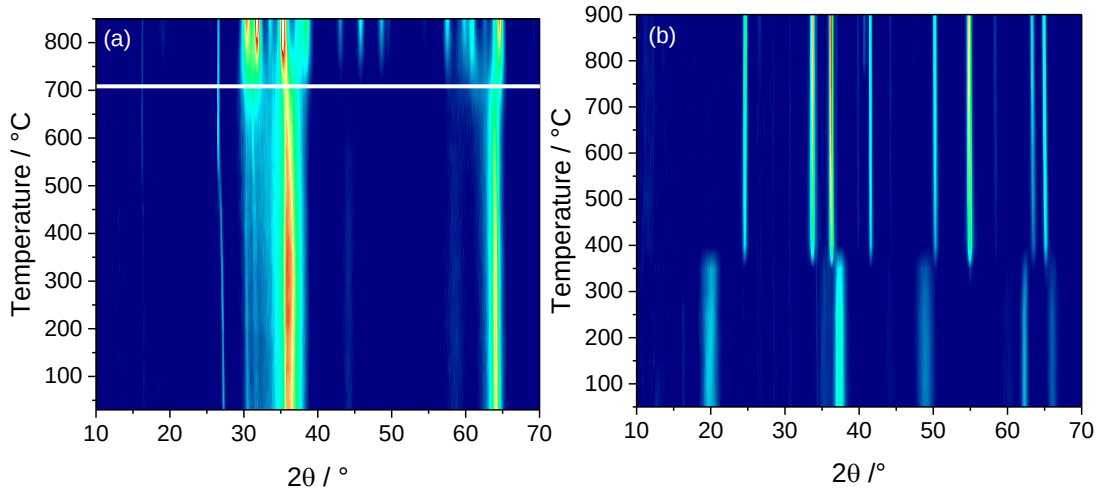

Figure 5.33 (a) *In situ* thermodiffractometry of γ-Ga_2O_3 with the white bar showing the onset of phase transformation into β-Ga_2O_3, (b) *in situ* thermodiffractometry of α-CrOOH showing transformation into Cr_2O_3 at ~350 °C.

A separate thermodiffraction experiment was done to heat the amorphous phase prepared by reaction of $Cr(acac)_3$ in 1,4-butanediol, here assigned γ-CrOOH, to see whether in the synthesis of γ-$Ga_{1.4}Cr_{0.6}O_3$ any of this amorphous phase was also present. As Figure 5.34 shows the amorphous phase transforms immediately into Cr_2O_3 at around 350 °C. The fact that no Cr_2O_3 forms in the *in situ* heating experiment of γ-$Ga_{1.4}Cr_{0.6}O_3$ at this temperature indicates that neither α or γ-CrOOH is present as an impurity phase in the synthesis of this mixed metal spinel. Further, the transformation of this amorphous phase into Cr_2O_3 at the low temperature of 350 °C is also suggestive that this amorphous phase is an oxyhydroxide, the proposed γ-CrOOH.

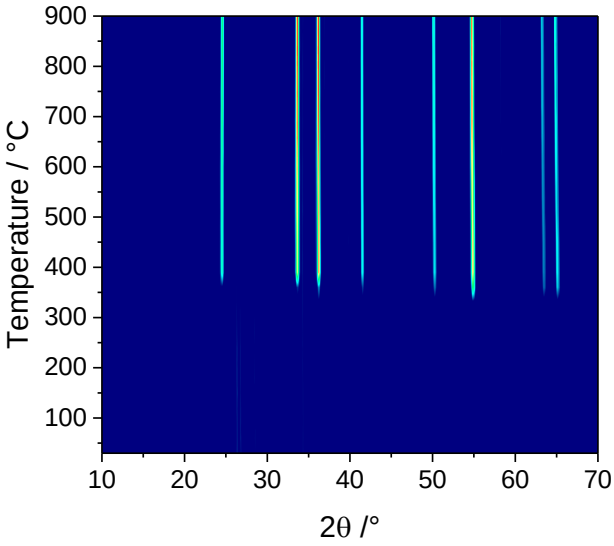

Figure 5.34 *In situ* thermodiffractometry of an amorphous chromium oxyhydroxide phase, nominally γ-CrOOH showing phase transformation into Cr_2O_3 at ~350 °C.

5.4.3.4 Magnetometry

The field cooled (FC) *M vs T* plot of γ-$Ga_{1.4}Cr_{0.6}O_3$ shows that this material is paramagnetic displaying linear Curie-Weiss behaviour to 50 K. The effective magnetic moment of the Cr^{3+} cation in this material was calculated as 3.85 μ_B which is in good agreement with the spin only formula calculation for an octahedral d^3 cation of 3.88 μ_B. The negative Weiss constant suggests a tendency for the Cr^{3+} spins to align antiferromagnetically.

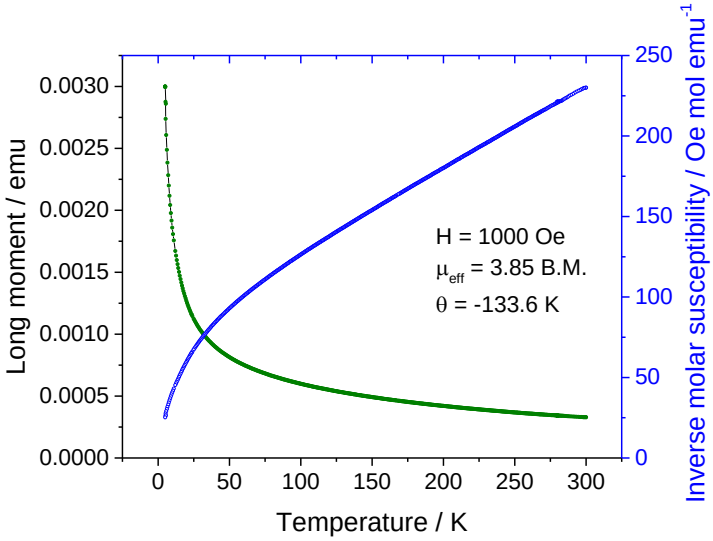

Figure 5.35 Field cooled (FC) magnetometry of γ-$Ga_{1.4}Cr_{0.6}O_3$ *(green)* showing simple paramagnetic behaviour, and inverse susceptibility *(blue)*.

The field cooled *M vs T* plot of α-CrOOH also shows simple paramagnetic behaviour obeying the Curie-Weiss law with inverse molar susceptibility from 300 to 25 K. The magnetic moment, which was calculated over the temperature range 25 – 300 K, was found to be 3.68 μ_B which is in good agreement with the spin only formula of 3.88 μ_B and in close agreement with the literature value of 3.74 μ_B.[67] The large negative Weiss constant is suggestive of a tendency for the spins to align antiferromagnetically.

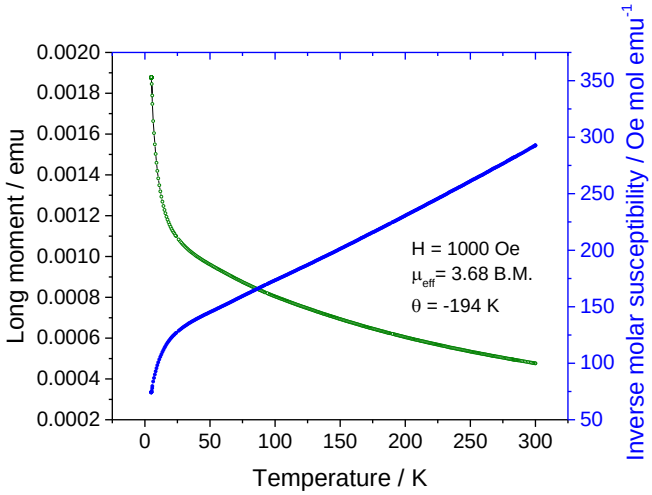

Figure 5.36 Field cooled (FC) magnetometry *(green)* of a sample of α-CrOOH showing simple paramagnetic behaviour and inverse molar susceptibility *(blue).*

5.5 Synthesis of a nano-crystalline manganese gallium oxide spinel

Chapter 3 presented the solvothermal synthesis of a cobalt gallium oxide and illustrated how the synthetic preparation, post-synthesis thermal treatment and the heating conditions strongly affect the crystal chemistry of the spinel. Therefore, other spinels prepared by low temperature synthesis techniques are also likely to contain a cation distribution different to the spinel of similar composition but prepared at high temperatures. A preliminary investigation into the synthesis and characterisation of a manganese gallium oxide is presented.

$MnGa_2O_4$ has been prepared by high temperature solid state reactions and largely shown to be a normal spinel with Mn^{2+} occupying the tetrahedral sites.[26] The spinel showed antiferromagnetic ordering with a Néel temperature of 33 K.[14] One-dimensional nanostructures of $MnGa_2O_4$ and Zn-doped $MnGa_2O_4$ have been reported[70] by thermal evaporation techniques but the only solvothermal synthesis of $MnGa_2O_4$, to date, required use of a microwave in the synthesis.[30]

In this work, it was found that if a manganese salt was reacted with Ga metal in ethanolamine then no reaction occurred and only formation of a brown gel at the bottom of the autoclave when gallium metal was used as the reagent or in the case of pre-formed γ-Ga_2O_3 only unreacted gallium oxide and formation of Mn_3O_4 was obtained. Therefore, a different approach was required to obtain $MnGa_2O_4$ from solvothermal reactions. The reaction was based on the synthesis of mixed metal Al^{3+} substituted Ga_2O_3 defect spinels presented in Chapter 4.

5.5.1 Synthesis

$Mn(acac)_3$ was prepared based on the method described by Bhattacharjee *et al*.[71] 5.0 g (31.7 mmol) of $KMnO_4$, (Fisher, 99%) was dissolved in the minimum amount of water aided by warming in a steam bath. 22.0 g (220.0 mmol) acetylacetone (Fisher, 99%) was then added to the solution with vigorous stirring. The mixture was stirred for twenty minutes under reflux and then cooled for thirty minutes with precipitation of dark brown crystals of $Mn(acac)_3$. These crystals were filtered by vacuum filtration and then washed several times with an acetone:water mixture (1:1 by volume). The crystals were then recrystallized by dissolving them in the minimum amount of hot toluene followed by addition of petroleum ether and cooled to around 0 °C.

In a typical synthesis of $MnGa_2O_4$, 0.4 g (1.09 mmol) of $Ga(acac)_3$ (Sigma, 99.99%) and 0.165 g (0.468 mmol) of $Mn(acac)_3$ were placed in a 23 ml PTFE liner with subsequent addition of 10 ml 2-propanol. The mixture was stirred at room temperature for 10 minutes before being sealed in a steel autoclave and placed in a fan-assisted oven pre-heated to 240 °C for 24 hours. After the reaction dwell time, the autoclave was removed from the oven and allowed to cool naturally to ambient temperature and collected by vacuum filtration. The solid product was then washed with copious amounts of acetone to yield a light brown powder. The isolated solid polycrystalline material was then dried overnight at 70 °C prior to any characterisation.

Reaction of $Mn(acac)_3$ with 2-propanol formed rocksalt-type MnO. $Mn(NO_3)_2{\cdot}4H_2O$ can also be used as the reagent to prepare $MnGa_2O_4$ using 2-propanol as the solvent and controlled reaction of this reagent alone in 2-propanol yields Mn_3O_4.

5.5.2 Powder X-ray diffraction

The room temperature powder XRD pattern of the manganese gallium oxide material prepared is shown as the red pattern in Figure 5.37(a). Very broad Bragg reflections suggest nano-sized particles and a large surface area. The material prepared is less crystalline than the pure nano-crystalline γ-Ga_2O_3 (prepared by similar solvothermal reaction) which is similar to what was observed with the aluminium substituted gallium oxides presented in Chapter 4, however a shift to lower angle occurs with the presence of manganese. This is in keeping with the larger size of the Mn^{2+} cation than the Ga^{3+} (Mn^{2+}: 0.66 Å (tetrahedral), 0.83 Å (octahedral) *cf.* Ga^{3+}: 0.47 Å (tetrahedral), 0.62 Å (octahedral)).[66] As expected the material could be indexed and the profile fitted to a cubic spinel group with space group $Fd\bar{3}m$, (Figure 5.37(b)) and a Pawley refinement of the lattice parameter showed an increase in the unit cell size compared to pure γ-Ga_2O_3 prepared by similar solvothermal reaction, (8.297(4) *cf.* 8.258 Å respectively). This is a smaller lattice parameter than for $MnGa_2O_4$ prepared by a high temperature synthesis (8.435 Å)[26] but a difference in the cation distribution in this poorly crystalline material prepared solvothermally compared to the arrangement prepared from high temperature synthesis could account for this observation.

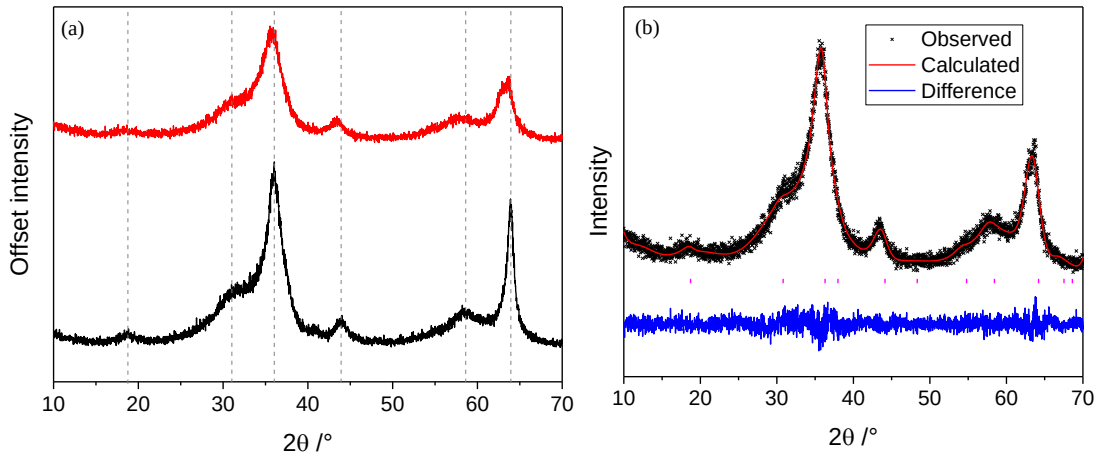

Figure 5.37 (a) nano-crystalline γ-Ga_2O_3 *(black)* and manganese gallium oxide *(red)* with grey dotted lines showing a shift to lower angle for the manganese spinel, (b) Pawley refinement of a sample of manganese gallium oxide prepared solvothermally.

5.5.3 XANES

XANES was measured at the Mn K-edge and shows that in the manganese gallium spinel manganese is present as Mn^{2+}, like in rock salt MnO (Figure 5.38). Transition metal monoxides are rarely stoichiometric[72] and so the presence of a small amount of Mn^{3+} might be expected, whereas in the spinel there could be a small amount of Mn^{3+}

if the spinel is partially manganese rich as has been observed in other spinels prepared solvothermally.[11] There is only a small pre-edge feature, though this is not as intense as the pre-edge in Mn_3O_4 and so it is unlikely that there is much tetrahedrally coordinated manganese indicating that $MnGa_2O_4$ prepared by this method is largely an inverse spinel. This is different to the high temperature material in the literature, which is a largely normal spinel and shows that, as the difference in lattice parameter indicated, there is a different cationic distribution in the spinel prepared by solvothermal synthesis than that prepared by a solid-state reaction.[14]

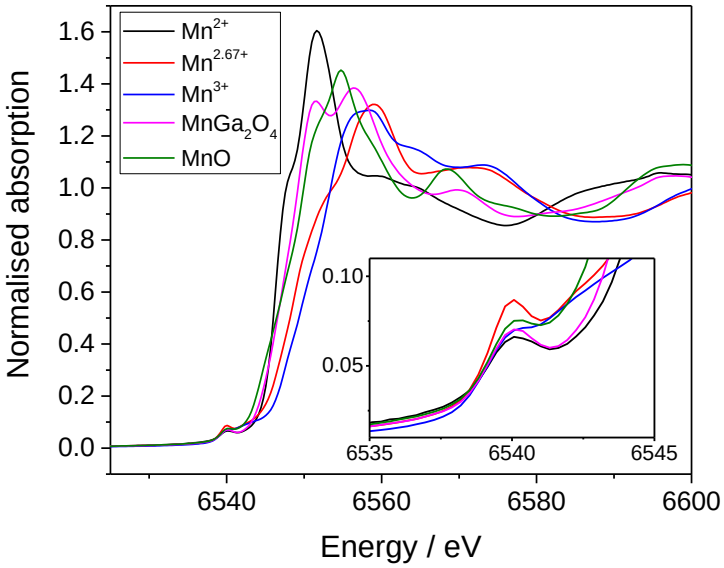

Figure 5.38 XANES spectra of manganese gallium oxide with relevant reference samples. (Mn^{2+} - $Mn(NO_3)_2{\cdot}4H_2O$; $Mn^{2.67+}$ - Mn_3O_4; Mn^{3+} - $Mn(acac)_3$)

5.5.4 In situ *X-ray thermodiffractometry*

In situ X-ray thermodiffractometry showed that the poorly crystalline $MnGa_2O_4$ spinel begins to phase separate at ~480 °C and then undergoes phase transformation into β-Ga_2O_3 upon reaching 700 °C (Figure 5.39(a)).

MnO, prepared from the solvothermal reaction of $Mn(acac)_3$ in 2-propanol, oxidises to Mn_2O_3 (bixbyite) at 480 °C (Figure 5.39(b)). The strongest Bragg reflections of Mn_2O_3 in this heating pattern at 24 and 32 °2θ correspond well with the two peaks observed in the heating map of $MnGa_2O_4$ at this temperature suggesting that in this spinel Mn_2O_3 is the material being ejected from the spinel structure at ~450 °C.

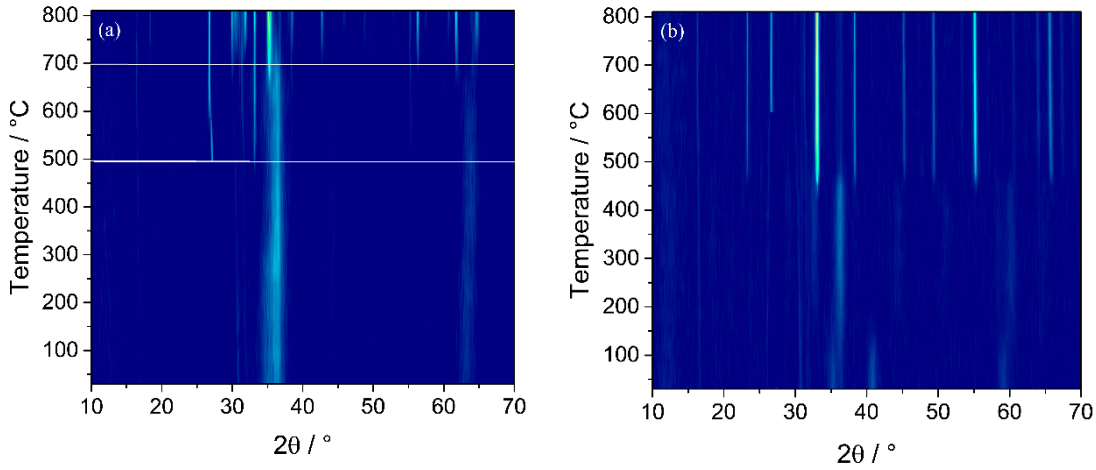

Figure 5.39 (a) *in situ* thermodiffractometry of manganese gallium oxide showing phase separation at 500 °C to Mn_2O_3 and then formation of β-Ga_2O_3 around 750 °C, (b) transformation of MnO to Mn_2O_3 occurring around 475 °C.

5.5.5 Magnetism

Field cooled *M vs T* magnetometry of a sample of $MnGa_2O_4$ shows simple paramagnetic behaviour and displays linear Curie-Weiss behaviour between the temperature range 50 – 300 K (Figure 5.40). The effective magnetic moment calculated was 5.53 μ_B. which is in close agreement with the spin only value of 5.92 μ_B for a high spin d^5 cation in octahedral coordination. This coordination is in agreement with the XANES analysis. A small negative Weiss constant is suggestive of the spins to align antiferromagnetically.

.

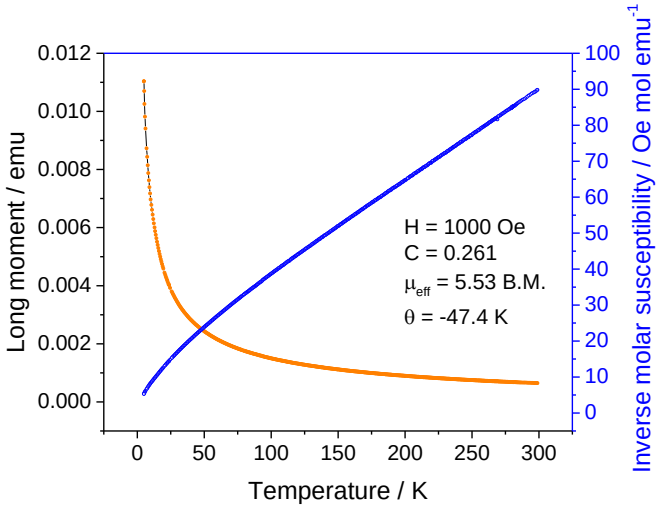

Figure 5.40 Field cooled magnetometry of a sample of manganese gallium oxide *(orange)* displaying simple paramagnetic behaviour and inverse molar susceptibility *(blue).*

5.6 Catalytic Application of $Ga_{2.52}V_{2.48}O_{7.31}(OH)_{0.69}$

5.6.1 Oxidative dehydrogenation of propane

It was mentioned briefly in the introduction that vanadium based catalysts have been found to be useful catalysts in the oxidative dehydrogenation of propane. In this section some catalytic data regarding the oxidative dehydrogenation of propane to propene using $Ga_{2.52}V_{2.48}O_{7.31}(OH)_{0.69}$ are presented. The aim is to dehydrogenate propane to propene in the presence of oxygen whilst avoiding the formation of CO, CO_2 and other unwanted side products such as coke.

5.6.2 Catalyst preparation

Two samples of $Ga_{2.52}V_{2.48}O_{7.31}(OH)_{0.69}$ were tested for oxidative propane dehydrogenation: one sample as-made and one sample fired to 300 °C (*i.e.* $Ga_{2.52}V_{2.48}O_8$) prior to testing. Since the testing is done at temperatures between 350 – 500 °C the as-made oxyhydroxide likely dehydrates to the oxide (see Section 5.3.5.3), but both were tested to see whether the as-made sample, which oxidises *in situ* has any improvement on selectivity than the pre-fired, "aged," oxide catalyst.

The catalysts were tested for propane oxy-dehydrogenation under a gas flow consisted of 20% propane and 20% oxygen in nitrogen. The temperature was varied between 350 and 500 °C, with the purpose of obtaining data at different conversion levels. The results are compared with a "standard" catalyst, commercial V_2O_5.

5.6.3 Results

Both $Ga_{2.52}V_{2.48}O_{7.31}(OH)_{0.69}$ and $Ga_{2.52}V_{2.48}O_{7.31}(OH)_{0.69}$ fired at 300 °C (*i.e.* $Ga_{2.52}V_{2.48}O_8$), are above the line of the "reference" material, V_2O_5, in the plot of selectivity *vs* conversion (Figure 5.41). This suggests that since the two gallium containing catalysts have similar activity that the as-made sample dehydrates to the oxide initially. This early work therefore suggests that this new material is more selective towards propylene than V_2O_5 when compared at the same conversions and therefore has potential for oxidative propane dehydrogenation and should be considered for further testing in this area of catalysis.

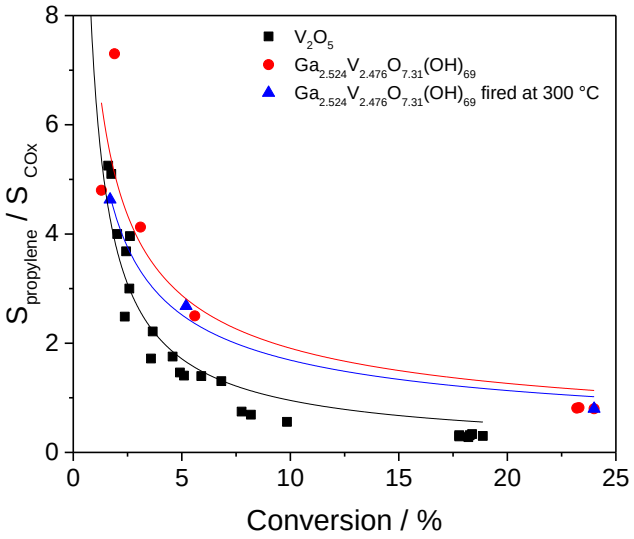

Figure 5.41 Selectivity *vs* conversion plot for $Ga_{2.52}V_{2.48}O_{7.31}(OH)_{0.69}$ compared against an industry reference, commercial V_2O_5.

One possible reason for the higher observed selectivity for propylene with this catalyst could be due to the formation of isolated active sites. Such behaviour has been studied previously for other catalysts used in this reaction.[73] Alternatively, the presence of a secondary surface metal (*i.e.* GaO_x) could lend itself to weakly adsorbing propane on the surface supplying the catalytically active VO_x site for propane activation. This has been observed for catalyst systems of V-Mo-O, and W-Mo-O.[74]

What is surprising is that the catalytic activity of vanadia in this reaction is typically associated with V^{5+} especially in the first step of the ODH cycle, whilst V^{3+} is not suitable for facile catalytic cycling.[32] The new material outperforms V_2O_5, yet contains a significant portion of V^{3+}. It could be that the surface of $Ga_{2.52}V_{2.48}O_{7.31}(OH)_{0.69}$ differs from the bulk structure, or that the surface chemistry changes from the as-made state to a V^{5+} rich state under the conditions used in the reaction. Powder XRD of the spent samples from this reaction reveals that the bulk structure is not completely retained after the catalytic cycle (Figure 5.42) which could mean that $Ga_{2.52}V_{2.48}O_{7.31}(OH)_{0.69}$ is only a precursor material to the catalytically active material. The identity of phases present after the catalytic cycling currently remains unclear.

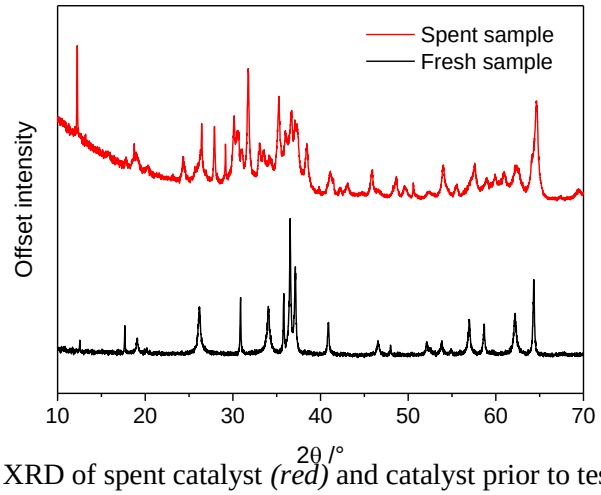

Figure 5.42 Powder XRD of spent catalyst *(red)* and catalyst prior to testing *(black)*.

5.7 Summary

In this work the solvothermal synthesis of a novel vanadium gallium oxyhydroxide, based on the structure of the $Ga_5O_7(OH)$, has been presented. It can be prepared by two different solvothermal routes offering a choice over crystallinity of the final material formed. Choice of regent, whether a V^{3+} or V^{5+} salt yields a material containing vanadium largely in the trivalent state. 1,4-butanediol retains the oxidation of the vanadium from the precursor in the final product, whilst 1:1 MEA:H_2O reduces the pentavalent vanadium to the trivalent state. Simultaneous neutron and X-ray refinement show that vanadium shares the octahedral metal sites with gallium but gallium exclusively occupies the tetrahedral site which accounts for 20% the total number of sites in the structure. The material is metastable and a cell contraction, likely due to dehydration, occurs around 300 °C before the material phase separates into other materials at 600 °C. The material shows potential as a catalyst in the oxidative dehydrogenation or propane, a reaction receiving increased attention over steam cracking and dehydrogenation reactions, outperforming a V_2O_5 catalyst, a standard used in industry against which to compare catalytic activity.

A new chromium substituted gallium oxide spinel has been prepared. This material is poorly crystalline, but has a large surface area. Though the material decomposes at 850 °C, it shows improved thermal stability over pure γ-Ga_2O_3 which decomposes around 650 °C. This is another example of a metastable material which would be inaccessible via high temperature synthesis.

Manganese gallium oxide has been synthesised by conventional solvothermal synthesis for the first time without the need for microwave assistance.

5.8 References

1 M. Marjzio, *J. Phys. Chem. Solids*, 1965, **26**, 1277–1280.

2 M. Yu, T. I. Draskovic and Y. Wu, *Inorg. Chem.*, 2014, **53**, 5845–5851.

3 Y. Maruyama, H. Irie and K. Hashimoto, *J. Phys. Chem. B*, 2006, **110**, 23274–23278.

4 B. V Merinov, S. L. Londar and Y. M. Zakharko, *Sov. Phys. Crystallogr*, 1988, **33**, 242–244.

5 V. Kahlenberg and C. S. J. Shaw, *Z. Krist.*, 2001, **216**, 206–209.

6 L. Biljana, V. Kahlenberg and J. Konzett, *Z. Anorg. Allg. CHem*, 2005, **43**, 2411–2415.

7 V. Kahlenberg and J. B. Parise, *Z. Krist.*, 2001, **216**, 210–214.

8 K. Kimura, M. Ohgaki, K. Tanaka, F. Marumo and H. Morikawa, *J. Solid State Chem.*, 1996, **194**, 186–194.

9 V. Kahlenberg, R. X. Fischer and J. B. Parise, *J. Solid State Chem.*, 2000, **154**, 612–618.

10 V. Kahlenberg, *Cryst. Res. Technol*, 2001, **3**, 319–326.

11 H. Y. Playford, A. C. Hannon, M. G. Tucker, M. R. Lees and R. I. Walton, *J. Phys. Condens. Matter*, 2013, **25**, 454212.

12 S. Stone, *J. Chem. Soc. A*, 1985, **81**, 1255–1261.

13 K. Sakoda and M. Hirano, *Ceram. Int.*, 2014, **40**, 15841–15848.

14 B. Boucher, A. G. Herpin and A. Oles, *J. Appl. Phys.*, 2012, **960**, 33–35.

15 K. Gurunathan, J. O. Baeg, S. M. Lee, E. Subramanian, S. J. Moon and K. jeong Kong, *Int. J. Hydrogen Energy*, 2008, **33**, 2646–2652.

16 C. Otero Arean and E. Garcia Diaz, *Mater. Chem.*, 1982, **7**, 675–683.

17 M. Inoue, T. Nishikawa, H. Otsu, H. Kominami and T. Inui, *J. Am. Ceram. Soc*, 1998, **81**, 1173–83.

18 B. Cros, A. Caramel and H. Kerner-Czeskleba, *Rev. Chim. Min.*, 1977, **14**, 563–571.

19 D. Weber, A. Stork, S. Nakhal, C. Wessel, C. Reimann, W. Hermes, T. Ressler, T. Bredow, R. Dronskowski and M. Lerch, *Inorg. Chem*, 2011, **50**, 6762–6766.

20 R. T. Claunch and M. M. Jones, *Inorg. Synth.*, 1963, **7**, 92–94.

21 A. F. Reid and T. M. Sabine, *J. Solid State Chem.*, 1970, **208**, 203–208.

22 J. P. Attfield, *APL Mater.*, 2015, **3**, 41510.

23 Y. Horibe, M. Shingu, K. Kurushima, H. Ishibashi, N. Ikeda, K. Kato and Y. Motome, *Phys. Rev. Lett.*, 2006, **96**, 86406.

24 K. Matsuno, T. Katsufuji, S. Mori, Y. Moritomo, A. Machida, E. Nishibori, M. Takata, M. Sakata, N. Yamamoto and H. Takagi, *J. Phys. Soc. Japan*, 2001, **70**, 1456–1459.

25 M. A. F. M. Da Silva, I. C. S. Carvalho, N. Cella, H. N. Bordallo and L. P. Sosman, *Opt. Mater.*, 2013, **35**, 543–546.

26 B. Boucher and A. Oles, *J. Phys. Fr.*, 1966, **27**, 51–56.

27 A. Oles, *Acta. Phys. Pol*, 1966, **30**, 125–164.

28 C. Huang, C. Su, M. Liao and C. Yeh, *Phys. Chem. Chem. Phys.*, 2009, **11**, 6331–6334.

29 D. L. Burnett, M. H. Harunsani, R. J. Kashtiban, H. Y. Playford, J. Sloan, A. C. Hannon and R. I. Walton, *J. Solid State Chem.*, 2014, **214**, 30–37.

30 F. Conrad, M. Bauer, D. Sheptyakov, S. Weyeneth, D. Jaeger, K. Hametner, P.-E. Car, J. Patscheider, D. Günther and G. R. Patzke, *RSC Adv.*, 2012, **2**, 3076–3082.

31 R. Gopinath and B. K. Patel, *Org. Lett.*, 2000, **2**, 577–579.

32 C. A. Carrero, R. Schloegl, I. E. Wachs and R. Schomaecker, *ACS Catal.*, 2014, **4**, 3357–3380.

33 X. Rozanska, R. Fortrie and J. Sauer, *J. Am. Chem. Soc.*, 2014, **136**, 7751–7761.

34 R. Grabowski, *Catal. Rev.*, 2006, **48**, 199–268.

35 F. Cavani, N. Ballarini and A. Cericola, *Catal. Today*, 2007, **127**, 113–131.

36 B. M. Weckhuysen and R. A. Schoonheydt, *Catal. Today*, 1999, **51**, 223–232.

37 B. M. Weckhuysen and R. A. Schoonheydt, *Catal. Today*, 1999, **51**, 215–221.

38 J. Yeob, D. Lee, K. Lee and Y. Wang, 2009, **146**, 260–264.

39 S. Liang, H. Zhang, M. Luo, K. Luo and P. Li, *Ceram. Int.*, 2014, **40**, 4367–4373.

40 H. Y. Chen, D. M. Hiller, J. E. Hundson, C. J. A. Westenbroek and E. I. du Pont de Nemours, *IEEE Trans. Magn.*, 1984, **20**, 24–26.

41 H. Dau, C. Limberg, T. Reier, M. Risch and S. Roggan, *ChemCatChem*, 2010, **2**, 724–761.

42 R. L. Richards, *Encycl. Inorg. Bioinorg. Chem.*, 2011, 1–11.

43 F. Sediri and N. Gharbi, *Mater. Sci. Eng. B*, 2005, **123**, 136–138.

44 I. Mjejri, A. Rougier and M. Gaudon, *Inorg. Chem.*, 2017, **56**, 1734–1741.

45 B. Goro, *Bull. Chem. Soc. Jpn.*, 1964, **37**, 1555–1557.

46 Y. Yanagida and M. Okumiya, *Bull. Chem. Soc. Jpn.*, 1969, **42**, 2247–2249.

47 Y. D. Ivakin, M. N. Danchevskaya and G. P. Muravieva, *Moscow Univ. Chem. Bull.*, 2005, **45**, 4–7.

48 M. Okumiya and G. Yamaguchi, *Bull. Chem. Soc. Jpn.*, 1971, 44, 1567–1570.

49 D. B. Tilley and R. A. Eggleton, *Clays Clay Miner.*, 1994, **42**, 485–488.

50 M. Okumiya, G. Yamaguchi, O. Yamada and S. Ono, *Bull. Chem. Soc. Jpn.*, 1971, 44, 418–423.

51 G. Yamaguchi, H. Yanagida and S. Ono, *Bull. Chem. Soc. Jpn.*, 1964, **37**, 752–754.

52 H. Y. Playford, A. C. Hannon, E. R. Barney and R. I. Walton, *Chem. Eur. J*, 2013, **19**, 2803–2813.

53 P. W. Stephens, *J. Appl. Cryst*, 1999, **32**, 281–289.

54 D. S. Cook, Y. Wu, K. Lienau, R. Moré, R. J. Kashtiban, O. V. Magdysyuk, G. R. Patzke and R. I. Walton, *Chem. Mater.*, 2017, **29**, 5053–5057.

55 C. Pan, P. Shen, W. L. Huang, S. L. Hwang, T. F. Yui and H. T. Chu, *J. Eur. Ceram. Soc.*, 2006, **26**, 2707–2717.

56 R. Demichelis, Y. Noel and C. Marcelo, *J. Phys. Conf. Ser.*, 2008, **117**, 12013.

57 B. Lavina, L. Z. Reznitskii and F. Bosi, *Phys. Chem. Miner.*, 2003, **30**, 599–605.

58 B. M. Gatehouse, I. E. Grey and E. H. Nickel, *Am. Mineral.*, 1983, **68**, 833–839.

59 S. C. Robinson, H. T. Evans, W. T. Schaller and J. J. Fahey, *Am. Mineral.*, 1957, **42**, 619–628.

60 W. H. Barnes and M. M. Qurashi, *Am. Mineral.*, 1952, **37**, 407–422.

61 A. W. Hanson, *Acta Cryst*, 1957, **11**, 703–709.

62 X. Zhang and Y. Xie, *Chem. Commun.*, 2011, **47**, 11252–11254.

63 F. M. Michel, L. Ehm, S. M. Antao, P. L. Lee, P. J. Chupas, G. Liu, D. R. Strongin, M. A. A. Schoonen, B. L. Phillips and J. B. Parise, *Science.*, 2007, **316**, 1726–1730.

64 Z. Johan and P. Picot, *Min. Petr. Mitt*, 1986, **35**, 67–75.

65 C. Ma and J. Beckett, *Am. Mineral.*, 2016, **101**, 1161–1170.

66 R. D. Shannon and C. T. Prewitt, *Acta Crystallogr. Sect. B*, 1969, **25**, 925–946.

67 A. N. Christensen, *Acta Chem. Scand. A*, 1976, **30**, 133–136.

68 W. C. Fernelius and J. E. Blanch, *Inorg. Chem.*, 1957, **5**, 130–131.

69 A. N. Christensen, P. Hansen and M. S. Lehmann, *J. Solid State Chem.*, 1977, **21**, 325–329.

70 J. Y. Lee, D. S. Kim, C. W. Na and J. Park, *J. Phys. Chem. C*, 2007, **111**, 12207–12212.

71 M. N. Bhattacharjee, N. Hill and D. T. Khathing, *J. Chem. Soc., Dalt. Trans.*, 1982, **0**, 669–670.

72 M. W. Davies and F. D. Richardson, *Trans. Faraday Soc*, 1959, **55**, 604–610.

73 R. K. Grasselli, *Top. Catal.*, 2002, **21**, 79–88.

74 B. Mitra, I. E. Wachs and G. Deo, *J. Catal.*, 2006, **240**, 151–159.

Chapter 6: Exploratory Hydrothermal Synthesis of Rhodium Materials

6. Exploratory Hydrothermal Synthesis of Rhodium Materials

6.1 Introduction

The platinum group metals (PGMs) are found in Groups 8, 9 and 10 of the 2nd and 3rd row transition series and include ruthenium, rhodium, palladium, osmium, iridium and platinum. Ternary platinum group metal oxides often display interesting magnetic and electronic properties, and other interesting quantum phenomena owing to strong spin-orbit coupling.[1] This is a common feature not only for the platinum group metals but for other transition metals in the 2nd and 3rd row. The larger spin-orbit coupling is on a similar energy range as, and therefore able to compete with, other interactions such as on-site Coulomb repulsion, crystal-field splitting and intersite hopping.[2] A few examples of platinum group metal oxides which display interesting properties include the high temperature antiferromagnetism found for $SrRu_2O_6$,[3] while Sr_2RuO_4 is a high temperature superconductor,[4] and $SrRuO_3$ is ferromagnetic.[5] Of the iridates superconductivity has been observed in Li_2IrO_3,[6] and postulated for Sr_2IrO_4,[7] whilst a spin liquid state has been found in the S=1/2 hyperkagome structure of antiferromagnetic $Na_4Ir_3O_8$.[8] The properties associated with some ternary rhodium oxides is outlined below. The ternary platinum metal oxides also find some limited use in catalysis, such as in the mitigation of exhaust fumes which has been reviewed recently.[9]

The lack of structural diversity among the binary platinum group oxides compared to first-row transition metal oxides is a consequence of the electronegative nature of the platinum metal itself. Their lack of affinity for oxygen is reflected in their reluctance to display flexibility in oxidation state when binding to oxygen and in their thermal stability since most precious metals readily lose oxygen and revert to the metallic state at high enough temperatures. For example, Rh_2O_3 is stable to 1100 °C before reducing back to the metallic state on further heating.[10] The reluctance of the platinum group metals to bind to oxygen is one reason for their wide use in catalysis.[9]

Complex oxides of the platinum group metals, typically containing an alkali and alkali-earth metal, are diverse and numerous oxides have been reported. Excellent reviews published on complex precious metal oxide chemistry can be found.[9,11] It is generally agreed that the introduction of an electropositive cation from Group 1 or 2

metal destabilises the oxygen p states causing increased covalent overlap with the precious metal d orbitals hence stabilising the material and explaining the increased structural diversity of complex metal oxides compared to the binary oxides.[9] By the same effect the presence of an electropositive cation can stabilise unusual oxidation states of the platinum group metal. This increased covalency results in greater electron density on the electronegative metal, and so can be regarded as an inductive effect.[9,12]

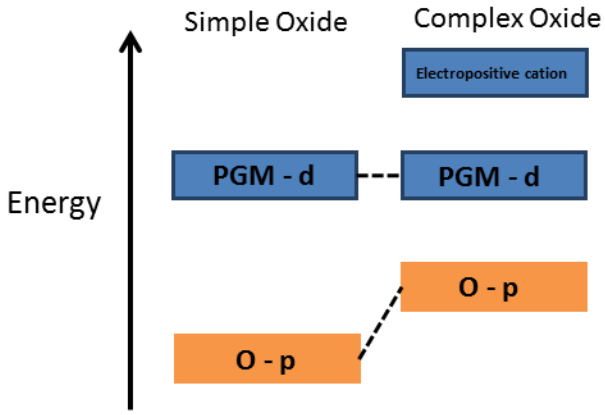

Figure 6.1 Destabilisation of O-p states by the presence of an electropositive cation causes increased overlap of O-p and PGM-d orbitals. Adapted from Seshadri *et al*.[9]

Rhodium oxide is similar to other platinum group metals in that it does not show too much flexibility in its oxidation states in binary compounds. Primarily trivalent, rhodium forms corundum-type Rh_2O_3 though high temperature and high pressure polymorphs are known.[10,13,14] RhO_2 can be prepared at high pressure and adopts the rutile structure which is a common structure type of the precious metals (for example, RuO_2, IrO_2).[15,16] The oxide chemistry of rhodium is largely dominated by the Rh^{3+} and Rh^{4+} as discussed below.

There are only two calcium rhodates reported in the literature.[17–20] $CaRh_2O_4$ adopts the $CaFe_2O_4$ structure and contains the diamagnetic Rh^{3+} cation. The fact that rhodium has d^6 configuration and is low spin in this material offers little towards electronic and magnetic applications. A $CaRhO_3$ perovskite has also been reported but requires a temperature close to 2000 °C and a pressure of 6 GPa.[21]

In contrast to calcium there is much greater structural diversity within the strontium rhodates. A further feature of these strontium rhodates is that most contain some Rh^{4+} which then presents an opportunity for electronic and magnetic properties. Sr_2RhO_4

and the isostructural Sr_2IrO_4 contains distorted Rh^{4+} octahedra. It is a 2D metallic conductor below 150 K. It does however require 1200 °C and an oxygen atmosphere to synthesise without impurity.[22,23] Hexagonal β-$SrRh_2O_4$ can also be prepared in a high temperature reaction from $SrCO_3$ and Rh metal requiring two periods of firing; the second at 1150 °C for 5 days.[24] The structure contains alternate layers of edge sharing RhO_6 octahedra with trigonal prismatic sites for Sr. An orthorhombic polymorph of $SrRh_2O_4$, which is isostructural with $CaRh_2O_4$ and $CaFe_2O_4$, has reportedly been synthesised by decomposition of $Sr_3Rh_2(OH)_{12}$ though this polymorph has never been properly characterised before and only a list of observed reflections given.[25] Subramanian *et al*. have reported the synthesis of rare-earth, and bismuth rhodium oxides which adopt the orthorhombic $CaFe_2O_4$ structure-type.[26]

Similar to $CaRhO_3$, the perovskite $SrRhO_3$ can also be synthesised from high temperature and high pressure synthesis.[27,28] There also exists bi-layered $Sr_3Rh_2O_7$ which similarly requires high temperature and high pressure (1500 °C and 6GPa). It is metallic and the expected local distortion around Rh^{4+} centres is a consequence of the t_{2g}^5 state.[29] The tri-layered $Sr_4Rh_3O_{10}$ perovskite is another example of a Rh^{4+} oxide.[30] $SrRhO_3$, $Sr_4Rh_3O_{10}$ and $Sr_3Rh_2O_7$ are part of a Ruddlesden-Popper series $Sr_{n+1}Rh_nO_{3n+1}$ (n = 1, 2 and ∞). $Sr_4Rh_3O_{10}$, similar to $Sr_3Rh_2O_7$, required a temperature and pressure of 1500 °C and 6 GPa for synthesis. $Sr_{10.5}Rh_{7.5}O_{24}$ is another example of a mixed valent Rh^{3+}/Rh^{4+} material.[31]

Most of these oxides require very high temperatures or very long reaction times to prepare. Polycrystalline $Sr_6Rh_5O_{15}$ can be prepared by solid state reaction at 850 °C and then 1150 °C for 9 days[32] but single crystals of the same phase can be prepared by a flux reaction in K_2CO_3 at slightly lower temperature of 1050 °C for 48 h.[33] Its structure was solved using traditional 3D, and 4D super-space group methods. $Sr_6Rh_5O_{15}$ belongs to the chain-type oxides $A_{3n+n}A'_nB_{n+3}O_{6n+9}$ with n = 1, which is related to the 2H-perovskite structure. The strontium rhodium oxides $Sr_4Rh_3O_{9+\delta}$ and $Sr_9Rh_7O_{21+\delta}$ are other examples of this family of oxides with n = 2 and n = 3, respectively. Unlike the commensurate n = 1 member, $Sr_6Rh_5O_{15}$, these oxides are incommensurate members of this family with extra added oxygen in the structure, since all materials contain $Rh^{3.6+}$. Synthesis of these phases is challenging owing to oxygen uptake occurring during heating and cooling. All three members show antiferromagnetism.[34]

A monoclinic hollandite structure with the chemical formula $Sr_{0.75}Rh_4O_8$ can be prepared under careful and controlled heating at 1050 °C for 160 h in an oxygen atmosphere. Heating above this temperature reportedly caused dissociation into β-$SrRh_2O_4$ and rhodium metal.[35]

Rh^{5+} can be stabilised in the Sr_3MRhO_6 structure (*M* = Na, Li). These materials are prepared by a molten alkali flux reaction at a low temperature of 600 °C.[36]

Another strontium rhodate where all rhodium is tetravalent is Sr_4RhO_6. This material requires multiple heating stages all in flowing O_2 with the final step requiring a temperature of 1250 °C for 15 days.[37] Weak antiferromagnetic alignment of the Rh^{4+} centres was observed. It was the first reported oxide of Rh^{4+} to display ordered magnetic spins. The Néel temperature is lower than for the iridium analogue and this is likely due to greater covalency owing to the more spatially diffuse Ir 5d orbitals.

A paper claiming the existence of three different strontium rhodium oxides ($Sr_3Rh_2O_{6.5}$, $SrRh_2O_4$, $SrRh_3O_{5.5}$) was published.[38] Both $Sr_3Rh_2O_{6.5}$, and $SrRh_2O_4$ were claimed to be hexagonal based on powder diffraction indexing, whilst $SrRh_3O_{5.5}$ was determined to be monoclinic. Further examination of the paper reveals that the chemical formula of the oxides was assigned based only on reaction stoichiometry. No formal structural investigation was properly undertaken and one of the oxides, $Sr_3Rh_2O_{6.5}$, shares a similar powder pattern with the $Sr_6Rh_5O_{15}$ and is likely a member of the $A_{3n+n}A'_nB_{n+3}O_{6n+9}$ family of oxides described above.

Far fewer oxides containing barium and rhodium have been reported. 4H-$BaRhO_3$ is known to exist[39,40] and there is also a hollandite structure, $Ba_{1.72}Rh_8O_{16}$.[40] 2H-$BaRhO_3$ has not yet been reported however the oxides $Ba_{11}Rh_{10}O_{30}$ and $Ba_{32}Rh_{29}O_{87}$ which are related to 2H-$BaRhO_3$ have been prepared.[41,42] The former contains Rh^{4+} and the latter mixed valent rhodium cations. Single crystals of $Ba_9Rh_8O_{24}$ have been grown by the zur Loye group[43] and it is structurally related to the 2H-perovskite family of oxides with a general formula $A_{3n+3m}A'_nB_{3m+n}O_{9m+6n}$, where A = alkaline-earth metal, A',B = a variety of metals including alkali, alkaline-earth, transition or main group or rare-earth. The structure is a result of the following stacking sequences: m[A_3O_9] and n[$A_3A'O_6$] layers with B filling the octahedral interstitials. They consist of one-dimensional chains of face-sharing trigonal prisms and octahedra. Sr_4PtO_6 is the n = 1, m = 0 member and forms in the $KCdCl_6$ structure-type. $Sr_4Fe_{0.73}Rh_{2.27}O_9$ synthesised

by the zur Loye group is a member of this family with m = 1 n = 3, whilst another strontium iron rhodium oxide $SrFe_{0.71}Rh_{0.29}O_3$ prepared by the same group contains Rh^{4+} and crystallises in the cubic perovskite space group.[44]

A variety of other mixed metal rhodates can be synthesised including delafossites ($NaRhO_2$[45,46] and $CuRhO_2$[47]); orthorhombic distorted perovskites with rare-earth cations;[48] oxides containing rhodium with rare-earth cations and transition metal cations;[49] and other structures, including pyrochlores, with cerium.[50] A rhodium bismuth pyrochlore is also known.[51] Rhodium is the only PGM that can be incorporated into the spinel structure at ambient pressure forming spinels with magnesium and *d*-block elements such as with zinc.[52]

With regards to synthesis of many complex metal oxides the conventional approach is to use high temperature reactions often with multiple grinding steps and long reaction times to facilitate diffusion of ions across grain boundaries. This usually means that the thermodynamically stable material is obtained. Soft chemical, *chimie-douce*, approaches such as sol-gel, and hydro(solvo)thermal reactions can be used to access metastable materials which would not normally be obtained by high temperature reactions as discussed in Chapter 2. Recently, a series of Group 2 ruthenium oxides prepared from hydrothermal synthesis in highly oxidising conditions was reported.[3] One of the materials prepared, $SrRu_2O_6$, contains Ru^{5+}, an unusual oxidation state for ruthenium, but also the material is antiferromagnetic with an extraordinarily high Néel temperature.[53] Flux reactions have also been employed to synthesise complex metal oxides and more recently hydrothermal reactions with high concentrations of sodium or potassium hydroxide , termed “hydroflux,” have shown to allow access to a range of new mixed metal hydroxides including first row transition metals and platinum group metals.[54,55] Very recently some new barium iron oxides were prepared from a wet hydroflux reaction in which a small volume of water is placed in an autoclave with a large amount of hydroxide.[56] These oxides were shown to be canted antiferromagnetic diferrites with exceptionally high magnetic ordering temperatures.

The low temperature synthesis of mixed-metal hydroxides can often afford new mixed metal oxides by gentle firing at elevated temperature to bring about dehydration.[54,55,57–59]

The low reactivity of rhodium oxide, which is predominantly used as the reagent in high temperature reactions of complex rhodium oxides, means that high temperature reactions usually require several days and multiple grinding steps to synthesise phase pure materials. The motivation behind this work was then to see whether mixed metal rhodium oxides could be prepared from low temperature hydrothermal (or hydroflux) reactions as a means to access new materials or known materials from a soft chemical route.

Rhodium, like other platinum group metals finds use in catalysis.[60,61] In particular, out of the platinum group metals rhodium has the highest activity for the oxidation of NO_x in exhaust streams in motor vehicle exhaust catalysts[61] and also has significant activity for the oxidation of hydrocarbons and carbon monoxide. It also has excellent resistance to being poisoned. However, the high cost of rhodium is its drawback and is the main reason why other cheaper metals are often investigated. The high cost of rhodium, along with the difficulty of oxidising Rh^{3+} under mild conditions, and the ease at which is reduces to the metallic state, is why complex rhodium oxides where rhodium is present in the bulk rather than in a catalytic amount on the surface of a support have hardly been studied at all for any catalysis.

6.2 Scope of this chapter

This chapter presents the findings from some exploratory work using rhodium chloride and salts from Group II as reagents in hydrothermal and hydroflux reaction. All materials formed by the hydroflux method were found to yield rhodium hydroxide materials. An attempt to understand their reaction pathway upon dehydration into oxides is presented. A new barium sodium rhodium hydroxide has been synthesised by the wet-hydroflux method and its structure solved by single crystal X-ray diffraction.

6.3 $Ca_3Rh_2(OH)_{12}$

6.3.1 Synthesis

In a typical synthesis, 0.10 g (0.38 mmol) of $RhCl_3 \cdot 3H_2O$ (Precious Metals Online, 99%) and 0.04 g (0.57 mmol) of $Ca(OH)_2$ (Aldrich; 96%) were added to 10 ml of 12 M KOH solution with stirring. The mixture was sealed in a 23 ml PTFE-lined steel autoclave and heated to 200 °C for 24 hours in a preheated fan oven. The autoclave was then cooled and the resulting precipitate was recovered by suction filtration to yield a brown powder. The material was dried at room temperature by washing with acetone.

6.3.2 Powder X-ray diffraction

The reaction of calcium hydroxide with rhodium chloride in potassium hydroxide affords the hydrogarnet material, $Ca_3Rh_2(OH)_{12}$, as inferred from powder X-ray diffraction. Using CaO_2 in place of the hydroxide also yielded the hydrogarnet and not an oxide material, unlike as has been observed for other hydrothermal reactions with PGMs.[3,62] Reaction in NaOH yielded an entirely different material (Section 6.4).

The powder XRD pattern of $Ca_3Rh_2(OH)_{12}$ is characterised by sharp and intense Bragg reflections indicative of a large crystallite size (Figure 6.2(a)). Rietveld refinement was undertaken for the calcium rhodium hydrogarnet using $Sr_3Fe_2(OH)_{12}$ as a starting model.[63]

During the refinement a small impurity phase of $Ca(OH)_2$ was observed and then included in the refinement (Figure 6.2(b)). The refinement proceeded smoothly to give a wRp = 10.3% (Table 6.1). The relative amounts of the hydrogarnet and $Ca(OH)_2$ from the Rietveld refinement were calculated as 86.99% and 13.01% respectively.

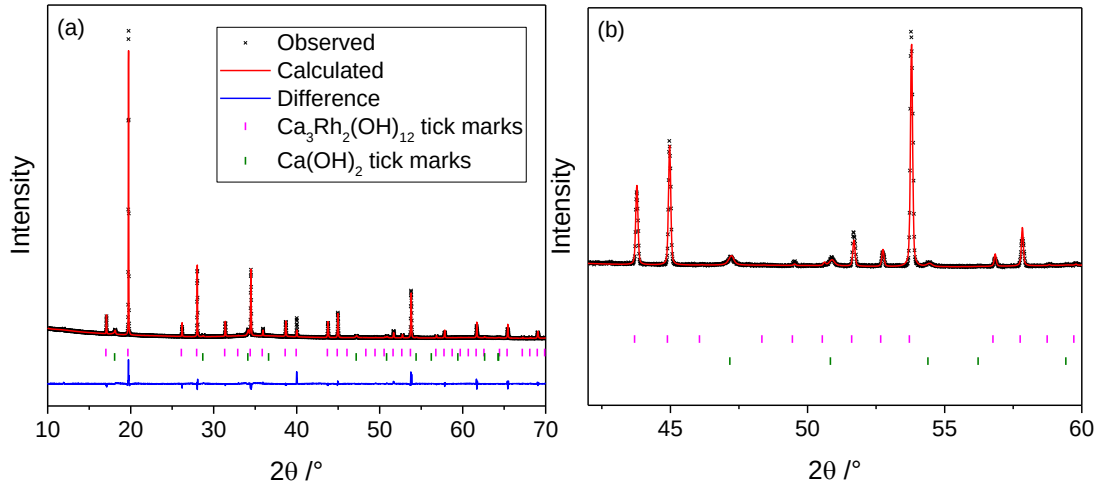

Figure 6.2 (a) Rietveld refinement of $Ca_3Rh_2(OH)_{12}$ obtained from powder X-ray data (λ = 1.5406 Å), (b) the refined model at higher angle.

Table 6.1 Refined crystal parameters for $Ca_3Rh_2(OH)_{12}$. Space group $Ia\bar{3}d$, a = 12.76028(10) Å. Rp = 6.6%, wRp = 10.3%.

Wyckoff Site	Atom	x	y	z	Occupancy	Beq / Å²
16a	Rh	0	0	0	1.0	2.12(56)
24c	Ca	0.125	0	0.25	1.0	2.12(56)
96h	O	0.0308(3)	0.0488(4)	0.6354(3)	1.0	0.4
96h	H	0.27256	0.22846	0.7122	1.0	0.4

*Hydrogen parameters were not refined and the coordinates and thermal parameter were taken from the published structure of the iron analogue.

The hydrogarnet structure is derived from the garnet structure ($A_3^{2+}B_2^{3+}(SiO_4)_3$) by removing the silicate groups and replacing them with hydroxide groups retaining symmetry and space group $Ia\bar{3}d$.[64] The B^{3+} cations adopt octahedral coordination, $\{B(OH)_6\}$, and are linked in such a way that dodecahedral sites are occupied by the larger A^{2+} cation. The tetrahedral site in the structure may be empty, partially or fully occupied by silicon. The first describes the silicon free hydrogarnet to which $Ca_3Rh_2(OH)_{12}$ clearly belongs. Hydrogarnets may offer an attractive route for thermal decomposition into novel oxides inaccessible by conventional solid-state synthesis.[65]

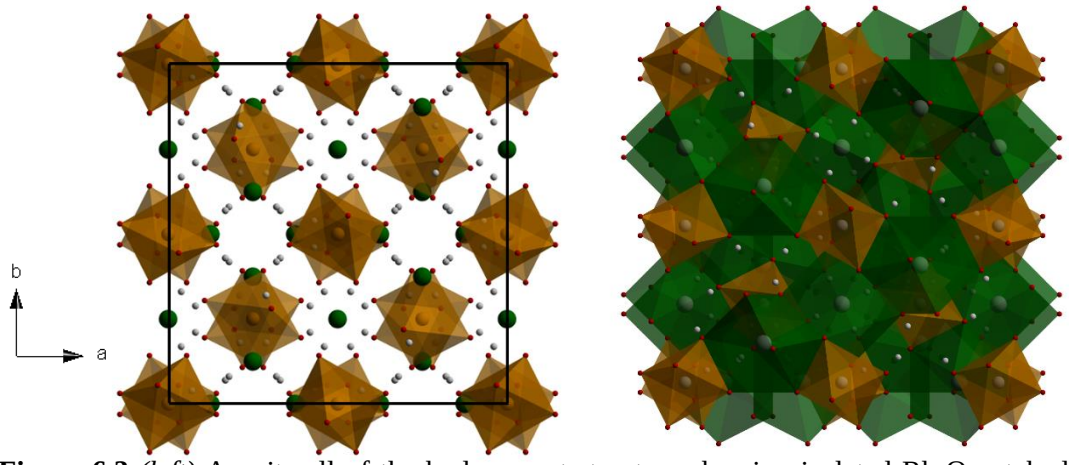

Figure 6.3 *(left)* A unit cell of the hydrogarnet structure showing isolated Rh-O octahedra *(gold)* and *(right)* Rh-O *(gold)* and Ca-O units *(green)*.

$Ca_3Rh_2(OH)_{12}$ was previously reported from a low temperature, high pressure hydrothermal synthesis (150 °C, 1000 bar) using rhodium oxide as the rhodium precursor.[64] Its structure, however, was not refined, with the authors providing only a list of observed reflections. This work is the first structure refinement of this material. The Rh-O bond distances are only slightly larger than for the Sr-Fe-O analogue (2.03 Å *cf.* 2.02 Å) which was used as the starting model and is expected since Rh^{3+} is only slightly larger than Fe^{2+} (0.665 Å *cf.* 0.645 Å).[63] The lattice parameter is, however, smaller than the $Sr_3Fe_2(OH)_{12}$ analogue (a = 13.202 Å *cf.* a = 12.76028(10)) since Ca^{2+} is smaller than Sr^{2+} (1.34 Å *cf.* 1.44 Å).[66]

6.3.3 Infrared spectroscopy

Infrared spectroscopy shows a sharp signal at 3600 cm^{-1} which can be assigned to the O-H stretching mode of the hydrogarnet (Figure 6.4). That it is not a broad signal suggests that it is of an O-H bond in the structure and not from hydrogen bonding between surface bound water molecules or other O-H containing molecular species.

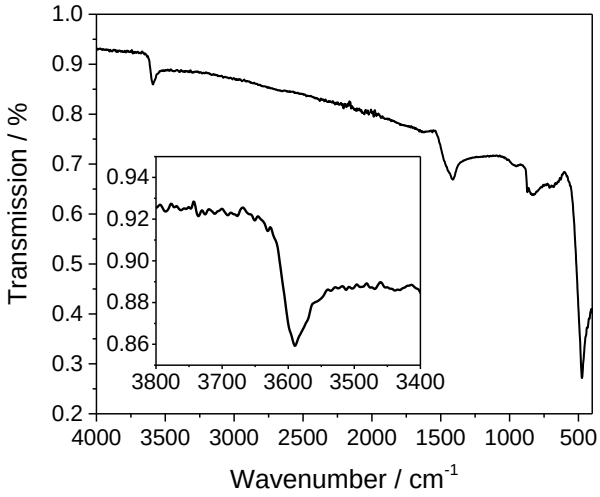

Figure 6.4 Infrared spectrum of $Ca_3Rh_2(OH)_{12}$ showing O-H stretching mode *(inset shows a close up on O-H stretching mode)*.

6.3.4 Thermal decomposition of $Ca_3Rh_2(OH)_{12}$

Early work on the decomposition of hydrogarnets suggested that their thermal decomposition proceeds as in Equation 6.1 and this was based on thermal analysis.[64]

$$A_3B_2(OH)_{12} \rightarrow A_3B_2O_6 + 6H_2O \text{ (at a temperature of 1000 °C)}$$

Equation 6.1

In situ thermodiffractometry reveals that $Ca_3Rh_2(OH)_{12}$ decomposes into an amorphous phase around 325 °C and this is supported by TGA showing an exotherm around the same temperature and a total mass loss of 25% which is indicative of a loss of six moles of H_2O (expected mass loss = 20.5%) assuming the presence of a small amount of $Ca(OH)_2$ impurity phase which can be seen to decompose in the TGA by a step around 580 °C in agreement with literature values.[67] The formation of new crystalline phases occurs around 650 °C. The powder X-ray diffraction pattern of a sample of $Ca_3Rh_2(OH)_{12}$ after being heated at 900 °C shows the presence of $CaRh_2O_4$ and CaO (Figure 6.5(c) and (d)). A thermal decomposition chemical equation can be written (Scheme 6.1).

$$Ca_3Rh_2(OH)_{12} \rightarrow CaRh_2O_4 + 2CaO + 6H_2O$$

Scheme 6.1

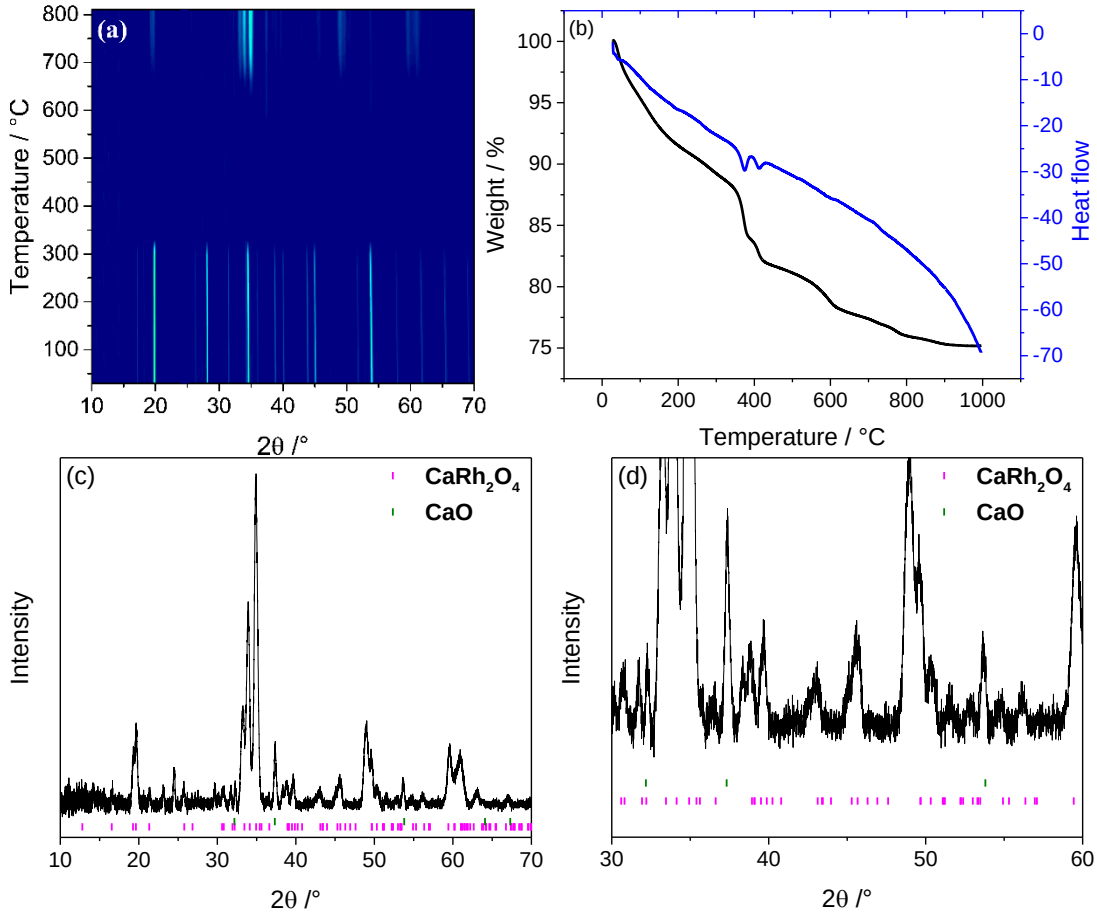

Figure 6.5 (a) *In situ* thermodiffractometry of $Ca_3Rh_2(OH)_{12}$, (b) TGA, (c) $Ca_3Rh_2(OH)_{12}$ after heating to 810 °C, (d) close-up showing CaO peaks *(green tick marks)*.

A phase pure sample of $CaRh_2O_4$ can be obtained by washing the fired sample with 2 M nitric acid to remove the calcium oxide impurity.

TEM and SEM shows that $CaRh_2O_4$ consists of rounded particles of ~100 nm diameter (Figure 6.6), whilst EDX via SEM confirms the ratio Ca:Rh as 1:2.

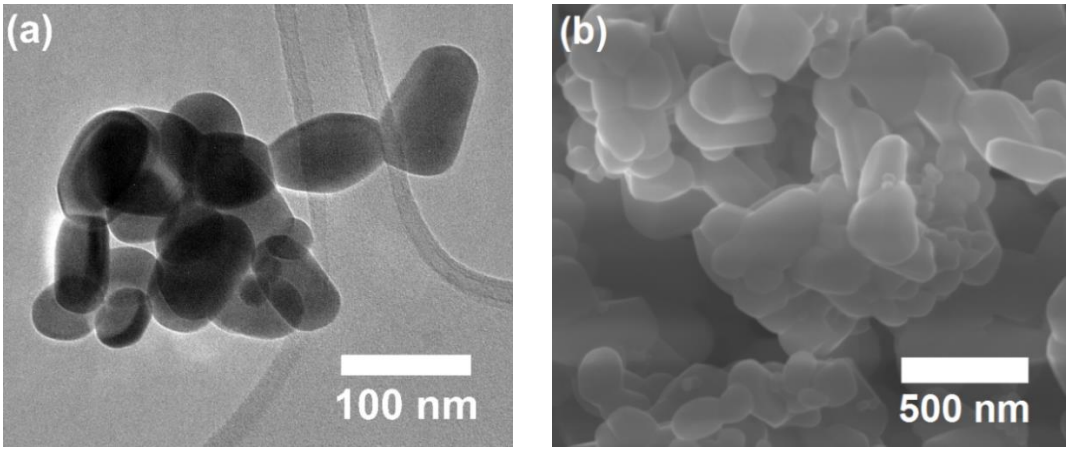

Figure 6.6 (a) TEM image and (b) SEM image of $CaRh_2O_4$.

Rietveld refinement was undertaken against X-ray data of $CaRh_2O_4$ using the structure refinement obtained by Yamaura *et al.*,[19] and the refined model is shown in Figure 6.7 and the refined crystal parameters in Table 6.2. The temperature factors were kept fixed at 0.3 throughout the refinement. These values were default values chosen by TOPAS.

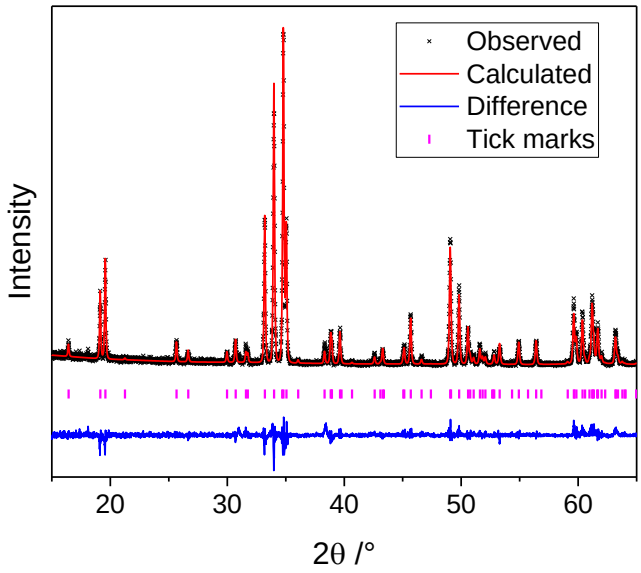

Figure 6.7 Rietveld refinement of $CaRh_2O_4$ using X-ray data (λ = 1.5406 Å).

Table 6.2 Refined crystal parameters for $CaRh_2O_4$. Space group *Pnma*, *a* = 9.0603(2) Å, *b* = 3.09854(7) Å, *c* = 10.7809(3) Å. Rp = 14.7%, wRp = 20.5%

Wyckoff Site	Atom	x	y	z	Occupancy	Beq / Å^2
4c	Ca	0.2405(8)	0.25	0.3375(7)	1.0	0.3
4c	Rh	0.0894(3)	0.25	0.5992(3)	1.0	0.3
4c	Rh	0.0558(3)	0.25	0.1151(3)	1.0	0.3
4c	O	0.300(2)	0.25	0.6737(16)	1.0	0.3
4c	O	0.363(2)	0.25	-0.0430(16)	1.0	0.3
4c	O	0.463(2)	0.25	0.2193(17)	1.0	0.3
4c	O	0.110(2)	0.25	-0.0795(15)	1.0	0.3

The lattice parameters obtained from the refinement are larger than those obtained from the single crystal structure refinement which was also measured at room temperature: *a* = 9.0354(3) Å, *b* = 3.0340(1) Å, *c* = 10.7062(3) Å.

The crystal structure of $CaRh_2O_4$ contains both edge and corner sharing Rh-O octahedra, all which edge share with 8-coordinate Ca (Figure 6.8).

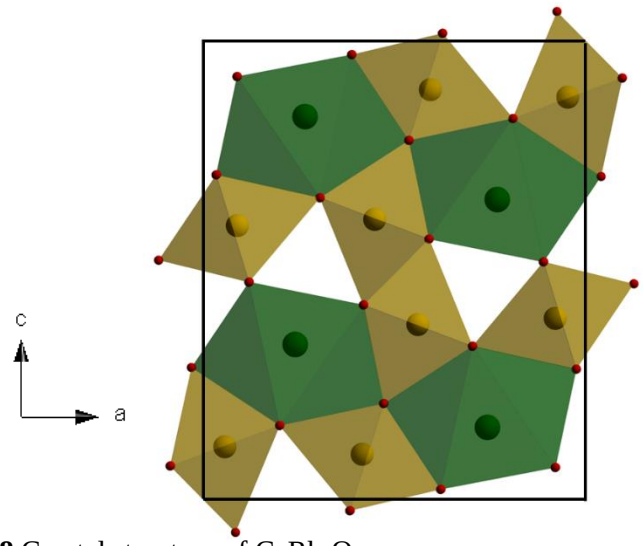

Figure 6.8 Crystal structure of $CaRh_2O_4$.

6.4 Synthesis and Thermal Decomposition of Ca-Na-Rh-(OH)

6.4.1 Synthesis

In a typical synthesis, 0.10 g (0.38 mmol) of $RhCl_3 \cdot 3H_2O$ (Precious Metals Online, 99%) and 0.014 g (0.19 mmol) $Ca(OH)_2$ (Aldrich; 96%) were added to 10 ml of 12 M NaOH solution with stirring. The mixture was sealed in a 23 ml PTFE-lined steel autoclave and heated to 200 °C for 24 hours in a preheated fan oven. The autoclave was then cooled and the resulting precipitate was recovered by suction filtration to yield a yellow powder. The material was dried at room temperature by washing with acetone.

6.4.2 Powder X-Ray Diffraction

The hydrogarnet structure described above is not isolated if sodium hydroxide is used in place of potassium hydroxide and instead forms a completely new material. Identification of this phase was complicated owing to the presence of some $Ca(OH)_2$ and an amorphous feature can be seen in the PXRD pattern under the first peak (Figure 6.9).

Control reactions using NaOH without the calcium salt yielded amorphous materials as did a controlled reaction of rhodium chloride and calcium salts using only water as the solvent. Therefore, both sodium and calcium are required to form the crystalline material.

Indexing the pattern provided a hexagonal cell with initial lattice parameters a = 5.836 Å, c = 4.783 Å. However, a smaller cell can instead be used with a unit cell a parameter of 3.36 Å and the fitted profile is shown in Figure 6.9 with refined lattice parameters of a = 3.36512(5) Å, c = 4.78277(11) Å using space group $P\bar{3}m1$. The space group and lattice parameters are very similar to those for Group 2 metal hydroxides, for example $Mg(OH)_2$ where a = 3.142(1) Å, c = 4.766(2) Å.

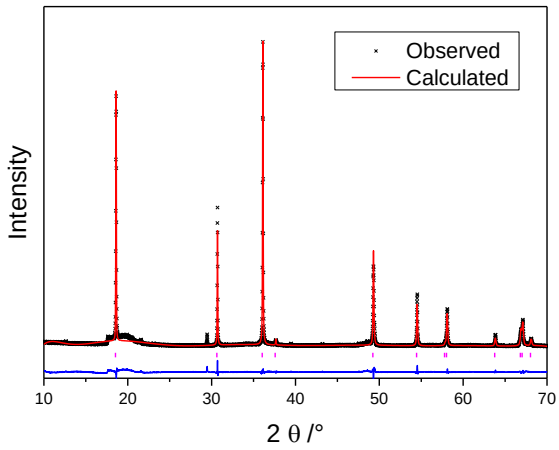

Figure 6.9 Pawley refinement of the Ca-Na-Rh-OH phase.

6.4.3 EDX

EDX analysis by SEM confirmed the presence of both calcium, sodium and rhodium in the structure in a ratio of approximately 1:1:1. A simulated powder pattern using the $Mg(OH)_2$ brucite structure with a formula $Ca_{0.33}Na_{0.33}Rh_{0.33}(OH)_2$ shows that there are significant discrepancies in the relative intensities of the Bragg reflections (Figure 6.10). The fact that the hydrogarnet forms when potassium hydroxide is used suggests that potassium is too large to fit in this hexagonal structure.

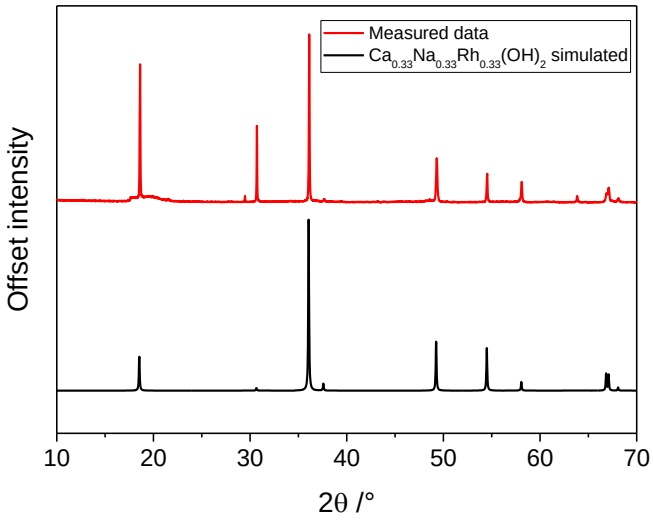

Figure 6.10 Simulated PXRD pattern of $Ca_{0.33}Na_{0.33}Rh_{0.33}(OH)_2$ using the brucite structure *(black)* and measured data for the Ca-Na-Rh-OH material *(red)*.

6.4.4 Infrared spectroscopy

Infrared spectroscopy shows a strong signal at 3600 cm^{-1} typical for an O-H stretching mode in oxyhydroxides or hydroxides (Figure 6.11).

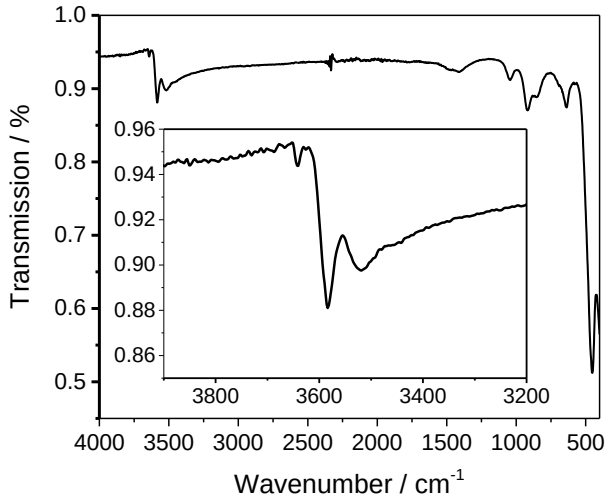

Figure 6.11 IR of Ca-Na-Rh-OH with inset showing a strong O-H stretching mode.

6.4.5 XANES

XANES analysis showed that in this material the rhodium is likely present as Rh^{3+} given the similarity in edge position of the material against the $CaRh_2O_4$ reference (Figure 6.12).

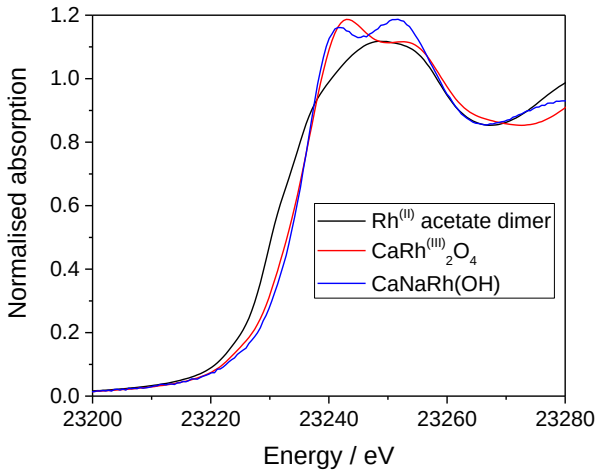

Figure 6.12 XANES spectra of Ca-Na-Rh-OH against suitable references indicating the presence of trivalent rhodium.

6.4.6 Thermal decomposition of the hexagonal Ca-Na-Rh-(OH) phase

In situ thermodiffractometry shows this phase is stable until around 350 °C before dehydration occurs to form an amorphous material (Figure 6.13). Crystalline phases can be seen to form at 600 °C with one phase being identified as CaO. TGA shows that a total mass loss of 20% is observed over the range 30 – 1000 °C. If the ratio of metals from EDX is taken, *i.e.* 1:1:1 then an empirical formula $CaNaRh(OH)_6$ may be assumed with 6 OH groups required to charge balance. The observed mass loss of 20% upon dehydration of this material agrees favourably with this empirical formula (expected mass loss = 20.2%). However, some of the total mass loss in the TGA is likely to come from the dehydration of $Ca(OH)_2$ impurity phase which thermally decomposes into CaO, and this must be considered.

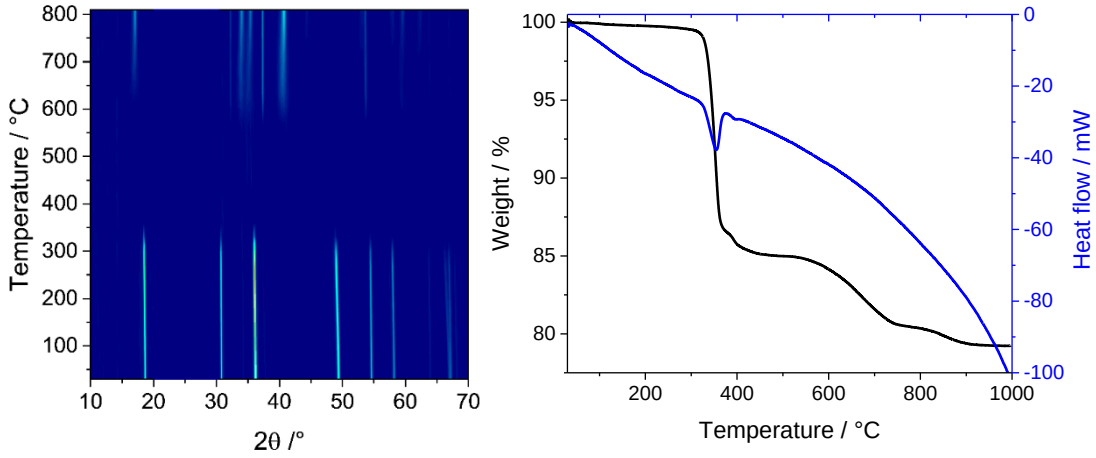

Figure 6.13 *In situ* thermodiffractometry of the hexagonal phase Ca-Na-Rh-OH showing decomposition around 350 °C.

The material heated to 810 °C was washed in dilute acid to remove the calcium oxide and leaving behind the other crystalline phase. Most of the reflections could be indexed to a hexagonal cell with lattice parameters that refined close to those expected for the delafossite $NaRhO_2$ (a = 3.0811(13) Å, c = 15.904(9) Å, space group $R\bar{3}m$) (Figure 6.14). The lattice parameters for $NaRhO_2$ reported in the literature were given as a = 3.0971(4) Å and c = 15.528(3) Å.[46] The refined lattice parameter c in this work is larger than the literature value. Two broad reflections (denoted *) in the powder pattern are not fitted to the delafossite structure. The temperature required to bring about formation of the delafossite from the amorphous precursor is much lower than required for a solid-state synthesis between two solid precursors which was 950 °C.

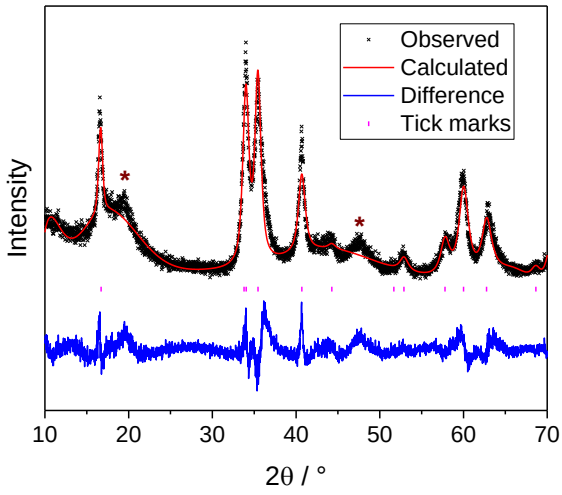

Figure 6.14 Pawley refinement showing $NaRhO_2$ isolated from the decomposition of Ca-Na-Rh-OH into $NaRhO_2$ and CaO.

If the CaO is not removed by acid washing then upon further heating to 1100 °C a solid-state reaction occurs between the two oxides resulting in formation of $CaRh_2O_4$ and some unreacted $NaRhO_2$.

6.5 $Sr_3Rh_2(OH)_{12}$

6.5.1 Synthesis

In a typical synthesis, 0.1 g (0.38 mmol) $RhCl_3 \cdot 3H_2O$ (Precious Metals Online, 99%) and 0.023 g (0.19 mmol) $Sr(OH)_2$ (Aldrich; 95%) were added to 10 ml, 12 M NaOH solution with stirring. The mixture was sealed in a 23 ml PTFE-lined steel autoclave and heated to 200 °C for 24 hours in a preheated fan oven. The autoclave was then cooled and the resulting precipitate was recovered by suction filtration to yield a bright yellow powder. The material was dried at room temperature by washing with acetone.

6.5.2 Powder X-Ray Diffraction

Highly crystalline and phase pure strontium rhodium hydrogarnet is obtained when rhodium chloride reacts with strontium hydroxide or strontium peroxide in the presence of a high concentration of potassium or sodium hydroxide under hydrothermal conditions. Choice of base (*i.e.* sodium or potassium hydroxide) did not affect the formation of the hydrogarnet. Similarly selecting a peroxide over hydroxide for the strontium reagent did not bring about formation of any oxide phases as had been found to be required for some ruthenium and iridium materials.[3,62,68] Although usually a phase pure material was formed in the reaction, occasionally single crystals of $SrCO_3$ would be formed in the reaction, sometimes large enough to be removed by mechanical separation. The natural propensity for NaOH and KOH to sequester CO_2 from the atmosphere is the likely reason for this.[69] Purging the reaction vessel with N_2 beforehand did not consistently prevent the formation of carbonates, which suggests the carbonate may already be in the KOH and NaOH.

Since a structure refinement of $Sr_3Rh_2(OH)_{12}$ has not yet been published the powder diffraction data of $Sr_3Rh_2(OH)_{12}$ were analysed using the $Sr_3Fe_2(OH)_{12}$ model[63] (Figure 6.15 and Table 6.3) as for $Ca_3Rh_2(OH)_{12}$. An excellent fit to the observed data was obtained. The refined lattice parameter a = 13.18564(6) Å is slightly smaller than that reported for the single crystal room temperature structure refinement of

$Sr_3Fe_2(OH)_{12}$, a = 13.202 Å but considering 6-coordinate high spin Fe^{3+} and 6-coordinate Rh^{3+} are similar in size (0.645 Å *cf.* 0.665 Å), this was not considered a significant problem. The bond valence sum calculated for rhodium using the Rh-O bond distance of 2.0513 Å gives a valency of 2.97+, which is in excellent agreement with the expected valence state of rhodium in this material. This Rh-O bond length is slightly larger than the reported Fe-O bond length of 2.0262 Å in $Sr_3Fe_2(OH)_{12}$.

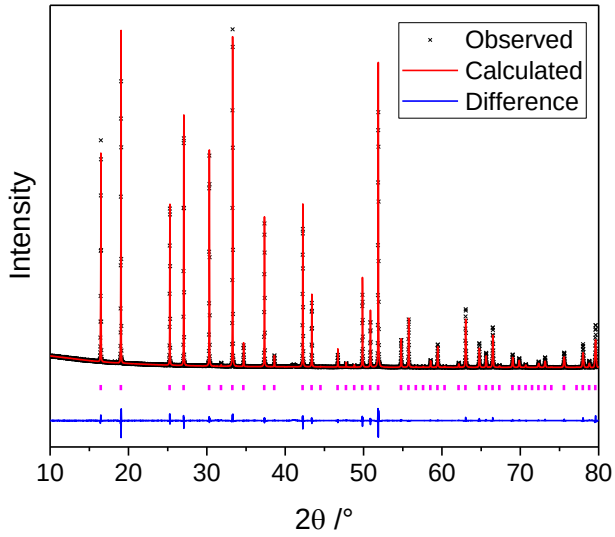

Figure 6.15 Rietveld refinement against X-ray diffraction data for $Sr_3Rh_2(OH)_{12}$.

Table 6.3 Refined crystal parameters for $Sr_3Rh_2(OH)_{12}$. Space group $Ia\bar{3}d$, a = 13.18564(6) Å. Rp = 10.5%, wRp = 15.7%.

Wyckoff Site	Atom	x	y	z	Occupancy	Beq / Å^2
16a	Rh	0	0	0	1.0	0.52(4)
24c	Sr	0.125	0	0.25	1.0	0.46(4)
96h	O	0.0308(3)	0.0546(4)	0.6423(3)	1.0	0.4
96h	H	0.180	0.081	0.789	1.0	0.4

*Hydrogen parameters were not refined.

6.5.3 Infrared spectroscopy

Infrared spectroscopy shows a sharp signal at ~3600 cm^{-1} which can be assigned to the O-H stretching mode of the hydrogarnet (Figure 6.16).

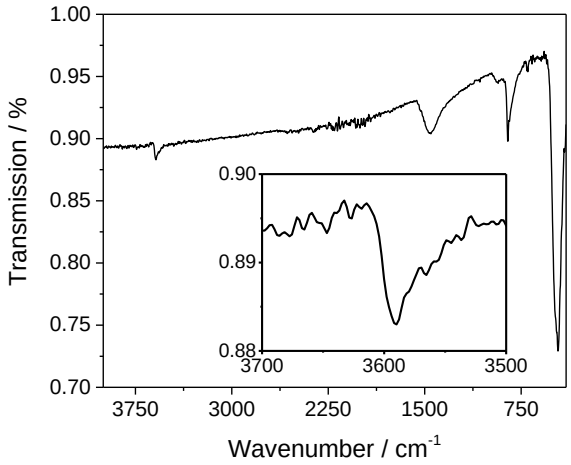

Figure 6.16 Infrared spectrum of $Sr_3Rh_2(OH)_{12}$ showing O-H stretching mode *(inset shows a close up on O-H stretching mode).*

6.5.4. Thermal decomposition of $Sr_3Rh_2(OH)_{12}$

In situ thermodiffractometry shows that decomposition of the hydrogarnet occurs around 350 °C (Figure 6.17(a)) and, unlike the decomposition of $Ca_3Rh_2(OH)_{12}$, growth of the crystalline decomposition product peaks occurs almost immediately and they continue to grow in intensity and the stable phase remains at 810 °C. TGA shows an exotherm and mass loss occurring at 350 °C and a total mass loss of around 14% (Figure 6.17(b)), which is in close agreement to the expected mass loss of 16% for a loss of 6 moles of water. Another step is observed at around 850 °C. As noted above, in the synthesis of $Sr_3Rh_2(OH)_{12}$ a small impurity of $SrCO_3$ was sometimes found. The step at 850 °C could be attributed to decomposition of $SrCO_3$ which usually decomposes between 900-1100 °C.[70]

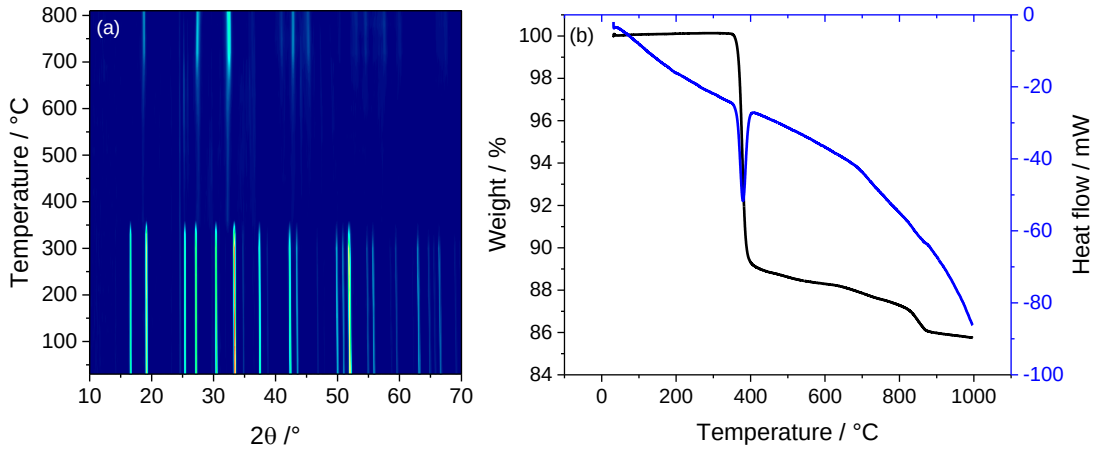

Figure 6.17 (a) *In situ* thermodiffractometry of $Sr_3Rh_2(OH)_{12}$, (b) TGA showing mass loss at the same decomposition temperature.

Thermal decomposition of $Sr_3Rh_2(OH)_{12}$ was reported by Ivanov-Emin and thermogravimetric analysis showed loss of water at two different temperatures.[25] This led the author to believe the decomposition product was $SrRh_2O_4$, isostructural with $CaRh_2O_4$ ($CaFe_2O_4$-orthohombic structure type). The structure given by Ivanov-Emin is based mainly on thermal analysis and only a list of observed reflections in the powder pattern of the decomposition product are given. Apparent similarity to $SrSc_2O_4$ further directed Ivanov-Emin to assign the structure to an orthorhombic crystal system. Although this does seem plausible since $Ca_3Rh_2(OH)_{12}$ decomposes into an orthorhombic $CaRh_2O_4$ material a simulation of the powder pattern indicates that this model should be rejected (Figure 6.18). In fact, orthorhombic $SrRh_2O_4$ with the $CaFe_2O_4$ structure has never been synthesised or characterised by any other group since Ivanov-Emin.

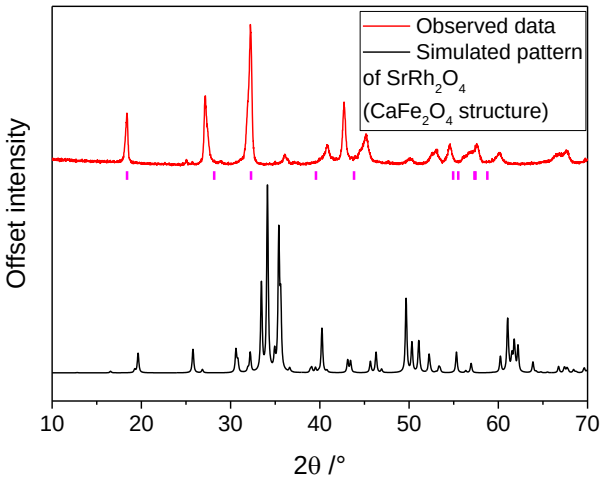

Figure 6.18 Observed data *(red)*, and simulated pattern of $SrRh_2O_4$ with the $CaFe_2O_4$ orthorhombic crystal system *(black)*, and tick marks *(magenta)* from the list of reflections reported by Ivanov-Emin.

Comparing the observed data of the strontium rhodium hydrogarnet decomposition product against strontium rhodates reported in the literature shows that the decomposition product most closely resembles $Sr_6Rh_5O_{15}$, though there are other possible candidates for the decomposition product (Figure 6.19).

.

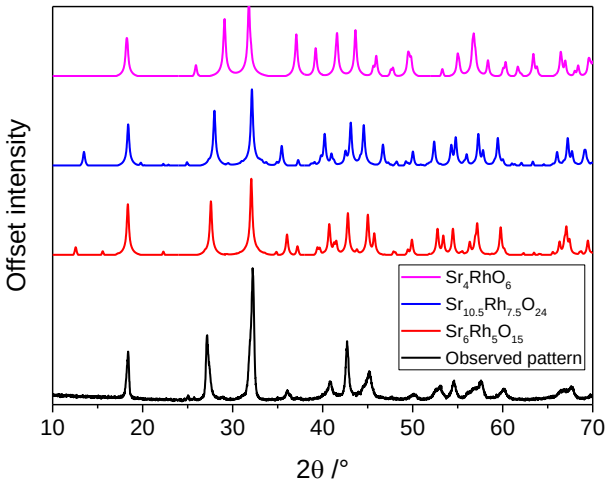

Figure 6.19 Measured data of $Sr_3Rh_2(OH)_{12}$ fired at 810 °C *(black)*, and simulated patterns of $Sr_6Rh_5O_{15}$ *(red)*, $Sr_{10.5}Rh_{7.5}O_{24}$ *(blue)* and Sr_4RhO_6 *(magenta)*.

As described above in the introduction to this chapter, $Sr_6Rh_5O_{15}$ is part of a family of oxides related to the 2H-perovskite structure: $Sr_4Rh_3O_{9+\delta}$ and $Sr_9Rh_7O_{21+\delta}$ are other members of this family,[32–34,41] and so it is likely that the decomposition product of $Sr_3Rh_2(OH)_{12}$ is also a member of this family.

In an attempt to improve the crystallinity and resolve the peaks to facilitate phase identification of the product, the material was placed into a furnace at 900 °C in air for 4 h. It was found that a portion of the sample had oxidised further to become Sr_2RhO_4 (Figure 6.20). Further annealing at 1100 °C did not significantly improve the crystallinity of either oxide phase nor was there any appreciable further transformation of the initial decomposition material into Sr_2RhO_4. When the experiment was heated under N_2 decomposition into rhodium metal occurred readily.

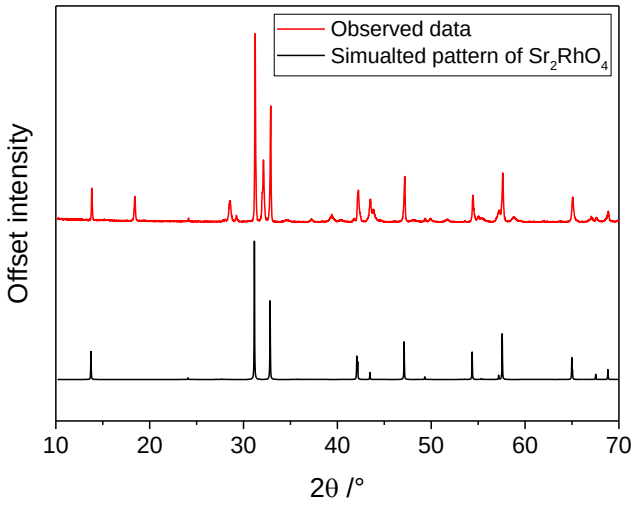

Figure 6.20 $Sr_3Rh_2(OH)_{12}$ fired at 1100 °C showing formation of some Sr_2RhO_4.

The thermal decomposition in air of $Sr_3Rh_2(OH)_{12}$ is clearly very different to $Ca_3Rh_2(OH)_{12}$ and is more complex to interpret. No rhodium metal or strontium oxide, the other expected decomposition products, were observed in the powder pattern, although it is possible that these materials are amorphous. Both the first decomposition product and Sr_2RhO_4 were found to be susceptible to dissolution in dilute acids so it was not possible to remove any strontium oxide phases that may be present or possible to isolate Sr_2RhO_4 as a phase pure material.

XANES analysis shows that in samples of the strontium rhodium hydrogarnet fired at 700 °C and 1100 °C there is a shift of the edge position to higher energy of the Rh^{3+} reference indicating the presence of Rh^{4+} (Figure 6.21). The first decomposition product is suspected to be a member of the $A_{3n+n}A'_nB_{n+3}O_{6n+9}$ family. All reported strontium rhodium oxide members contain $Rh^{3.6+}$. There is little change in the edge position or shape between the first decomposition product and the material fired at 1100 °C which would be expected since this is a mixture of both the $Rh^{3.6+}$ material and only a small amount of $Sr_2Rh^{4+}O_4$.

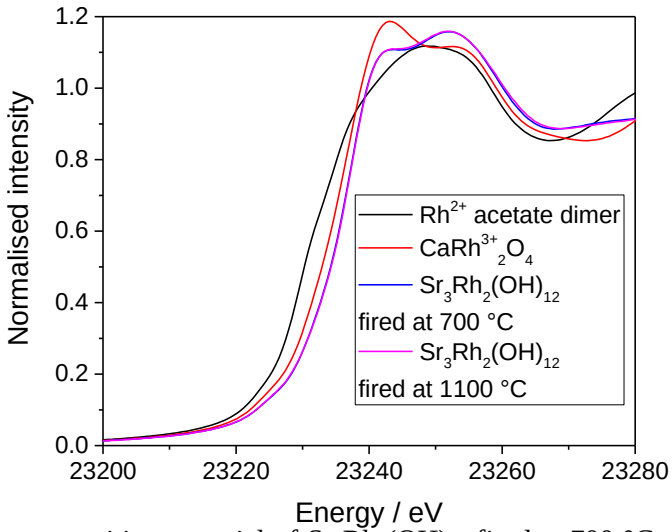

Figure 6.21 Decomposition material of $Sr_3Rh_2(OH)_{12}$ fired at 700 °C and 1100 °C showing little change in the edge position.

6.6 $BaNaRh(OH)_6$

6.6.1 Synthesis

6.6.1.1 Polycrystalline sample

In a typical synthesis, 0.1 g (0.38 mmol) $RhCl_3 \cdot 3H_2O$ (Precious Metals Online, 99%) and 0.032 g (0.19 mmol) $Ba(OH)_2$ (BDH; 97%) were added to 10 ml, 12 M NaOH solution with stirring. The mixture was sealed in a 23 ml PTFE-lined steel autoclave and heated to 200 °C for 24 hours in a preheated fan oven. The autoclave was then cooled and the resulting precipitate was recovered by suction filtration to yield a gold coloured powder.

6.6.1.2 Single crystal sample

In a recent paper by zur Loye *et al.* a modified hydroflux method was published optimised for single crystal growth of some new barium iron oxide materials.[56] This method, termed the wet hydroflux synthesis, requires large amounts of hydroxide and small volumes of water. The wet hydroflux reportedly takes advantage of the Lux-Flood oxoacidity of the hydroxide melt by virtue of hydroxide ion autodissociation (Scheme 6.2). By adjusting the degree of oxoacidity in the flux melt, the degree of solubility of the transition metal oxide, and presumably transition metal hydroxides, can be changed.[69] This method was selected in an attempt to grow single crystals of $BaRhNa(OH)_6$. Many different conditions were tested to try and grow single crystals, including changing the barium precursor, temperature, time, amount of base, volume of water, heating/cooling rate, and the best conditions are given below.

$$2OH^- \longleftrightarrow H_2O + O^{2-}$$

Scheme 6.2

To grow single crystals of $BaNaRh(OH)_6$, 0.1 g (0.38 mmol) $RhCl_3 \cdot 3H_2O$ (Precious Metals Online, 99%) and 0.032 g (0.19 mmol) BaO_2 (Aldrich; ≥95%) and 4.0 g (0.1 mol) NaOH (Fischer, ≥97%) were added to a PTFE-line steel autoclave and 2 ml distilled water was added without stirring. The autoclave was sealed and placed in an oven set to ramp to 200 °C at 300 °C h^{-1}, and held for 24 h and then cooled to room

temperature at 6 °C h^{-1}. The crystals formed were separated from the flux using hot water, aided by gentle stirring, followed by vacuum filtration with acetone used to dry the crystals.

6.6.2 Powder X-ray diffraction

PXRD showed that the polycrystalline material is highly crystalline and that there are no barium impurity phases such as $Ba(OH)_2$ (Figure 6.22), unlike the calcium and strontium phases for which alkali-earth hydroxides were frequently encountered as by-products. Occasionally a small rhodium metal impurity was found in some samples. The reflections observed in the powder XRD pattern could all be indexed to a primitive tetragonal cell with lattice parameters a = 8.3156 Å, c = 8.4520 Å with a selection of space groups possible ($P4_2/ncm, P4_22_12, P4$, for example) but no unique space group could be determined from powder XRD. A Pawley refinement using space group $P4_2/ncm$ provided refined lattice parameters of a = 8.3145(3) Å, c = 8.4482(5) Å.

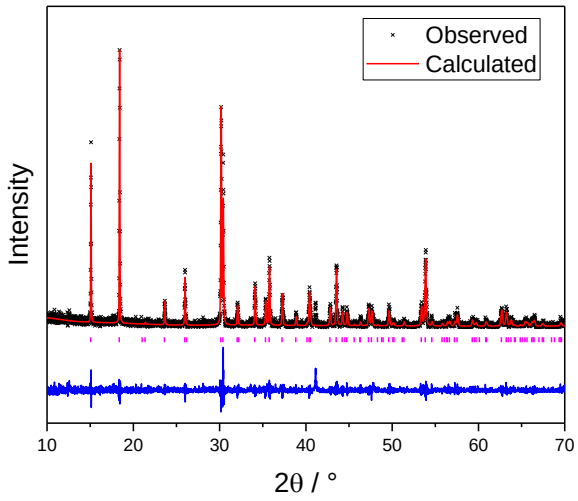

Figure 6.22 Pawley refinement against measured data of $BaNaRh(OH)_6$.

At higher concentrations of $Ba(OH)_2$ different phases were observed in the diffraction pattern (Section 6.7).

A hydrogarnet $Ba_3Rh_2(OH)_{12}$ was not observed or synthesised through these experiments and this is likely due to the large size of barium. A barium hydrogarnet would require a trivalent cation larger than Fe^{3+} or Ga^{3+} but smaller than rare earth cations[64] and as such barium hydrogarnets have only been observed containing scandium and indium.[58]

6.6.3 Single Crystal Structure Solution

Single crystal data were collected at 150 K from a yellow diamond like crystal, which was selected from a sample which was largely polycrystalline powder.

The crystal structure is shown in Figure 6.23 and crystal cell parameters are provided below in Table 6.4. Full details of the structure solution are given in Appendix A.

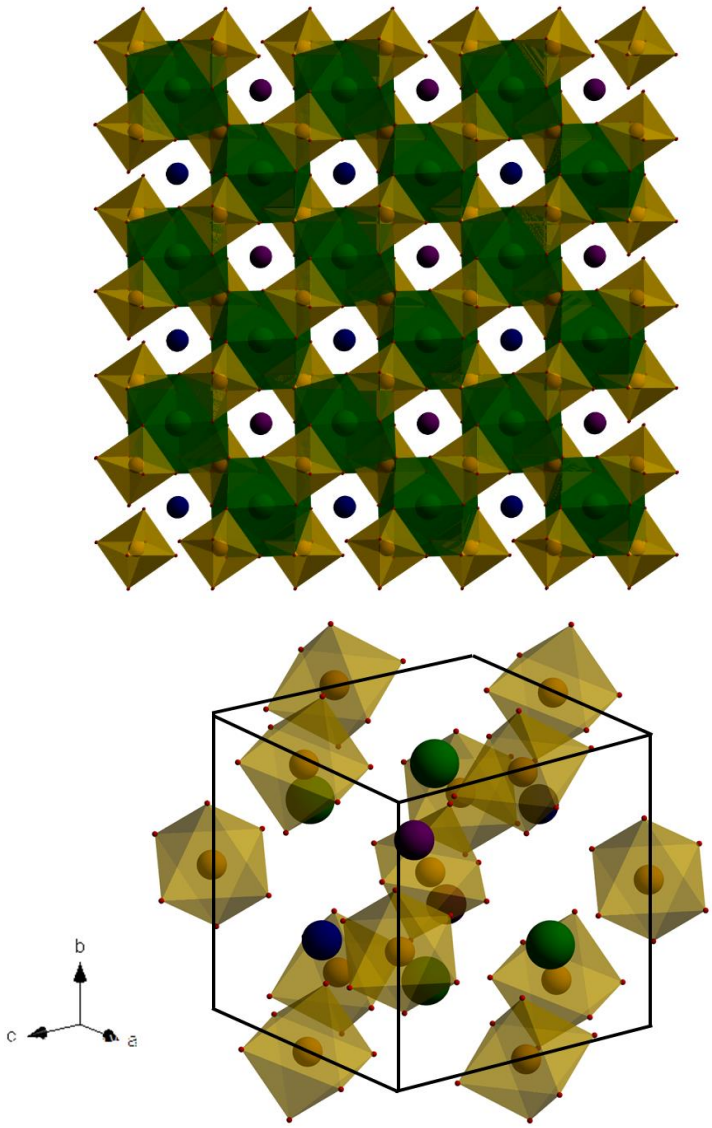

Figure 6.23 *(top)* 3x3x3 super-cell of the crystal structure of $BaNaRh(OH)_6$, *(bottom)* unit cell of $BaNaRh(OH)_6$ showing the isolated, tilted Rh-O octahedra. Gold spheres are Rh, green spheres Ba, blue spheres and purple sphere represent crystallographically different Na sites, red spheres are O.

Table 6.4 Refined single crystal parameters for $BaNaRh(OH)_6$ space group $P4_2/n$, (no. 86), a = 8.28420 Å, c = 8.41980 Å.

Wyckoff site	Atom	x	y	z	Occupancy	Uiso / Å^2
4e	Ba	1/4	3/4	0.79014	1.0	0.009
4d	Rh	1/2	1/2	1/2	1.0	0.006
2b	Na1	1/4	1/4	3/4	1.0	0.014
2a	Na2	1/4	1/4	1/4	1.0	0.026
8g	O1	0.45356	0.26059	0.54711	1.0	0.010
8g	O2	0.44558	0.45874	0.26546	1.0	0.010
8g	O3	0.26183	0.54071	0.54598	1.0	0.011

The structure consists of Rh-O octahedra which are not connected to each other but instead share edges with the barium or sodium ions. This is not unusual as isolated $M(OH)_6$ units are found frequently in mixed-metal hydroxides especially when a high positive charge is present on the metal centre such as found in double hydroxides such as MSn$(OH)_6$ (M = Li, Ba, Sr).[54] The barium is 10 coordinate with Ba-O bond distances ranging from 2.69 – 3.09 Å with an average bond length of 2.86 Å close to expected Ba-O distances.[54] Sodium occupies two different sites in the crystal structure both in 8 coordination. The bond distances range from 2.402 – 2.960 Å for Na1 with an average distance of 2.681 Å, and 2.373 – 3.018 Å for Na2 with an average bond distance of 2.696 Å. Bond valence sums calculated from these distances are provided in Table 6.5. All bond valence sums show excellent agreement with the expected except for Ba1, which is calculated as 2.32. However, if the contribution of the two furthest Ba-O bond distances (3.09 Å) is neglected then the bond valence sum reduces to 2.08.

Table 6.5 Bond valence sums for all metals in $BaNaRh(OH)_6$.

Metal	Coordination	Average bond distance / Å	BVS / vu
Rh1	6	2.051	2.97
Ba1	10	2.850	2.32
Na1	8	2.681	0.96
Na2	8	2.696	1.00

The simulated powder XRD pattern using the crystal structure as obtained from single crystal diffraction is in excellent agreement with the measured powder XRD pattern and Rietveld refinement against room temperature powder X-ray diffraction data using the model solved from the single crystal data shows an excellent fit to the observed data (Figure 6.24). The refined crystals parameters from powder XRD are shown in Table 6.6. The hydrogen positions were not added to the model as it would not be possible to observe hydrogen amongst the barium and rhodium electron density.

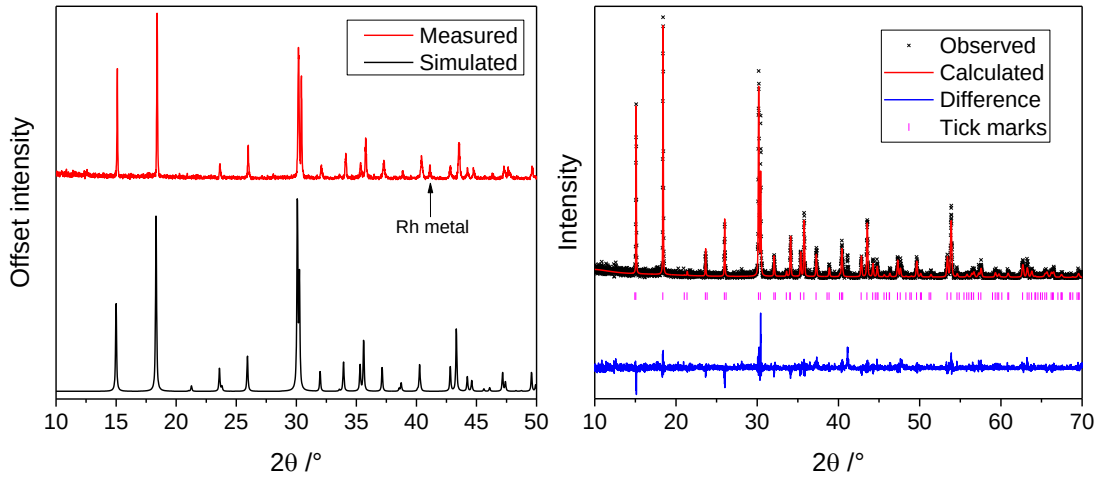

Figure 6.24 *(left)* Simulated powder XRD pattern *(black)* using the model obtained from single crystal structure solution, and observed data from a polycrystalline sample *(red)*, *(right)* Rietveld fit to observed data from a polycrystalline sample of $BaNaRh(OH)_6$.

Table 6.6 Refined crystal parameters for $BaNaRh(OH)_6$ from powder XRD using the model obtained from the single crystal solution. Parameters in italics indicate refined parameters.

Wyckoff site	Atom	x	y	z	Occupancy	Beq / Å^2
4e	Ba	¼	3/4	*0.7876(3)*	1.0	*1.103*
4d	Rh	½	1/2	½	1.0	*0.7395*
2b	Na1	¼	1/4	¾	1.0	0.014
2a	Na2	¼	1/4	¼	1.0	0.006
8g	O1	*0.4462(3)*	*0.2724(2)*	*0.54603(2)*	1.0	0.010
8g	O2	*0.4467(3)*	*0.4516(1)*	*0.2626(2)*	1.0	0.010
8g	O3	*0.2407(1)*	*0.5348(2)*	*0.5442(2)*	1.0	0.011

NB The sodium and oxygen thermal parameters were kept fixed throughout the refinement.

6.6.4 Scanning Electron Microscopy (SEM)

SEM on a small single crystal showed the morphology of the hydroxide crystals (Figure 6.25). Energy dispersive X-ray analysis (EDX) using a scanning electron microscope suggested the presence of the metals barium, rhodium and also sodium in

approximately 1:1:1 ratio, in agreement with the structure solved by single crystal X-ray diffraction. Although in the reaction the ratio of Ba:Rh was 1:2, there was clear evidence of unreacted rhodium due to the yellow coloured supernatant upon filtration. Reactions conducted using KOH formed a different phase (Section 6.7) further suggesting that sodium is in the structure and that potassium is likely too big to occupy a site in this material.

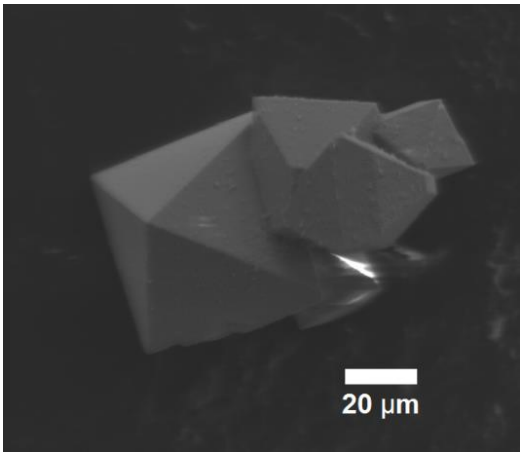

Figure 6.25 SEM imagining of $BaNaRh(OH)_6$ single crystals.

6.6.5 XANES

XANES measured on B18 at the Rh K-edge on a polycrystalline sample of $BaNaRh(OH)_6$ shows that rhodium is present as Rh^{3+} as the edge position is very close to the Rh^{3+} reference. This is consistent with the bright yellow colour of the sample typical for the presence of octahedral trivalent rhodium (Figure 6.26).[71]

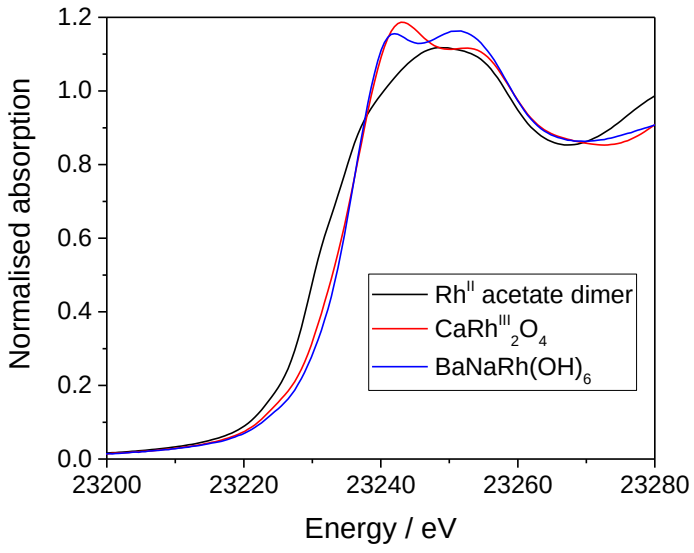

Figure 6.26 XANES spectra of $BaNaRh(OH)_6$ and relevant references.

6.6.6 Infrared Spectroscopy

The infrared spectrum of $BaNaRh(OH)_6$ does not show a clear O-H stretching mode expected around 3500 cm^{-1} but this is likely because it is masked by the large surface O-H stretching band recorded for this material around this wavenumber (Figure 6.27).

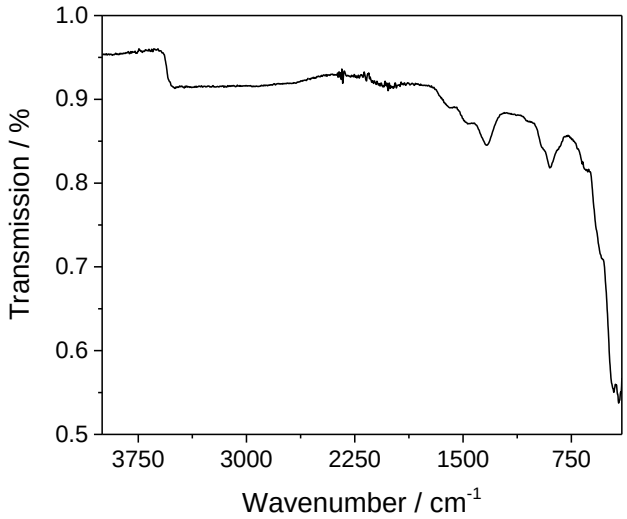

Figure 6.27 IR spectrum of $BaNaRh(OH)_6$.

6.6.7 Thermal decomposition of $BaNaRh(OH)_6$

In situ powder XRD on heating $BaNaRh(OH)_6$ to 810 °C shows that at around 325 °C the phase begins to collapse with the emergence of a transient phase which itself exists only between 325 °C and 500 °C (Figure 6.28(a)). A third phase can be seen to form at around 400 °C and remains the only stable phase after heating to 810 °C. As yet no oxide candidate for this material has been identified, though the observed reflections are similar in position and intensity to $Sr_6Rh_5O_{15}$ (but shifted to lower angle consistent with the larger Ba^{2+} cation). TGA also shows a mass loss at ~305 °C of ~10% (Figure 6.28(b)), which is lower than expected for a loss of 3 moles of H_2O from $BaNaRh(OH)_6$, which would be expected to be ~15%. A small but non-negligible mass uptake between 700 and 800 °C could possibly be attributed to oxidation of a rhodium metal impurity followed by subsequent reduction at elevated temperatures back to rhodium metal.

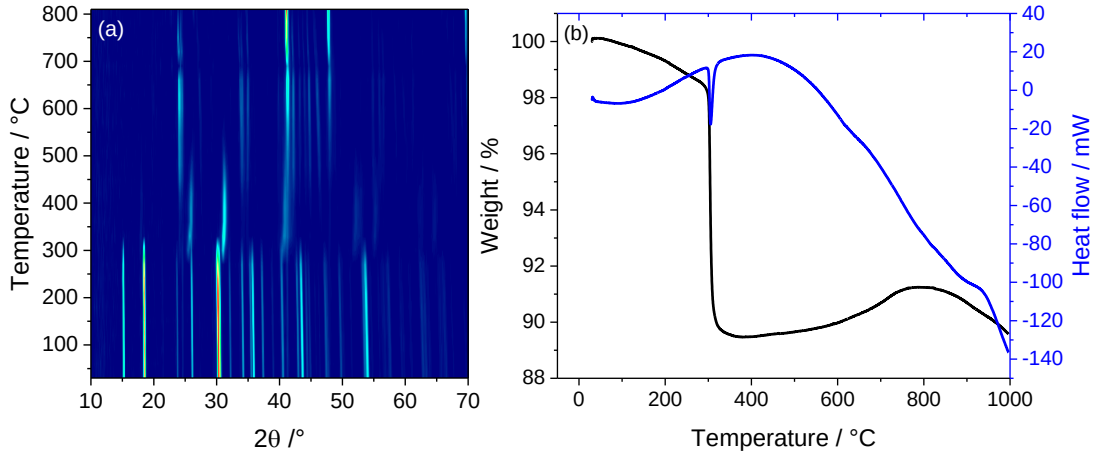

Figure 6.28 (a) *In situ* thermodiffractometry of $BaNaRh(OH)_6$ (b) TGA of $BaNaRh(OH)_6$.

The decomposition product from the hexagonal Ca-Na-Rh-(OH) phase showed formation of the $NaRhO_2$ delafossite, which then partially forms $CaRh_2O_4$ at higher temperatures. It might be expected that the delafossite might also form during decomposition of $BaNaRh(OH)_6$ but this is not observed upon heating. Neither transient phase or the material isolated from heating to 810 °C could be identified though as mentioned above the reflections are similar to those observed in $Sr_6Rh_5O_{15}$ (Figure 6.29). A Pawley refinement of a $Ba_6Rh_5O_{15}$ using initial lattice parameters from the strontium model was attempted but owing to the large hexagonal cell (a = 9.6517 Å, c = 13.0480 Å), a large number of possible reflections were allowed and so although reflections were fitted it is highly unlikely that the refined lattice parameters are real. Further annealing at 900 °C serves to improve the crystallinity of this phase and at higher temperatures (1100 °C) another phase can be seen to form (Figure 6.29).

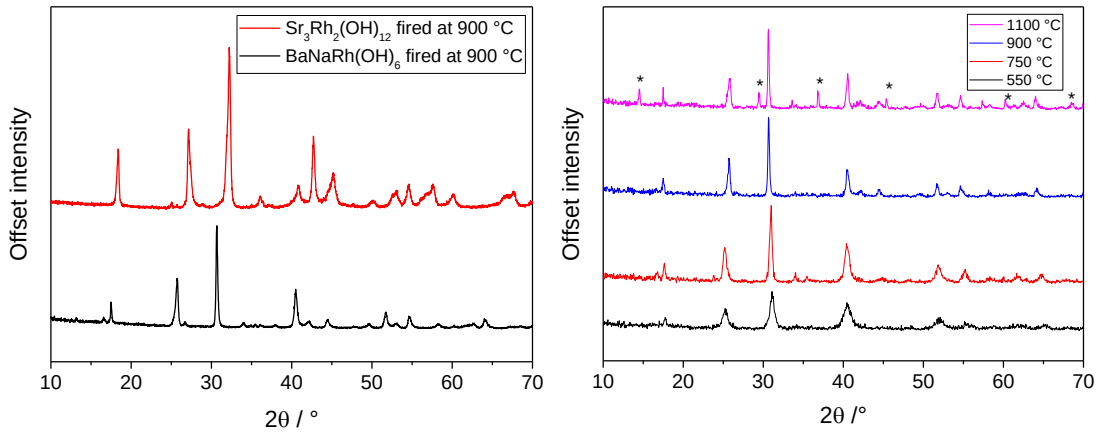

Figure 6.29 *(left)* Decomposition product of $BaNaRh(OH)_6$ fired at 900 °C *(black)* compared against the observed powder pattern of the decomposition product of $Sr_3Rh_2(OH)_{12}$ fired at 900 °C *(red)*, *(right)* Decomposition of $BaNaRh(OH)_6$ at various temperatures. *denotes growth of a secondary phase.

XANES analysis also shows that, like for the $Sr_3Rh_2(OH)_{12}$ decomposition oxide, that the oxidation state of this material formed from $BaNaRh(OH)_6$ fired at 700 °C is likely to be mixed valent Rh^{3+}/Rh^{4+} owing to the shift of the Rh K-edge position to higher energy when compared against the $CaRh_2O_4$ reference material (Figure 6.30).

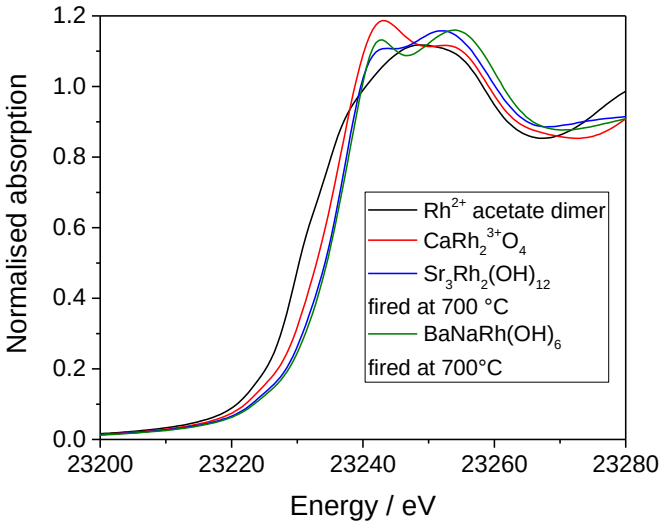

Figure 6.30 XANES of the $BaNaRh(OH)_6$ sample fired at 700 °C with relevant standards.

6.6.8 ^{23}Na MAS NMR

^{23}Na MAS NMR confirms the well-ordered nature of the material showing two well-defined Na signals (Figure 6.31) consistent with two Na environments which is consistent with the single crystal structure solution. The quadrupolar coupling constants are quite large which is consistent with distorted 8-coordinate environments (Figure 6.32), which is found for both sodium cations.

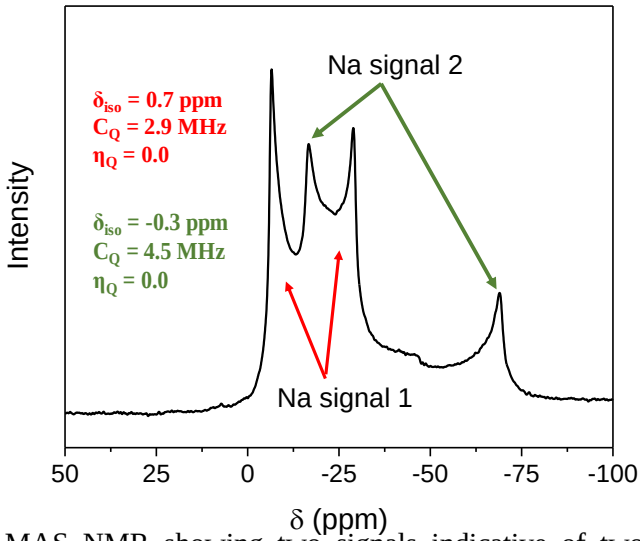

Figure 6.31 ^{23}Na MAS NMR showing two signals indicative of two Na environments consistent with the single crystal structure of $BaRhNa(OH)_6$.

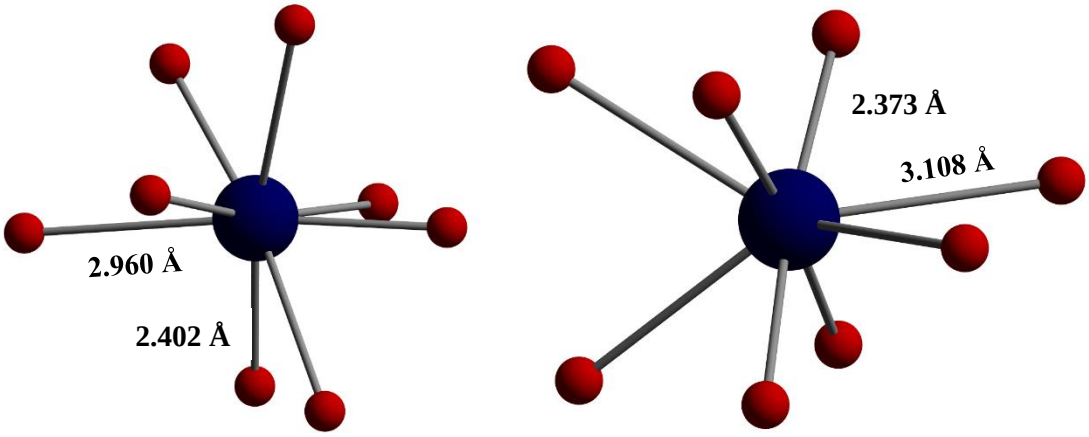

Figure 6.32 *(left)* 8-coordinate Na1, *(right)* 8-coordinate Na2, with some bond distances labelled.

6.7 Synthesis of other Ba-Rh-OH phases

It was found that if a ratio 2:1 of Ba:Rh was used instead then an entirely different phase was obtained (Figure 6.33).

Similar conditions were found for the barium ruthenium oxyhydroxides reported from hydrothermal synthesis where an excess of barium peroxide resulted in the formation of a different, but phase pure, barium ruthenium oxyhydroxide.[3,68]

Powder XRD of the product from a 1:1 ratio of Ba:Rh in NaOH reaction showed that both the tetragonal $BaNaRh(OH)_6$ and an as yet unknown material are both present.

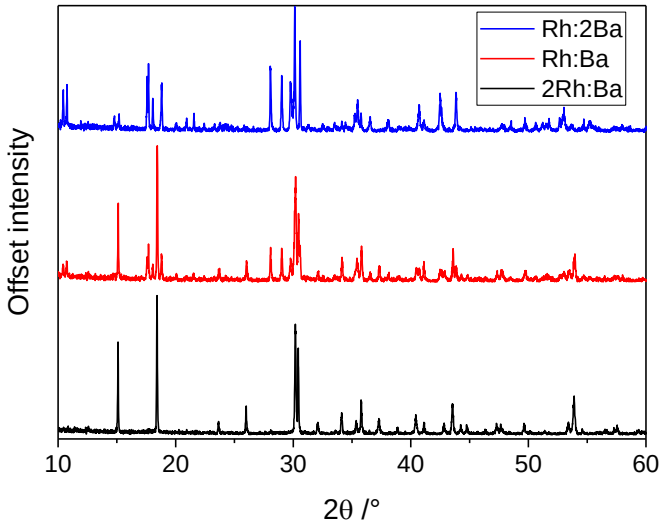

Figure 6.33 Powder pattern showing how different phases emerge from the reaction depending on the stoichiometry of Ba:Rh.

In situ thermodiffractometry and TGA both suggest that like the tetragonal $BaNaRh(OH)_6$ this new material is a hydroxide (Figure 6.34) since the temperature at which this phase decomposes at is very similar to the other hydroxide phases presented earlier in this Chapter. A loss of 10% in the TGA is similar to the other rhodium hydroxides presented. EDX by SEM also showed that Na was unlikely to be in the structure and showed that a ratio of 1:1 Ba:Rh means an empirical formula $BaRh(OH)_5$ can be proposed. A theoretical 14% mass loss should be observed in the TGA, which is a little higher than what is really observed. Attempts to index the material have as yet been unsuccessful. This itself might indicate that this sample is a mixed phase of two or more materials though the *in situ* thermodiffractometry shows that all peaks in this material disappear at the same time, which is suggestive that the material is single phase. The presence of low angle peaks suggests that it likely has a large unit cell.

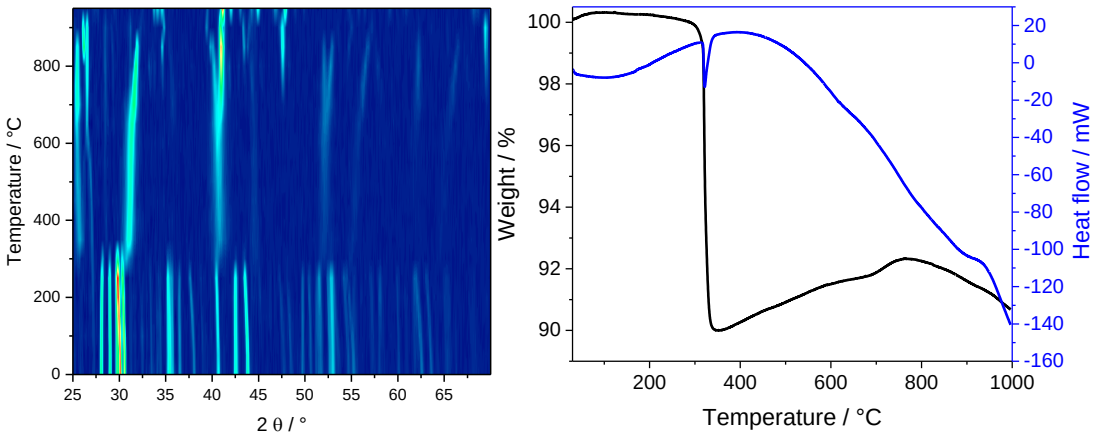

Figure 6.34 *In situ* thermodiffractometry of the unknown Ba-Rh-OH phase, *(right)* TGA-trace of the unknown barium rhodium hydroxide material.

The $BaKRh(OH)_6$ analogue of the $BaNaRh(OH)_6$ material was inaccessible when KOH was used in place of NaOH. In reactions to make polycrystalline powders where 10 ml distilled water was used only a brown material amorphous to X-rays was isolated. However, when the volume of water was reduced to 2 ml (wet hydroflux as opposed to hydroflux) it was found that a crystalline material was formed. The Bragg reflections could be fitted to a hexagonal cell in space group $P\bar{3}1m$ with lattice parameters a = 6.27847(6) Å, c = 13.44955(19) Å. In a recent paper by zur Loye *et al.* a new barium iron oxide and a potassium substituted barium iron oxide were prepared by a similar wet hydroflux method.[56] The unit cell refined for $K_{0.22}Ba_{0.89}Fe_4O_7$ was reported as a = 5.1532(2) Å, c = 13.8134(16) Å and the structures of these iron oxides were solved in space group $P\bar{3}1c$. These materials reported by zur Loye are claimed to be oxides whereas the low decomposition temperature of 300 °C of Ba-K-Rh-OH (Figure 6.35) suggests that this rhodium material is a hydroxide like all the other materials presented in this chapter. EDX suggested the metal composition of Ba:K:Rh as 1:1:1.

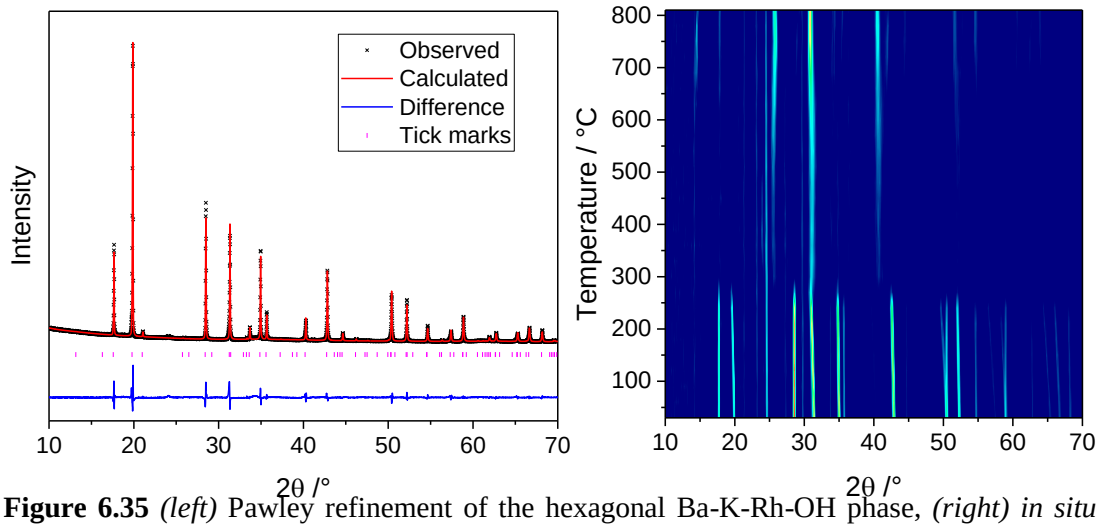

Figure 6.35 *(left)* Pawley refinement of the hexagonal Ba-K-Rh-OH phase, *(right) in situ* thermodiffractometry of the same phase showing decomposition around 300 °C.

6.8 Summary

Two rhodium hydrogarnets have been prepared which have received little attention in previous research. A study into the synthesis and decomposition of $Sr_3Rh_2(OH)_{12}$ was reported in 1983 by Ivanov-Emin,[25] whilst $Ca_3Rh_2(OH)_{12}$ features only in a table of silicon-free hydrogarnets by Morán-Miguélez *et al.*[64] This work reports the first structural refinement to determine crystal structure parameters. $Ca_3Rh_2(OH)_{12}$ decomposes readily into an amorphous phase preceding the formation of $CaRh_2O_4$ at 650 °C. $CaRh_2O_4$ has previously been synthesised but by high temperature reactions requiring reaction times of days due to the reactivity of rhodium oxide. The thermal decomposition pathway of $Sr_3Rh_2(OH)_{12}$ does not give orthorhombic $SrRh_2O_4$ with the $CaFe_2O_4$ structure-type as proposed by Ivanov-Emin, but instead likely phase separates forming crystalline $Sr_6Rh_5O_{15}$ or a similar member of this family, which further partially decomposes at a higher temperature into Sr_2RhO_4. There is no evidence for the formation of the orthorhombic $SrRh_2O_4$ material in this work or indeed in the literature apart from in the study reported by Ivanov-Emin which means that the hexagonal β-$SrRh_2O_4$ is likely the only known polymorph to date.

A new phase in the Ca-Na-Rh-(OH) system, has been synthesised when sodium hydroxide is used in the hydroflux instead of potassium hydroxide. The material was indexed to a hexagonal cell with a crystal structure similar to simple Group II hydroxides bearing the $Mg(OH)_2$ structure type. The material initially decomposes

into a delafossite, $NaRhO_2$, which is acid stable, and CaO. If the latter is not removed by washing with acid then reaction between the delafossite and the calcium oxide occurs at higher temperatures ~1100 °C yielding formation of some $CaRh_2O_4$.

A new hexahydroxometallate $BaNaRh(OH)_6$ has been synthesised, its structure characterised by single crystal X-ray diffraction, and its thermal decomposition investigated by TGA and powder X-ray diffraction. ^{23}Na solid state MAS NMR confirmed the presence of two ordered Na sites.

When the reagent ratio or solvothermal synthetic approach is altered slightly other new phases emerge from the reaction. This hydroflux method, developed by the zur Loye team, shows the potential and scope for discovery of new metastable hydroxometallate materials which may offer a simple route to new oxide materials via thermal decomposition, as well as allowing the growth of larger crystals for structural analysis.

6.9 References

1 W. Witczak-Krempa, Y. B. Kim and L. Balents, *Ann. Rev. Condens. Matt. Phys*, 2014, **5**, 57–82.

2 R. Arita, J. Kunes, A. V Kozhevnikov, A. G. Eguiluz and M. Imada, *Phys. Rev. Lett*, 2012, **108**, 86403.

3 C. I. Hiley, M. R. Lees, J. M. Fisher, D. Thompsett, S. Agrestini, R. I. Smith and R. I. Walton, *Angew. Chem., Int. Ed*, 2014, **126**, 4512–4516.

4 K. Ishida, H. Mukuda, Y. Kitaoka, K. Asayama, Z. Q. Mao, Y. Mori and Y. Maeno, *Nature*, 1998, **396**, 658–660.

5 J. M. Longo, P. M. Raccah and J. B. Goodenough, *J. Appl. Phys.*, 1968, **39**, 1327–1328.

6 Y. You, I. Kimchi and A. Vishwanath, *Phys. Rev. B*, 2012, **86**, 85145.

7 F. Wang and T. Senthil, *Phys. Rev. Lett*, 2011, **106**, 136402.

8 Y. Okamoto, M. Nohara, H. Aruga-katori and H. Takagi, *Phys. Rev. Lett*, 2007, **99**, 137207.

9 J. A. Kurzman, L. M. Misch and R. Seshadri, *Dalton Trans.*, 2013, **42**, 14653–67.

10 G. Bayer and H. G. Wiedemann, *Thermochim. Acta*, 1976, **15**, 213–226.

11 H. Müller-Buschbaum, *Z. Anorg. Allg. Chem*, 2007, **633**, 1289–1306.

12 J. Etourneau, J. Portier and F. Menil, *J. Alloys Compd.*, 1992, **188**, 1–7.

13 J. W. M. Biesterbos and J. Hornstra, *J. Less-Common Met.*, 1973, **30**, 121–125.

14 K. R. Poeppelmeier and G. B. Ansell, *J. Cryst. Growth*, 1981, **51**, 587–588.

15 O. Muller and R. Roy, *J. Less-Common Met.*, 1968, **16**, 129–146.

16 R. D. Shannon, *Solid State Commun.*, 1968, **6**, 139–143.

17 A. Banerjee, R. Prasad and V. Venugopal, *Thermochim. Acta*, 2004, **417**, 59–65.

18 K. Yamaura, Q. Huang, M. Moldovan and D. P. Young, *Phys. B*, 2006, **380**, 1134–1135.

19 K. Yamaura, Q. Huang, M. Moldovan, D. P. Young, A. Sato, Y. Baba, T. Nagai, Y. Matsui and E. Takayama-muromachi, *Chem. Mater.*, 2005, **17**, 359–365.

20 K. T. Jacob and Y. Waseda, *J. Solid State Chem.*, 2000, **150**, 213–220.

21 K. Yamaura and E. Takayama-Muromachi, *Phys. C*, 2006, **445**–**448**, 54–56.

22 M. Itoh, T. Shimura, Y. Inaguma and Y. Morii, *J. Solid State Chem.*, 1995, 118, 206–209.

23 T. Shimura, M. Itoh and T. Nakamura, *J. Solid State Chem.*, 1992, **98**, 198–200.

24 A. L. Hector, W. Levason and M. T. Weller, *Eur. J. Solid State Inorg. Chem.*, 1998, **35**, 679–687.

25 B. N. Ivanov-Emin, *Russ. J. Inorg. Chem*, 1983, **28**, 557.

26 H. Mizoguchi, L. N. Zakharov, A. P. Ramirez, W. J. Marshall, A. W. Sleight and M. A. Subramanian, *Inorg. Chem.*, 2009, **48**, 204–8.

27 B. J. Kennedy, K. Yamaura and E. Takayama-Muromachi, *J. Phys. Chem. Solids*, 2004, **65**, 1065–1069.

28 K. Yamaura, Q. Huang, D. P. Young, M. Arai and E. Takayama-Muromachi, *Phys. B Condens. Matter*, 2003, **329**–**333**, 820–821.

29 K. Yamaura, Q. Huang, D. Young, Y. Noguchi and E. Takayama-Muromachi, *Phys. Rev. B*, 2002, **66**, 134431.

30 K. Yamaura, Q. Huang, D. P. Young and E. Takayama-Muromachi, *Chem. Mater.*, 2004, **16**, 3424–3430.

31 K. Boulahya, M. Hernando, A. Varela, J. M. González-Calbet, M. Parras and U. Amador, *Chemistry*, 2002, **8**, 4973–9.

32 J. B. Claridge and H. C. zur Loye, *Chem. Mater.*, 1998, **10**, 2320–2322.

33 K. E. Stitzer, A. El Abed, J. Darriet and H. C. zur Loye, *J. Am. Chem. Soc.*, 2001, **123**, 8790–8796.

34 J. B. Claridge and H. C. zur Loye, *Mat. Res. Soc. Symp. Proc*, 1999, **547**, 183–189.

35 J. R. Plaisier, A. A. C. van Vliet and D. J. W. IJdo, *J. Alloys Compd.*, 2001, **314**, 56–61.

36 B. A. Reisner and A. M. Stacy, *J. Am. Chem. Soc.*, 1998, **120**, 9682–9683.

37 J. F. Vente, J. K. Lear and P. D. Battle, *J. Mater. Chem.*, 1995, **5**, 1785–1789.

38 R. Horyń, Z. Bukowski, M. Wolcyrz and a. J. Zaleski, *J. Alloys Compd.*, 1997, **262**–**263**, 267–270.

39 B. L. Chamberland and J. B. Anderson, *J. Solid State Chem.*, 1981, **39**, 114–119.

40 T. Siegrist, E. M. Larson and B. L. Chamberland, *J. Alloys Compd.*, 1994, **210**, 13–17.

41 H.-C. zur Loye, Q. Zhao, D. E. Bugaris and W. M. Chance, *CrystEngComm*, 2012, **14**, 23–39.

42 K. E. Stitzer, A. El Abed, J. Darriet and H.-C. zur Loye, *J. Am. Chem. Soc.*, 2004, **126**, 856–64.

43 K. E. Stitzer, M. D. Smith, J. Darriet, and H.-C zur Loye, *Chem. Commun.*, 2001, **0**, 1680–1681.

44 J. N. Mwamuka, W. R. Gemmill, K. E. Stitzer, M. D. Smith and H. C. zur Loye, *J. Alloys Compd.*, 2004, **377**, 91–97.

45 Y. Saeed, N. Singh and U. Schwingenschlögl, *Sci. Rep.*, 2014, **4**, 4390.

46 K. Hobbie and R. Hoppe, *Z. Anorg. Allg. Chem*, 1988, **565**, 106–110.

47 R. Hinogami, K. Toyoda, M. Aizawa, S. Yoshii, T. Kawasaki and H. Gyoten, *Electrochem. commun.*, 2013, **35**, 142–145.

48 R. B. Macquart, M. D. Smith and H.-C. zur Loye, *Cryst. Growth Des.*, 2006, **6**, 1361–1365.

49 A. E. Smith, A. W. Sleight and M. A. Subramanian, *Mater. Res. Bull.*, 2010, **45**, 460–463.

50 H. Mizoguchi, L. N. Zakharov, N. S. P. Bhuvanesh, A. W. Sleight and M. A.

Subramanian, *J. Solid State Chem.*, 2011, **184**, 1381–1386.

51 B. J. Kennedy, *Mater. Res. Bull.*, 1997, **32**, 479–483.

52 H. Mizoguchi, M. Hirano, S. Fujitsu, T. Takeuchi, K. Ueda and H. Hosono, *Appl. Phys. Lett.*, 2002, **80**, 1207–1209.

53 C. I. Hiley, D. O. Scanlon, A. A. Sokol, S. M. Woodley, A. M. Ganose, S. Sangiao, J. M. De Teresa, P. Manuel, D. D. Khalyavin, M. Walker, M. R. Lees and R. I. Walton, *Phys. Rev. B*, 2015, **92**, 104413.

54 H. Mizoguchi, N. S. P. Bhuvanesh, Y. Kim, S. Ohara and P. M. Woodward, *Inorg. Chem.*, 2014, **53**, 10570–10577.

55 D. E. Bugaris, M. D. Smith and H. C. zur Loye, *Inorg. Chem.*, 2013, **52**, 3836–3844.

56 T. Ferreira, G. Morrison, W. M. Chance, S. Calder, M. D. Smith and H. C. zur Loye, *Chem. Mater.*, 2017, **29**, 2689–2693.

57 W. M. Chance, D. E. Bugaris, A. S. Sefat and H. C. zur Loye, *Inorg. Chem.*, 2013, **52**, 11723–11733.

58 W. Kwestroo, H. C. A. van Gerven and H. A. M. van Hal, *Mater. Res. Bull.*, 1977, **12**, 161–164.

59 G. Li, S. Feng, L. Li, X. Li and W. Jin, *Chem. Mater.*, 1997, **9**, 2894–2901.

60 J. Gustafson, R. Westerström, A. Resta, A. Mikkelsen, J. N. Andersen, O. Balmes, X. Torrelles, M. Schmid, P. Varga, B. Hammer, G. Kresse, C. J. Baddeley and E. Lundgren, *Catal. Today*, 2009, **145**, 227–235.

61 A. Russell and W. S. Epling, *Catal. Rev.*, 2011, **53**, 337–423.

62 K. Sardar, J. Fisher, D. Thompsett, M. R. Lees, G. J. Clarkson, J. Sloan, R. J. Kashtiban and R. I. Walton, *Chem. Sci.*, 2011, **2**, 1573.

63 N. N. Nevskii, B. N. Ivanov-Emin, N. A. Nevskaya, G. Z. Kasiev and N. V Belov, *Dokl. Akad. Nauk SSSR*, 1982, **264**, 857–858.

64 E. Morán-Miguélez, M. A. Alario-Franco and J. C. Joubert, *Mater. Res. Bull.*, 1986, **21**, 107–113.

65 H. Zhang, T. Wang, X. Chen and W. Zhu, *Particuology*, 2016, **24**, 8–13.

66 R. D. Shannon and C. T. Prewitt, *Acta Crystallogr. Sect. B*, 1969, **25**, 925–946.

67 N. G. Dave and S. K. Chopa, *J. Am. Ceram. Soc.*, 1966, **49**, 575–576.

68 C. I. Hiley, M. R. Lees, D. L. Hammond, R. J. Kashtiban, J. Sloan, R. I. Smith and R. I. Walton, *Chem. Commun.*, 2016, **52**, 6375–6378.

69 M. W. Chance, PhD Thesis, University of South Carolina, 2014.

70 P. Ptá, E. Bartoní and T. Opravil, *Ceram. Int.*, 2015, **41**, 115–126.

71 H. Hata, Y. Kobayashi, V. Bojan, W. J. Youngblood and T. E. Mallouk, *Nano Lett.*, 2008, **8**, 794–799.

Chapter 7: Summary and Further Work

7. Summary and Further Work

This thesis has presented oxides, oxyhydroxides, and hydroxides, some which are new, that have been prepared by a variety of different solvothermal reactions. Structural analysis and characterisation by a variety of different techniques have been employed in an effort to understand the structure of these materials presented. Some materials were screened as catalysts for various reactions of relevance to industry. The results are summarised in the following few pages, with suggestions of future work that would be needed to further understand the materials.

7.1 Chapter 3

The first section of this chapter presented the findings from an *in situ* powder X-ray diffraction experiment of the crystallisation of a cobalt gallium oxide prepared under solvothermal conditions. The synthesis of the cobalt gallate prepared using a solvent mixture ratio 1:1 (volume) of H_2O:ethanolamine (MEA) occurs via two layered double hydroxides prior to the crystallisation of the spinel. The fast acquisition time using high energy X-rays allowed for the reaction to be followed *in situ*, and despite diffraction from PTFE and steel of the reaction vessel, some structural analysis of each phase was possible; in particular analysis of the lattice parameters' evolution with time. A short lived layered double hydroxide was observed during the first fifteen minutes of the reaction. This metastable material would likely to have never been observed by conventional laboratory X-ray techniques and quenching experiments to detect it would be very time consuming. The reaction conducted in ethanolamine only showed that only the cobalt gallate spinel formed without observation of any transient phases. The onset of formation of both spinels occurred at approximately the same time. The spinel prepared in ethanolamine only was found to be much less crystalline than the spinel prepared in the mixed solvent. Photocatalytic measurements revealed that both spinels showed similar activity as water oxidation catalysts.

Further experiments to probe this crystallisation pathway would include varying the temperature of reaction in order to obtain quantitative kinetic information about the reaction (rates and then activation energies from Arrhenius plots, for example). Experiments where the ratio of MEA:H_2O is varied might also prove useful in determining how much water is required to bring about the formation of the LDH phases. In the MEA only reaction there is still some water present from

$Co(NO_3)_2 \cdot 6H_2O$. Clearly however this amount of water is not sufficient to cause the formation of layered hydroxide species. Numerous off-line experiments were undertaken in order to isolate the first transient LDH but none was successful, likely due to reasons listed earlier in this chapter. More experiments with use of the *in situ* X-ray beam would be useful in attempting to isolate this kinetically stable product to determine its chemical composition. Reactions varying the stoichiometric ratio or even a reaction using cobalt nitrate only would be useful in studying the composition of the LDHs formed *in situ*. This work also suggests that despite the large volume of publications on LDH synthesis, structure and stability[1–8] there are potentially novel metastable LDHs with different metal compositions that may be accessible via solvothermal synthesis.

The second section of Chapter 3 showed that the spinel $Co_{1.146}Ga_{1.861}O_{3.932}$ can be prepared from solvothermal reaction of pre-formed γ-Ga_2O_3 and cobalt nitrate in a 1:1 MEA:H_2O solvent mixture. The structure was refined against powder neutron diffraction data and found to be slightly oxide deficient. The as-made material is metastable and a rearrangement of the cations occurs with temperature and found to be largely irreversible upon cooling to room temperature. XANES analysis at the Co K-edge showed that the rearrangement of cations occurred without oxidation of Co^{2+}. A good fit to the PDF was obtained using the average structure model obtained from analysis of the Bragg diffraction, although the slightly poorer fit of the low *r*-region indicates some local disorder present in the material.

7.2 Chapter 4: Polymorphism of $Ga_{2-x}Al_xO_3$

7.2.1 γ-$Ga_{2-x}Al_xO_3$

A range of solvents were screened and 2-propanol was found optimal in the solvothermal synthesis of the mixed metal defect spinel solid solution γ-Ga_2O_3-γAl_2O_3 at 240 °C. Up to ~90% Al^{3+} can be incorporated into the spinel by this method and there is no need for a firing step after the solvothermal reaction to induce crystallinity. ^{27}Al and ^{71}Ga MAS NMR found that aluminium and gallium preferentially occupy octahedral and tetrahedral sites, respectively. A combined NMR study allowed for distribution of metal in the spinels to be proposed and to postulate where the vacancies are located within the spinel. Al^{3+} substitution was found to

enhance the thermal stability of the spinel phase, and phase transformation occurred directly into the beta polymorph up to 65% Al^{3+}, beyond which phase separation into a mixture of both α and β-$(Ga,Al)_2O_3$ occurred. Unlike in the spinel phases aluminium was found to occupy both tetrahedral and octahedral sites in the beta polymorph which was confirmed by Rietveld analysis of powder X-ray data and solid-state ^{27}Al MAS NMR.

In terms of further work a PDF analysis study would be very useful in further studying the disordered structures of these spinels. It has been found previously that as the crystallinity of γ-Ga_2O_3 decreases the number of crystallographically different occupied non-spinel sites increases[9,10] so it is likely this would be also be the case in these new materials. Furthermore, not only would an increased number of non-spinel sites have to be included, but the ratio of Ga:Al would need to be maintained and the composition justly spread over all sites: therefore, it is likely that Reverse Monte Carlo (RMC) analysis of the total scattering would be required in order to build a model that fully describes the complex structure of the spinels.

7.2.2 $Ga_{5-x}Al_xO_7(OH)$

The system $Ga_{5-x}Al_xO_7(OH)$ was synthesised and studied. This material had been reported previously by other authors but incorrectly described as $GaAlO_3$. The oxyhydroxide displays anisotropic peak broadening in the XRD data, which is a likely consequence of the large hexagonal plates observed by electron microscopy. Up to 30% Al^{3+} (x = 1.5) could be incorporated into the structure by using 1,4-butanediol as the synthesis solvent. Solid-state ^{27}Al MAS NMR showed that Al^{3+} almost exclusively occupies the octahedral sites in these materials. Thermal decomposition of this phase showed that the materials decomposed into a mixture of κ- and ε-$Ga_{2-x}Al_xO_3$ prior to phase transformation into the thermodynamically stable β-$Ga_{2-x}Al_xO_3$. A reinvestigation into the thermal decomposition of $Ga_5O_7(OH)$ also showed that the oxyhydroxide decomposed into ε- and κ-Ga_2O_3 around 450 °C but whether this is a mixture of binary oxides or a disordered intergrowth remains un-resolved. A more crystalline sample of κ-Ga_2O_3 (still with some ε-Ga_2O_3 present) can be prepared by hydrothermal treatment of $Ga_5O_7(OH)$ at 480 °C. A high temperature solvothermal reaction of Ga metal in 1:1 H_2O:MEA around this temperature might also lead to a direct pathway to either or both of these polymorphs and would be worth investigating

with suitable equipment. Other exploratory synthesis could be to continue attempting to prepare $Ga_{5-x}Fe_xO_7(OH)$, since it has been surprising that this material could not be prepared by the 1,4-butanediol method. If it is possible to prepare this oxyhydroxide it is expected it would decompose into materials κ-$Ga_{2-x}Fe_xO_3$ of which κ-$Ga_{1.0}Fe_{1.0}O_3$ is a well-known member and well-studied, because it is both ferromagnetic and piezoelectric.[11]

7.2.3 Catalysis

Whilst α-, β- and γ-Ga_2O_3 as catalyst supports for palladium in the diesel oxidation reaction were not found to show any favourable activity over γ-Al_2O_3, some early experiments have shown that mixed-metal β-$Ga_{2-x}Al_xO_3$ may show better activity as supports for palladium compared to both pure β-Ga_2O_3 and α-Al_2O_3 in the semi-hydrogenation of acetylene. Further investigation should be carried out using these beta polymorphs in acetylene semi-hydrogenation under a wider range of temperatures and as a function of oxide surface area and Pd loading. Other techniques, such as Pd K-edge XANES and EXAFS would help elucidate the nature of Pd on the gallium oxide based supports, in particular to confirm the hypothesis that the alloy Pd_2Ga is present.

7.3 Chapter 5: Solvothermal Reactions of Gallium Precursors and Early First Row Transition Metal Salts

In Chapter 5 the synthesis and characterisation of a new vanadium gallium oxyhydroxide, a new chromium substituted gallium oxide spinel, and a manganese gallium oxide spinel were presented.

A new vanadium gallium oxyhydroxide was prepared by a simple solvothermal reaction of gallium metal and sodium orthovanadate in an aqueous ethanolamine solvent. The average structure, refined from simultaneous powder neutron time-of-flight (PND), and powder X-ray diffraction (PXRD), was shown to be analogous to the structure of the minerals tohdite (akdalaite), nolanite and ferrihydrite. The hydrogen site was found to be partially occupied giving the chemical formula $Ga_{2.52}V_{1.48}O_{7.31}(OH)_{0.69}$. Significant anisotropic peak broadening was observed in the powder XRD pattern likely due to the hexagonal plate nature of the material, whilst in both the PXRD and PND data a small 2θ offset was observed in the reflections

attributed to micro-strain within the crystallite. V K-edge XANES confirmed the expected oxidation state in $Ga_{2.52}V_{1.48}O_{7.31}(OH)_{0.69}$ as $V^{\sim 3.1+}$.

Around 300 °C the material dehydrates with subsequent oxidation of the vanadium (which was confirmed by XANES) and contraction of the unit cell. The material subsequently decomposes around 550 °C. The material showed promise as a catalyst in the oxidative dehydrogenation of propane reaction to produce olefins, and is currently being screened at the Johnson Matthey Technology Centre for other gas-phase reactions.

Chromium has been substituted into the defect spinel γ-Ga_2O_3 for the first time. The synthesis was based on the 1,4-butanediol synthesis first presented in Chapter 4. PXRD showed that the material was very poorly crystalline. XANES confirmed that Cr was present in the trivalent state, as expected, and that it was very likely all in octahedral coordination.

A manganese gallium oxide has been prepared by solvothermal synthesis in 2-propanol. The only previous solvothermal synthesis of this material used a microwave-assisted solvothermal reaction.[12] In this literature synthesis of the Mn-Ga spinel manganese sulfate and gallium nitrate were dissolved in deionised water followed by adjustment of the solution to pH 12. The mixture was then sealed and reacted in a microwave at 180 °C for 60 minutes. pH control was cited as being a key control over synthesising phase pure manganese gallate. The synthesis of manganese gallate in this work can take place from simple reaction using a variety of manganese salts, and gallium acetylacetonate in 2-propnaol or 1,4-butanediol without any other steps required such as pH control. The spinel is different to the analogous spinel prepared at high temperature: Mn K-edge XANES suggested that the spinel was largely an inverse spinel, whereas $MnGa_2O_4$ prepared by a solid-state reaction was found to be a largely normal spinel.[13,14] The microwave-solvothermal manganese gallate was not characterised in detail, since the paper focussed on the complex mixed-metal Co-Mn-Ga spinel which showed higher activity as a water oxidation catalyst. The new manganese gallium spinel is also metastable decomposing around 500 °C into respective binary oxides of manganese and gallium, showing that it could not be made at high temperature.

Further work regarding a more detailed structural investigation of the vanadium gallium oxyhydroxide would involve a PDF study, combined with RMC to build models to look at vanadium/gallium distribution and to study the potential local disorder in the material and how it deviates from the average structure.

The chromium and manganese gallium oxide spinels are very poorly crystalline and detailed analysis of their average structures was not possible from conventional Rietveld analysis of the Bragg scattering. A PDF and RMC study of both spinels would be highly desired in order to characterise the internal atomic structure of these materials. Though it is unlikely the Cr/γ-Ga_2O_3 material will not find use in any catalysis owing to the possibility of toxic Cr^{6+} forming, the manganese gallium oxide spinel may be of use if, for example, it were to be incorporated into $CoGa_2O_4$ (which can be prepared by a similar reaction), as a spinel $(Co,Mn)Ga_2O_4$ has been tested and shown to be a useful water oxidation catalyst.[12]

7.4 Chapter 6: Exploratory Hydrothermal Synthesis of Rhodium Materials

In this chapter, the findings from an investigation into the synthesis of rhodium materials by hydrothermal synthesis was presented. Unlike previous work in Warwick on similar reactions involving the precious metals ruthenium and iridium, where ternary oxides containing highly oxidised metal could be isolated, such as $SrRu_2O_6$,[15] $Ca_{1.45}Ru_2O_7$[15] and $Na_{0.27}Sr_{0.73}IrO_{3.77}$,[16] for rhodium, hydroxides of Rh^{3+} are found to form. Two hydrogarnets were prepared by mild hydrothermal reactions, $Ca_3Rh_2(OH)_{12}$ and $Sr_3Rh_2(OH)_{12}$. These hydrogarnets had been reported previously but analysis of the average structure by diffraction techniques was lacking until this work. The calcium rhodium hydrogarnet thermally decomposes into $CaRh_2O_4$, which can be isolated phase-pure by washing away the CaO also formed, whilst the strontium hydrogarnet behaves differently and decomposes into a material that appears to be a member of the $Sr_6Rh_5O_{15}$ family. The choice of mineraliser was found to be important in these reactions, as if KOH was substituted for NaOH in the reaction between $RhCl_3$ and $Ca(OH)_2$ then a new phase in the Ca-Na-Rh-OH system was formed. This material has yet to be identified but IR, TGA and thermodiffractometry suggest it is likely a hydroxide. Upon gentle heating the material decomposes into $NaRhO_2$, a delafossite.

Further work would include attempting to grow single crystals of the hydroxide phase in order to solve the structure of this material.

A new material $BaNaRh(OH)_6$ was prepared by hydrothermal reaction. Its structure was solved by single crystal X-ray diffraction: the material contains isolated Rh-O octahedra, with 2 crystallographically different 8-coordinate Na^+ sites, and a 10 coordinate Ba^{2+}. The presence of two ordered Na sites with a high coordination was confirmed by solid state ^{23}Na MAS NMR.

Further work would involve ascertaining the hydrogen positions in this structure. This may be possible from a powder neutron diffraction study if the material can be deuterated. It is unlikely that X-ray diffraction alone would be able to locate the hydrogen positions in the presence of the heavy scatterers barium and rhodium. The thermal decomposition product of this material is currently inconclusive and further work in trying to identify unit cell parameters for this material needs to be undertaken. Rh K-edge XANES has shown that the decomposition product contains a portion of Rh^{4+} and therefore this oxide material may display interesting magnetic and/or electronic properties, which remain to be investigated. Changes in the reaction such as which base is used or how much solvent and reagent result in new phases forming. A hexagonal phase is obtained with KOH, and a low water volume, whilst an amorphous phase is formed when the volume of water is increased. Through optimisation of the reaction parameters single crystals of this hexagonal phase might possibly be obtained which would clearly facilitate structure solution. In the NaOH reaction, a high concentration of $Ba(OH)_2$ leads to the formation of a crystalline but unidentifiable phase. Attempts to grow single crystals of this phase have currently been unsuccessful but further reactions may prove fruitful in obtaining crystals to identify the structure of this phase. The work from this Chapter is summarised in Figure 7.1, and the results will hopefully soon be written up as a paper.

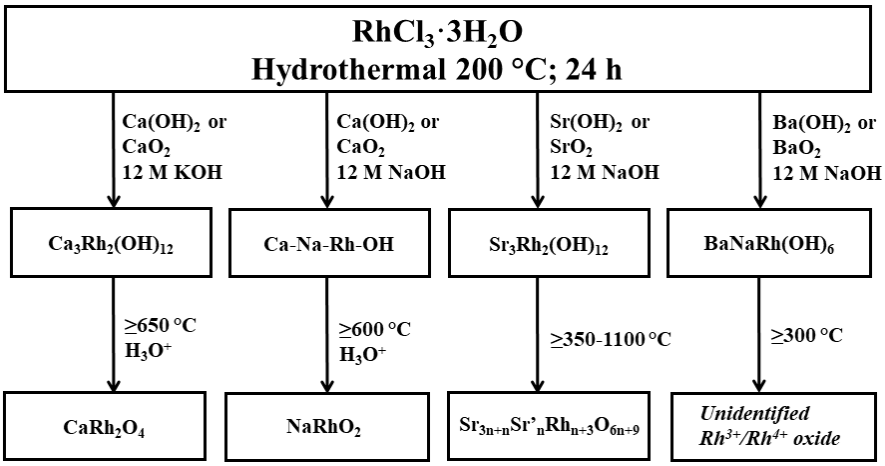

Figure 7.1 Summary of hydrothermal synthesis of rhodium materials and their decomposition products.

7.5 General concluding remarks

The solvothermal synthesis work with gallium salts is summarised in Figure 7.2. Not all materials displayed in Figure 7.2 were presented in earlier chapters in this thesis due to shortage of space but are included here for completeness.

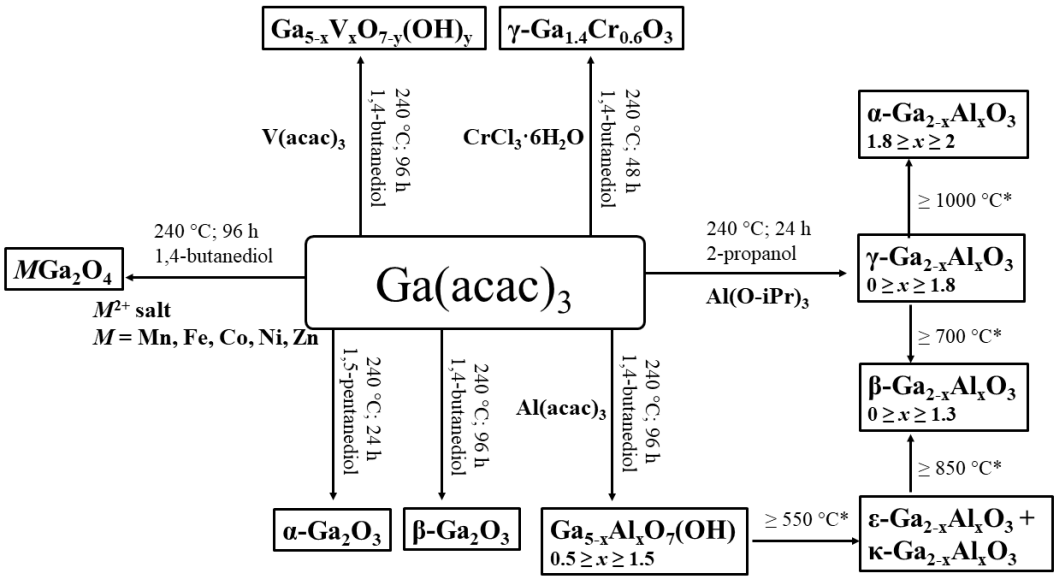

Figure 7.2 Solvothermal synthesis of materials prepared using $Ga(acac)_3$ as a reagent. *denotes heating in air (*i.e.* not solvothermal).

The work regarding reactions from gallium metal is summarised in Figure 7.3 along with some results on the synthesis of $Ga_5O_7(OH)$ and γ-Ga_2O_3 previously reported by Playford *et al.*[17] The synthesis of GaOOH and α-Ga_2O_3 were also taken from the

literature[18] but are included to show the versatility of gallium metal in hydro(solvo)thermal reactions, and the interconversion of gallium oxide polymorphs.

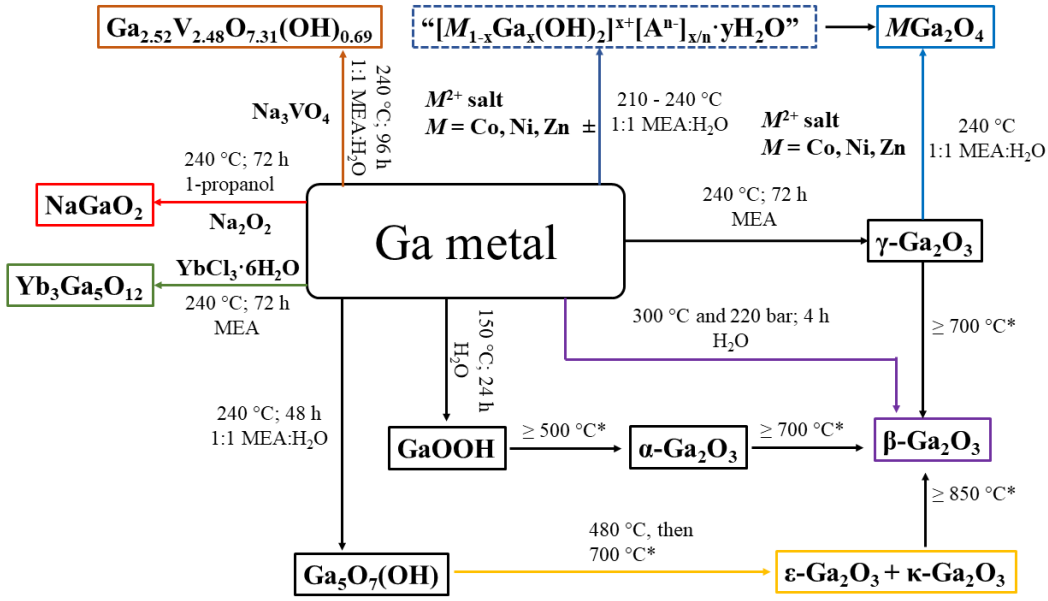

Figure 7.3 Hydro(solvo)thermal synthesis of materials which can be prepared, in many cases, directly from gallium metal. *denotes heating in air (*i.e.* not hydro(solvo)thermal). ± - a layered double hydroxide was observed when cobalt nitrate was used, but the other metals do form mixed-metal spinels at 240 °C under the conditions given. The dashed box represents a transient phase during the solvothermal reaction. Coloured boxes and arrows denote where a new material has been prepared, or where a known material has been prepared from a previously unreported synthesis.

The work is this thesis has shown that a wide variety of different materials can be prepared by solvothermal reactions using gallium based precursors. It is anticipated that other, potentially novel, mixed-metal gallium containing materials could also be prepared under solvothermal conditions by altering the solvent used, and likely by changing the temperature and duration of the experiment. This work would be timely because of the recent growth in interest in gallium oxide polymorphs for electronic applications,[19–22] the use of nanocrystalline spinel oxides in photocatalysis[23] and the use of supported Pd_2Ga alloy as a catalyst for various organic transformations, for which several papers have appeared during the course of the work described in this thesis.[24–26] New routes to these materials with control of crystal form would be very beneficial.

7.6 References

1 S. Britto, A. V. Radha, N. Ravishankar and P. V. Kamath, *Solid State Sci.*, 2007, **9**, 279–286.

2 D. G. Evans and R. C. T. Slade, *Struct. Bond.*, 2006, **119**, 1–87.

3 I. Pausch, *Clays Clay Miner.*, 1986, **34**, 507–510.

4 Z. P. Xu and H. C. Zeng, *Chem. Mater.*, 1999, **11**, 67–74.

5 J. He, M. Wei, B. Li, Y. Kang, D. G. Evans and X. Duan, *Layer. Double Hydroxides*, 2006, **119**, 89–119.

6 N. Iyi, K. Fujii, K. Okamoto and T. Sasaki, *Appl. Clay Sci.*, 2007, **35**, 218–227.

7 V. Rives, *Mater. Chem. Phys.*, 2002, **75**, 19–25.

8 G. G. C. Arizaga, K. G. Satyanarayana and F. Wypych, *Solid State Ionics*, 2007, **178**, 1143–1162.

9 H. Y. Playford, A. C. Hannon, M. G. Tucker, D. M. Dawson, S. E. Ashbrook, R. J. Kastiban, J. Sloan and R. I. Walton, *J. Phys. Chem. C*, 2014, **118**, 16188−16198.

10 H. Y. Playford, A. C. Hannon, M. G. Tucker, M. R. Lees and R. I. Walton, *J. Phys. Condens. Matter*, 2013, **25**, 454212.

11 S. C. Abrahams, J. M. Reddy and J. L. Bernstein, *J. Chem. Phys.*, 1965, **42**, 3957–3968.

12 F. Conrad, M. Bauer, D. Sheptyakov, S. Weyeneth, D. Jaeger, K. Hametner, P.-E. Car, J. Patscheider, D. Günther and G. R. Patzke, *RSC Adv.*, 2012, **2**, 3076–3082.

13 B. Boucher, A. G. Herpin and A. Oles, *J. Appl. Phys.*, 2012, **960**, 33–35.

14 B. Boucher and A. Oles, *J. Phys. Fr.*, 1966, **27**, 51–56.

15 C. I. Hiley, M. R. Lees, J. M. Fisher, D. Thompsett, S. Agrestini, R. I. Smith and R. I. Walton, *Angew. Chem.*, 2014, **126**, 4512–4516.

16 K. Sardar, J. Fisher, D. Thompsett, M. R. Lees, G. J. Clarkson, J. Sloan, R. J. Kashtiban and R. I. Walton, *Chem. Sci.*, 2011, **2**, 1573.

17 H. Y. Playford, A. C. Hannon, E. R. Barney and R. I. Walton, *Chem. Eur. J*, 2013, **19**, 2803–2813.

18 J. C. Lavalley, M. Daturi, V. Montouillout, G. Clet, C. Otero Areán, M. Rodríguez Delgado and A. Sahibed-dine, *Phys. Chem. Chem. Phys.*, 2003, **5**, 1301–1305.

19 X. Xia, Y. Chen, Q. Feng, H. Liang, P. Tao, M. Xu and G. Du, *Appl. Phys. Lett.*, 2016, **108**, 1–6.

20 I. Cora, F. Mezzadri, F. Boschi, M. Bosi, M. Čaplovičová, G. Calestani, I. Dódony, B. Pécz and R. Fornari, *CrystEngComm*, 2017, **19**, 1509–1516.

21 M. Higashiwaki, K. Sasaki, H. Murakami, Y. Kumagai, A. Koukitu, A. Kuramata, T. Masui and S. Yamakoshi, *Semicond. Sci. Technol.*, 2016, **31**, 34001.

22 A. E. Romanov, S. I. Stepanov, V. I. Nikolaev and V. E. Bougrov, *Rev. Adv. Mater. Sci*, 2016, **44**, 63–86.

23 M. Hirano, K. Sakoda and Y. Hirose, *J. Sol-Gel Sci. Technol.*, 2016, **77**, 348–354.

24 A. Haghofer, K. Föttinger, F. Girgsdies, D. Teschner, A. Knop-Gericke, R. Schlögl and G. Rupprechter, *J. Catal.*, 2012, **286**, 13–21.

25 H. Lorenz, R. Thalinger, E.-M. Köck, M. Kogler, L. Mayr, D. Schmidmair, T. Bielz, K. Pfaller, B. Klötzer and S. Penner, *Appl. Catal. A Gen.*, 2013, **453**, 34–44.

26 K. Föttinger, *Catal. Today*, 2013, **208**, 106–112.

Appendix A

Appendix A

Chapter 4

Refinement statistics for all β-$Ga_{2-x}Al_xO_3$ samples

Table A.1 Refined crystal parameters for β-$Ga_{1.8}Al_{0.2}O_3$ a = 12.17969(16) Å, b = 3.02652(4) Å, c = 5.79034(8) Å, β = 103.8996(11) °, Space group $C2/m$, Rp = 15.1%, wRp = 21.6%

Atom	Wyckoff site	*x*	*y*	*z*	Occupancy	Beq / Å^2
Ga1	4i	0.09020(19)	0	-0.2068(5)	0.923(7)	0.20(11)
Al1	4i	0.09020(19)	0	-0.2068(5)	0.071(7)	0.20(11)
Ga2	4i	0.34139(17)	0	-0.3129(4)	0.871(7)	0.75(13)
Al2	4i	0.34139(17)	0	-0.3129(4)	0.129(7)	0.75(13)
O1	4i	0.1619(7)	0	0.107(2)	1	0.2(3)
O2	4i	0.4963(7)	0	0.2551(12)	1	0.2(3)
O3	4i	0.8277(6)	0	0.425(2)	1	0.3(3)

Table A.2 Refined crystal parameters for β-$Ga_{1.6}Al_{0.4}O_3$ a = 12.12962(16) Å, b = 3.01117(4) Å, c = 5.76915(8) Å, β = 103.9386(10) °, Space group $C2/m$, Rp = 13.0%, wRp = 18.3%

Atom	Wyckoff site	*x*	*y*	*z*	Occupancy	Beq / Å^2
Ga1	4i	0.09058(17)	0	-0.2058(4)	0.864(5)	0.45(8)
Al1	4i	0.09058(17)	0	-0.2058(4)	0.136(5)	0.45(8)
Ga2	4i	0.34117(15)	0	-0.3137(4)	0.736(5)	0.44(8)
Al2	4i	0.34117(15)	0	-0.3137(4)	0.264(5)	0.44(8)
O1	4i	0.1621(5)	0	0.1106(15)	1	0.20(19)
O2	4i	0.4969(5)	0	0.2556(9)	1	0.6(2)
O3	4i	0.8272(5)	0	0.431(16)	1	0.20(17)

Table A.3 Refined crystal parameters for β-$Ga_{1.4}Al_{0.6}O_3$ a = 12.0711(2) Å, b = 2.99309(5) Å, c = 5.74510(11) Å, β = 103.9722(16) °, Space group $C2/m$, Rp = 13.7%, wRp = 17.7%

Atom	Wyckoff site	*x*	*y*	*z*	Occupancy	Beq / Å^2
Ga1	4i	0.09149(19)	0	-0.2059(4)	0.788(5)	0.77(9)
Al1	4i	0.09149(19)	0	-0.2059(4)	0.212(5)	0.77(9)
Ga2	4i	0.34206(16)	0	-0.3125(4)	0.612(5)	0.6(1)
Al2	4i	0.34206(16)	0	-0.3125(4)	0.388(5)	0.6(1)
O1	4i	0.1607(5)	0	0.1120(16)	1	0.2(19)
O2	4i	0.4971(5)	0	0.2581(9)	1	0.2(19)

O3	4i	0.8273(5)	0	0.4262(17)	1	0.2(19)

Table A.4 Refined crystal parameters for β-$Ga_{1.2}Al_{0.8}O_3$ a = 12.04817(12) Å, b = 2.98611(3) Å, c = 5.73543(6) Å, β = 104.0053(8) °, Space group $C2/m$, Rp = 14.3%, wRp = 19.6%

Atom	Wyckoff site	*x*	*y*	*z*	Occupancy	Beq / Å^2
Ga1	4i	0.09110(18)	0	-0.2046(4)	0.713(5)	0.79(8)
Al1	4i	0.09110(18)	0	-0.2046(4)	0.287(5)	0.79(8)
Ga2	4i	0.34211(17)	0	-0.3131(4)	0.487(5)	0.33(9)
Al2	4i	0.34211(17)	0	-0.3131(4)	0.513(5)	0.33(9)
O1	4i	0.1630(5)	0	0.1109(13)	1	0.36(17)
O2	4i	0.4962(5)	0	0.2570(9)	1	0.20(19)
O3	4i	0.8268(5)	0	0.4350(13)	1	0.20(17)

Table A.5 Refined crystal parameters for β-$Ga_{1.0}Al_{1.0}O_3$ a = 11.99483(11) Å, b = 2.97101(25) Å, c = 5.71499(5) Å, β = 104.0448(7) °, Space group $C2/m$, Rp = 11.1%, wRp = 15.1%

Atom	Wyckoff site	*x*	*y*	*z*	Occupancy	Beq / Å^2
Ga1	4i	0.09117(14)	0	-0.2047(3)	0.618(3)	0.54(6)
Al1	4i	0.09117(14)	0	-0.2047(3)	0.382(3)	0.54(6)
Ga2	4i	0.34169(14)	0	-0.3139(3)	0.382(3)	0.52(8)
Al2	4i	0.34169(14)	0	-0.3139(3)	0.618(3)	0.52(8)
O1	4i	0.1623(4)	0	0.108(1)	1	0.2(13)
O2	4i	0.4967(4)	0	0.2570(7)	1	0.2(14)
O3	4i	0.8261(4)	0	0.433(1)	1	0.2(13)

Table A.6 Refined crystal parameters for β-$Ga_{0.8}Al_{1.2}O_3$ a = 11.94422(14) Å, b = 2.95565(3) Å, c = 5.69198(7) Å, β = 104.0603(9) °, Space group $C2/m$, Rp = 13.2%, wRp = 18.2%

Atom	Wyckoff site	*x*	*y*	*z*	Occupancy	Beq / Å^2
Ga1	4i	0.09080(17)	0	-0.2051(4)	0.506(4)	0.74(8)
Al1	4i	0.09080(17)	0	-0.2051(4)	0.494(4)	0.74(8)
Ga2	4i	0.34135(17)	0	-0.3148(4)	0.294(4)	0.49(9)
Al2	4i	0.34135(17)	0	-0.3148(4)	0.706(4)	0.49(9)
O1	4i	0.1622(4)	0	0.1085(11)	1	0.8
O2	4i	0.4966(4)	0	0.2575(8)	1	0.8
O3	4i	0.8264(4)	0	0.4329(11)	1	0.8

Table A.7 Refined crystal parameters for β-$Ga_{0.7}Al_{1.3}O_3$, a = 11.90851(10) Å, b = 2.94608(3) Å, c = 5.67840(5) Å, β = 104.0810(8) °, Space group $C2/m$, Rp = 11.4%, wRp = 15.5%

Atom	Wyckoff site	*x*	*y*	*z*	Occupancy	Beq / Å^2
Ga1	4i	0.0907(14)	0	-0.2052(3)	0.463(3)	0.73(7)
Al1	4i	0.0907(14)	0	-0.2052(3)	0.537(3)	0.73(7)
Ga2	4i	0.31483(14)	0	-0.3150(3)	0.237(3)	0.64(8)
Al2	4i	0.31483(14)	0	-0.3150(3)	0.763(3)	0.64(8)
O1	4i	0.1614(3)	0	0.1098(9)	1	0.8
O2	4i	0.4970(4)	0	0.2580(6)	1	0.57(4)
O3	4i	0.8268(3)	0	0.4315(9)	1	0.47(9)

Chapter 5

Synthesis of V_2O_3 and $VO(acac)_2$ XANES reference samples

V_2O_3

0.4 g (1.15 mmol) of $V(acac)_3$ (Aldrich, 97%) was added to a PTFE liner with addition of 10 ml 2-propanol. The liner was placed inside a stainless-steel autoclave which was then set inside a fan-assisted preheated oven at 240 °C. The reaction was left for 24 hours and then removed to cool naturally to ambient temperature. The material was collected by vacuum filtration and dried overnight to yield black nano-crystalline V_2O_3, as confirmed by powder XRD.

$VO(acac)_2$

This synthesis was based on the method by Rowe and Jones.[1] 10 g (0.06 mol) of V_2O_5 (Aldrich, 99.99%) was added to a round-bottomed flask with 30 ml DI water, followed by addition of 20 ml conc. sulfuric acid, and 50 ml ethanol. The material was heated to reflux with condenser attached. In accordance with that reported by Rowe and Jones, over the course of 30 minutes, the V_2O_5 slurry darkened as the mixture was heated, then turned light-green, and finally a dark blue, indicating the presence of the vanadyl cation. The mixture was filtered and then returned to the round bottomed flask followed by addition of 25 ml acetylacetonate. The mixture was then neutralized by very slow addition of a solution of 40 g sodium carbonate dissolved in 50 ml DI water. The slow addition is necessary to prevent

excess frothing. The crude $VO(acac)_2$ was isolated by vacuum filtration, and then recrystallized in the minimum amount of hot chloroform. The yield was ~70%.

Chapter 6

Crystal structure determination of $BaNaRh(OH)_6$

A yellow diamond shaped crystal was selected from a sample containing about 80% powder and 20% of a more crystalline material

Note - There was a G alert from the cif checker saying it may be a higher symmetry space group (P4(2)/mnc. This was investigated by attempted solution and refinement in the higher space group and but this gave a higher Rint (~5%) and required a model with disordered and partially occupied oxygens so was abandoned.

Experimental

Single crystals of $BaNaO_6Rh$ were grown from the method described in Chapter 6. A suitable crystal was selected and mounted on a glass fibre with Fromblin oil and placed on a Rigaku Oxford Diffraction SuperNova diffractometer with a duel source (Cu at zero) equipped with an AtlasS2 CCD area detector. The crystal was kept at 150(2) K during data collection. Using Olex2 [1], the structure was solved with the ShelXT [2] structure solution program using Intrinsic Phasing and refined with the ShelXL [3] refinement package using Least Squares minimisation.

1 Dolomanov, O.V., Bourhis, L.J., Gildea, R.J, Howard, J.A.K. & Puschmann, H. (2009), J. Appl. Cryst. 42, 339-341.
2 Sheldrick, G.M. (2015). Acta Cryst. A71, 3-8.
3 Sheldrick, G.M. (2015). Acta Cryst. C71, 3-8.

Crystal Data for $BaNaO_6Rh$ (M =359.24 g/mol): tetragonal, space group $P4_2/n$ (no. 86), a = 8.28420(10) Å, c = 8.41980(10) Å, V = 577.834(16) $Å^3$, Z = 4, T = 150(2) K, μ(MoKα) = 9.657 mm^{-1}, *Dcalc* = 4.129 g/cm^3, 13160 reflections measured ($6.9° \leq 2\Theta \leq 65.584°$), 1023 unique ($R_{int}$ = 0.0324, R_{sigma} = 0.0157) which were used in all calculations. The final R_1 was 0.0211 ($I > 2\sigma(I)$) and wR_2 was 0.0505 (all data).

Table 1 Crystal data and structure refinement for dc2.

Identification code	dc2
Empirical formula	$BaNaO_6Rh$
Formula weight	359.24
Temperature/K	150(2)
Crystal system	tetragonal
Space group	$P4_2/n$
a/Å	8.28420(10)
b/Å	8.28420(10)
c/Å	8.41980(10)
α/°	90
β/°	90
γ/°	90
Volume/Å^3	577.834(16)
Z	4
ρ_{calc}g/cm^3	4.129
μ/mm^{-1}	9.657
F(000)	640.0
Crystal size/mm^3	0.18 × 0.18 × 0.18 yellow diamond

Radiation	MoKα (λ = 0.71073)
2Θ range for data collection/°	6.9 to 65.584
Index ranges	$-12 \le h \le 12$, $-11 \le k \le 11$, $-12 \le l \le 12$
Reflections collected	13160
Independent reflections	1023 [R_{int} = 0.0324, R_{sigma} = 0.0157]
Data/restraints/parameters	1023/0/43
Goodness-of-fit on F^2	1.273
Final R indexes [I>=2σ (I)]	R_1 = 0.0211, wR_2 = 0.0490
Final R indexes [all data]	R_1 = 0.0258, wR_2 = 0.0505
Largest diff. peak/hole / e Å^{-3}	1.00/-1.53

Table 2 Fractional Atomic Coordinates (×10^4) and Equivalent Isotropic Displacement Parameters (Å^2×10^3) for dc2. U_{eq} is defined as 1/3 of of the trace of the orthogonalised U_{IJ} tensor.

Atom	*x*	*y*	*z*	U(eq)
Ba1	2500	7500	7901.3(3)	9.10(8)
Rh1	5000	5000	5000	5.99(8)

Na1	2500	2500	7500	13.7(5)
Na2	2500	2500	2500	26.3(8)
O3	2618(3)	5407(3)	5459(3)	10.5(4)
O1	4536(3)	2606(3)	5471(3)	9.9(4)
O2	4456(3)	4587(3)	2654(3)	9.8(4)

Table 3 Anisotropic Displacement Parameters ($Å^2×10^3$) for dc2. The Anisotropic displacement factor exponent takes the form: $-2\pi^2[h^2a^{*2}U_{11}+2hka^*b^*U_{12}+\ldots]$.

Atom	U_{11}	U_{22}	U_{33}	U_{23}	U_{13}	U_{12}
Ba1	11.25(13)	8.84(13)	7.21(13)	0	0	-3.14(8)
Rh1	5.92(16)	6.16(16)	5.89(15)	-0.09(11)	-0.19(11)	-0.02(10)
Na1	15.6(8)	15.6(8)	9.8(12)	0	0	0
Na2	4.4(7)	4.4(7)	70(2)	0	0	0
O3	8.9(10)	11.4(11)	11.2(11)	-1.2(8)	1.3(8)	1.7(8)
O1	12.1(11)	8.5(10)	9.2(10)	1.7(8)	1.9(8)	0.6(8)
O2	11.7(10)	10.3(10)	7.3(10)	-0.8(8)	-1.3(8)	-0.5(8)

Table 4 Bond Lengths for dc2.

Atom	Atom	Length/Å	Atom	Atom	Length/Å
Ba1	$Rh1^1$	3.42065(13)	Rh1	$O1^6$	2.059(2)

Ba1	Rh1[2]	3.42065(14)	Rh1	O2	2.054(2)
Ba1	O3[2]	2.767(2)	Rh1	O2[6]	2.054(2)
Ba1	O3[3]	2.692(2)	Na1	O3	2.960(2)
Ba1	O3	2.691(2)	Na1	O3[5]	2.960(2)
Ba1	O3[1]	2.767(2)	Na1	O3[8]	2.960(2)
Ba1	O1[4]	2.813(2)	Na1	O3[9]	2.960(2)
Ba1	O1[5]	2.813(2)	Na1	O1[8]	2.402(2)
Ba1	O2[2]	2.914(2)	Na1	O1	2.402(2)
Ba1	O2[1]	2.914(2)	Na1	O1[9]	2.402(2)
Ba1	O2[6]	3.093(2)	Na1	O1[5]	2.402(2)
Ba1	O2[7]	3.093(2)	Na2	O1[10]	3.018(2)
Rh1	Na1[6]	3.60684(3)	Na2	O1[11]	3.018(2)
Rh1	Na1	3.60684(3)	Na2	O1	3.018(2)
Rh1	Na2[6]	3.60684(3)	Na2	O1[8]	3.018(2)
Rh1	Na2	3.60684(3)	Na2	O2[10]	2.373(2)
Rh1	O3	2.039(2)	Na2	O2[11]	2.373(2)
Rh1	O3[6]	2.039(2)	Na2	O2[8]	2.373(2)
Rh1	O1	2.059(2)	Na2	O2	2.373(2)

[1]-1/2+Y,1-X,1/2+Z; [2]1-Y,1/2+X,1/2+Z; [3]1/2-X,3/2-Y,+Z; [4]+Y,3/2-X,3/2-Z; [5]1/2-Y,+X,3/2-Z; [6]1-X,1-Y,1-Z; [7]-1/2+X,1/2+Y,1-Z; [8]1/2-X,1/2-Y,+Z; [9]+Y,1/2-X,3/2-Z; [10]1/2-Y,+X,1/2-Z; [11]+Y,1/2-X,1/2-Z

Table 5 Bond Angles for dc2.

Atom	Atom	Atom	Angle/°
$Rh1^{1}$	Ba1	$Rh1^{2}$	117.794(7)
$O3^{1}$	Ba1	$Rh1^{2}$	89.93(5)
O3	Ba1	$Rh1^{2}$	91.52(5)
$O3^{3}$	Ba1	$Rh1^{2}$	139.70(5)
$O3^{2}$	Ba1	$Rh1^{2}$	36.58(5)
$O3^{3}$	Ba1	$Rh1^{1}$	91.52(5)
O3	Ba1	$Rh1^{1}$	139.70(5)
$O3^{1}$	Ba1	$Rh1^{1}$	36.58(5)
$O3^{2}$	Ba1	$Rh1^{1}$	89.93(5)
O3	Ba1	$O3^{1}$	126.49(5)
$O3^{3}$	Ba1	$O3^{2}$	126.49(5)
$O3^{1}$	Ba1	$O3^{2}$	77.77(10)
$O3^{3}$	Ba1	$O3^{1}$	126.49(5)
O3	Ba1	$O3^{2}$	126.49(5)
O3	Ba1	$O3^{3}$	80.38(10)
$O3^{2}$	Ba1	$O1^{4}$	70.82(7)
$O3^{2}$	Ba1	$O1^{5}$	64.56(7)
$O3^{3}$	Ba1	$O1^{4}$	79.09(7)
$O3^{1}$	Ba1	$O1^{5}$	70.82(7)
$O3^{8}$	Na1	$Rh1^{11}$	141.90(5)
$O3^{11}$	Na1	$Rh1^{10}$	83.72(4)
$O3^{8}$	Na1	Rh1	83.72(4)
$O3^{5}$	Na1	$Rh1^{11}$	83.72(4)
O3	Na1	$Rh1^{2}$	83.72(4)
$O3^{11}$	Na1	$Rh1^{2}$	141.90(5)
$O3^{5}$	Na1	Rh1	141.90(5)
$O3^{5}$	Na1	$Rh1^{2}$	34.42(4)
O3	Na1	Rh1	34.42(4)
$O3^{5}$	Na1	$Rh1^{10}$	98.48(5)
$O3^{11}$	Na1	$Rh1^{11}$	34.42(4)
O3	Na1	$Rh1^{11}$	98.48(5)
$O3^{8}$	Na1	$Rh1^{2}$	98.48(5)
O3	Na1	$O3^{11}$	109.03(9)
$O3^{8}$	Na1	$O3^{5}$	109.03(9)
O3	Na1	$O3^{5}$	109.69(5)
$O3^{11}$	Na1	$O3^{8}$	109.69(5)
O3	Na1	$O3^{8}$	109.69(5)
$O3^{11}$	Na1	$O3^{5}$	109.69(5)

O3	Ba1	O1^{4}	158.95(7)	O1^{5}	Na1	Rh1	91.88(6)
O3^{1}	Ba1	O1^{4}	64.56(7)	O1^{5}	Na1	Rh1^{10}	90.52(6)
O3	Ba1	O1^{5}	79.09(7)	O1^{11}	Na1	Rh1^{11}	32.95(5)
O3^{3}	Ba1	O1^{5}	158.95(7)	O1^{5}	Na1	Rh1^{2}	32.95(5)
O3	Ba1	O2^{1}	105.88(7)	O1^{11}	Na1	Rh1^{10}	142.86(5)
O3^{2}	Ba1	O2^{2}	61.11(7)	O1	Na1	Rh1^{2}	142.86(5)
O3	Ba1	O2^{6}	105.92(7)	O1^{8}	Na1	Rh1^{11}	91.88(6)
O3	Ba1	O2^{2}	67.51(7)	O1	Na1	Rh1	32.95(5)
O3^{2}	Ba1	O2^{1}	126.46(7)	O1	Na1	Rh1^{11}	90.52(6)
O3^{2}	Ba1	O2^{7}	127.51(6)	O1^{11}	Na1	Rh1^{2}	91.88(6)
O3^{2}	Ba1	O2^{6}	68.07(7)	O1	Na1	Rh1^{10}	91.88(6)
O3^{1}	Ba1	O2^{6}	127.51(7)	O1^{8}	Na1	Rh1	142.86(5)
O3^{3}	Ba1	O2^{2}	105.88(7)	O1^{8}	Na1	Rh1^{10}	32.95(5)
O3^{1}	Ba1	O2^{7}	68.07(7)	O1^{5}	Na1	Rh1^{11}	142.86(5)
O3^{1}	Ba1	O2^{2}	126.46(7)	O1^{8}	Na1	Rh1^{2}	90.52(6)
O3^{3}	Ba1	O2^{1}	67.51(7)	O1^{11}	Na1	Rh1	90.52(6)
O3^{3}	Ba1	O2^{6}	59.64(7)	O1	Na1	O3^{11}	68.91(7)
O3^{1}	Ba1	O2^{1}	61.11(7)	O1	Na1	O3^{5}	169.37(7)
O3	Ba1	O2^{7}	59.64(7)	O1	Na1	O3	62.24(7)
O3^{3}	Ba1	O2^{7}	105.92(7)	O1^{8}	Na1	O3^{5}	68.91(7)
O1^{4}	Ba1	Rh1^{1}	36.97(5)	O1^{11}	Na1	O3	68.91(7)

O1[5]	Ba1	Rh1[1]	107.21(5)	O1[8]	Na1	O3[8]	62.24(7)
O1[5]	Ba1	Rh1[2]	36.97(5)	O1[8]	Na1	O3	169.37(7)
O1[4]	Ba1	Rh1[2]	107.21(5)	O1[5]	Na1	O3	80.95(7)
O1[4]	Ba1	O1[5]	121.71(9)	O1[11]	Na1	O3[8]	169.37(7)
O1[4]	Ba1	O2[2]	123.09(7)	O1[5]	Na1	O3[11]	169.37(7)
O1[4]	Ba1	O2[7]	122.42(6)	O1	Na1	O3[8]	80.96(7)
O1[5]	Ba1	O2[1]	123.09(7)	O1[11]	Na1	O3[5]	80.96(7)
O1[4]	Ba1	O2[6]	67.12(6)	O1[5]	Na1	O3[8]	68.91(7)
O1[5]	Ba1	O2[2]	61.55(7)	O1[11]	Na1	O3[11]	62.24(7)
O1[5]	Ba1	O2[7]	67.12(6)	O1[5]	Na1	O3[5]	62.24(7)
O1[4]	Ba1	O2[1]	61.55(7)	O1[8]	Na1	O3[11]	80.96(7)
O1[5]	Ba1	O2[6]	122.42(6)	O1[5]	Na1	O1	120.38(7)
O2[1]	Ba1	Rh1[1]	36.76(5)	O1[11]	Na1	O1[5]	120.38(7)
O2[7]	Ba1	Rh1[2]	103.49(4)	O1[8]	Na1	O1	120.38(7)
O2[6]	Ba1	Rh1[2]	85.58(4)	O1[5]	Na1	O1[8]	89.35(11)
O2[2]	Ba1	Rh1[2]	36.76(5)	O1[11]	Na1	O1[8]	120.38(7)
O2[7]	Ba1	Rh1[1]	85.58(4)	O1[11]	Na1	O1	89.35(11)
O2[6]	Ba1	Rh1[1]	103.49(4)	Rh1[11]	Na2	Rh1[12]	109.913(1)
O2[2]	Ba1	Rh1[1]	151.03(5)	Rh1	Na2	Rh1[13]	109.913(1)
O2[1]	Ba1	Rh1[2]	151.03(5)	Rh1[12]	Na2	Rh1[13]	108.592(1)
O2[2]	Ba1	O2[7]	110.70(8)	Rh1	Na2	Rh1[11]	108.592(1)

O2[1]	Ba1	O2[7]	67.97(8)	Rh1[11]	Na2	Rh1[13]	109.913(1)
O2[6]	Ba1	O2[7]	162.60(9)	Rh1	Na2	Rh1[12]	109.913(1)
O2[2]	Ba1	O2[1]	171.82(9)	O1[14]	Na2	Rh1	141.98(4)
O2[1]	Ba1	O2[6]	110.70(8)	O1	Na2	Rh1[13]	141.98(4)
O2[2]	Ba1	O2[6]	67.97(8)	O1	Na2	Rh1[12]	100.35(4)
Ba1[8]	Rh1	Ba1[9]	180.0	O1[14]	Na2	Rh1[11]	100.35(4)
Ba1[8]	Rh1	Na1	72.454(2)	O1[15]	Na2	Rh1[13]	34.79(4)
Ba1[8]	Rh1	Na1[7]	107.546(2)	O1[15]	Na2	Rh1	100.35(4)
Ba1[9]	Rh1	Na1[7]	72.454(2)	O1	Na2	Rh1	34.79(4)
Ba1[9]	Rh1	Na1	107.546(2)	O1[11]	Na2	Rh1[12]	141.98(4)
Ba1[9]	Rh1	Na2	72.454(2)	O1	Na2	Rh1[11]	81.59(4)
Ba1[8]	Rh1	Na2	107.546(2)	O1[15]	Na2	Rh1[12]	81.59(4)
Ba1[9]	Rh1	Na2[7]	107.546(2)	O1[11]	Na2	Rh1[13]	100.35(4)
Ba1[8]	Rh1	Na2[7]	72.454(2)	O1[14]	Na2	Rh1[13]	81.59(4)
Na1	Rh1	Na1[7]	180.0	O1[11]	Na2	Rh1[11]	34.79(4)
Na2	Rh1	Na1	71.408(1)	O1[11]	Na2	Rh1	81.59(4)
Na2[7]	Rh1	Na1	108.592(1)	O1[14]	Na2	Rh1[12]	34.79(4)
Na2	Rh1	Na1[7]	108.592(1)	O1[15]	Na2	Rh1[11]	141.98(4)
Na2[7]	Rh1	Na1[7]	71.408(1)	O1	Na2	O1[14]	133.39(6)
Na2	Rh1	Na2[7]	180.0	O1[14]	Na2	O1[15]	68.04(9)
O3	Rh1	Ba1[9]	53.98(7)	O1	Na2	O1[15]	133.39(6)

O3	Rh1	Ba1[8]	126.02(7)	O1[14]	Na2	O1[11]	133.39(6)
O3[7]	Rh1	Ba1[8]	53.98(7)	O1[15]	Na2	O1[11]	133.39(6)
O3[7]	Rh1	Ba1[9]	126.02(7)	O1	Na2	O1[11]	68.04(9)
O3[7]	Rh1	Na1	124.86(7)	O2[14]	Na2	Rh1[13]	141.12(6)
O3	Rh1	Na1	55.14(7)	O2[15]	Na2	Rh1[11]	90.32(5)
O3	Rh1	Na1[7]	124.86(7)	O2[11]	Na2	Rh1[11]	32.61(6)
O3[7]	Rh1	Na1[7]	55.14(7)	O2[11]	Na2	Rh1[12]	90.32(5)
O3[7]	Rh1	Na2[7]	69.51(7)	O2[14]	Na2	Rh1[12]	32.61(6)
O3	Rh1	Na2	69.51(7)	O2	Na2	Rh1	32.61(6)
O3[7]	Rh1	Na2	110.49(7)	O2[11]	Na2	Rh1	141.12(6)
O3	Rh1	Na2[7]	110.49(7)	O2[15]	Na2	Rh1[12]	141.12(6)
O3[7]	Rh1	O3	180.0	O2[14]	Na2	Rh1	90.32(5)
O3[7]	Rh1	O1[7]	86.67(10)	O2	Na2	Rh1[12]	93.34(5)
O3	Rh1	O1[7]	93.33(10)	O2	Na2	Rh1[11]	141.12(6)
O3[7]	Rh1	O1	93.33(10)	O2[15]	Na2	Rh1[13]	32.61(6)
O3	Rh1	O1	86.67(10)	O2	Na2	Rh1[13]	90.32(5)
O3[7]	Rh1	O2	90.14(9)	O2[14]	Na2	Rh1[11]	93.34(5)
O3[7]	Rh1	O2[7]	89.86(9)	O2[11]	Na2	Rh1[13]	93.34(5)
O3	Rh1	O2[7]	90.14(9)	O2[15]	Na2	Rh1	93.34(5)
O3	Rh1	O2	89.86(9)	O2	Na2	O1[11]	110.93(7)
O1	Rh1	Ba1[9]	124.73(7)	O2	Na2	O1	63.38(7)

O1	Rh1	Ba1^{8}	55.27(7)	O2^{15}	Na2	O1	115.63(7)
O1^{7}	Rh1	Ba1^{8}	124.73(7)	O2	Na2	O1^{14}	115.63(7)
O1^{7}	Rh1	Ba1^{9}	55.27(7)	O2^{11}	Na2	O1	110.93(7)
O1	Rh1	Na1	39.38(6)	O2	Na2	O1^{15}	70.01(7)
O1^{7}	Rh1	Na1^{7}	39.38(6)	O2^{15}	Na2	O1^{15}	63.38(7)
O1	Rh1	Na1^{7}	140.62(6)	O2^{11}	Na2	O1^{11}	63.38(7)
O1^{7}	Rh1	Na1	140.62(6)	O2^{14}	Na2	O1^{14}	63.38(7)
O1^{7}	Rh1	Na2	123.22(7)	O2^{15}	Na2	O1^{14}	110.93(7)
O1	Rh1	Na2^{7}	123.22(7)	O2^{11}	Na2	O1^{15}	115.63(7)
O1^{7}	Rh1	Na2^{7}	56.78(7)	O2^{15}	Na2	O1^{11}	70.01(7)
O1	Rh1	Na2	56.78(7)	O2^{14}	Na2	O1	70.01(7)
O1	Rh1	O1^{7}	180.0	O2^{14}	Na2	O1^{15}	110.93(7)
O2	Rh1	Ba1^{8}	121.92(6)	O2^{14}	Na2	O1^{11}	115.63(7)
O2	Rh1	Ba1^{9}	58.08(6)	O2^{11}	Na2	O1^{14}	70.01(7)
O2^{7}	Rh1	Ba1^{9}	121.92(6)	O2^{11}	Na2	O2^{15}	90.172(6)
O2^{7}	Rh1	Ba1^{8}	58.08(6)	O2	Na2	O2^{15}	90.172(6)
O2	Rh1	Na1	109.84(6)	O2	Na2	O2^{14}	90.172(6)
O2^{7}	Rh1	Na1	70.16(6)	O2	Na2	O2^{11}	173.72(11)
O2	Rh1	Na1^{7}	70.16(6)	O2^{15}	Na2	O2^{14}	173.72(11)
O2^{7}	Rh1	Na1^{7}	109.84(6)	O2^{11}	Na2	O2^{14}	90.172(6)
O2^{7}	Rh1	Na2	141.50(6)	Ba1	O3	Ba1^{9}	100.93(8)

O2	Rh1	Na2[7]	141.50(6)	Ba1	O3	Na1	94.56(7)
O2[7]	Rh1	Na2[7]	38.50(6)	Ba1[9]	O3	Na1	163.86(9)
O2	Rh1	Na2	38.50(6)	Rh1	O3	Ba1	106.66(10)
O2[7]	Rh1	O1[7]	89.08(9)	Rh1	O3	Ba1[9]	89.44(8)
O2[7]	Rh1	O1	90.92(9)	Rh1	O3	Na1	90.44(8)
O2	Rh1	O1	89.08(9)	Ba1[8]	O1	Na2	152.92(9)
O2	Rh1	O1[7]	90.92(9)	Rh1	O1	Ba1[8]	87.76(8)
O2[7]	Rh1	O2	180.0	Rh1	O1	Na1	107.67(10)
Rh1[10]	Na1	Rh1[2]	108.592(1)	Rh1	O1	Na2	88.43(8)
Rh1	Na1	Rh1[2]	109.913(1)	Na1	O1	Ba1[8]	105.39(8)
Rh1[11]	Na1	Rh1[10]	109.913(1)	Na1	O1	Na2	101.31(8)
Rh1[11]	Na1	Rh1	108.592(1)	Ba1[9]	O2	Ba1[7]	157.97(8)
Rh1[11]	Na1	Rh1[2]	109.913(1)	Rh1	O2	Ba1[7]	93.41(8)
Rh1	Na1	Rh1[10]	109.913(1)	Rh1	O2	Ba1[9]	85.16(7)
O3[11]	Na1	Rh1	98.48(5)	Rh1	O2	Na2	108.89(10)
O3	Na1	Rh1[10]	141.90(5)	Na2	O2	Ba1[9]	103.16(8)
O3[8]	Na1	Rh1[10]	34.42(4)	Na2	O2	Ba1[7]	98.11(7)

[1]1-Y,1/2+X,1/2+Z; [2]-1/2+Y,1-X,1/2+Z; [3]1/2-X,3/2-Y,+Z; [4]+Y,3/2-X,3/2-Z; [5]1/2-Y,+X,3/2-Z; [6]-1/2+X,1/2+Y,1-Z; [7]1-X,1-Y,1-Z; [8]+Y,1/2-X,3/2-Z; [9]1-Y,1/2+X,-1/2+Z; [10]1-Y,-1/2+X,1/2+Z; [11]1/2-X,1/2-Y,+Z; [12]1-Y,-1/2+X,-1/2+Z; [13]-1/2+Y,1-X,-1/2+Z; [14]+Y,1/2-X,1/2-Z; [15]1/2-Y,+X,1/2-Z

References

1 R. A. Rowe and M. M. Jones, *Inorg. Synth.*, 1957, **5**, 114–115.